Studies on Novel Catalyst Designs for C-H Activation

by

Pawan Kumar
10CC20A26080

A thesis submitted to the
Academy of Scientific & Innovative Research
for the award of the degree of
DOCTOR OF PHILOSOPHY

in

SCIENCE

Under the supervision of

Dr. Vinod C. Prabhakaran

CSIR- National Chemical Laboratory, Pune

Academy of Scientific and Innovative Research AcSIR
Headquarters, CSIR-HRDC campus
Sector 19, Kamla Nehru Nagar,
Ghaziabad, U.P. – 201 002, India

September-2024

CERTIFICATE

This is to certify that the work incorporated in this Ph.D. thesis entitled ***“Studies on Novel Catalyst Designs for C-H Activation”*** submitted by **Mr. Pawan Kumar** to the Academy of Scientific and Innovative Research (AcSIR), in fulfillment of the requirements for the award of the Degree of ***Doctor of Philosophy in Science***, embodies original research work carried out by the student. We, further certify that this work has not been submitted to any other University or Institution in part or full for the award of any degree or diploma. Research material(s) obtained from other source(s) and used in this research work has/have been duly acknowledged in the thesis. Image(s), illustration(s), figure(s), table(s) etc., used in the thesis from other source(s), have also been duly cited and acknowledged.

Psingh

Pawan Kumar
Research Scholar
Date: 13/09/2024

Dr. Vinod C. Prabhakaran
Supervisor
Date: 13/09/2024

STATEMENTS OF ACADEMIC INTEGRITY

I, **Pawan Kumar**, a Ph.D. student of the Academy of Scientific and Innovative Research (AcSIR) with Registration No. **10CC20A26080,** hereby undertake that the thesis entitled "**Studies on Novel Catalyst Designs for C-H Activation**" has been prepared by me and that the document reports original work carried out by me and is free of any plagiarism in compliance with the UGC Regulations on *"Promotion of Academic Integrity and Prevention of Plagiarism in Higher Educational Institutions (2018)"* and the CSIR Guidelines for "*Ethics in Research and in Governance (2020)*".

Psingh

Mr. Pawan Kumar
Date: 13/09/2024
Place: CSIR-NCL, Pune

It is hereby certified that the work done by the student, under my/our supervision, is plagiarism-free in accordance with the UGC Regulations on *"Promotion of Academic Integrity and Prevention of Plagiarism in Higher Educational Institutions (2018)"* and the CSIR Guidelines for "*Ethics in Research and in Governance (2020)*".

Dr. Vinod C. Prabhakaran
Date: 13/09/2024
Place: CSIR-NCL, Pune

Acknowledgment

Pursuing a Ph.D. is akin to embarking on an extensive journey filled with unique experiences that lead you down an uncharted path toward a clearly defined goal. When you finally reach that destination and reflect on your journey, you come to appreciate that every effort and challenge was worthwhile. The minor achievements and unexpected insights, the setbacks and sudden breakthroughs, the knowledge gained in your field, and the friendships formed in the lab, all contribute to this remarkable adventure. Completing this PhD thesis represents the culmination of a journey that would not have been possible without the support and encouragement of numerous individuals.

First and foremost, I would like to express my profound gratitude to my supervisor, Dr. Vinod C. Prabhakaran, whose unwavering guidance, insightful feedback, and patience have been instrumental in completing this work. His dedication to excellence and constant encouragement prompted me to explore new ideas and refine my research, ultimately making this thesis a reality. My sincere admiration and respect for him cannot be expressed in words and will be cherished eternally.

I owe a great deal of gratitude to my advisory committee members, Dr. Santhosh S. Babu, Dr. Sreekumar Kurungot, Dr. Jayaraj Nithyanandhan, and Dr. Putla Sudarsanam (former member), for their expertise and constructive feedback that significantly influenced my research. Their insightful suggestions and discussions were vital in helping me navigate challenges. I am also thankful to Dr. Ashish Lele, the Director of the National Chemical Laboratory in Pune, Dr. V. V. Bokade (Head of the Catalysis Division), Dr. S. B. Umbarkar, and Dr. C. S. Gopinath (former HODs) for giving me this opportunity and providing all necessary infrastructure and facilities to carry out my research work at esteemed institute.

My heartfelt thanks extend to my seniors, Dr. Sharad Gupta, Dr. Govind Porwal, Dr. Betsy KJ, and Dr. Yogita, for their guidance and support throughout my PhD journey. I appreciate my lab-mates at Cat&MOSS, Anuradha, Sanket, Jyotsna, Pooja, Twinkle, Srishti, Arundhati, Mithra, Sharon, Chetan, and Srinath, for fostering a stimulating and collaborative environment. Special thanks to Anuradha and Dr. Sharad Gupta for their invaluable camaraderie, advice, and moral support. I also want to acknowledge the former members of Cat&MOSS (Sisira, Bhargavi, Manali, Yashi, Richa, Annie, Hridya, Safa) for their significant contributions to my PhD experience.

I am also deeply grateful to my collaborators, Iqra, Nikhil, Neeta, Abharana, Dr. Ali Haider, Dr. Bhattacharya, Dr. Rajashri, Dr. Biplab Ghosh, Dr. Tanmay, Dr. S. Krishnamurthy, Dr. T.G. Ajithkumar, and Dr. Sapna Ravindranathan. Your innovative ideas, constructive feedback, and teamwork have enriched my research experience and significantly enhanced the quality of this work. I have learned so much from each of you, and I cherish the collaborative spirit we cultivated.

I would like to extend my sincere gratitude to Dr. Jean-Philippe Dacquin for his exceptional care and invaluable support throughout my time at Lille University in France. I take this moment to acknowledge his significant contributions in enhancing my scientific thinking and knowledge. I am also deeply thankful to Dr. Sebastien Royer and Dr. Jeremy Dhainaut for their kindness and concern during my stay. My appreciation goes out to all my lab colleagues at UCCS, Lille University, and the technical staff for their assistance in completing my work. Lastly, I express my heartfelt thanks to Ganesh, Aditi, Neethu, Subham and Jash for their care and support during my time in Lille.

I would like to thank Dr. Sunita Barve, Mr. Gati Krushna Nayak, and the other library staff for their invaluable support and for granting me access to the library. I also appreciate the ACSIR Coordinators and staff for their assistance with documentation throughout this process. I sincerely thank the CAF team (Tushar, Chetan, Medha, Anirudh) for their help in characterization slots. Additionally, I am thankful to all the scientific and non-scientific personnel at CSIR-NCL for their support during my time as a research student.

I am thankful for my batchmates at NCL, including Sonu, Ankit, Aman, Biplab, Chandni, Kajal, Jyoti, Umasharan, Himanshu, Nittan, Hrishi, Sidharth, Subhashree, Ashwini, Tazeen, and Mahima, who made this journey enjoyable and motivating. My 'Apni Rasoi' partners (Vishal, Manish, Dr. Lavanya, and Dr. Prashant) with whom I learned cooking together and share countless moments of joy. Your encouragement and guidance have truly been the cherry on the cake, providing me with the motivation and strength to persevere through the challenges of my PhD journey. My friends and colleagues from NCL, Dr. Himanshu, Dr. Abha, Dr. Kritika Gour, Dr. Jyoti, Dr. Nitin, Dr. Sphurti, Dr. Yayati, Dr. Rohit (Sr. and Jr.), Dr. Swapnil, Viksit, Bharath, Dr. Prem, Pawan, Dr. Dharmender, Soumya, Sangram, Inderjeet, Kranti, Arindam, Niveditha, Kailash baba, Vidya, Chirag, Priyam, Zeel, Amrutha, Pratiksha, Debjit, Akshay, Vijay, Yogesh, Jayesh, Mr. Jha, Anoushka, Bhagyashree (M & L), Tanaji, Sahil, Kiran Asokan, Geethu, Thanashekar, Abdulla, Shikha, Srijith, Jeshna, Rajlaxmi, Yogeshwar, Sambha Ji, Akash, Saroj and others. I am very thankful to all of you for the support.

I am very thankful to my trek partners, Tumpa, Dr. Ravi, Honey, Chunnu and Teena, with whom I created a lot of memories. I thank my friends Abhishek, Upendra, Ankush, Ketan, Aakash, Rani, and Piyush for their support and help in the PhD journey.

I would like to express my heartfelt gratitude to the student bodies 'NCL SciLogy' and 'NCL-TEC' for their unwavering commitment to skill development among students. As a member of these organizations, I had the unique opportunity to engage in various initiatives to enhance fellow students' skills and competencies.

I would like to express my heartfelt gratitude to my Jigri friends Shripal, Ajay, Gajender, Prateek, and Rajni, whose steadfast motivation and support have significantly influenced my personal growth. Their encouragement has been a cornerstone in shaping my character and aspirations. I am truly thankful for their friendship, which has been a source of strength and inspiration, making this journey all the more memorable.

I would like to express my heartfelt gratitude to my MSc friends Vinay, Mannu, Neha, and Priyanka for their unwavering support and encouragement throughout my PhD journey. I would like to express my heartfelt gratitude to my esteemed teachers, Dr. Minakshi, Mrs. Sarita, Mrs. Rekha, Rajesh Sir, Sakti Sir, and Sushil Sir. Their guidance and support have been crucial as I navigated the complexities of this academic endeavor.

I want to express my deepest gratitude to my family for their unwavering support and encouragement throughout my PhD journey. To my parents, who instilled the values of perseverance and hard work, your belief in me has been my constant source of strength. Your sacrifices and love have made this accomplishment possible.

To my spouse, Keerti Chauhan, your patience, understanding, and endless support have been my anchor during the most challenging times. Her patience and understanding during the long hours of research and writing have been invaluable, and her belief in my abilities has motivated me to persevere through the challenges. Keerti has been my partner, confidence, and cheerleader, celebrating each milestone with me and providing comfort during moments of doubt. This achievement is as much hers as it is mine, and I am profoundly grateful for her love and support throughout this endeavor. Thank you for standing by my side through every high and low.

I would like to express my deepest gratitude to my sisters, Sonika and Monika, for their unwavering love, care and support throughout my PhD journey. Their constant encouragement and belief in me have been a driving force in helping me reach this milestone. I am forever indebted to them for their countless sacrifices to ensure my success. I would also like to thank my brothers-in-law, Toni Singh and Vinay Singh, for their steadfast support, kindness and understanding during the challenging times of my doctoral studies. Their presence gave me a strong foundation to pursue my dreams. I am truly blessed to have such an amazing family who have stood by me every step of the way. To my dearest niece and nephews (Neha, Nikhil, Vritika and Mishika), Your laughter, joy, and boundless energy have been a constant source of inspiration and motivation throughout this journey. I am so fortunate to have such a supportive family. Finally, to my extended family, your encouragement and prayers have meant the world to me. Thank you for always believing in my potential. This thesis is as much yours as it is mine.

I would also like to acknowledge the financial support from CSIR-UGC, without which this research would not have been possible. Their support gave me the necessary resources and peace of mind to focus on my work.

Finally, to all those who contributed to this thesis in ways big and small, whether mentioned by name or not, I extend my heartfelt thanks. Your support, encouragement, and belief in me have been the foundation for this work.

Above all, I owe it all to Almighty God for granting me the wisdom, health, and strength to undertake this research task and enable me to complete it.

Pawan Kumar

…..Dedicated to My family…..

Table of Contents

Chapter 1: General Introduction……………………………………………………1

1.1 C-H activation…………………………………………………………………….…2

1.1.1 Homogeneous catalysis……………………………………………………….3

1.1.2 Heterogeneous catalysis………………………………………………………3

1.2 Catalytic reactions over heterogeneous catalysts…………………………………………4

1.2.1 Benzene oxidation………………………………………………………………4

1.2.2 Methane Oxidation……………………………………………………………7

1.2.3 Cyclohexane Oxidation………………………………………………………12

1.3 Heterogeneous Catalysts for C-H activation……………………………………...13

1.3.1 Metal Nanoparticles…………………………………………………………13

1.3.2 Metal Oxide Catalysts………………………………………………………..13

1.3.3 Supported Metal/Metal Oxides………………………………………………15

1.3.4 Composite/mixed metal oxides……………………………………………...16

1.4 Characterizations……………………………………………………………………18

1.4.1 X-ray diffraction (XRD)……………………………………………………..18

1.4.2 Fourier Transformed Infrared Spectroscopy (FT-IR)…………………………..19

1.4.3 X-Ray Photoelectron Spectroscopy (XPS)……………………………………..20

1.4.4 Inductively Coupled Plasma-Atomic Emission Spectrometry (ICP-AES)…..…20

1.4.5 Transmission electron microscope (TEM)……………………………………...20

1.4.6 Scanning electron microscopy (SEM)…………………………………………..21

1.4.7 N_2 sorption analysis…………………………………………...………..21

1.4.8 Thermo-gravimetric analysis (TGA)……………………………………………22

1.4.9 X-Ray Absorption Spectroscopy (XAS)………………………………………..22

1.4.10 Gas Chromatography (GC)……………………………………………………23

1.4.11 Nuclear Magnetic Resonance (NMR) Spectroscopy……………………..……24

1.4.12 Contact Angle Analysis………………………………………………………..24

1.5 Objective and scope of the thesis……………………………………………………25

1.6 Organization of the thesis…………………………………………………………...26

1.7 References…………………………………………………………………………..28

Chapter 2A: Benzene Hydroxylation using La_2CuO_4 Perovskite………………..35

2A.1 Introduction……………………………………………………………….….36

2A.2 Experimental and methods…………………………………………………..….37

2A.2.1 Materials…………………………………………………………...……37

2A.2.2 Synthesis of La-Cu-based oxides……………………………………………..37

2A.2.3 Catalyst Characterisation……………………………………………………..38

2A.2.4 Catalytic Activity test…………………………………………………………39

2A.2.5 Product Calculations……………………………………………………….39

2A.2.6 General procedure for recyclability test………………………………………40

2A.2.7 Product Extraction……………………………………………………………40

2A.3 Results and Discussion…………………………………………………………40

2A.3.1.X-Ray Diffraction………………………………………………………………40

2A.3.2 X-Ray Photoelectron Spectroscopy……………………………………………..41

2A.3.3 Electron Microscopy……………………………………………………………43

2A.3.4 FTIR……………………………………………………………………………..44

2A.3.5 TGA……………………………………………………………………………..45

2A.3.6 N_2 Porosimetry……………………………………………………………..46

2A.3.7 Catalytic Activity of La-Cu-based catalyst in Benzene Hydroxylation………47

2A.3.7.1 Effect of Cu molar ratio……………………………………………47

2A.3.7.2 Effect of Reaction Conditions………………………………………48

2A.3.7.3 Screening Experiments……………………………………………..50

2A.3.7.4 Catalyst Recovery and Reuse………………………………………51

2A.3.7.5 Spent Catalyst Analysis……………………………………………..52

2A.3.8 Mechanistic Aspect……………………………………………………...54

2A.4 Conclusions………………………...…………………………………………...55

2A.5 References…………………………………………………………………………56

Chapter 2B: Shaped Perovskite Synthesis and Applications……………………..…60

2B.1 Introduction……………………………………………………………………..61

2B.2 Experimental Section……………………………………………………….....…62

2B.2.1 Materials and methods……………………………………………….…….62

2B.2.2 Synthesis……………………………………………………………………...62

2B.2.3 Characterizations……………………………………………………….……..63
2B.2.4 Catalytic Activity Test……………………………………………….…..…64
2B.3 Results and Discussion……………………………………………………………64
2B.3.1 Electron Microscopy……………………………………………………….64
2B.3.2 X-Ray Diffraction ……………………………………………………….70
2B.3.3 X-Ray Photoelectron Spectroscopy…………………………………………...71
2B.3.4 Electron Paramagnetic Resonance…………………………………..….72
2B3.5 Electron Energy Loss Spectra…………………………………………………72
2B.3.6 N_2 sorption analysis……………………………………………...……73
2B.3.7 Catalytic activity…………………………………………………………...73
2B.4 Conclusions...……………………………………………………………………...76
2B.5 References…………………………………………………………………………78

Chapter 3: Continuous flow methane oxidation to methanol using H_2 and O_2…..79

3.1 Introduction…………………………………………………………………………...80
3.2 Experimental Section……………………………………………………….…….81
3.2.1 Materials………………………………………………………………….…….81
3.2.2 Catalyst Synthesis………………………………………………………………81
3.2.2.1Synthesis of Hydrophobic Silica (HS)…………………………………...…81
3.2.2.2 Synthesis of FeHS catalyst……………………………………………….....82
3.2.2.3 Synthesis of AuHS and AuFeHS catalyst……………………………………..82
3.2.3 Catalyst Characterization…………………………………………………………82
3.2.4 Catalytic Activity Test………………………………………………………..86
3.3 Result and Discussion………………………………………………………………89
3.3.1 Contact Angle………………………………………………………………..89
3.3.2 FTIR Spectroscopy…………………………………………………………..90
3.3.3 X-Ray Diffraction………………………………………………………….....91
3.3.4 N_2 sorption analysis……………………………………………………….91
3.3.5 Electron Microscopy……………………………………………………….....93
3.3.6 Solid-State NMR Spectroscopy…………………………………………….…..96
3.3.7 X-ray photoelectron spectroscopy…………………………………………...……97
3.3.8 X-ray Absorption Spectroscopy (XAS)……………………………………………99

3.3.9 Catalytic Activity……………………………………………………….…..101

3.3.9A Methane Oxidation to Methanol…………………………………..……101

3.3.9B Methane Oxidation to Acetic Acid……………………………….…..105

3.3.10 Spent Catalyst Analysis……………………………………………...….107

3.4 Theoretical Studies………………………………………………………...108

3.4.1 Computational Details………………………………………………...108

3.4.2. Density Functional Theory Computations……………………………....109

3.5 Conclusions……………………………………………………………...……112

3.6 References……………………………………………………………………113

Chapter 4: Oxidation of Methane to Formic Acid under Mild Conditions……...118

4.1 Introduction……………………………………………………………...119

4.2 Experimental Section…………………………………………………...….120

4.2.1 Materials……………………………………………………………....120

4.2.2 Catalyst Synthesis……………………………………………………..120

4.2.2.1 Synthesis of NZ……………………………………………….…..120

4.2.2.2 Synthesis of FeNZ catalyst…………………………………….…..120

4.2.2.3 Synthesis of AuNZ catalyst……………………………………….121

4.2.2.4 Synthesis of AuFeNZ catalyst…………………………………….121

4.2.3 Characterizations………………...…………………………...….122

4.2.4 Catalytic activity for methane partial oxidation to formic acid………..123

4.3 Result and Discussion……………………………………………………...125

4.3.1 X-Ray Diffraction……………………………………………………..125

4.3.2 Electron microscopy…………………………………………………..126

4.3.3 X-ray photoelectron spectroscopy…………………………………….127

4.3.4 X-Ray Absorption Spectroscopy…………………………………….....129

4.3.5 Solid-state NMR……………………………………………………....131

4.3.6 N_2 sorption analysis………………………………………………...132

4.3.7 Methane oxidation to Formic acid ……………………..……………...133

4.3.8 Spent Catalyst Analysis………………………………………………..138

4.4 Theoretical Calculations…………………………………………………...139

4.5 Conclusions………………………………………………………………..146

4.6 References……………………………………………………………………..………..147

Chapter 5: Summary and Conclusion…………………………………………….150

Abbreviations

DRIFT	Diffuse reflectance Infrared Fourier Transform Spectroscopy
ICP-AES	Inductively Coupled Plasma-Atomic Emission Spectrometry
FTS	Fischer–Tropsch Synthesis
XRD	X-Ray Diffraction
FT-IR	Fourier Transformed Infrared Spectroscopy
XPS	X-ray Photoelectron Spectroscopy
TEM	Transmission Electron Microscopy
HRTEM	High Resolution Transmission Electron Microscopy
SEM	Scanning Electron Microscopy
EDAX	Energy Dispersive X-ray Analysis
FESEM	Field Emission Scanning Electron Microscopy
BET	Brunauer-Emmett-Teller
TGA	Thermo-Gravimetric Analysis
GC	Gas Chromatography
FID	Flame Ionization Detector
XAS	X-Ray Absorption Spectroscopy
XANES	X-ray Absorption Near Edge Spectroscopy
EXAFS	Extended X-ray Absorption Fine Structure
NMR	Nuclear Magnetic Resonance
MAS	Magic-Angle Spinning
DP	Deposition Precipitation
NPs	Nanoparticles
SMSI	Strong Metal Support Interaction
SBA	Santa Barbara Amorphous
STP	Standard Temperature and Pressure
TEOS	TEOS Tetraethyl Ortho Silicate

List of Figures

Figure No.	Figure Caption	Page No.
1.1	Illustration of C-H bond activation.	3
1.2	Existing routes for methane conversion to hydrocarbons.	10
1.3	Historic view of the development of catalytic material for methane activation.	10
1.4	Schematic illustration of X-ray absorption K-edge showing XANES and EXAFS regions.	23
2A.1	Crystal structure of La_2CuO_4.	38
2A.2	XRD patterns of various La-Cu-based catalysts.	41
2A.3	XPS spectrums of 50LCO:O 1s (a), La 3d (b), Cu 2p O (c), La 3d (c), and Cu auger spectrum (d).	42
2A.4	Electron microscopic images of various catalysts: FESESM image of 50LCO (a), TEM image of 50 LCO (b) and HRTEM image of 50LCO (c and d), FESEM image of 100LCO and TEM image of 100LCO.	43
2A.5	Elemental mapping and SAED pattern of 50LCO.	44
2A.6	FTIR spectrum of various catalysts (a), 50LCO, and 100LCO (b).	45
2A.7	TG-DTA curve of 50LCO.	46
2A.8	N_2 adsorption-desorption isotherm of 50LCO catalyst.	46
2A.9	Catalytic activity of various catalysts (a) and recyclability test of 50LCO catalyst(b).	47
2A.10	Effect of the temperature (a) and H_2O_2 amount (b) on the catalytic activity of 50LCO.	48
2A.11	Recyclability tests for the catalytic activity of various catalysts.	51
2A.12	XRD patterns of various spent catalysts: 50LCO (a), 100LCO (b), and 5LCO (c)	53
2A.13	XPS spectrum of spent 50LCO catalyst: La 3d (a) and Cu 2p (b).	54
2A.14	Proposed mechanism of benzene oxidation at the catalyst surface.	54
2B.1	FESEM images of $LaFeO_3$ with the different synthesis times 24 h (a), 36 h (b), and 48 h (c).	65
2B.2	FESEM images of various $LaFeO_3$ synthesized by varying KOH amounts.	66
2B.3	EDS elemental mapping of LFOC (a), LFOHR (b).	67
2B.4	HRTEM images of LFOC (a), LFOHR (b) and LFORR (c).	67
2B.5	Elemental mapping of LFOC cube (a), LFOHR (b) and LFORR (c).	67
2B.6	FESEM images of various-shaped $LaFeO_3$ after heat treatment LFOC(a), LFOHR (b).	68
2B.7	FESEM images of A-site doped, i.e., La with Ba (a-b), and B-site doped, i.e., Fe with Cu (c-d), $LaFeO_3$.	69

2B.8	FESEM images of La-M-based perovskite oxide; M= Cu (a-b), Mn (c-d), Ni (e-f), and Co (g-h).	69
2B.9	XRD spectrum of various catalysts.	70
2B.10	XRD spectrum of various catalysts.	71
2B.11	Fe 2p (a), O 1s (b) XPS spectrum of various catalysts.	71
2B.12	EPR spectrum of various-shaped $LaFeO_3$.	72
2B.13	EEL spectrum of various-shaped $LaFeO_3$: LFOC (a), LFOHR (b) and LFORR (c).	73
2B.14	Catalytic activity of various-shaped $LaFeO_3$.	74
3.1	Schematic presentation of AFHS catalyst synthesis.	83
3.2	Contact angle measurement of SBA-15 (a), HS (b), and AuFeHS (c).	89
3.3	FTIR analysis of SBA-15 and HS.	90
3.4	DRIFT IR spectrum of AuFeHS catalyst treated with H_2 and O_2 gases.	91
3.5	XRD patterns of various catalysts.	91
3.6	N_2 sorption isotherm of HS and AuFeHS.	92
3.7	TEM images of SBA-15 (a) and HS (b).	93
3.8	HR-TEM analysis of AFHS (a-c) and particle size histogram(d)	94
3.9	Elemental mapping of AuFeHS.	94
3.10	STEM-HAADF image of FHS and AFHS (a and b), Electron Energy Loss Spectra of FeHS and AuFeHS (c and d respectively).	95
3.11	STEM Line analysis of AuFeHS	95
3.12	^{29}Si MAS spectrum of various catalysts.	96
3.13	^{23}Na MAS spectrum of various catalysts.	97
3.14	Fe 2p XPS spectrum of FeHS (a), AuFeHS (b), Au 4f XPS spectrum of AuHS (c), AuFeHS(d).	98
3.15	Na 1s XPS spectrum of AuFeHS.	99
3.16	Normalized XANES spectra at Fe K-edge and Au L_3-edge of various catalysts, (a,b) respectively. Experimental $\chi(R)$ vs. R data of Au-Fe catalyst measured at Fe K-edge and Au L_3-edge respectively (c,d), along with best fit theoretical plots.	100
3.17	Catalytic activity of, various catalysts (a), AuFeHS under different reaction pressures (b), in the batch process. Reaction Conditions: 50 mg Catalyst, 60 °C, 0.5 h, 900 rpm.	102
3.18	^1H NMR profile of reaction mixture in H_2O+D_2O for qualitative analysis (batch process). 50 mg Catalyst, 20 bar (1:1:2::d-O_2:d-H_2:CH_4), 0.5 h, 60 °C, 900 rpm.	103
3.19	^1H NMR profile of reaction mixture in DMSO-d_6 for H_2O_2 qualitative analysis. Reaction Conditions: 50 mg Catalyst, 10 bar (1:1::d-O_2:d-H_2), 0.5 h, 60 °C, 900 rpm.	103

3.20	Potentiometric titration curve of methane partial oxidation in batch process.	104
3.21	Catalytic activity of various catalysts (a) of AuFeHS under different reaction pressures in the continuous flow process under atmospheric conditions.	104
3.22	Catalytic activity of AuFeHS, at various reaction temperatures in a batch process (a), in the continuous flow process (b).	105
3.23	Catalytic activity of various catalysts under continuous flow process.	106
3.24	^{1}H NMR profile of reaction mixture in H_2O+D_2O for qualitative analysis (batch process). 50 mg Catalyst, 20 bar (15 bar CH_4 + 5 bar CO), 1 h, 60 °C, 0.025 M H_2O_2 (20 mL), 900 rpm.	107
3.25	HR-TEM image of AuFeHS spent catalyst and particle size histogram (inset).	108
3.26	Optimized ground state structure of the AuFeHS catalyst formed by depositing a Fe-doped Au cluster onto an amorphous hydrophobic silica surface.	109
3.27	Density of States (DOS) of AuFeHS structure.	110
3.28	Free energy diagrams depicting the methane to methanol pathways on AuFeHS catalyst.	111
4.1	XRD spectrum of various catalysts.	123
4.2	FESEM images of various catalysts (a-d), Elemental mapping of 0.1FeNZ (e), and 0.1AuNZ (f).	124
4.3	High resolution-TEM images of the 0.1Au0.1FeNZ (a-c), Elemental mapping of 0.1Au0.1FeNZ (d).	125
4.4	STEM line analysis of 0.1Au0.1FeNZ.	126
4.5	Fe 2p XPS spectrum of 0.1FeNZ (a) and 0.1Au0.1FeNZ (b) catalysts.	126
4.6	Au 4f XPS spectrum of 0.1AuNZ and 0.1Au0.1FeNZ catalysts.	127
4.7	Normalized XANES spectra at Fe K-edge of various catalysts (a), Experimental $\chi(R)$ vs. R data of Au-Fe catalyst measured at Fe K-edge (b).	129
4.8	^{29}Si MAS spectrum of various catalysts: (a) NZ, (b) 0.1FeNZ, (c) 0.1AuNZ, and (d) 0.1Au0.1FeNZ.	130
4.9	^{23}Na MAS spectrum of various catalysts.	130
4.10	N_2 adsorption and desorption isotherm of various catalysts.	131
4.11	Catalytic activity of, various catalysts (a), and 0.1Au0.1FeNZ at 50-80 °C (b), in batch process. Reaction Conditions: 50 mg catalyst,10 bar CH_4, 0.5 h, 900 rpm, 5 M H_2O_2 (20 mL)	134
4.12	Catalytic activity of, various catalysts (a), and 0.1Au0.1FeNZ at 50-80 °C (b). Reaction Conditions: 50 mg catalyst, 10 bar CH_4, 0.5 h, 900 rpm, 5 M H_2O_2 (20 mL)	134

4.13	Catalytic activity of various catalysts at different reaction conditions in the batch process. Reaction Conditions: 50 mg catalyst. 0.5 h, 60 °C, 900 rpm.	135
4.14	^{1}H NMR profile of reaction mixture in H_2O+D_2O (NMR solvent) using KHP as internal standard. Chemical Shift (ppm) 2.0 (Acetic acid), 3.3 (Methanol), 3.8 (MethylHydroperoxide), 7.6 (KHP) and 8.3 (Formic acid). Reaction conditions: 50 mg 1010AuFeNZcatalyst. 0.5 h, 60 °C, 5 M H_2O_2 (20 mL).	137
4.15	Catalytic activity of 0.1Au0.1FeNZ in the continuous flow process.	137
4.16	XRD spectrum (a), Fe 2p XPS spectrum (b), Au4f spectrum of spent 0.1Au0.1FeNZ (c).	138
4.17	(a) Structure of Na-ZSM-5 (b) Fe-oxide cluster along with cationic gold species anchored on Al sites within the zeolite framework (c) The DFT-simulated pathway over the AuFeNZ for methane activation, (i) optimized initial state (ii) transition state, and (iii) final state.	140
4.18	The DFT-simulated pathway over the (a) Au (111) and (b) Au_{38} nanoparticle for the C-H bond activation in methane to CH_3 radical.	141
4.19	The DFT-simulated pathway for methanol formation in AuFeNZ catalyst.	141
4.20	The DFT-simulated calculation for the C-H bond activation of the CH_4 over the mononuclear Fe species anchored in zeolite (a) The optimized initial state (IS), transition state (TS), and final state (FS) for methane activation in Fe Na'-ZSM-5 (b) within zeolite framework of Fe Na''-ZSM-5 (c) within zeolite Au/Fe Na''-ZSM-5. For clarity, only the active sites and the zeolite ring are depicted.	142
4.21	The DFT-simulated calculation for the H_2O_2 dissociation into OH radicals (a) The optimised initial state (IS), transition state (TS), and final state (FS) over the slab Au (111) (b) Radical (OH) formation Au_{38} nanoparticle.	143
4.22	(a-d) The DFT-simulated pathway over the Au (111) for the oxidation of CH_3OH to HCOOH using H_2O_2 as the oxidant. For clarity, only the top layer of metal is depicted.	144
4.23	(a) The DFT-simulated pathway over the Au (111) for directly oxidizing CH_3OH to HCOOH using H_2O_2 as the oxidant. (b) Proposed reaction scheme of reaction pathway for methanol activation and (c) formaldehyde activation to formic acid in AuFeNZ. (activation energy in kJ/mole)	145

List of Schemes

Scheme No.	Scheme Caption	Page No.
1.1	Illustration of phenol production by cumene process.	5

List of Tables

Table No.	Table Caption	Page No.
2A.1	Catalytic activity of various catalysts under different reaction conditions.	49
2A.2	Catalytic activity of 50LCO catalyst under different reaction conditions	51
2B.1	Sample preparation conditions of various shapes of $LaFeO_3$.	65
2B.2	Morphological parameter of various shapes of $LaFeO_3$.	66
2B.3	N_2 sorption analysis of various shapes of $LaFeO_3$.	73
2B.4	Catalytic activity of various catalysts for cyclohexane oxidation.	74
2B.5	Catalytic activity of LFORR for cyclohexane oxidation at different time intervals	76
2B.6	Catalytic activity of various catalysts for Benzene Oxidation.	76
3.1	N_2 adsorption-desorption analysis data of HS and AuFeHS.	93
3.2	Catalytic activity of various catalysts under batch process	103
3.3	Catalytic activity of various catalysts under batch process	107
3.4	ΔG calculation for CH_4 activation of various catalysts	112
4.1	EXAFS fitting parameters for Fe K-edge.4.1	129
4.2	N_2 adsorption-desorption analysis data of various catalysts.	132
4.3	Catalytic activity of various catalysts under controlled experiments	136
4.4	Catalytic activity data of various catalysts in batch process	137
4.5	Literature comparison of methane conversion under mild conditions using H_2O_2 as oxidants.	138

Chapter 1

General Introduction

1.1 C-H activation

The conversion of saturated and unsaturated hydrocarbons is a crucial and impactful topic of research in chemistry.[1–4] The development of this area has been interesting for decades, and new routes for transforming hydrocarbons into more valuable products, such as ketones, alcohol acids, etc., have been reported. However, the hydrocarbons' nonpolarizable bonds make the hydrocarbons' activation a chemical challenge.

The activation of any molecule refers to the increase in the molecule's activity generated by some action. C-H bond activation is a process that aims to transform the typically strong carbon-hydrogen (C-H) bond into a weaker and more reactive bond. This allows for the subsequent modification or functionalization of the molecule, introducing various functional groups or forming new carbon-carbon bonds. Activating the C-H bond makes it more susceptible to further chemical reactions, expanding the possibilities for molecular transformations and synthesizing more complex compounds.[5] When a particle, such as a metal atom or ion, binds to an unsaturated bond, it can activate the unsaturated species, potentially resulting in either addition or cleavage reactions. For instance, π-π-complexation can activate olefin and arene π -π-bonds, but saturated compounds do not possess this benefit. It is rational to suggest that enhancing the reactivity of a σ-bond, for instance, a C-H bond, is a way to activate this bond towards a reagent.[6] Consequently, the bond can split and produce two distinct entities instead of the original species.

Chemical syntheses that leverage C-H bond activation constitute a prominently researched domain within the field of chemistry.[7–9] The activation of C-H bonds involves a series of mechanistic steps that break stable carbon-hydrogen bonds in organic compounds. This process aims to facilitate the modification of these molecules, ultimately producing more intricate intermediate or end compounds, often incorporating C-O, C-C, and C-N bonds. Breaking the C-H bond allows cost-effective starting materials to be converted into commercially valuable compounds.[10–12]

The application of C–H bond activation chemistry signifies more than just a progressive step in synthetic methods; it has far-reaching consequences that extend beyond organic chemistry. The compounds produced through this approach have applications in various scientific disciplines, including materials science, biology, physics, and energy research. Significant research efforts are currently focused on developing catalysts that can enhance the activation of these bonds. The driving force behind this work is the ability to convert simple hydrocarbons into more complex molecules through C-H activation. This approach offers several advantages, including improved atom efficiency and overall cost-effectiveness, the potential for reactions to be carried out under milder conditions with less toxic or expensive reactants, and enhanced selectivity for functional group positions.

C-H activation can be done using the two catalytic processes.

1.1.1 Homogeneous catalysis: In homogeneous catalysis, both the reactants and the catalysts are present in the same phase, usually as liquids. While various homogeneous catalysts have been discovered, contemporary methodology revolves around organometallic and coordination complexes, owing to their atom economy. Transition metal-catalyzed C–H functionalization has emerged as a crucial and indispensable method in organic synthesis.[12–16] Homogeneous catalysis has been widely explored for the C-H activation but is out of the scope of the thesis and will not be discussed elsewhere.

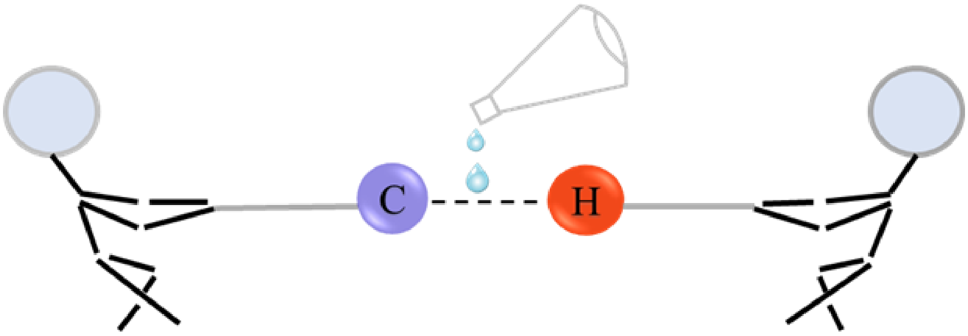

Figure 1.1 Illustration of C-H bond activation.

1.1.2 Heterogeneous catalysis: In the case of heterogeneous catalysis, the catalyst and the reactants are in different physical states, with the catalyst usually being a solid material that interacts with liquid or gaseous reactants. This means the catalyst is not dissolved in the reaction mixture but provides a surface on which the reactants can adsorb and undergo chemical transformations. The solid catalyst can be in various forms, such as powders, pellets, or coatings on a support material, and its high surface area allows for efficient interaction with the reactants. Heterogeneous catalysis is often favored over homogeneous catalysis because it allows for simpler separation and reuse of the catalyst. Typically, heterogeneous catalysts are 'supported' on a secondary material that enhances their mechanical stability and provides an optimal surface area for catalytic activity. The actual reactions occur at the active sites of these supported catalysts, which benefit from the effective surface area provided by the support material, allowing for better dispersion of the active sites. Additionally, these supports can influence the reaction rates by interacting with the catalyst, sometimes significantly enhancing the overall catalytic process. The important performance indices of any catalytic reaction are conversion and selectivity. When developing an efficient, sustainable, and cost-effective catalyst, it is crucial to consider additional factors such as separation, recyclability, and thermal stability. These parameters are essential for ensuring the overall effectiveness and practicality of the catalyst in various applications.[17,18]

1.2 Catalytic reactions over heterogeneous catalysts

Identifying a lead molecule for the C-H activation and conducting intensive research for its transformation is highly desirable[19–21]. In this thesis, the activation and transformation of molecules with strong C-H bonds, such as benzene, methane, and cyclohexane, are attempted using novel heterogeneous catalysts.

1.2.1 Benzene oxidation

Benzene, also referred to as benzol, is an aromatic hydrocarbon. It is a clear, colorless liquid with a sweet smell, highly volatile and flammable, and has poor solubility in water. Often found as a pollutant in air, soil, and water, benzene is a natural by-product of pyrolysis, mainly resulting from human activities.[22] Benzene is a known carcinogen released into the environment by several industries, such as chemical manufacturing, petrochemicals, paint and coatings, and steel production.[23]

Benzene plays a crucial role as a fundamental chemical raw material in the energy and industry sectors.[24] This versatile compound is a starting material or intermediary in manufacturing plastics, resins, synthetic fiber, dyes, detergents, pharmaceuticals, and pesticides.[25,26] While it occurs naturally in gasoline, its use as a fuel additive varies based on producer requirements. However, the utilization of benzene as a solvent has decreased recently due to its classification as a hazardous compound and carcinogen. Complete oxidation of benzene to CO_2 has also been adopted as a pathway for the removal but results in the emission of greenhouse gas (CO_2), hence indirectly a threat to the ecosystem.[27,28] So, converting benzene to value-added products is the best way for the removal/utilization of this volatile organic carbon species. [29,30]

In this context, researchers worldwide are keenly interested in converting benzene to value-added products.[31–33] However, there are a lot of difficulties in efficiently converting this moiety to value-added products. Benzene is a highly stable molecule because of the conjugated bond, with high C-H bond energy.[34] Overoxidation of the products under the reaction conditions makes it difficult to produce the desired product selectively.[35] For the catalytic conversion, various value-added products can be derived from benzene, such as ethylbenzene, cyclohexane, cumene, maleic anhydride etc. Converting benzene to phenol is highly desirable among all these products. Phenol, a crucial industrial precursor, finds extensive applications in manufacturing diverse chemical compounds. These include bisphenol A, a key component in producing epoxy resins and polycarbonate plastics, as well as phenolic resins, which are widely used in the adhesives, construction materials, and automotive industries. Additionally, phenol serves as a raw material for the synthesis of aniline, a precursor for polyurethanes, and salicylamide, a pharmaceutical intermediate. The recent surge in demand for phenol-derived products can be attributed to the rapid growth of the electronic communication, automobile, and construction sectors worldwide. [36,37] This increased reliance on phenol-based materials has led to a significant rise in the overall demand for phenol as an essential industrial raw material. Phenol is traditionally produced through the cumene process [38], which involves three main stages:

- Benzene is alkylated with propylene in the vapor phase, catalyzed by an acid catalyst such as phosphoric acid (H_3PO_4), to produce cumene. Before 1990, this process was carried out in the gas phase, but modern alkylation processes employ zeolite catalysts and are conducted in the liquid phase.
- Cumene is oxidized to cumene hydroperoxide using molecular oxygen in a non-catalytic reaction with air.
- Cumene hydroperoxide is cleaved to produce phenol and acetone with the aid of homogeneous acid catalysis using sulfuric acid. The cumene process has been the primary method for phenol production since its development, providing a reliable and efficient means of obtaining this important chemical compound.

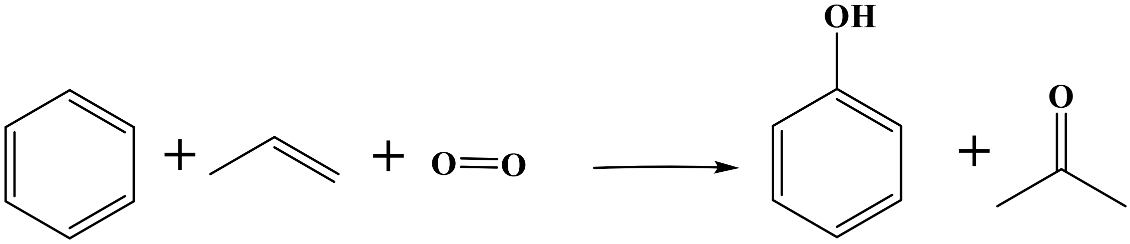

Scheme 1.1 Illustration of phenol production by cumene process.

The cumene process accounts for approximately 90% of global phenol production. Despite its widespread use, this method has notable drawbacks, including extreme reaction conditions characterized by high temperatures and pressures and strongly acidic environments. These factors contribute to a low phenol yield of less than 5% and significant environmental pollution.[39] Consequently, there is a pressing need to explore alternative synthetic methods for more efficient and environmentally friendly phenol.

There has been considerable interest in the one-step conversion of benzene to phenol utilizing suitable catalysts and oxidizing agents. Although achieving a high conversion rate of benzene to phenol through oxidation processes is theoretically feasible, experimental findings suggest that accomplishing this goal is quite difficult. The most researched method involves the direct hydroxylation of benzene using oxidizing agents such as N_2O,[40] O_2,[41] H_2O_2,[42,43] and a combination of O_2 and H_2.[44]

Achieving high phenol selectivity by using N_2O as an oxidant requires high reaction temperatures and limited N_2O sources. The efficiency of the catalyst reported when using air or O_2 as an oxidant is far from the realization of industrial applications. Hydrogen peroxide is widely considered the preferred oxidant due to its production of only water as a by-product and its simplicity, environmental friendliness, and cost-effectiveness.[45] However, the hydroxylation reaction of benzene with only the oxidant present and without a catalyst is slow and cannot efficiently oxidize benzene into phenol.[46] The catalytic transformation of benzene into phenol represents a highly efficient and direct approach for the single-stage conversion of this aromatic hydrocarbon into the valuable phenolic compound. This catalytic process offers a streamlined pathway that avoids multiple intermediate steps, making it an attractive option for industrial-scale phenol production from readily available benzene feedstock.

Several homogeneous catalysts have been evaluated for benzene hydroxylation using H_2O_2 as an oxidant, including polyoxometalates, Schiff bases, ionic liquids, and Fenton reagents.[47–50] However, the observed benzene conversion rates were very low, and recovering the catalyst from the reaction medium posed a significant challenge. So, The single-step transformation of benzene into phenol, utilizing a heterogeneous catalyst and environmentally friendly hydrogen peroxide as the oxidizing agent under mild reaction conditions, presents a promising pathway that has generated significant research interest. The challenges associated with the direct conversion of benzene to phenol include the inherent stability of benzene and the tendency of phenol to undergo overoxidation, leading to the formation of polyphenols. Consequently, there is significant interest within the scientific community in developing catalysts that can effectively facilitate this conversion. Recent advancements have led to creating an effective heterogeneous catalyst composed of earth-abundant elements, specifically designed in the form of perovskites, which operate under mild reaction conditions to transform benzene into phenol selectively.

1.2.2 Methane Oxidation

Methane (CH_4), a primary component of natural gas and a potent greenhouse gas (GHG), affects the earth's temperature and climate system.[51] Its transportation over long distances is economically challenging.[52] It is released into the atmosphere from various human-caused and natural sources. Anthropogenic activities, such as the operation of landfills, oil and gas extraction, agricultural practices, coal mining, combustion processes, wastewater treatment facilities, and certain industrial operations, contribute significantly to methane emissions. These human-influenced sources play a major role in the increased methane concentration in the Earth's atmosphere, which has implications for global climate change.[53]

Methane ranks as the second most common greenhouse gas produced by human activities, following carbon dioxide, and accounts for about 16% of global emissions. This gas is more than 28 times more effective than CO_2 in trapping atmospheric heat, significantly contributing to climate change.[54] Over the past two centuries, methane concentrations in the atmosphere have more than doubled, primarily due to human activities. This increase contributes significantly to global warming and is a precursor to harmful tropospheric ozone, a pollutant that poses health risks.[55,56] Methane is a powerful greenhouse gas with a much shorter atmospheric lifespan than carbon dioxide, meaning that substantial reductions in methane emissions could quickly and effectively mitigate atmospheric warming. Prompt action could also help decrease tropospheric ozone levels, curb dangerous climate feedback loops, and provide vital benefits for public health, the environment, and the economy. One of the most promising strategies for addressing methane emissions involves its catalytic conversion into valuable products. This approach utilizes methane effectively and aids in the fight against global warming. Transforming methane directly into commercially valuable chemicals and fuels, such as methanol and various oxygenates, represents a crucial and efficient method for converting methane into high-value products, thereby contributing to a more sustainable and economically advantageous energy landscape.

The thermochemical characteristics of methane contribute significantly to the molecule's stability, making it challenging to activate and convert. Methane exhibits a tetrahedral structure with four equivalent C−H bonds, resulting from the sp^3 hybridization of its central carbon atom. The C−H bond length is 1.087 Å, and the H-C-H configuration's angle between the hydrogen atoms is 109.5°. Furthermore, methane has no dipole moment and a relatively low polarizability of $2.84\times10{-}40\ C^2\cdot m^2\cdot J{-}12.84\times10{-}40C^2\cdot m^2\cdot J{-}1$, indicating that a strong local electric field is necessary for it to become polarized, which is essential for nucleophilic or electrophilic attacks.[57] Additionally, methane possesses the most robust C−H bond strength among all alkanes, with a bond dissociation energy (BDE) of 439.3 $kJ\cdot mol^{-1}$ under standard conditions. This high energy requirement underscores its status as the least reactive alkane.[58].

Coupled with the above, the high energy gap between the occupied and unoccupied orbits of methane makes it difficult to activate the C-H bond of the molecule. If activated, controlling the selectivity toward the desired product in the reaction is another challenge. For example, the products derived from partial methane oxidation are more prone to over-oxidation, resulting in thermodynamically favorable CO_2 formation. In this situation, selectively oxidizing methane to partially oxidized products is challenging under mild conditions. Therefore, tuning the reaction process and the material design is highly desirable, as it can selectively oxidize the methane to the desired oxygenates.

Ways of activation: Methane can be activated without catalysts, but this process necessitates significantly elevated temperatures, typically exceeding 1200 °C. This activation occurs through the homolytic cleavage of C-H bonds, a phenomenon called homogeneous pyrolysis or decomposition.[60] The pyrolytic processes consist of intricate networks of radical reactions, resulting in a diverse range of products. The primary compounds generated from this process include ethylene (C_2H_4), acetylene (C_2H_2), and benzene (C_6H_6), alongside hydrogen gas (H_2) that is free from carbon oxides (CO_x).[61,62] Catalytic methane activation by heterogeneous catalysts presents a practical approach for producing value-added chemicals and fuels. In the context of activating carbon-hydrogen bonds on metal catalysts, there are three distinct mechanisms:

1. Direct Activation: A metal-carbon sigma bond is formed as an intermediate or final product through the catalyst directly interacting with methane.

2. Indirect Activation: The metal does not make direct contact with the carbon-hydrogen bond.

3. Activation via Reactive Intermediates: A metal complex facilitates the formation of a reactive species that can then attack the carbon-hydrogen bond.

Despite the challenges and difficulties associated with methane activation, significant progress has been made in converting methane to chemicals. Producing valuable hydrocarbons from methane cost-effectively and efficiently is essential for practical uses. Over the past few decades, researchers have explored various direct and indirect catalytic routes to convert methane into a diverse range of hydrocarbons (Figure 1.2).

Indirect Route: Methane primarily serves as a precursor for generating syngas, which consists of carbon monoxide (CO) and hydrogen (H_2). This syngas is essential for processes such as Fischer-Tropsch synthesis (FTS) and methanol production. Different reforming methods, such as steam reforming, dry reforming, partial oxidation, and auto-thermal reforming, enable the generation of carbon monoxide and hydrogen in varying ratios.[63–65] To optimize the hydrogen-to-carbon monoxide ratio for FTS applications, the water-gas shift reaction is typically employed in conjunction with methane reforming. A variety of products can be produced using this well-known FTS route. For example, methanol, a versatile key intermediate produced from syngas, can produce value-added products using established technologies such as methanol for gasoline, olefins, hydrocarbons, and aromatics.[66–69] Although this indirect route provides ways to produce value-added products, the high energy required for this reforming process limits its application at a small scale. Alternative methods would be necessary to convert smaller amounts of methane in remote locations.

Direct route: Significant research efforts have been taken to replace the indirect synthesis gas route. Various catalytic processes encompass the one-step partial oxidation of methane to produce methanol, formic acid, and formaldehyde, as well as the oxidative coupling of methane to generate ethylene and ethane. Additionally, non-oxidative dehydroaromatization is aimed at producing aromatic compounds.[70–74]

The selective and direct conversion of methane into methanol and other oxygenates at low temperatures has been an elusive goal for over a century. The theoretical benefits of this process are clear; even modest reserves of methane could be effectively transformed into methanol using an oxidizing agent. As a liquid at ambient temperature, the resulting methanol would facilitate easier separation, transportation, and application in various downstream chemical processes. This thesis will explore the catalysts developed for the selective partial oxidation of methane to produce different liquid oxygenates, exploring their design and effectiveness in detail.

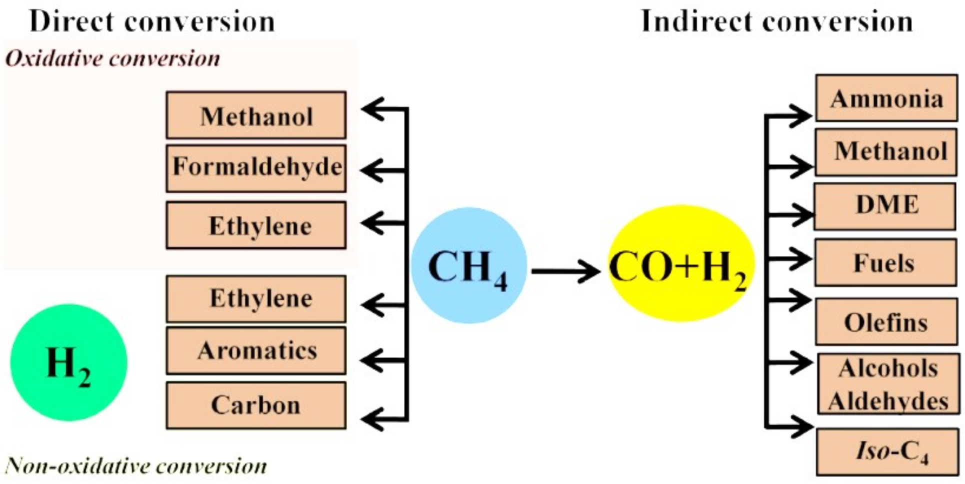

Figure 1.2 Existing routes for methane conversion to hydrocarbons.[75]

Historic view:

Developing an efficient heterogeneous catalyst for Methane oxidation to liquid oxygenates is a significant chemical process with implications for energy production and environmental sustainability. The field has evolved considerably over the past few decades, driven by advances in heterogeneous catalysis.

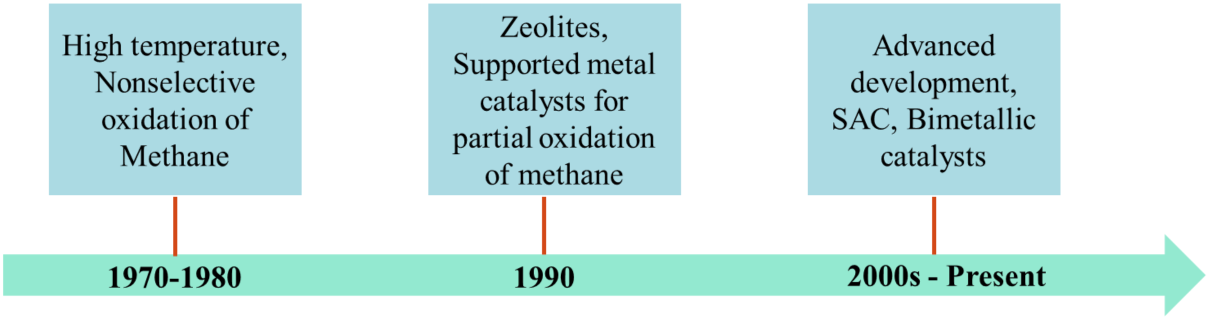

Figure 1.3 Historical view of the development of catalytic material for Methane activation

1. Early Research and Challenges (1970s - 1980s)

- **Initial Focus:** The early research in the 1970s and 1980s primarily focused on thermal processes for methane oxidation. As discussed above, these processes typically require high temperatures (above 500 °C), leading to non-selective oxidation products such as carbon dioxide (CO_2), carbon monoxide (CO), and a mixture of hydrocarbons.

- **Catalytic Challenges:** During this period, catalysts like molybdenum and vanadium oxides were explored, but they exhibited low selectivity towards desired products like methanol. The difficulty lay in activating the strong C-H bond of methane without over-oxidizing the methane to CO_2.

2. Emergence of Heterogeneous Catalysis (1990s)

- **Zeolites and Transition Metal Catalysts:** The 1990s marked a significant shift towards using heterogeneous catalysts, particularly zeolites, and supported metal catalysts. Researchers discovered that when incorporated into zeolite frameworks, certain transition metals could activate methane at lower temperatures and pressures.
    - **Copper-Exchanged Zeolites (Cu/ZSM-5):** One landmark discovery was using Cu/ZSM-5 catalysts. Studies by Groothaert et al. showed that copper sites within the ZSM-5 framework could catalyze the selective oxidation of methane to methanol.[76] This was a breakthrough in achieving higher selectivity for methanol at lower temperatures.
    - **Iron-Based Catalysts:** Iron-exchanged zeolites (Fe-ZSM-5) also emerged as promising catalysts, with the ability to selectively oxidize methane to methanol using nitrous oxide (N_2O) as an oxidant.[77]

3. Refinement and Innovation (2000s - Present)

- **New Catalytic Systems:** The 2000s saw the development of more sophisticated catalytic systems, including single-site catalysts, bimetallic catalysts, and advanced nanomaterials.
    - **Single-Site Catalysis:** Research into single-site catalysts, where isolated metal atoms are embedded in a support material, has been a primary focus. These catalysts, such as single-atom iron or copper dispersed in zeolites, offer high activity and selectivity for methane oxidation. The unique environment around these single sites allows precise control over the reaction, minimizing unwanted over-oxidation.[78,79]
    - **Metal-Organic Frameworks (MOFs):** MOFs have also been explored as potential catalysts for methane oxidation. These materials offer tunable pore

structures and the ability to incorporate various metal centers, making them versatile platforms for catalysis.[80]

  - **Bimetallic Catalysts:** The synergistic effects of bimetallic catalysts (e.g., Pd-Cu, Pt-Pd, Au-Pd) have been leveraged to improve the efficiency and selectivity of methane oxidation.[81,82] These catalysts can combine the strengths of two metals, enhancing their catalytic properties.

- **Green Chemistry Approaches:** Recent research has focused on developing catalysts that operate under environmentally benign conditions, such as using water or oxygen as the oxidant instead of harsher chemicals like N_2O or H_2O_2.

- **Mechanistic Insights:** Advances in characterization techniques, such as X-ray absorption spectroscopy (XAS) and high-resolution electron microscopy, have provided more profound insights into these catalysts' active sites and reaction mechanisms. Understanding these mechanisms has been crucial in designing more efficient and selective catalysts.

1.2.3 Cyclohexane Oxidation

The selective conversion of cyclohexane into high-value products poses a significant challenge due to the importance of the resulting oxidized products, which serve as intermediates in producing caprolactam and adipic acid.[83] KA oil (cyclohexanone and cyclohexanol) has a global consumption of approximately 10^6 tons annually.[84] Adipic acid is a significant aliphatic dicarboxylic acid derived from cyclohexane; however, only a small percentage is obtained from phenol.[85] The industrial synthesis of adipic acid from cyclohexane is done through a two-step procedure. Initially, cyclohexane undergoes oxidation to produce a mixture of cyclohexanone (a ketone) and cyclohexanol (an alcohol) in a small quantity of cobalt, chromium, and copper, all under moderate temperature and pressure conditions.[86] In the subsequent step, this mixture, referred to commercially as KA oil, is further oxidized using nitric acid to yield adipic acid.[87] The current commercial process for oxidizing cyclohexane is limited to a low conversion rate of about 4% to ensure reasonable selectivity.[88] The oxidation of cyclohexane is challenging due to the significant amount of energy required to break the carbon-hydrogen bonds. This high activation energy means that severe reaction conditions must be employed, such as subjecting the reactants to elevated temperatures ranging from 413 to 433 K and pressures between 1 to 2 MPa.[89] The current processes suffer from low yields, poor selectivity, and high waste production.[90,91] Given the significant demand for these oxidation products and the energy-intensive nature of the existing processes, there is a pressing need for a more effective, stable, feasible, and sustainable catalytic process. This thesis uses shaped metal oxide perovskite catalysts for the selective oxidation of cyclohexane to KA oil and establishes a correlation between structure and activity.

1.3 Heterogeneous Catalysts for C-H activation

The application of heterogeneous catalysts in C-H activation has garnered significant interest due to their ease of removal and the potential for recycling. .[92,93] When metal leaching is kept to a minimum, these systems can enhance the sustainable utilization of precious metals. The research group led by Glorius has reported multiple cases of direct arylation involving (hetero)aryls using straightforward Pd/C catalysts, as well as the pioneering undirected C−H thiolation of electron-rich heteroarenes utilizing Pd/Al_2O_3.[94–97] In 2015, Lei and Zhao introduced a catalytic system for the Fujiwara−Moritani reaction that featured bipyridine-bound Pd on mesoporous organosilica (MPO). Kinetic studies indicated that this system exhibited superior catalytic performance compared to the corresponding homogeneous system, achieved a longer catalyst lifespan by inhibiting the formation of Pd(0) aggregates, and enabled the reaction to be conducted in a continuous flow setup.[98]

1.3.1 Metal Nanoparticles: As nanoparticles are reduced to the nanometer scale, their surface-to-volume ratio increases, enhancing catalytic activity.[99] Single atoms, nanoclusters, and nanoparticles exhibit distinct electronic and geometric structures, imparting different catalytic properties. These structural disparities are evidenced in both thermal and photo-induced processes.[100] Over the past decade, there has been a growing focus among scientists in the field of catalysis on the evolution of surface structures of nanoparticles. Among the metal nanoparticles, gold nanoparticles (Au NPs) have been extensively utilized in the oxidative C–H activation of less reactive cycloalkanes.[101]

1.3.2 Metal Oxide catalysts: Catalysis involving metal oxides is a significant area within heterogeneous catalysis, encompassing a broad spectrum of industrial processes and catalyst types. This includes widely used materials such as silica, alumina, clays, zeolites, and various metal oxides like TiO_2, ZnO, and ZrO_2. Additionally, it covers porous and mesoporous metal oxides, polyoxometallates (POMs) of Keggin or Dawson types, and phosphates such as vanadium phosphorus oxide (VPO) and iron phosphate ($FePO_4$). Multi-component mixed oxides, including molybdates, antimonates, and tungstates, as well as perovskites and hexaaluminates, also play crucial roles. The prominence of metal oxides in catalysis emerged in the mid-1950s, primarily due to their effectiveness in catalyzing oxidation and acid-base reactions. They are vital in producing petrochemicals, intermediates, fine chemicals, pharmaceuticals, and biomass transformation processes.

Metal oxides have gained significant attention in C–H activation due to their exceptional catalytic activity, reusing ability, and stability at elevated temperatures. Among the various applications, one essential process involves forming C–O bonds to create valuable new materials. This involves oxidizing C–H bonds on the catalyst's surface. Metal oxides demonstrate significant efficacy in oxidation reactions owing to the presence of oxygen atoms within their crystal lattice. This characteristic enables them to donate or absorb oxygen atoms throughout the reaction process. Additionally, surface engineering techniques can create oxygen vacancies in the lattice framework, which can help stabilize different oxygenated intermediates involved in the reaction. Additionally, metal oxide catalysts' redox and acid-base properties aid in furthering oxidation reactions. Notably, using non-noble metal oxides as catalysts, the hydroxylation of various aliphatic and aromatic compounds can produce essential industrial products like alcohols, aldehydes, and acids in an environmentally friendly manner, eliminating the need for harsh and toxic chemicals. The oxidation of methane, the most basic hydrocarbon found on Earth, along with other small aliphatic hydrocarbons such as ethane and propane, plays a crucial role in producing a wide range of products. Unburned methane and other aliphatic hydrocarbons, commonly originating from natural gas plants and incomplete fuel combustion in engines, pose significant health and environmental hazards as toxic air pollutants. Converting these gases through catalytic oxidation can produce important chemicals like formic acid, ethanol, methanol, and propanol, which have various industrial applications. However, activating the strong C–H bonds in aliphatic hydrocarbons like methane, ethane, and propane poses a significant challenge in producing these value-added products. Researchers have been exploring metal oxide-based catalysts for an efficient conversion process.[102–104] Recently, Kiatsaengthong *et al.* demonstrated the oxidative coupling of methane (OCM) reaction with La_2O_3 catalyst modified with various metal oxides, including SrO, BaO, MgO and CaO. The researchers discovered that lanthanum oxide (La_2O_3) modified with strontium oxide (SrO) and barium oxide (BaO) exhibits more moderately strong basic sites and a higher amount of oxygen vacancies compared to La_2O_3 modified with magnesium oxide (MgO) or calcium oxide (CaO). Consequently, La_2O_3 modified with SrO and BaO demonstrated superior catalytic activity in the oxidative coupling of methane (OCM) reaction compared to La_2O_3

modified with MgO or CaO. The results indicate that the catalytic performance is primarily influenced by the surface basic sites and the oxygen species adsorbed on the surface, which are closely linked to oxygen vacancies within the catalyst's structure.[105] In a similar way, a lot of metal oxide catalysts have been explored for the various C-H activation reactions.[106–108]

1.3.3 Supported Metal/Metal Oxides

Utilizing metal oxides as supports has attracted considerable attention in the field of heterogeneous catalysis, particularly for selective oxidation reactions. This process involves applying an oxide layer onto the surface of another oxide, known as the support. The supported oxide (denoted as M) connects with the support (S) via bridging M-O-S bonds, which are partially established through interactions with surface hydroxyl groups.[109] The selection of support materials such as silica, mesoporous silicas like SBA-15, alumina, silica-alumina, carbon, zeolites and metal-organic frameworks (MOFs) plays a crucial role in determining the effectiveness of catalysts. These supports can enhance the uniform distribution of metal oxide particles, improve electron conductivity crucial for redox reactions, and boost thermal conductivity, which is an essential factor for both exothermic and endothermic reactions in industrial applications. In a notable study, Acharyya et al. demonstrated a straightforward method for converting benzene to aniline using a highly active $Cu^{2+}/CuCr_2O_4$ nanostructured catalyst, effectively activating the C-H bond to form C-N bonds.[110] Various metal oxide catalysts have been developed to activate different kinds of C-H bonds for important industrial reactions.[111–114]

Supported single-atom catalysts (SACs) can accomplish a balance between high activity and stability by leveraging the metal-support interaction. The support material helps in anchoring the single metal atoms, decreasing their surface free energy and preventing sintering into larger nanoparticles. At the same time, the strong interaction between the metal and support creates a unique electronic environment for the single atoms, maximizing the number of active sites per metal atom. Various support materials have been explored for SACs, including graphitic carbon, metal oxides, porous silicates like zeolites, and porous organic polymers or metal-organic frameworks (MOFs). The choice of support is critical, as it not only stabilizes the single atoms but also influences their catalytic properties through electronic and steric effects. Ongoing research aims to optimize the metal-support interaction further to develop highly active and stable SACs for diverse energy conversion applications.[80,115] The crystalline characteristics of the support enable a catalyst design that achieves atomic-level precision. This allows for the manipulation of structures such as single-atom catalysts, diatomic sites, multiatomic sites (both homonuclear and heteronuclear), and atomic interfaces. Doing so makes it possible to control catalytic activity and selectivity, leading to valuable insights into structure-performance relationships.

For example. the C- H activation of methane via oxidation to methanol has been attempted using H_2O_2 at mild temperatures (50–95 °C) in the presence of Pd_1O_4 single-sites (0.01 wt.% Pd) anchored on the internal surface of the micropores of ZSM-5.[116] Each palladium (Pd) site could convert approximately two methane molecules into methanol every second, resulting in a turnover frequency (TOF) of around 7,103 h^{-1}. Rhodium (Rh) has also been extensively utilized for the selective transformation of methane into methanol. Kwon et al. successfully synthesized a single Rh atom supported on zirconia (ZrO_2) through a process involving wet impregnation followed by calcination.[78] The Rh SAC demonstrated a reasonable level of activity in methane activation and conversion. Specifically, the catalyst produced 1 methanol molecule per hour per rhodium atom. However, this performance was not as high as that of a palladium single-atom catalyst supported on ZSM-5 zeolite (Pd SAC/ZSM-5), tested under comparable conditions. Those conditions included using an aqueous solution of hydrogen peroxide (H_2O_2) as the oxidant at a temperature of 70 °C. SACs have been utilized for other reactions like C-H activation of aliphatic alkanes,[117] cycloalkanes,[118] and arenes.[119,120]

1.3.4 Composite/mixed metal oxides

Although single-site catalysis is crucial for gaining insights into heterogeneous catalytic mechanisms at the atomic scale, multicomponent composite catalysts are often favored for their ability to deliver enhanced catalytic performance. These catalysts typically offer increased activity, better selectivity, and a reduction in environmentally detrimental byproducts.[121–123] The composite catalyst is a unique mixture formed by combining multiple components. In this advanced catalytic system, the precise arrangement and distribution of minor components within the bulk and on the surface of the major phase are key to determining the catalyst's functions and performance. These composite oxides are carefully synthesized through complex co-precipitation and sol-gel hydrolysis methods, followed by controlled thermal treatment. This method frequently leads to a notable improvement in catalytic performance, attributed to the larger surface area and the high concentration of active sites present on the surfaces of the nanoparticles. Moreover, an important aspect is the potential synergistic catalytic effect observed in many nanocomposite catalysts. This effect refers to a cooperative interaction between different components and/or active sites within a single catalyst, leading to substantially or even remarkably improved catalytic performance beyond the simple sum of the contributions from the individual components. Catalytic synergies can arise when interactions between various catalyst system components lead to significant improvements in key performance metrics. For instance, the catalytic activity, reactant conversion efficiency, product selectivity, and catalyst lifetime may all be enhanced through synergistic effects. These effects can occur due to interactions between the different active catalytic materials themselves or between the catalysts and their supporting structures. Researchers have observed and documented numerous examples of such synergistic phenomena in catalysis.[124,125] While synergistic effects in multicomponent catalysts have been widely reported across various reaction systems, the potential synergistic effects and underlying mechanisms are not yet fully understood due to the complexity of interactions between different catalyst components. However, based on extensive research on nanocomposite catalysts, it is believed that synergistic effects do exist in certain composite catalyst-involved reactions and may play a significant or even decisive role in catalytic processes such as selective catalytic oxidation and reduction reactions. This thesis explored the effect of synergistic interactions between catalyst components for C-H activation reactions in chapters 3 and 4.

The existing literature indicates mixed metal oxides display a diverse range of nonstoichiometric characteristics. For instance, A_xBO_3 perovskites, a specific category of mixed metal oxides, often exhibit cation deficiencies at A or B sites. These nonstoichiometric traits and the resulting vacancies play a crucial role in determining the catalytic behavior of these materials, as they introduce defects and alter the redox and electrical properties of the solids. A notable example is WO_3, which functions as an insulator, whereas A_xWO_3 transitions to a semiconductor at lower x values and behaves as a metal at higher x values. Oxygen-deficient perovskites have garnered significant interest over the past three decades due to their remarkable oxygen storage capabilities, akin to ceria-doped oxides, and their fascinating redox properties, which are advantageous for C-H activation reactions.[126,127] Kawi and colleagues [128] recently conducted a study on the effects of substituting different metals in the B site for methane's C–H activation. Their findings revealed that a catalyst precursor from Cu-substituted Ni exhibited the highest initial catalytic activity. This was attributed to the increased availability of Ni and the presence of mobile lattice oxygen species capable of activating C–H bonds. As a result, there was a notable enhancement in catalytic performance right from the onset of the reaction. This resulted in a significant improvement in catalytic activity even at the beginning of the reaction. De Chen and colleagues also explored the impact of oxygen vacancy formation energy on the catalytic activity and selectivity in perovskite materials in La-Fe-based perovskites.[129] Supported Bimetallic combinations have also been explored, showing the synergistic effect among the metal sites for methane partial oxidation.[81,130]

1.4 Characterizations

Characterizing heterogeneous catalysts is crucial for understanding the relationship between their structure, properties, and activity. Various microscopic and spectroscopic methods are available to enhance our comprehension of catalytic systems. In the upcoming section, we will offer a concise overview of the characterization techniques employed for analyzing nano-catalysts in this thesis.

1.4.1 X-ray diffraction (XRD)

The X-ray powder diffraction method is extensively applied to examine solids, particularly crystalline or polycrystalline substances, to obtain valuable data on crystalline phases, crystallite dimensions, and unit cell parameters. The interaction of the sample with incident rays leads to constructive interference when the conditions of Bragg's law are satisfied. (Bragg's equation is provided below.)

$$n\lambda = 2d\sin\theta$$

where n is the order of diffraction (normally an integer), λ is the wavelength of X-rays used, d is the interplanar distance, and θ is the angle between X-rays and the diffracting lattice plane. The X-ray peaks have significance in calculating the crystallite size through the Scherer equation, which relates the crystallite size to the full width at half maximum (FWHM) of the peak as:

$$\tau = \frac{k\lambda}{\beta\cos\theta}$$

where τ is the mean crystallite size, λ is the wavelength of X-rays, k is the constant often taken as 0.9, β is the FWHM, and θ is the angle between the beam and the normal to reflecting plane. In the current thesis work, small and wide-angle X-ray analyses on the solid powder catalysts were measured. The XRD measurements are done on the Rigaku Miniflex 2200PC using Cu Kα radiation (λ=0.15418 nm). The analysis conditions are provided in the experimental section of each working chapter.

1.4.2 Fourier Transformed Infrared Spectroscopy (FTIR)

The analysis by infrared spectroscopy relies on the unique frequencies of internal vibrations exhibited by compounds. This technique is crucial in determining the structure and purity of the examined material or compound. The specific absorbance patterns indicate the material's molecular structure or the orientation of its bonds, effectively serving as distinct markers. Throughout the thesis work, FTIR analysis of the KBr mixed pelletized samples is conducted using a Thermo Fischer FTIR spectrometer.

Diffuse reflectance Infrared Fourier Transform Spectroscopy (DRIFTS), is utilized to analyze powders and rough surface solids. This technique is primarily applied to powders because it relies on the scattering of radiation within the sample. When incident light strikes a sample, it may produce a single reflection from the surface (specular reflectance) or multiple reflections, resulting in diffusely scattered light across a wide area. This diffusely scattered light is utilized in DRIFTS measurements. The collection optics in the DRIFTS accessory are specifically designed to reject specularly reflected radiation and capture as much of the diffuse reflected light as possible.

Generally, theories that describe diffuse reflectance phenomena consider plane-parallel layers within the sample with light scattering in all directions. The observed reflectance spectrum using the Kubelka–Munk equation is a ratio of the single beam spectra of the sample diluted by KBr powder against pure powder KBr and is defined as:

$$f(R_\infty) = \frac{(1 - R_\infty)^2}{2R_\infty} = \frac{K}{s} = \frac{C}{k}$$

where K is the absorption coefficient, and s is the scattering coefficient of the sample material. The reflectance, R_∞, indicates the sample is thick enough that no radiation reaches the back surface. The above predicts a linear relationship between K and the maximum $f(R_\infty)$ value for each peak provided s is constant. The scattering coefficient depends on the particle size and packing and must remain constant for reproducible results. Lastly, C is the concentration of the sample and k is related to the sample's particle size and molar absorptivity, $k = s/2.303e$. The IR spectrums in Chapter 2 are recorded on a Perkin Elmer Infrared Spectrometer, and the other spectrums are recorded using a Thermo scientific IR instrument equipped with an MCT detector. The Harrick setup was fitted with a ZnSe window, and a temperature controller equipped with a thermocouple was used for heating treatment.

1.4.3 X-Ray Photoelectron Spectroscopy (XPS)

X-ray Photoelectron Spectroscopy (XPS) is a highly effective investigative technique widely used in heterogeneous catalysis. This surface-sensitive method provides insight into the active catalyst surface's elemental composition and chemical state. XPS, also known as Electron Spectroscopy for Chemical Analysis (ESCA), operates on the principle of the photoelectric effect. By irradiating the sample with X-rays of energy hν (using Al Kα or Mg Kα as a source), XPS generates spectra by measuring the kinetic energy (K.E) of the photoelectrons ejected from the sample with binding energy (B.E). This technique is exclusively surface-sensitive with a mean free path of 10 nm. The binding energy (B.E) is determined using the equation:

$$\text{K.E.} = h\nu - \text{B.E} - \Phi$$

where Φ, ν, and h represent the instrument's work function, the radiation frequency, and Planck's constant, respectively. XPS measurements yield valuable information such as identifying elements, composition, oxidation state, and coordination environment, among other characteristics. Binding energies, specific to each component and composition, are evaluated based on their peak area and sample cross-section for photoemission.

XPS measurements were carried out using a Thermo Scientific K alpha+ spectrometer using micro-focused and monochromated Al Kα radiation with an energy of 1486.6 eV. The pass energy for the spectral acquisition was kept at 50 eV for individual core levels. The electron flood gun was utilized to provide charge compensation during data acquisition. The peak fitting of the individual core levels was done using Avantage software with a smart-type background.

1.4.4 Inductively Coupled Plasma-Atomic Emission Spectrometry (ICP-AES)

This spectroscopic tool detects and quantifies the trace elements in the analyzed sample. For a given element, the ICP-AES technique is most common for selecting energy emitted at specific wavelengths out of multiple wavelengths. This emission's intensity indicates the element's concentration within the sample, which is helpful for qualitative and quantitative analysis. The ICP-AES analysis in Chapter 2 was carried out using SPECTRO make ARCOS, Simultaneous ICP Spectrometer (SAIF, IIT Bombay)

1.4.5 Transmission electron microscope (TEM)

TEM is an electron microscopic technique that provides the morphology and visualization at the atomic scale of the sample, where the high-energy electron beam is transmitted through the specimen to generate a 2D image of the sample. The image is obtained from the interaction of the incident electrons with the specimen, where the electron beam is transmitted through the sample. These transmitted electrons are magnified and focused by the electron optics onto a photographic plate, fluorescent screen, or charge-coupled device (CCD). Using an electron source over an optical light source offers the advantage of high resolution at the nanometer level due to the lower de-Broglie wavelength. High-resolution transmission electron microscope (HRTEM) is a visualization mode of TEM that provides deep atomic-level imaging to understand the crystallographic structure of the sample. It can give information about the plane exposed, an essential aspect of catalysis. The modified features of TEM include the scanning transmission electron microscopy (STEM) and high-angle annular dark-field (HAADF) imaging modes, which can provide information regarding the elemental composition and distribution of atoms in nanomaterials by coupling with the energy dispersive spectroscopy (EDS). The TEM analysis in this thesis was done using FEI Technai instruments (TF 30) by drop-casting the diluted samples on carbon-coated copper grids. The HRTEM and HAADF STEM analysis was done on JEOL JEM-F200 HRTEM.

1.4.6 Scanning electron microscopy (SEM)

Scanning Electron Microscopy (SEM) is a highly effective electron microscopic technique employed to study the surface topography of samples in three dimensions. By visually analyzing specimens with a focused beam of electrons, SEM aids in identifying material wear properties such as morphology, composition, particle number, and size. This technique detects backscattered or secondary electrons from the sample for analysis. In this thesis, SEM analyses were performed in CSIR NCL on a Quanta 200 instrument equipped with an energy-dispersed X-ray detector (EDS) for the samples' detailed morphology and composition analysis. Field emission scanning electron microscopy (FESEM) is also a significant tool in material characterization, which is widely applicable to understanding the topographic details of the material. It is an advanced version of SEM and provides much higher magnification than the regular SEM. FESEM offers detailed information about nanostructure morphology. FESEM analyses were performed in CSIR NCL on a FEITM NOVA NANOSEM 450 instrument.

1.4.7 N_2 sorption analysis

N_2 physisorption is a promising tool for obtaining information about solid materials' textural properties using liquid N_2 as a probe molecule. Several methods have been developed to extract other textural properties, such as pore volume, pore size, and external surface area. The Barrett-Joyner-Halenda (BJH) method is the most common method for calculating pore size distribution. The BET equation can be represented as:

$$\frac{1}{V_a[\frac{P^o}{P}-1]}=\frac{C-1}{V_m C}\times\frac{P}{P^o}+\frac{1}{V_m C}$$

where P is the equilibrium absorption pressure, P^o is the saturation pressure of the adsorbate at analysis temperature, V_a is the volume of N_2 adsorbed at pressure P, and V_m is the volume of adsorbate for monolayer adsorption. C is the BET constant related to heat of adsorption and liquefaction. This method is widely used for measuring the surface area of solid material by physical adsorption of the gas molecule by the following equation:

$$S=\frac{V_m N_\alpha}{m\times 22400}$$

where N is the Avogadro constant, α is the cross-sectional area covered by one adsorbate molecule, which is 0.162 nm2 for N_2, and m is the weight of the sample.

In this thesis, N_2 adsorption analysis was carried out using Autosorb 1C (Catalyis Division, CSIR-NCL). The details of the experimental condition are given in each working chapter's experimental section.

1.4.8 Thermo-gravimetric analysis (TGA)

TGA technique is used to determine thermal stability and fraction of volatile compounds present in materials. In this technique, the differential weight variation of a material is tracked either as a function of increasing temperature or time. TGA can be used to characterize fresh materials' decomposition patterns and for spent catalyst analysis to know carbon deposition and phase change, etc., during reaction. Specifically, in Chapter 2, TGA was carried out using the Diamond Pyris instrument (Catalysis Division, CSIR-NCL).

1.4.9 X-Ray Absorption Spectroscopy (XAS)

X-ray Absorption Spectroscopy (XAS) is a valuable spectroscopic technique for analyzing materials' electronic and geometric properties. This method provides valuable insights into local structures and unoccupied electronic states. XAS experiments are typically carried out at synchrotron radiation facilities, which offer tunable and powerful X-rays. These high-energy X-rays can excite a core-level electron of an atom to an empty bound state known as an excitonic state below the ionization threshold or to the continuum above the ionization potential. A typical XAS dataset typically exhibits three central regions.

1. The absorption threshold is determined by the transition of excited electrons to the lowest unoccupied states.

2. XANES (X-ray Absorption Near Edge Spectroscopy) comprises the ejection of photoelectrons from the core level to the quasi-bound state with kinetic energy in the 10-100 eV range above the chemical potential. These transitions give rise to multiple scattering resonances of the photoelectron. The pre-edge and near-edge regions in the spectrum contribute to the XANES spectrum.

3. EXAFS- The ejected photoelectrons have particle and wave nature and can be scattered back from the neighboring atoms in the lattice. This interaction can give rise to interference patterns at higher energy regions (beyond 100 eV) and Extended X-ray Absorption Fine Structure (EXAFS).

4. X-ray Absorption Spectroscopy (XAS) analysis in Chapter 2 was carried out at the Ti K edge in fluorescence mode at the Scanning EXAFS Beamline (BL-9) at the INDUS-2 Synchrotron Source (2.5 GeV, 100 mA) at the Raja Ramanna Centre for Advanced Technology (RRCAT), Indore, India.

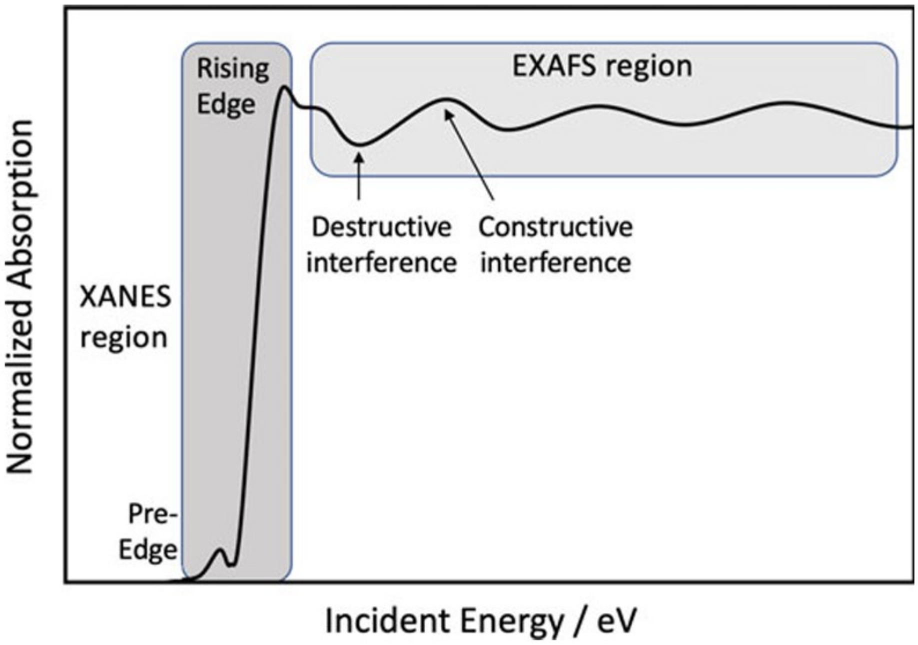

Figure 1.4 Schematic illustration of X-ray absorption K-edge showing XANES and EXAFS regions.[131]

1.4.10 Gas Chromatography (GC)

Gas chromatography is an analytical tool used to separate, identify and quantify components present in the sample. This method is based on the differential adsorption and desorption of each element (analyte) onto a stationary phase. The mobile phase, either a gas or a solvent mixture, will carry the sample through the long stationary phase and will get adsorbed. Based on the affinity of the analyte with the stationary phase, the elution of the analyte varies. The stronger the interaction, the slower the analyte elution will be. Based on the above process, separation of the analyte happens, and retention time varies; finally, the analyte reaches the detector and will be identified and quantified.

In this thesis, gas chromatography was analyzed using a NUCON 5765 gas chromatograph instrument equipped with both TCD and FID detectors.

1.4.11 Nuclear Magnetic Resonance (NMR) Spectroscopy

NMR is a spectroscopic tool that acquires information about the local magnetic field around atomic nuclei. Thus, the physical and chemical nature of the material can be identified by utilizing the magnetic properties of atomic nuclei under consideration. The sample is placed in the external magnetic field, and the spectrum is produced by the interaction of atomic nuclei with the magnetic field under nuclear magnetic resonating conditions. Nuclei with an odd number of neutrons and protons, which have a nuclear spin (I) greater than zero, produce a nuclear magnetic moment (μ) when exposed to an external magnetic field (B_o). This results in observing chemical shifts in peaks caused by secondary magnetic fields generated by interacting neighboring electrons with the nuclei. These secondary magnetic fields oppose the external magnetic field, leading to the shielding of the nucleus. In solid-state NMR spectroscopy, the anisotropic properties of the solid play a dominant role, often leading to peak broadening compared to conventional solution-based NMR. Two essential approaches are utilized to obtain well-defined solid-state NMR data: proper sample orientation to limit the range of sample orientations and reduction of anisotropic nuclear magnetic interactions through sample spinning. The latter involves fast spinning of the sample around the magic angle (MAS) for nuclei with a spin of ½. The chemical shift values obtained from the analysis can be used to discern the coordination environment around the nuclei, which can, in turn, correlate with the molecule's structure in the material. solid-state NMR experiments (^{23}Na and ^{29}Si) in chapters 3 and 4 were performed on a JEOL-400 spectrometer, operating at a magnetic field strength of 9.4 T and the single pulse ^{1}H MAS experiments were done at Bruker AV NEO 500MHz equipped with a 2.5mm trigamma probe at a sample rotation frequency of 32 kHz.

1.4.12 Contact Angle Analysis

Water contact angle measurements are used to determine the hydrophilicity or hydrophobicity of a surface, which is crucial for evaluating the effectiveness of surface treatments and catalytic processes. The measurement is performed using a sessile drop or captive bubble technique in static or dynamic mode If the water droplet spreads across the surface, creating a contact angle of less than 90°, the surface is considered hydrophilic. Conversely, the surface is considered hydrophobic if the water does not spread, which results in a contact angle greater than 90°.

1.5 Objective and scope of the thesis

Silica and silica-based materials have attracted considerable interest in research due to their exceptional characteristics, including thermal stability, a large surface area, adjustable porosity, and the ease with which they can be modified with various transition metals. These features contribute to their widespread use and practicality as support materials. However, creating small-sized metal nanoparticles (NPs) with numerous under-coordinated sites on silica supports poses significant challenges, primarily due to weak interactions between the metal and the support. This weakness can lead to sintering, which is uncontrolled particle size growth under elevated temperatures and harsh reaction conditions, adversely affecting catalytic performance. To address the issues of thermal instability and sintering, small metal nanoparticles can be anchored or encapsulated within porous silica supports. This approach enhances the thermal stability of the nanoparticles by restricting their mobility and ensuring that the active metal sites remain accessible, effectively mitigating the sintering problem. Organic moieties can be anchored onto their surface or framework to create a suitable environment conducive to interacting reactant molecules and allowing for the effective and easy diffusion of the product molecules. Nanoparticles of very small size (a few nanometers) can be decorated on the surface of the modified silica, creating highly functional and tailor-made catalysts. The bimetallic combination of the metals can also show the synergistic effect, hence the enhanced catalytic activity. In this thesis, methods have been developed to synthesize small-sized gold (Au) and iron (Fe) nanoparticles (NPs) that are supported on a modified porous silica substrate. These strategies are designed to be straightforward, cost-effective, and scalable.

The primary objective of this research is to create efficient heterogeneous catalysts capable of activating C-H bonds, with a particular emphasis on industrially relevant hydrocarbons such as cyclohexane, benzene, and methane. This involves several key areas:

1. Catalyst Design: Creating and analyzing new catalysts to selectively activate C-H bonds under mild conditions, focusing on improving catalytic performance, stability, and selectivity.

2. Mechanistic understanding: Investigating the pathways of C-H activation and subsequent oxidation processes to understand the factors influencing efficiency and selectivity.

3. Process Optimization: Evaluating reaction conditions to maximize yield and selectivity of desired oxidation products while minimizing by-product formation.

4. Industrial Relevance: Assessing the scalability and applicability of developed catalytic systems to reduce energy consumption and environmental impact and improve process economics.

5. Comparative Analysis: Comparing the performance of developed catalysts against existing commercial catalysts to demonstrate improvements in efficiency, selectivity, and sustainability for industrial processes. Ultimately, the aim is to contribute to sustainable and economically viable industrial processes for producing value-added chemicals from hydrocarbon feedstocks using innovative catalytic technologies.

1.6 Organization of the thesis:

- **Chapter 1:** This chapter introduces C-H Activation, various routes of the C-H activation, benzene oxidation, methane oxidation, cyclohexane oxidation, metal/metal oxides heterogeneous catalysts and various characterization tools utilized for the analysis of the catalytic material.
- **Chapter 2A:** Chapter 2A focuses on designing and synthesis of perovskite materials for use in heterogeneous catalysis. The material synthesized through sol-gel methods demonstrates promising catalytic activity in the one-step conversion of benzene to phenol using H_2O_2 as an oxidant. The La_2CuO_4 perovskite catalyst exhibits high catalytic activity and can be recycled, highlighting the potential of perovskite materials in heterogeneous catalysis.
- **Chapter 2B:** Chapter 2B focuses on the design and synthesis of shape-dependent perovskite catalysts and their potential application in the industrially significant cyclohexane to KA oil reaction. The synthesis process developed enables the incorporation of various transition metals at the B site, with La occupying the A site to produce the shaped perovskites. This chapter delves into the development and discussion of various shapes of different perovskite oxides.
- **Chapter 3:** In this chapter, SBA-15 is subjected to hydrophobic silica modification, subsequently leading to the deposition of Au and Fe onto the silica surface, resulting in high catalytic activity for the partial oxidation of methane to methanol through the use of *in-situ* generated H_2O_2. Advanced catalytic techniques and theoretical studies offer

valuable insights into efficient methane conversion. The ability to produce methanol continuously at ambient pressure presents promising prospects for industrialization.

- **Chapter 4:** In this chapter, a bimetallic catalyst was synthesized and tested for the efficient conversion of methane to formic acid. The catalyst consisted of Au and Fe deposited on the surface of Na-ZSM5. The synergistic effect between Au and Fe, facilitated by Na, led to high activity and selectivity in producing formic acid under mild reaction conditions in both batch and continuous processes. The material's efficiency was confirmed through these tests. Theoretical studies provided in-depth insights into the synergistic effect and the efficient production of formic acid.
- **Chapter 5:** In this chapter, we summarize the conclusions drawn from our investigation into the design of various catalytic systems for C-H activation. The role of active sites, the synergistic effects between metals, and the modification of the support all play crucial roles in achieving efficient conversion and selectivity through C-H activation.

1.7 References

[1] L. Ya. Margolis, **1963**, pp. 429–501.

[2] S. A. C. Carabineiro, *Catalysts* **2024**, *14*, 111.

[3] M. N. Siddiquee, M. M. Hossain, N. Nazemifard, *The Chemical Record* **2022**, *22*, DOI 10.1002/tcr.202200022.

[4] A. Martins, N. Nunes, A. P. Carvalho, L. M. D. R. S. Martins, *Catalysts* **2022**, *12*, 154.

[5] E. L. Muetterties, M. J. Krause, *Angewandte Chemie International Edition in English* **1983**, *22*, 135–148.

[6] A. E. Shilov, A. A. Shteinman, *Coord Chem Rev* **1977**, *24*, 97–143.

[7] R. H. Crabtree, A. Lei, *Chem Rev* **2017**, *117*, 8481–8482.

[8] T. Dalton, T. Faber, F. Glorius, *ACS Cent Sci* **2021**, *7*, 245–261.

[9] W. R. Gutekunst, P. S. Baran, *Chem Soc Rev* **2011**, *40*, 1976.

[10] Y. Segawa, T. Maekawa, K. Itami, *Angewandte Chemie International Edition* **2015**, *54*, 66–81.

[11] J. Yang, *Org Biomol Chem* **2015**, *13*, 1930–1941.

[12] B. Liu, F. Hu, B.-F. Shi, *ACS Catal* **2015**, *5*, 1863–1881.

[13] Z. Huang, H. N. Lim, F. Mo, M. C. Young, G. Dong, *Chem Soc Rev* **2015**, *44*, 7764–7786.

[14] N. J. Gunsalus, A. Koppaka, S. H. Park, S. M. Bischof, B. G. Hashiguchi, R. A. Periana, *Chem Rev* **2017**, *117*, 8521–8573.

[15] S. Tani, T. N. Uehara, J. Yamaguchi, K. Itami, *Chem. Sci.* **2014**, *5*, 123–135.

[16] C. Pradhan, R. A. Jagtap, P. P. Samal, S. Krishnamurty, B. Punji, *Green Chemistry* **2023**, *25*, 9733–9743.

[17] C. M. Friend, B. Xu, *Acc Chem Res* **2017**, *50*, 517–521.

[18] L. Liu, A. Corma, *Chem Rev* **2018**, *118*, 4981–5079.

[19] H. Shoukat, A. A. Altaf, M. Hamayun, S. Ullah, S. Kausar, M. Hamza, S. Muhammad, A. Badshah, N. Rasool, M. Imran, *ACS Omega* **2021**, *6*, 19606–19615.

[20] C.-W. Chang, J. T. Miller, *Appl Catal A Gen* **2022**, *643*, 118753.

[21] Y.-D. Shan, S.-H. Wu, Y.-L. Wang, C. Wang, S.-Q. Zhi, Y. Liu, X. Han, *Inorg Chem* **2023**, *62*, 4872–4882.

[22] H. Bahadar, S. Mostafalou, M. Abdollahi, *Toxicol Appl Pharmacol* **2014**, *276*, 83–94.

[23] F. Adam, R. Thankappan, *Chemical Engineering Journal* **2010**, *160*, 249–258.

[24] Q. Meng, J. Yan, R. Wu, H. Liu, Y. Sun, N. Wu, J. Xiang, L. Zheng, J. Zhang, B. Han, *Nat Commun* **2021**, *12*, 4534.

[25] B. A. Vaughan, M. S. Webster-Gardiner, T. R. Cundari, T. B. Gunnoe, *Science (1979)* **2015**, *348*, 421–424.

[26] Q. Meng, J. Yan, R. Wu, H. Liu, Y. Sun, N. Wu, J. Xiang, L. Zheng, J. Zhang, B. Han, *Nat Commun* **2021**, *12*, 4534.

[27] H. Huang, Y. Xu, Q. Feng, D. Y. C. Leung, *Catal Sci Technol* **2015**, *5*, 2649–2669.

[28] Y. Guo, D.-P. Yang, M. Liu, X. Zhang, Y. Chen, J. Huang, Q. Li, R. Luque, *J Mater Chem A Mater* **2019**, *7*, 8832–8844.

[29] P. R. Makgwane, S. S. Ray, *J Mol Catal A Chem* **2015**, *398*, 149–157.

[30] H. Xin, A. Koekkoek, Q. Yang, R. van Santen, C. Li, E. J. M. Hensen, *Chemical Communications* **2009**, 7590.

[31] J. Xie, X. Li, J. Guo, L. Luo, J. J. Delgado, N. Martsinovich, J. Tang, *Nat Commun* **2023**, *14*, 4431.

[32] Y. Guo, D.-P. Yang, M. Liu, X. Zhang, Y. Chen, J. Huang, Q. Li, R. Luque, *J Mater Chem A Mater* **2019**, *7*, 8832–8844.

[33] K. Brezinsky, *Prog Energy Combust Sci* **1986**, *12*, 1–24.

[34] R. Mistri, M. Rahaman, J. Llorca, K. R. Priolkar, S. Colussi, B. C. Ray, A. Gayen, *J Mol Catal A Chem* **2014**, *390*, 187–197.

[35] S. Mishra, R. Bal, R. K. Dey, *Molecular Catalysis* **2021**, *499*, 111310.

[36] T. Zhang, X. Nie, W. Yu, X. Guo, C. Song, R. Si, Y. Liu, Z. Zhao, *iScience* **2019**, *22*, 97–108.

[37] W. Han, W. Xiang, Z. Meng, S. Dong, Y. Lv, *Colloids Surf A Physicochem Eng Asp* **2023**, *670*, 131529.

[38] R. J. Schmidt, *Appl Catal A Gen* **2005**, *280*, 89–103.

[39] T. Tsuji, A. A. Zaoputra, Y. Hitomi, K. Mieda, T. Ogura, Y. Shiota, K. Yoshizawa, H. Sato, M. Kodera, *Angewandte Chemie International Edition* **2017**, *56*, 7779–7782.

[40] I. Yuranov, D. A. Bulushev, A. Renken, L. Kiwi-Minsker, *Appl Catal A Gen* **2007**, *319*, 128–136.

[41] H. Guo, Z. Chen, F. Mei, D. Zhu, H. Xiong, G. Yin, *Chem Asian J* **2013**, *8*, 888–891.

[42] K. M. Parida, D. Rath, *Appl Catal A Gen* **2007**, *321*, 101–108.

[43] L. Hu, C. Wang, L. Ye, Y. Wu, B. Yue, X. Chen, H. He, *Appl Catal A Gen* **2015**, *504*, 440–447.

[44] S. Niwa, M. Eswaramoorthy, J. Nair, A. Raj, N. Itoh, H. Shoji, T. Namba, F. Mizukami, *Science (1979)* **2002**, *295*, 105–107.

[45] T. Jiang, W. Wang, B. Han, *New Journal of Chemistry* **2013**, *37*, 1654.

[46] A. M. Al-Sabagh, F. Z. Yehia, Gh. Eshaq, A. E. ElMetwally, *ACS Sustain Chem Eng* **2017**, *5*, 4811–4819.

[47] P. K. Khatri, B. Singh, S. L. Jain, B. Sain, A. K. Sinha, *Chem. Commun.* **2011**, *47*, 1610–1612.

[48] J. Peng, F. Shi, Y. Gu, Y. Deng, *Green Chemistry* **2003**, *5*, 224–226.

[49] K. Nomiya, K. Yagishita, Y. Nemoto, T. Kamataki, *J Mol Catal A Chem* **1997**, *126*, 43–53.

[50] W. Jiang, W. Zhu, H. Li, Y. Chao, S. Xun, Y. Chang, H. Liu, Z. Zhao, *J Mol Catal A Chem* **2014**, *382*, 8–14.

[51] S. Kirschke, P. Bousquet, P. Ciais, M. Saunois, J. G. Canadell, E. J. Dlugokencky, P. Bergamaschi, D. Bergmann, D. R. Blake, L. Bruhwiler, P. Cameron-Smith, S. Castaldi, F. Chevallier, L. Feng, A. Fraser, M. Heimann, E. L. Hodson, S. Houweling, B. Josse, P. J. Fraser, P. B. Krummel, J.-F. Lamarque, R. L. Langenfelds, C. Le Quéré, V. Naik, S. O'Doherty, P. I. Palmer, I. Pison, D. Plummer, B. Poulter, R. G. Prinn, M. Rigby, B. Ringeval, M. Santini, M. Schmidt, D. T. Shindell, I. J. Simpson, R. Spahni, L. P. Steele, S. A. Strode, K. Sudo, S. Szopa, G. R. van der Werf, A. Voulgarakis, M. van Weele, R. F. Weiss, J. E. Williams, G. Zeng, *Nat Geosci* **2013**, *6*, 813–823.

[52] D. T. Allen, V. M. Torres, J. Thomas, D. W. Sullivan, M. Harrison, A. Hendler, S. C. Herndon, C. E. Kolb, M. P. Fraser, A. D. Hill, B. K. Lamb, J. Miskimins, R. F. Sawyer, J. H. Seinfeld, *Proceedings of the National Academy of Sciences* **2013**, *110*, 17768–17773.

[53] N. Unger, D. T. Shindell, D. M. Koch, M. Amann, J. Cofala, D. G. Streets, *Journal of Geophysical Research: Atmospheres* **2006**, *111*, DOI 10.1029/2005JD006518.

[54] In *Climate Change 2013 – The Physical Science Basis*, Cambridge University Press, **2014**, pp. 659–740.

[55] D. T. Shindell, G. Faluvegi, N. Bell, G. A. Schmidt, *Geophys Res Lett* **2005**, *32*, DOI 10.1029/2004GL021900.

[56] A. J. Turner, C. Frankenberg, E. A. Kort, *Proceedings of the National Academy of Sciences* **2019**, *116*, 2805–2813.

[57] R. D. Amos, *Mol Phys* **1979**, *38*, 33–45.

[58] Y.-R. Luo, *Comprehensive Handbook of Chemical Bond Energies*, CRC Press, **2007**.

[59] C. Li, Q. Xin, *J Phys Chem* **1992**, *96*, 7714–7718.

[60] C. Guéret, M. Daroux, F. Billaud, *Chem Eng Sci* **1997**, *52*, 815–827.

[61] H. F. Abbas, W. M. A. Wan Daud, *Int J Hydrogen Energy* **2010**, *35*, 1160–1190.

[62] N. Sánchez-Bastardo, R. Schlögl, H. Ruland, *Chemie Ingenieur Technik* **2020**, *92*, 1596–1609.

[63] S. Ayabe, H. Omoto, T. Utaka, R. Kikuchi, K. Sasaki, Y. Teraoka, K. Eguchi, *Appl Catal A Gen* **2003**, *241*, 261–269.

[64] M. ZAHEDINEZHAD, S. ROWSHANZAMIR, M. EIKANI, *Int J Hydrogen Energy* **2009**, *34*, 1292–1300.

[65] J. H. Lunsford, *Catal Today* **2000**, *63*, 165–174.

[66] S. Lin, Y. Zhi, W. Chen, H. Li, W. Zhang, C. Lou, X. Wu, S. Zeng, S. Xu, J. Xiao, A. Zheng, Y. Wei, Z. Liu, *J Am Chem Soc* **2021**, *143*, 12038–12052.

[67] I. Pinilla-Herrero, E. Borfecchia, T. Cordero-Lanzac, U. V. Mentzel, F. Joensen, K. A. Lomachenko, S. Bordiga, U. Olsbye, P. Beato, S. Svelle, *J Catal* **2021**, *394*, 416–428.

[68] D. Rojo-Gama, L. Mentel, G. N. Kalantzopoulos, D. K. Pappas, I. Dovgaliuk, U. Olsbye, K. P. Lillerud, P. Beato, L. F. Lundegaard, D. S. Wragg, S. Svelle, *J Phys Chem Lett* **2018**, *9*, 1324–1328.

[69] P. Tian, Y. Wei, M. Ye, Z. Liu, *ACS Catal* **2015**, *5*, 1922–1938.

[70] C. Hammond, N. Dimitratos, R. L. Jenkins, J. A. Lopez-Sanchez, S. A. Kondrat, M. Hasbi ab Rahim, M. M. Forde, A. Thetford, S. H. Taylor, H. Hagen, E. E. Stangland, J. H. Kang, J. M. Moulijn, D. J. Willock, G. J. Hutchings, *ACS Catal* **2013**, *3*, 689–699.

[71] A. K. Md. L. Rahman, M. Kumashiro, T. Ishihara, *Catal Commun* **2011**, *12*, 1198–1200.

[72] T. Akiyama, R. Sei, S. Takenaka, *Catal Sci Technol* **2021**, *11*, 5273–5281.

[73] D. Kiani, S. Sourav, J. Baltrusaitis, I. E. Wachs, *ACS Catal* **2019**, *9*, 5912–5928.

[74] S. Ma, X. Guo, L. Zhao, S. Scott, X. Bao, *Journal of Energy Chemistry* **2013**, *22*, 1–20.

[75] S. V. Konnov, *Petroleum Chemistry* **2022**, *62*, 280–290.

[76] M. H. Groothaert, P. J. Smeets, B. F. Sels, P. A. Jacobs, R. A. Schoonheydt, *J Am Chem Soc* **2005**, *127*, 1394–1395.

[77] V. I. Sobolev, K. A. Dubkov, O. V. Panna, G. I. Panov, *Catal Today* **1995**, *24*, 251–252.

[78] Y. Kwon, T. Y. Kim, G. Kwon, J. Yi, H. Lee, *J Am Chem Soc* **2017**, *139*, 17694–17699.

[79] Q. Shen, C. Cao, R. Huang, L. Zhu, X. Zhou, Q. Zhang, L. Gu, W. Song, *Angewandte Chemie International Edition* **2020**, *59*, 1216–1219.

[80] Y.-S. Wei, M. Zhang, R. Zou, Q. Xu, *Chem Rev* **2020**, *120*, 12089–12174.

[81] B. Yu, L. Cheng, S. Dai, Y. Jiang, B. Yang, H. Li, Y. Zhao, J. Xu, Y. Zhang, C. Pan, X. Cao, Y. Zhu, Y. Lou, *Advanced Science* **2023**, *10*, DOI 10.1002/advs.202302143.

[82] J. H. Carter, R. J. Lewis, N. Demetriou, C. Williams, T. E. Davies, T. Qin, N. F. Dummer, D. J. Morgan, D. J. Willock, X. Liu, S. H. Taylor, G. J. Hutchings, *Catal Sci Technol* **2023**, *13*, 5848–5858.

[83] S. Van de Vyver, Y. Román-Leshkov, *Catal. Sci. Technol.* **2013**, *3*, 1465–1479.

[84] *Ullmann's Encyclopedia of Industrial Chemistry*, Wiley, **2003**.

[85] K. C. Hwang, A. Sagadevan, *Science (1979)* **2014**, *346*, 1495–1498.

[86] B. Sarkar, P. Prajapati, R. Tiwari, R. Tiwari, S. Ghosh, S. Shubhra Acharyya, C. Pendem, R. Kumar Singha, L. N. Sivakumar Konathala, J. Kumar, T. Sasaki, R. Bal, *Green Chemistry* **2012**, *14*, 2600.

[87] D. Duprez, F. Cavani, *Handbook of Advanced Methods and Processes in Oxidation Catalysis*, IMPERIAL COLLEGE PRESS, **2014**.

[88] C. Wang, L. Chen, Z. Qi, *Catal Sci Technol* **2013**, *3*, 1123.

[89] R. A. Sheldon, J. K. Kochi, **1976**, pp. 272–413.

[90] H. Hattori, Y. Ide, S. Ogo, K. Inumaru, M. Sadakane, T. Sano, *ACS Catal* **2012**, *2*, 1910–1915.

[91] R. Goyal, B. Sarkar, S. Sameer, A. Bag, A. Bordoloi, *ACS Appl Nano Mater* **2019**, *2*, 5989–5999.

[92] S. Santoro, S. I. Kozhushkov, L. Ackermann, L. Vaccaro, *Green Chemistry* **2016**, *18*, 3471–3493.

[93] S. Hübner, J. G. de Vries, V. Farina, *Adv Synth Catal* **2016**, *358*, 3–25.

[94] S. Vásquez-Céspedes, A. Ferry, L. Candish, F. Glorius, *Angewandte Chemie International Edition* **2015**, *54*, 5772–5776.

[95] K. D. Collins, R. Honeker, S. Vásquez-Céspedes, D.-T. D. Tang, F. Glorius, *Chem Sci* **2015**, *6*, 1816–1824.

[96] D. D. Tang, K. D. Collins, J. B. Ernst, F. Glorius, *Angewandte Chemie International Edition* **2014**, *53*, 1809–1813.

[97] D.-T. D. Tang, K. D. Collins, F. Glorius, *J Am Chem Soc* **2013**, *135*, 7450–7453.

[98] H. Duan, M. Li, G. Zhang, J. R. Gallagher, Z. Huang, Y. Sun, Z. Luo, H. Chen, J. T. Miller, R. Zou, A. Lei, Y. Zhao, *ACS Catal* **2015**, *5*, 3752–3759.

[99] S. Linic, P. Christopher, H. Xin, A. Marimuthu, *Acc Chem Res* **2013**, *46*, 1890–1899.

[100] L. Liu, A. Corma, *Chem Rev* **2018**, *118*, 4981–5079.

[101] R. Liu, H. Huang, H. Li, Y. Liu, J. Zhong, Y. Li, S. Zhang, Z. Kang, *ACS Catal* **2014**, *4*, 328–336.

[102] F. Arena, R. Di Chio, L. Filiciotto, G. Trunfio, C. Espro, A. Palella, A. Patti, L. Spadaro, *Appl Catal B* **2017**, *218*, 803–809.

[103] Z. Liu, E. Huang, I. Orozco, W. Liao, R. M. Palomino, N. Rui, T. Duchoň, S. Nemšák, D. C. Grinter, M. Mahapatra, P. Liu, J. A. Rodriguez, S. D. Senanayake, *Science (1979)* **2020**, *368*, 513–517.

[104] H.-Y. Li, Y.-L. Guo, Y. Guo, G.-Z. Lu, P. Hu, *J Chem Phys* **2008**, *128*, DOI 10.1063/1.2832324.

[105] D. Kiatsaengthong, K. Jaroenpanon, P. Somchuea, T. Chukeaw, M. Chareonpanich, K. Faungnawakij, H. Sohn, G. Rupprechter, A. Seubsai, *ACS Omega* **2022**, *7*, 1785–1793.

[106] A. Modi, W. Ali, P. R. Mohanta, N. Khatun, B. K. Patel, *ACS Sustain Chem Eng* **2015**, *3*, 2582–2590.

[107] S. Priyadarshini, P. J. Amal Joseph, M. Lakshmi Kantam, *Tetrahedron* **2014**, *70*, 6068–6074.

[108] J. Rafique, S. Saba, T. E. A. Frizon, A. L. Braga, *ChemistrySelect* **2018**, *3*, 328–334.

[109] M. A. Bañares, *Catal Today* **1999**, *51*, 319–348.

[110] S. S. Acharyya, S. Ghosh, R. Bal, *Chem. Commun.* **2014**, *50*, 13311–13314.

[111] M. Ishida, Y. Masumoto, R. Hamada, S. Nishiyama, S. Tsuruya, M. Masai, *Journal of the Chemical Society, Perkin Transactions 2* **1999**, 847–854.

[112] B. M. Weckhuysen, D. Wang, M. P. Rosynek, J. H. Lunsford, *J Catal* **1998**, *175*, 347–351.

[113] N. S. Sanjini, S. Velmathi, *Journal of Porous Materials* **2016**, *23*, 1527–1535.

[114] W. Zhao, Y. Shi, Y. Jiang, X. Zhang, C. Long, P. An, Y. Zhu, S. Shao, Z. Yan, G. Li, Z. Tang, *Angewandte Chemie International Edition* **2021**, *60*, 5811–5815.

[115] R. Gusmão, M. Veselý, Z. Sofer, *ACS Catal* **2020**, *10*, 9634–9648.

[116] W. Huang, S. Zhang, Y. Tang, Y. Li, L. Nguyen, Y. Li, J. Shan, D. Xiao, R. Gagne, A. I. Frenkel, F. F. Tao, *Angewandte Chemie* **2016**, *128*, 13639–13643.

[117] M. D. Marcinkowski, M. T. Darby, J. Liu, J. M. Wimble, F. R. Lucci, S. Lee, A. Michaelides, M. Flytzani-Stephanopoulos, M. Stamatakis, E. C. H. Sykes, *Nat Chem* **2018**, *10*, 325–332.

[118] E. Yuan, M. Zhou, P. Jian, X. Hou, *Appl Surf Sci* **2023**, *613*, 155886.

[119] Y. Liu, Y. Zhou, J. Li, Q. Wang, Q. Qin, W. Zhang, H. Asakura, N. Yan, J. Wang, *Appl Catal B* **2017**, *209*, 679–688.

[120] H. Zhou, Y. Zhao, J. Gan, J. Xu, Y. Wang, H. Lv, S. Fang, Z. Wang, Z. Deng, X. Wang, P. Liu, W. Guo, B. Mao, H. Wang, T. Yao, X. Hong, S. Wei, X. Duan, J. Luo, Y. Wu, *J Am Chem Soc* **2020**, *142*, 12643–12650.

[121] M. J. Climent, A. Corma, S. Iborra, *Chem Rev* **2011**, *111*, 1072–1133.

[122] A. Primo, P. Concepción, A. Corma, *Chemical Communications* **2011**, *47*, 3613.

[123] R. Arrigo, M. Hävecker, R. Schlögl, D. S. Su, *Chemical Communications* **2008**, 4891.

[124] G. A. Somorjai, J. Y. Park, *Angewandte Chemie International Edition* **2008**, *47*, 9212–9228.

[125] H.-L. Jiang, Q. Xu, *J Mater Chem* **2011**, *21*, 13705.

[126] F. Polo-Garzon, V. Fung, J. Zhang, Z. Bao, H. M. Meyer, M. Kidder, Z. Wu, *ACS Catal* **2022**, *12*, 11845–11853.

[127] F. Polo-Garzon, V. Fung, J. Zhang, Z. Bao, H. M. Meyer, M. Kidder, Z. Wu, *ACS Catal* **2022**, *12*, 11845–11853.

[128] K. Sutthiumporn, T. Maneerung, Y. Kathiraser, S. Kawi, *Int J Hydrogen Energy* **2012**, *37*, 11195–11207.

[129] H. Chang, E. Bjørgum, O. Mihai, J. Yang, H. L. Lein, T. Grande, S. Raaen, Y.-A. Zhu, A. Holmen, D. Chen, *ACS Catal* **2020**, *10*, 3707–3719.

[130] X. Yu, B. Wu, M. Huang, Z. Lu, J. Li, L. Zhong, Y. Sun, *Energy & Fuels* **2021**, *35*, 4418–4427.

[131] D. S. Moore, **2022**, pp. 183–198

Chapter 2A

Benzene Hydroxylation using La_2CuO_4 Perovskite

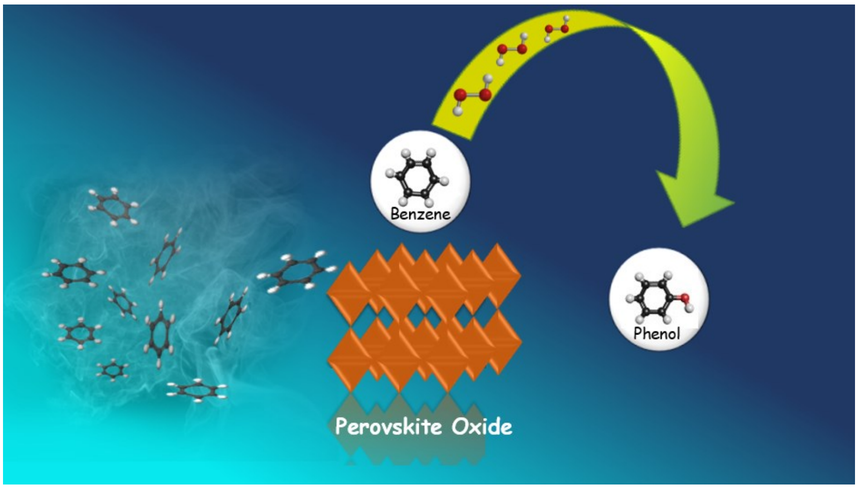

This chapter is adapted from

P. Kumar, A. Vijay Jagtap, S. Gupta, C. P. Vinod, La−Cu based heterogeneous perovskite catalyst for highly selective benzene hydroxylation under mild conditions. *Chem Asian J.* **2022**, 17, e202200788

2A.1 Introduction

Production of industrially important fine chemicals and feedstocks from inexpensive and naturally abundant petroleum-derived hydrocarbons is one of the hot research topics, yet a long-standing challenge remains.[1,2] Due to stringent environmental regulations, the community intensely explores the development of new catalytic technologies operating under benign conditions. Research into converting benzene to phenol through direct C-H activation has garnered significant attention from scientists globally. Phenol is recognized as a vital raw material in the chemical sector, serving as a precursor for a wide array of essential products and intermediates, including resins, fungicides, pesticides, preservatives, pharmaceuticals, caprolactam, and adipic acid.[3–5] As discussed in Chapter 1, the Cumene process used for producing phenol on an industrial scale has several limitations, including low yields, the formation of hazardous by-products like cumene hydroperoxide, and a complex multi-step reaction pathway. This has given enough scope for improving this process.[6] Developing a one-step heterogeneous process for converting benzene into phenol using H_2O_2 as an oxidant with high conversion and selectivity is of great interest.[7,8] Heterogeneous catalysts are advantageous because of the easy separation/recovery of solid catalytic material from the process, leading to a greener pathway and lesser pollution[9,10]. Recently, novel heterogeneous catalysts, such as zeolites[11,12], noble metal-based catalysts[13–15] and transition metal nanomaterials (especially Cu, Fe, and V)[16–22], have been developed for this reaction. A recent report shows ~71% benzene conversion with 91% selectivity for phenol using Cu_1-N_2/HCNS single-atom catalyst[17]. Supported metal oxides are also explored where Cu/Fe-SBA-15 shows ~35% benzene conversion with 90% phenol selectivity[19]. Much research has been done using different catalytic systems, but most suffer from low stability, tedious synthesis methods, and excess expensive oxidants.

Perovskites are a category of inorganic materials that have garnered significant interest in various fields of materials chemistry, yet their potential in catalysis remains underexplored. Renowned for their stability and the ease of scalable synthesis, perovskites are ideal candidates for use as catalysts in fine chemical production. These materials typically follow the general chemical formula ABO_3, where "A" denotes a large-radius ion such as a rare-earth or alkaline metal, "B" signifies a transition metal, and "O" represents oxygen. The A-site cations maintain the structural integrity of perovskites, while the B-site cations are responsible for their catalytic properties [26]. Recently, perovskite nanomaterials have been employed in various catalytic processes, including methane activation, CO_2 reduction, epoxidation reaction, etc.[26–31] Compared to mixed metal oxide catalysts, perovskite-type catalysts exhibit superior thermal stability and flexible valence states of transition metal ions, enhancing their redox capabilities.[32] Additionally, cations at the A or B sites often coordinate with other ions like oxygen, forming defects such as oxygen vacancies, which can optimize catalytic performance. Generally, perovskite exists in various structural forms, among which the A_2BO_4 class is known as layered perovskite.[33]

This study presents La_2CuO_4, a perovskite oxide identified as an effective catalyst for the one-step hydroxylation of benzene to phenol under mild conditions. La_2CuO_4 has an orthorhombic distortion with a tetragonal K_2NiF_4 structure[34] comprising stacked CuO_2 and LaO layers (Figure 2A.1). Each copper atom is octahedrally coordinated by six oxygen atoms, forming interconnected octahedra within the perovskite framework. This unique structural configuration of La_2CuO_4 perovskite will provide variable oxidation states for the Cu (B site cation) in our catalyst material. As reported on supported Cu-based catalysts, we envisage that such defect centers can play a key role in benzene hydroxylation.[17,35]

2A.2 Experimental methods

2A.2.1 Materials

All chemicals were used without further purification. Copper (II) nitrate trihydrate and citric acid monohydrate were purchased from Himedia, and Lanthanum nitrate hexahydrate was purchased from Loba Chemie PVT. Limited. Benzene was purchased from Sigma Aldrich, and HPLC-grade acetonitrile was purchased from Thomas Baker for reaction.

2A.2.2 Synthesis of La-Cu-based oxides

All samples with different Lanthanum-Copper ratios were prepared using the citrate sol-gel method, which allows the formation of amorphous citrates of metals with broad flexibility of compositions. In this method, lanthanum metal precursor $La(NO_3)_3 \cdot 6H_2O$ and Cu metal precursor $Cu(NO_3)_2 \cdot 3H_2O$ were mixed with the desired mole ratio in 20 mL distilled water (18 MΩ cm) under stirring at 70 °C for 1 h. Citric acid was added to the metal salts at a molar ratio of 1:2 (total metal ion/citric acid) to ensure the complete complexation of metal ions. The resulting solution was stirred at 70 °C to form a gel. The gel was then dried at 70-100 °C for 12 h to remove the remaining water. The hygroscopic material was calcined in 2 steps, first at 400 °C for 4 h followed by 800 °C for 4 h. In a typical synthesis batch, 1 gm of catalyst was made with phase purity. Materials were named xLCO, where x is the molar ratio of Cu metal with respect to La metal × 100. For example, if the Cu: La molar ratio is 0.5:1, the sample is named 50LCO; if it is 1:1, it is named 100LCO. All the synthesized catalysts were tested for benzene hydroxylation reaction.

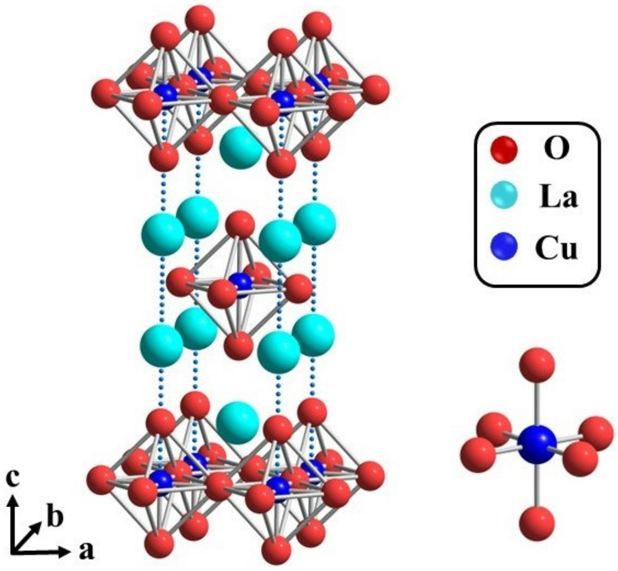

Figure 2A.1 Crystal structure of La_2CuO_4.

2A.2.3 Catalyst Characterisation

The X-ray diffraction (XRD) patterns of the samples were recorded on a powder X-ray diffractometer (Rigaku Miniflex 2200PC), using Cu-Ka radiation (λ = 0.15405 nm) in the 2θ range of 10–80° at a scanning rate of 3° min^{-1}.

N_2 adsorption-desorption isotherms and pore size distributions of the samples were collected using an Autosorb 1C Quantachrome, USA. The program consisted of adsorption and desorption branches and was performed typically at 77 K after a quartz tube with 50mg of the sample was dewatered and degassed for 10 h at 300 °C and under a 1 MPa vacuum. Calculation of the specific surface area was done by the Brunauer-Emmett-Teller (BET) method at P/P_0=0.06–0.3.

Thermogravimetry differential thermal analysis (TG-DTA, Pyris Diamond) was used to analyze the catalyst's formation mechanism and crystallization temperature.

FTIR absorbance spectra were obtained in the wavenumber range between 1000 and 400 cm^{-1} using a Perkin Elmer Infrared Spectrometer.

FESEM characterization was performed on a NOVA NANO SEM field emission scanning electron microscope. TEM analysis was carried out using the TECHNAI FEI instrument. The samples for TEM analysis were prepared in Iso-propyl alcohol and dried completely before analysis.

X-ray photoelectron spectroscopy (XPS) measurements were carried out using a Thermo Scientific Kalpha + spectrometer using micro-focused and monochromated Al Kα radiation with energy 1486.6 eV. The peak fitting of the individual core levels was done using Avantage software with a smart-type background. All the binding energies were calibrated with respect to C 1s as the reference (284.7 eV).

2A.2.4 Catalytic Activity test

The catalytic activities of catalysts were tested for the hydroxylation of benzene to phenol using H_2O_2 as an oxidizing agent. The reaction was carried out in a 25 mL two-necked flask, equipped with a condenser. The reaction temperature was adjusted by immersing the flask in a thermally controlled oil bath. Benzene (0.5 mL), acetonitrile (0.5 mL), water (1 mL), and a certain amount of catalyst were fed into a two-necked flask. After that, a certain amount of H_2O_2 (30%) was introduced sequentially to the stirred mixture. The catalytic activity was evaluated at a different reaction temperature range of 30-70 ℃ and at a different reaction time in the 1-24 h range. After the reaction, the mixture was centrifuged to remove the solid catalyst. Then, the liquid product was collected and analyzed using a NUCON GC equipped with a Db6 column and flame ionization detector. Gaseous product analysis was done using a methanizer in the FID detector.

2A.2.5 Product Calculations:

Reactant conversion and product selectivity were calculated using the response factor method.

$$\text{Benzene Conversion}(\%) = \frac{\text{Amount of Benzene after the reaction}}{\text{Amount of Benzene before reaction}} \times 100$$

$$\text{Phenol Selectivity (\%)} = \frac{\text{Amount of Phenol}}{\text{Total amount of products}} \times 100$$

Hydrogen peroxide efficiency was calculated using theoretical calculation using the following equation.[36]

$$\mathrm{H_2O_2}\ \text{efficiency (\%)} = \frac{\text{Moles of Benzene reacted}}{\text{Moles of } \mathrm{H_2O_2} \text{ used}} \times 100$$

For example, = (5.6 mmol × 0.51 /4.4 mmol of H_2O_2) ×100 = 64.9 %

After the reaction, no remaining H_2O_2 was observed in the final solution of the reaction.

2A.2.6 General procedure for recyclability test:

Following each reaction, a centrifugal separator extracted the catalyst from the reaction mixture. The recovered catalyst was washed multiple times with acetonitrile, followed by drying at 60-70 °C for several hours. After drying, the catalyst was reutilized for the next catalytic cycle, which was carried out at 60 °C for 5 h. Phenol selectivity was calculated as the percentage of phenol, the desired product, relative to the total products, including both phenol and by-products.

2A.2.7 Product Extraction:

Product extraction was carried out using a well-known distillation process. First, the reaction mixture was passed through sodium sulfate to remove water content. Subsequently, acetonitrile and benzene were removed using a rotary evaporator at 50 °C under vacuum. The resulting product was subjected to a high vacuum to eliminate all remaining water. The crystalline solid product was then extracted from the flask and weighed. Selectivity was determined based on the reaction mixture's GC data. The isolated yield of the product was 60-70% of the GC results. The loss in the theoretical and physical yields is because of the smaller reaction scale, where a small error results in the subsequent product loss.

2A.3 Results and Discussion

2A.3.1 X-Ray Diffraction

X-ray diffraction patterns were obtained for various La-Cu-based catalysts synthesized using the sol-gel method, calcined at 800 °C. When the XRD spectrums of various La-Cu-based materials were compared, we found that when the copper molar ratio was less than 1:0.5, lanthanum metal formed different hydroxide, oxide, and carbonate phases (Figure 2A.2).

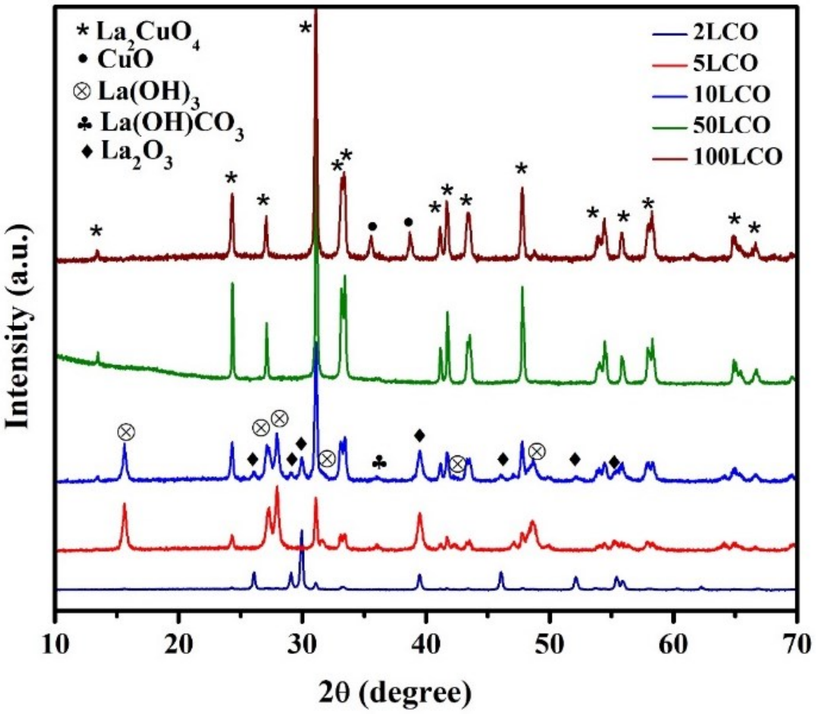

Figure 2A.2 XRD patterns of various La-Cu-based catalysts.

Meanwhile, a monophasic perovskite oxide (La_2CuO_4) with an orthorhombic structure (space group Fmmm) was formed when the molar ratio reached 1:0.5 (JCPDS 038-0709).[31] A further increment in the Cu amount by maintaining the Cu: La molar ratio as 1:1, two extra peaks (35.53° and 37.72°) of tenorite-CuO were observed along with the perovskite phase of La_2CuO_4.

2A.3.2 X-Ray Photoelectron Spectroscopy

The curve-fitting of the core levels was used to make qualitative and quantitative analyses. The O 1s spectrum could be deconvoluted into three components at binding energy (BE) = 528.8, 531.4, and 533.8 eV (Figure 2A.3a) attributed to the surface lattice oxygen species (O_L), adsorbed oxygen (O_A) species, and molecularly adsorbed water species, respectively.[37]

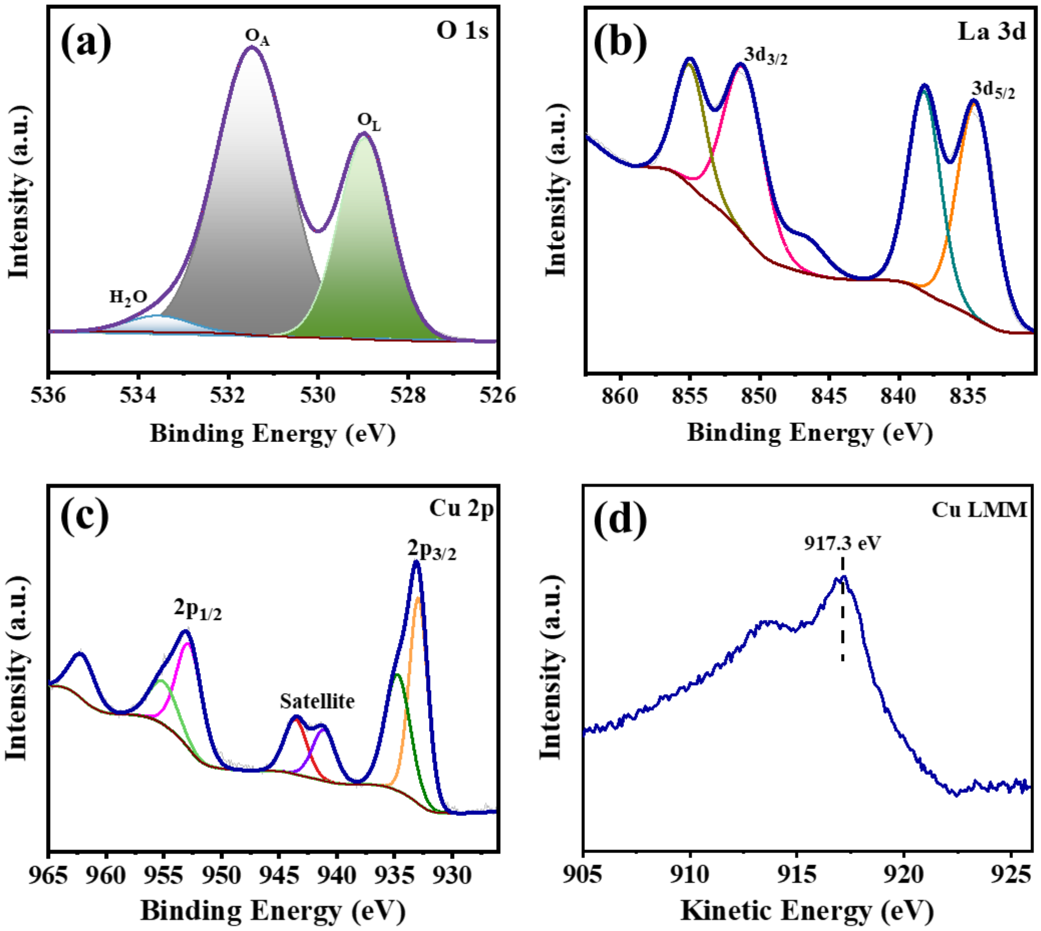

Figure 2A.3 XPS spectrums of 50LCO: O 1s (a), La 3d (b), Cu 2p (c), La 3d (c), and Cu Auger spectrum (d).

It should be noted that the adsorbed oxygen is associated with oxygen vacancy, and its significant presence in the O 1s spectrum indicates abundant surface defects.[38–41] La 3d XPS spectrum shows two broad peaks with significant doublets in the range of 830–840 eV and 847–857 eV, which correspond to La 3d$_{5/2}$ and La 3d$_{3/2}$ respectively (Figure 2A.3b). The specific peaks at 833.6, 837.7, 850.5, and 854.6 eV are attributed to La^{3+}, confirming that the oxidation state of La in 50LCO is largely +3.

For Cu 2p XPS spectra of the catalyst, the binding energy for Cu 2p$_{3/2}$ is detected at 933 and 934.3 eV, confirming the presence of Cu^{1+} and Cu^{2+} species (Figure 2A.3c). Shake-up satellite peaks at BE = 940.9 and 943.3 eV are the signature of Cu^{2+}.[42]

It should be noted that the metallic Cu^{0} appears at the same binding energy of 933 eV as that of Cu^{1+}. To further confirm the presence of Cu^{1+}, Cu LMM Auger was measured, which gave a broad kinetic energy peak centered around 917.3 eV with no signature for Cu^0 at 918.6 eV, establishing the presence of both Cu^{1+} and Cu^{2+} in the sample (Figure 2A.3d).[43]

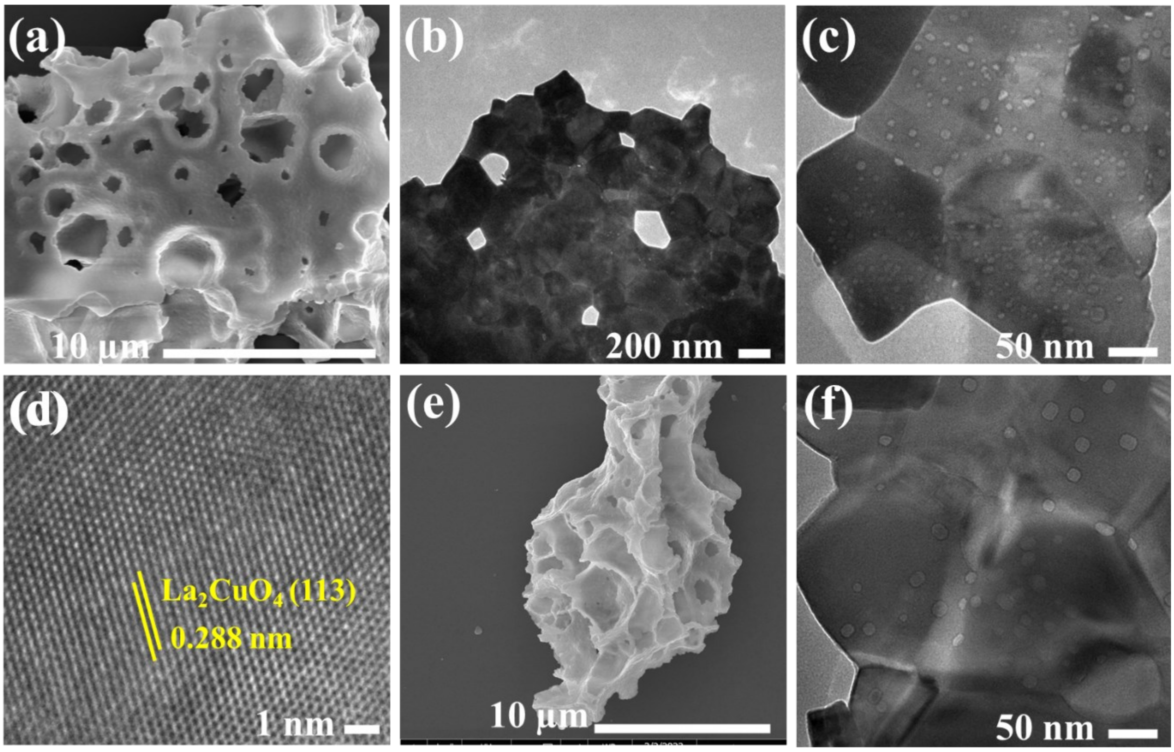

Figure 2A.4 Electron microscopic images of various catalysts: FESESM image of 50LCO (a), TEM image of 50 LCO (b) and HRTEM image of 50LCO (c and d), FESEM image of 100LCO and TEM image of 100LCO.

2A.3.3 Electron Microscopy

The morphology details of the catalyst materials were revealed using electron microscopy (Figure 2A.4). The macroporous nature of the material is confirmed by the FESEM (Figure 2A.4a), where large pores of approx 1-2 µm were visible on the surface. TEM analysis confirmed that metal particles are not of a specific shape or size and can be classified into flake-type morphology. The big particles are in the size range of 100-250 nm, but along with these large size particles, tiny particles of the spherical shape of size in the range of 10-20 nm are also present on the surface of bigger particles (Figure 2A.4 b and c). HRTEM analysis technique further supports the XRD as the lattice spacing (d = 0.288 nm) resembles the La_2CuO_4 (113) plane (Figure 2A.4d). The similar surface information was observed in the case of 100LCO (Figure 2A.4 e and f).

Elemental mapping further confirms the homogeneous distribution of all elements across the surface. (Figure 2A.5). Fast Fourier transformation image confirms the presence of the orthorhombic phase of the bilayer system in 50LCO (inset Figure 2A.5).

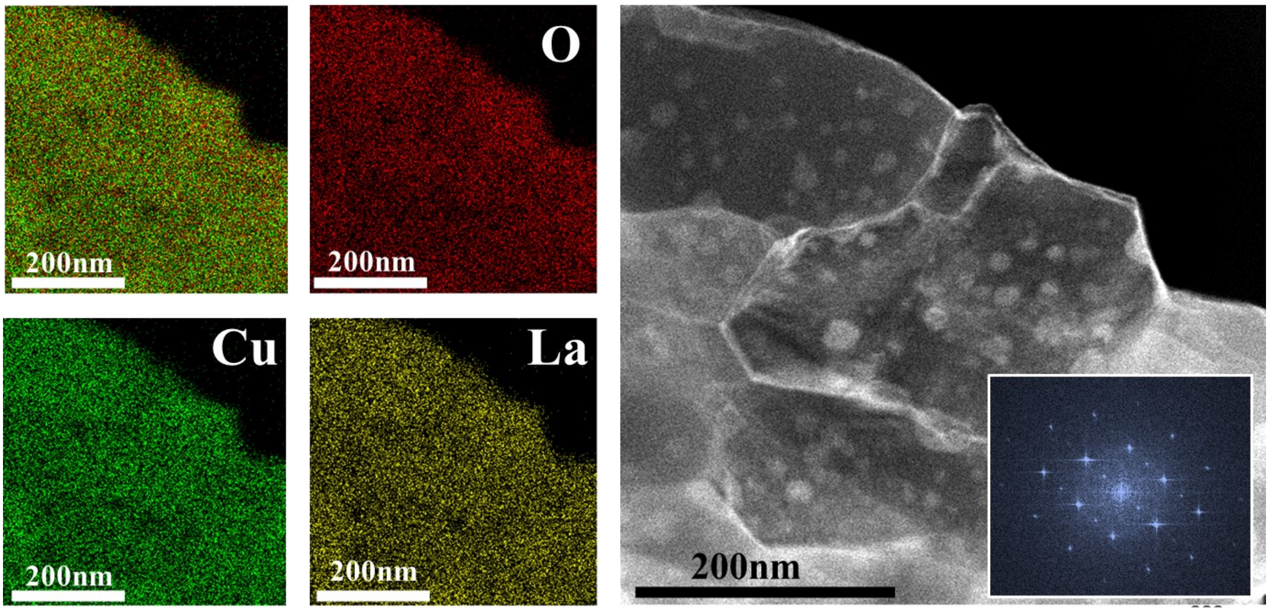

Figure 2A.5 Elemental mapping and SAED pattern of 50LCO.

2A.3.4 FTIR

The catalyst was further characterized to get the details of the internal vibrations of the material. Figure 2A.6a shows the FTIR spectra of the various La-Cu-based mixed metal oxides. The FTIR spectra of 2LCO, 5LCO, and 10LCO display a distinct peak at 3609 cm^{-1}, which is associated with the bulk hydroxyl groups derived from $La(OH)_3$. Also, the peaks at 1477 cm^{-1} and 1384 cm^{-1} are the stretching modes of carbonate. This confirms the presence of phase-separated La_2O_3 species, which are expected to produce surface carbonate.[44]

The FTIR of 50LCO and 100LCO perovskite revealed two distinct vibration bands at wavenumbers 678 and 511 cm^{-1}, which correspond to the stretching vibration of La–O and Cu–O bond within the orthorhombic La_2CuO_4 phase (Figure 2A.6b).[45] The 100LCO catalyst, which has a higher molar ratio of copper to lanthanum (1:1), exhibits additional bands in its IR spectrum compared to catalysts with lower copper content. Specifically, the presence of a band at 593 cm^{-1} is attributed to the Cu–O stretching mode, indicating the formation of a secondary CuO phase. The appearance of the 593 cm^{-1} band suggests that the high copper content leads

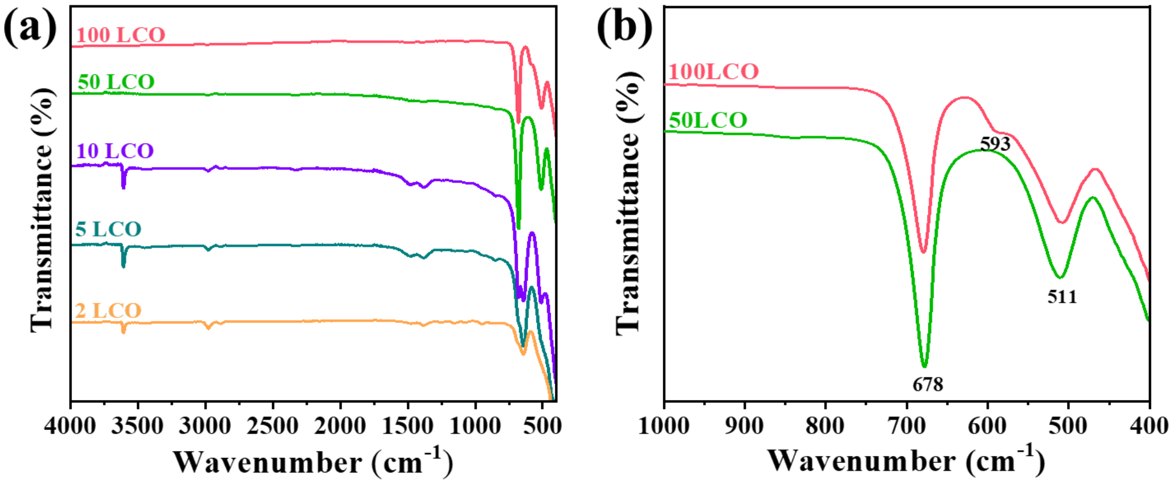

Figure 2A.6 FTIR spectrum of various catalysts (a), 50LCO, and 100LCO (b).

to segregate CuO from the perovskite lattice, forming a second phase within the catalyst.[46] So, the FTIR data also indicates the phase purity of the 50LCO catalyst.

2A.3.5 TGA

The thermal stability of the prepared material was evaluated using thermogravimetric analysis (TGA). Figure 2A.7 presents the TG-DTA analysis of a 10 mg sample of dried 50LCO. The TGA curve indicates a gradual weight reduction occurring between 100 and 270 °C, attributed to the removal of solvent water, crystal water from citric acid, and citrate from the gel.[47] Furthermore, the TGA and DTA curves reveal a notable weight loss in the 300 to 520 °C range, likely resulting from the oxidative combustion or breakdown of citric acid and its derivatives. Beyond 700 °C, no additional weight loss was recorded, indicating that the calcination temperature for the catalyst should exceed 700 °C to ensure complete decomposition of the organic materials.

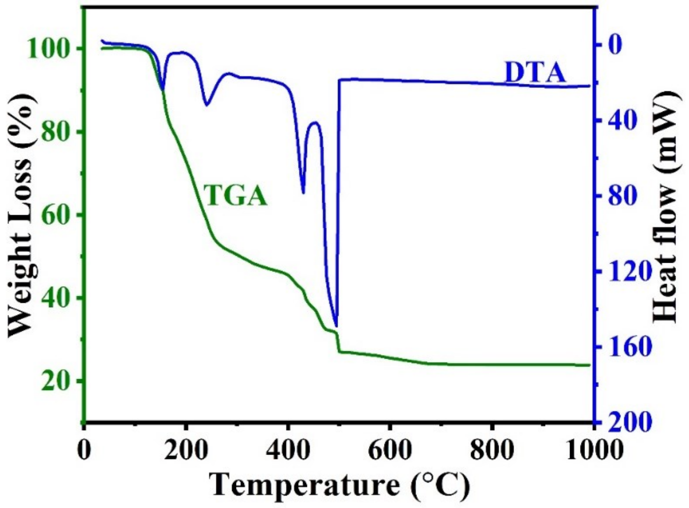

Figure 2A.7 TG-DTA curve of 50LCO.

2A.3.6 N_2 Porosimetry

Nitrogen adsorption-desorption isotherms at 573K for material reveal that the specific surface area was 66 m^2/g for 50LCO catalyst (Figure 2A.8). The present study reports one of the highest specific surface areas for La_2CuO_4 material, possibly due to mesopores and macropores in the structure.[42,48,49]

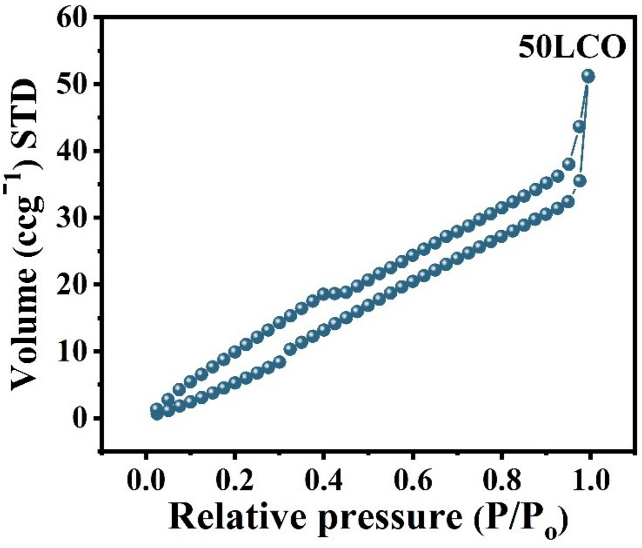

Figure 2A.8 N_2 adsorption-desorption isotherm of 50LCO catalyst.

2A.3.7 Catalytic Activity of La-Cu-based catalyst in Benzene Hydroxylation

The synthesized material was further tested for the benzene hydroxylation using H_2O_2 as an oxidant. In the oxidation reaction, phenol was observed as the primary product, while catechol, benzoquinone, and hydroquinone were observed as side liquid products. Analysis of gaseous products confirmed that CO and CO_2 are present as gaseous by-products, but their contribution in conversion and selectivity was less than 0.01% and was neglected.

2A.3.7.1 Effect of Cu molar ratio: Initially, the catalytic activity for the benzene hydroxylation was tested by varying the molar ratio of metals (Cu: La). While comparing the various copper lanthanum-based oxide systems, we found that when the Cu molar ratio was 0.02 with respect to La, the conversion of benzene was 38% only, but when the Molar ratio was increased to 0.5, the conversion of benzene increased to 51% with high phenol selectivity of >99% (Figure 2A.9a). From here, catalytic activity might depend on the copper content in the system. However, this assumption was wrong because when we increased the metal molar ratio to 1, an increment in the activity was not observed. So, it is clear that the monophasic system La_2CuO_4 is showing the best activity compared to other La-Cu-based oxide systems.

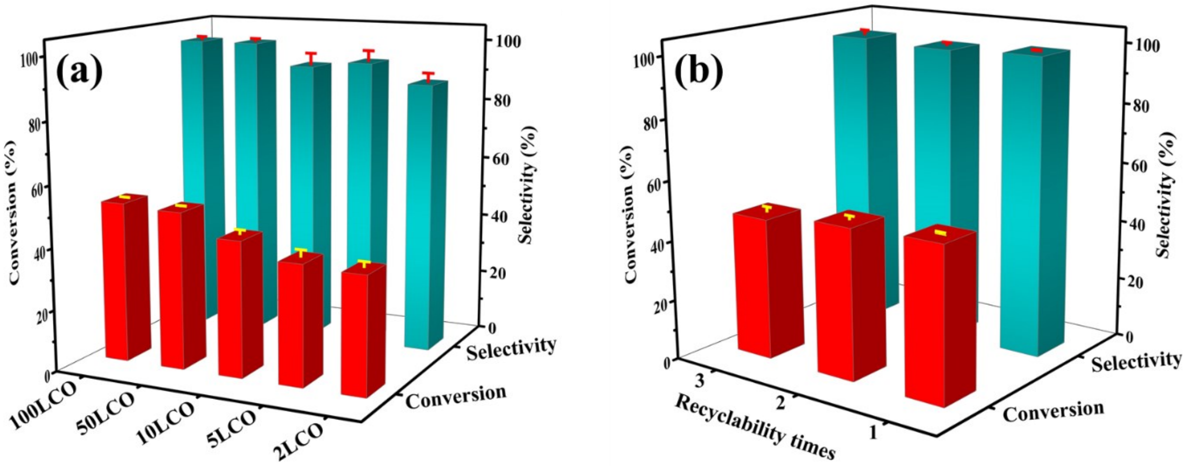

Figure 2A.9 Catalytic activity of various catalysts (a) and recyclability test of 50LCO catalyst(b). Reaction conditions: Benzene (0.5 mL), Catalyst (20 mg), Water (1 mL), Acetonitrile (0.5 mL), H_2O_2 (0.5 mL), 60 °C, 5 h.

Although the turnover no. will be high in low Cu molar ratio catalysts, the recyclability test made this expectation wrong (detailed discussion later in the section). At the same time, recyclability up to 3 cycles confirms the stability of the 50LCO as an efficient catalytic material (Figure 2A.9b).

2A.3.7.2 Effect of Reaction Conditions: The benzene conversion was investigated in a temperature range between 30 to 70 °C while maintaining the same reaction conditions. With the increase in temperature, the percentage of benzene conversion increases effectively. Still, the phenol selectivity rises to 60 °C but decreases afterward because of the formation of overoxidized products at higher temperatures. The best activity was observed at 60 °C with high conversion and selectivity (Figure 2A.10a).

In catalytic reactions, the kinetics are a critical measure of a catalyst's effectiveness. A constant or declining yield of phenol over time indicates that the radical chain reaction has ceased, halting the further oxidation of phenol.

The impact of reaction time on the hydroxylation of benzene was examined for 1 to 24 h, as shown in Table 2A.1. The data obtained demonstrates that benzene conversion is positively correlated with reaction time, peaking at 51% after 5 h of hydroxylation. After this point, while benzene conversion continues to rise, the selectivity for phenol diminishes, leading to a reduction in the overall yield of phenol.

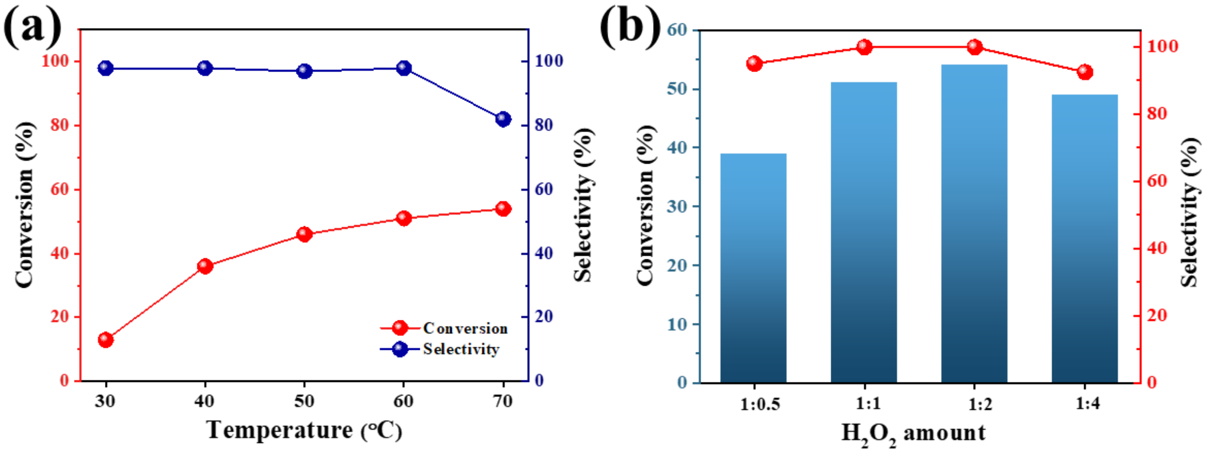

Figure 2A.10 Effect of the temperature (a) and H_2O_2 amount (b) on the catalytic activity of 50LCO.

Consequently, extending the benzene hydroxylation duration negatively impacts phenol yield, as prolonged exposure leads to further oxidation of phenol. This results in the formation of side products such as hydroquinone and catechol. Therefore, it can be concluded that after 5 hours of benzene oxidation, a significant portion of the peroxide radical species interacts with the phenol generated rather than facilitating the activation of the reactant molecules. Compared to the existing literature,[50–52] a high benzene conversion with excellent phenol selectivity within 5 h of reaction time indicates the efficiency of 50LCO. This can be attributed to abundant surface sites in 50LCO that activate the H_2O_2 molecules.

Table 2A.1 Catalytic activity of various catalysts under different reaction conditions.

S. No.	Catalyst	Time (h)	Conv. (%)	Phenol Selectivity (%)	Catechol Selectivity (%)	Hydroquinone Selectivity (%)	Benzoquinone Selectivity (%)
1	50LCO	0.5	23	84	0	0	16
2	50LCO	1	41	86	0	0	14
3	50LCO	3	44	92	0	0	8
4	50LCO	5	51	>99	0.3	0.6	0
5	100LCO	5	52	>99	0.4	0.5	0
6	50LCO	8	56	78	14	8	0
7	50LCO	24	64	73	13	14	0
8	50LCO[a]	5	46	84	9	0	7
9	50LCO[b]	8	60	74	14	12	0
10	50LCO[c]	5	49	92	5	3	0

Reaction conditions: Benzene (0.5 mL), Catalyst (20 mg), Water (1 mL), Acetonitrile (0.5 mL), H_2O_2 (0.5 mL), 60 °C, 5 h.

[a] when H_2O_2 (500 µL) was added single time instead of sequentially

[b] when H_2O_2 (1mL) was added sequentially up to 7 h (1:2)

[c] when Benzene:H_2O_2 is 1:4.

An increase in the H_2O_2 amount from 1:1 to 1:2 resulted in a marginal increment in the benzene conversion, meaning that the overall H_2O_2 efficiency is compromised (Figure 2A.10b). Also, an increment in the H_2O_2 amount decreases the phenol selectivity due to the over-oxidation products. Interestingly, further experiments proved that the mode of adding H_2O_2 also influences the conversion and phenol selectivity. When H_2O_2 was added sequentially, reactivity data was markedly different. When the reaction time was 1 h, 500 µL/h of H_2O_2 was added upfront (Table 2A.1 entry 2), which led to the fast decomposition of H_2O_2, resulting in lower phenol selectivity (86%) and conversion (41%). This would imply a competition of the excess amount of OH radicals formed, taking either a decomposition pathway to form water or over-oxidizing the formed phenol to polyphenols. In the case of a 3 h reaction, H_2O_2 addition was around 166 µL/h, leading to an increase in conversion (44%) and selectivity (92%). However, an optimum condition for benzene hydroxylation was observed when the reaction was carried out for 5 h (Table 2A.1 entry 4) with sequential every-hour addition of H_2O_2 (100 µL/h). When the H_2O_2 (500 µL) was added initially, and the reaction was carried out for 5 h (Table 2A.1 entry 8), lower conversion and selectivity were observed, similar to the 1 h experiment discussed above (Table 2A.1). Following the sequential addition protocol with increased oxidant amount was also not beneficial (Table 2A.1 entry 9) as 8 h reaction data showed 60% conversion with 74% selectivity. This implies that increasing the time and peroxide amount improves the conversion, but excess peroxide in the reaction mixture produces over-oxidized products. The overall hydrogen peroxide efficiency was 64.9% for a 1:1 system for a 5 h sequential addition reaction, which is very high for any benzene hydroxylation reaction attempted using H_2O_2 as an oxidant.[51–54] To the best of our knowledge, this represents one of the highest peroxide efficiencies reported till now.

2A.3.7.3 Screening Experiments: Several screening experiments have been done to authenticate the study better. Table 2A.2 shows that when no catalyst was present, only 0.9% of benzene was converted to phenol, confirming that the reaction was catalytic. Benzene oxidation was tested with other oxidants like molecular oxygen and tert-butyl hydroperoxide. Molecular oxygen could not insert the oxygen atom in the benzene's C-H bond, resulting in low activity. In the case of TBHP, selectivity was not up to the mark because of the faster decomposition of peroxide. The use of H_2O_2 governs a greener pathway and higher catalytic activity.

Table 2A.2 Catalytic activity of 50LCO catalyst under different reaction conditions.

Sr. No.	**Catalyst**	**Oxidant**	**Benzene Conversion (%)**	**Phenol Selectivity (%)**	**Other oxygenates Selectivity (%)**
1	No Catalyst	H_2O_2	1.3	99.9	0
2	50LCO	-	0.7	99.9	0
3	50LCO	H_2O_2	51	99.9	0
4	50LCO	O_2	0.5	99.9	0
5	50LCO	TBHP	56	65.1	34.9

2A.3.7.4 Catalyst Recovery and Reuse: To check the durability of the La-Cu-based catalysts in benzene hydroxylation, several experiments were tested using the recovered catalyst utilizing the same conditions employed previously. After the completion of each catalytic cycle, the catalyst was recovered by centrifugation, washed multiple times with

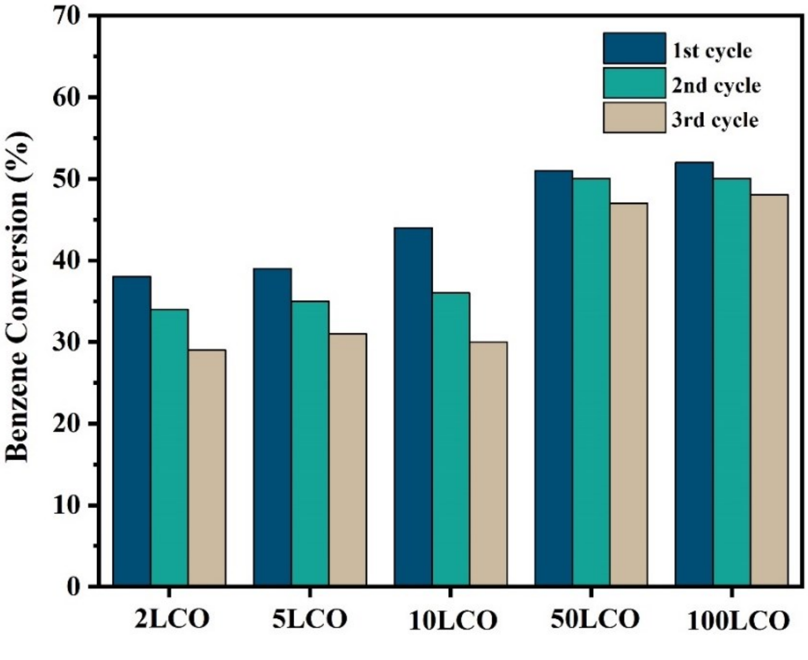

Figure 2A.11 Recyclability tests for the catalytic activity of various catalysts. Reaction conditions: Benzene (0.5 mL), Catalyst (20 mg), Water (1 mL), Acetonitrile (0.5 mL), H_2O_2 (0.5 mL), 60 °C, 5 h.

acetonitrile, dried at 60 °C for 12h, and used for the catalytic reaction without any post-treatment.

In Figure 2A.11, we can see that when we tested the various catalysts for recyclability, there was a noticeable decrement in the activity after each cycle in the case of a low Cu content catalyst. This may be because of the leaching of the active phase from the catalyst, as confirmed by XRD. However, in the case of 50LCO and 100LCO, the activity was maintained after each cycle, making this system worthy. The results clearly show that there is only a small decrease in the benzene conversion and phenol selectivity after the 3rd cycle using a 50LCO catalyst under the same reaction conditions. From this, we can conclude that the employed 50LCO is robust enough to withstand the challenging reaction conditions of the benzene hydroxylation process, but it was not the same in the case of a lower Cu content catalyst.

2A.3.7.5 Spent Catalyst Analysis: The perovskite phase of the regenerated catalyst was analyzed through X-ray diffraction (XRD) to confirm that there were no phase changes during its catalytic performance. The XRD patterns for both the fresh and regenerated catalysts are presented in Figure 2A.12. The XRD results for the recovered catalyst, identified as 50LCO, indicate that it maintained its phase during the benzene hydroxylation process; however, a minor reduction in peak intensity was noted. 100LCO catalyst also does not undergo any phase transformation after the catalytic reaction, which means it also has structural stability (Figure 2A.12b). However, the scenario was different in the case of 5LCO. We can easily see the phase transformation or the active phase leaching after the reaction, which indicates instability. XPS analysis of 50LCO also confirms the retention of La and Cu after the reaction (Figure 2A.13).

Moreover, the reactivity comparison of La_2CuO_4 (i.e., 50LCO) was also made with other La-M (M= Fe, Ni) perovskites. It was found that La-Cu-based perovskite material shows the best activity for benzene hydroxylation reaction.

The results in the article are based on data analysis done using the gas chromatography technique. Still, quantitative and qualitative analysis was also tested by product extraction from the reaction mixture using the solvent evaporation technique, and the extracted product yield was 60-70% of the result shown by the GC. This can be because of the volatile nature of the benzene and manual errors during the extraction process. As this is a small-scale reaction and a minute manual error will show a noticeable difference in the data, the volatile nature of benzene is also a participant in this difference.

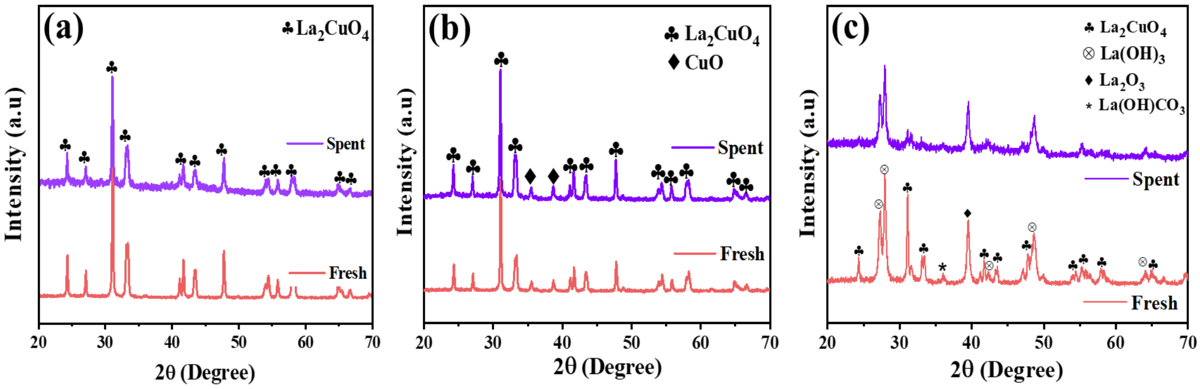

Figure 2A.12 XRD patterns of various spent catalysts: 50LCO (a), 100LCO (b), and 5LCO (c)

To investigate the heterogeneity of the catalyst, a hot filtration test was conducted. This involved separating the catalyst from the reaction mixture using filter paper while the reaction was still underway. A sample was then taken from the filtered reaction solution and analyzed using gas chromatography (GC). This allowed for an assessment of whether any catalytic activity continued in the absence of the original catalyst material, which would suggest the presence of leached, active species in the solution. The GC analysis provided quantitative data on the composition of the filtered sample, enabling conclusions to be drawn about the homogeneity or heterogeneity of the catalyst under the reaction conditions. The reaction was further carried on up to the final time, and the reaction mixture was analyzed after the completion of the reaction. In this test, it was found that there was no increment in the activity when the catalyst was removed from the reaction mixture, which confirms the heterogeneity of the material.

It isn't easy to compare the results in the present work with the previously reported systems in literature because of different reaction parameters. Perovskite oxides have not been much explored for this reaction. Whereas most single-atom catalytic systems need a high amount of H_2O_2, metal oxide-based systems do not have high activity or selectivity. One can conclude that the La-Cu-based perovskite system performs reasonably well under milder conditions than other systems.

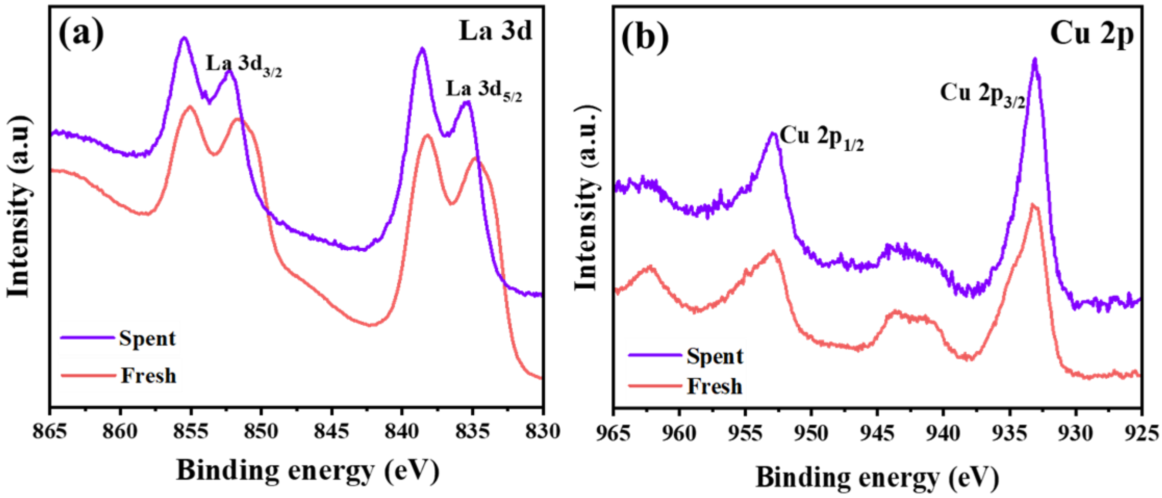

Figure 2A.13 XPS spectrum of spent 50LCO catalyst: La 3d (a) and Cu 2p (b).

2A.3.8 Mechanistic Aspect From the above experimental observations, it is clear that copper acts as the active site for benzene hydroxylation in the LCO catalyst system. Based on the previous studies and our evidence, a plausible mechanism for benzene hydroxylation is proposed for the La-Cu-based perovskite catalyst (Figure 2A.14).[55,56]

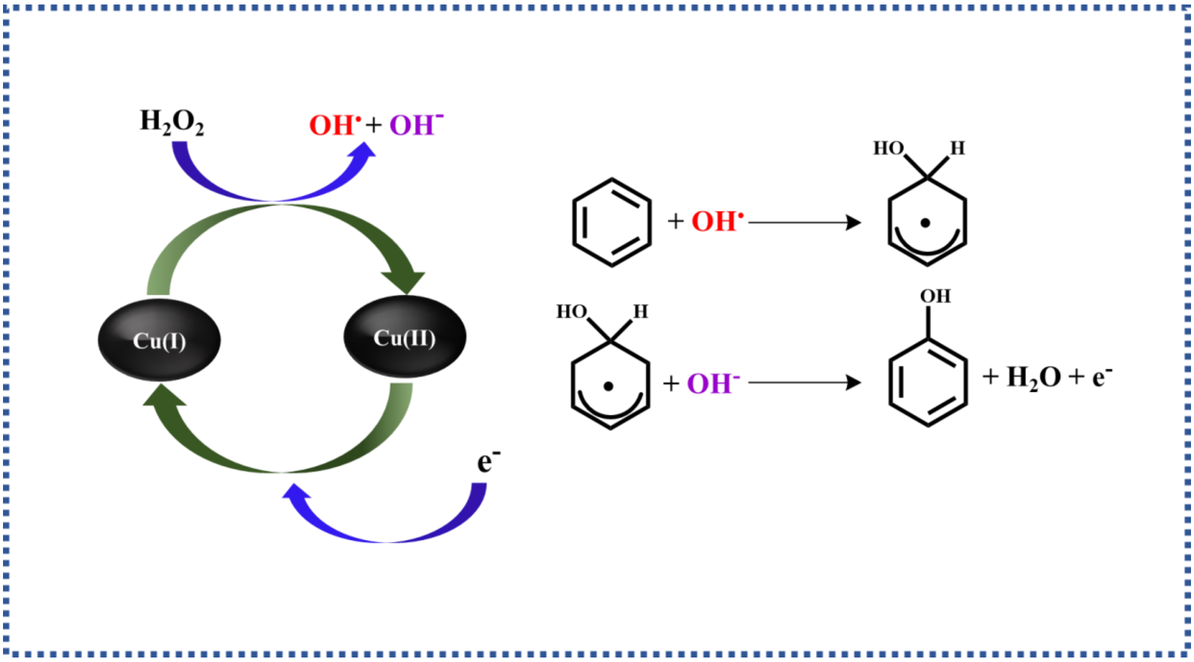

Figure 2A.14 Proposed mechanism of benzene oxidation at the catalyst surface.

It has been reported that Cu(I) in an aqueous solution may behave as a ‘‘Fenton-like’’ catalyst because of the redox behavior of Cu^{1+}/Cu^{2+}.[57] So, in the 1st step of the reaction, H_2O_2 gets activated over the catalyst surface and forms $OH^{\bullet}$ and OH^{-} species, converting Cu^{1+} to Cu^{2+}. Then, the $OH^{\bullet}$ reacts with benzene and forms hydroxycyclohexadienyl radical. The formed radical species undergo self-destruction to form phenol and release electrons and H^{+} ions[56]. The liberated H^{+} reacts with OH^{-} to form a non-dissociated water molecule, and the released electron is captured by the catalyst, resulting in the conversion of Cu^{2+} to Cu^{1+}.

2A.4 Conclusions

Exploring La-Cu-based perovskite catalysts for the one-step oxidation of benzene to phenol presents a significant advancement in green chemistry. These catalysts demonstrate the potential for high selectivity and efficiency in converting benzene, a stable aromatic compound, into phenol, a valuable chemical intermediate. The unique properties of La-Cu perovskites, including their structural stability and ability to facilitate electron transfer, enhance the catalytic process under mild conditions. This approach simplifies the reaction pathway and minimizes the formation of by-products, addressing a common challenge in selective oxidation reactions. Moreover, using abundant and environmentally friendly oxidants, such as hydrogen peroxide, in conjunction with these catalysts aligns with sustainable practices in chemical synthesis. The findings indicate that optimizing reaction conditions, including temperature, solvent choice, and catalyst loading, can further improve the yield and selectivity of phenol production The exceptional peroxide efficiency observed in the reaction underscores the effectiveness of the catalyst and the process. The La-Cu-based oxides were synthesized using the sol-gel method and then tested for one-step benzene oxidation. The perovskite La_2CuO_4 displayed a selective hydroxylation of benzene to phenol with a 51% conversion rate, achieving a high selectivity of over 99% within 5 h using H_2O_2 as an oxidant. Advanced characterization tools were instrumental in deeply investigating the material’s properties. This study presents a promising strategy as an alternative to traditional processes for the selective hydroxylation of benzene. It represents a significant step forward in utilizing perovskite materials for catalytic purposes within the field of chemistry.

2A.5 References

[1] C. Shan, L. Zhu, L.-B. Qu, R. Bai, Y. Lan, *Chem Soc Rev* **2018**, *47*, 7552–7576.

[2] J. A. Leitch, C. G. Frost, *Chem Soc Rev* **2017**, *46*, 7145–7153.

[3] Y. Gu, Q. Li, D. Zang, Y. Huang, H. Yu, Y. Wei, *Angewandte Chemie International Edition* **2021**, *60*, 13310–13316.

[4] W. Wang, N. Li, L. Shi, Y. Ma, X. Yang, *Appl Catal A Gen* **2018**, *553*, 117–125.

[5] R. Meimani, Z. Aghajani, G. R. Najafi, *Research on Chemical Intermediates* **2018**, *44*, 3947–3958.

[6] R. J. Schmidt, *Appl Catal A Gen* **2005**, *280*, 89–103.

[7] G. Ding, W. Wang, T. Jiang, B. Han, H. Fan, G. Yang, *ChemCatChem* **2013**, *5*, 192–200.

[8] T. Tsuji, A. A. Zaoputra, Y. Hitomi, K. Mieda, T. Ogura, Y. Shiota, K. Yoshizawa, H. Sato, M. Kodera, *Angewandte Chemie International Edition* **2017**, *56*, 7779–7782.

[9] K. Tian, W.-J. Liu, S. Zhang, H. Jiang, *Green Chemistry* **2016**, *18*, 5643–5650.

[10] S. S. Acharyya, S. Ghosh, S. Adak, T. Sasaki, R. Bal, *Catal. Sci. Technol.* **2014**, *4*, 4232–4241.

[11] R. Bal, M. Tada, T. Sasaki, Y. Iwasawa, *Angewandte Chemie - International Edition* **2006**, *45*, 448–452.

[12] H. Xin, A. Koekkoek, Q. Yang, R. van Santen, C. Li, E. J. M. Hensen, *Chemical Communications* **2009**, 7590.

[13] Z. Hou, L. Dai, Y. Liu, J. Deng, L. Jing, W. Pei, R. Gao, Y. Feng, H. Dai, *Appl Catal B* **2021**, *285*, DOI 10.1016/j.apcatb.2020.119844.

[14] S. M. Hosseini, M. Ghiaci, S. A. Kulinich, W. Wunderlich, B. H. Monjezi, Y. Ghorbani, H. S. Ghaziaskar, A. Javaheri Koupaei, *Appl Surf Sci* **2020**, *506*, DOI 10.1016/j.apsusc.2019.144644.

[15] X. Ma, R. Dang, Z. Liu, F. Yang, H. Li, T. Guo, J. Luo, *Chem Eng Sci* **2020**, *211*, DOI 10.1016/j.ces.2019.115274.

[16] J. Xu, Y. Hong, M. J. Cheng, B. Xue, Y. X. Li, *Microporous and Mesoporous Materials* **2019**, *285*, 223–230.

[17] T. Zhang, X. Nie, W. Yu, X. Guo, C. Song, R. Si, Y. Liu, Z. Zhao, *iScience* **2019**, *22*, 97–108.

[18] H. Zhou, Y. Zhao, J. Gan, J. Xu, Y. Wang, H. Lv, S. Fang, Z. Wang, Z. Deng, X. Wang, P. Liu, W. Guo, B. Mao, H. Wang, T. Yao, X. Hong, S. Wei, X. Duan, J. Luo, Y. Wu, *J Am Chem Soc* **2020**, *142*, 12643–12650.

[19] Y. Wu, X. Zhang, F. Wang, Y. Zhai, X. Cui, G. Lv, T. Jiang, J. Hu, *Ind Eng Chem Res* **2021**, *60*, 8386–8395.

[20] P. R. Makgwane, S. S. Ray, *J Mol Catal A Chem* **2015**, *398*, 149–157.

[21] Y. Dong, X. Zhan, X. Niu, J. Li, F. Yuan, Y. Zhu, H. Fu, *Microporous and Mesoporous Materials* **2014**, *185*, 97–106.

[22] N. S. Sanjini, S. Velmathi, *Journal of Porous Materials* **2016**, *23*, 1527–1535.

[23] X. Du, J. Li, G. Niu, J. H. Yuan, K. H. Xue, M. Xia, W. Pan, X. Yang, B. Zhu, J. Tang, *Nat Commun* **2021**, *12*, DOI 10.1038/s41467-021-23788-4.

[24] F. Ali, C. Roldán-Carmona, M. Sohail, M. K. Nazeeruddin, *Adv Energy Mater* **2020**, *10*, DOI 10.1002/aenm.202002989.

[25] Y. Hu, T. Niu, Y. Liu, Y. Zhou, Y. Xia, C. Ran, Z. Wu, L. Song, P. Müller-Buschbaum, Y. Chen, W. Huang, *ACS Energy Lett* **2021**, *6*, 2917–2943.

[26] L. Yang, Y. Jiao, X. Xu, Y. Pan, C. Su, X. Duan, H. Sun, S. Liu, S. Wang, Z. Shao, *ACS Sustain Chem Eng* **2022**, *10*, 1899–1909.

[27] L. He, Y. Zhang, Y. Zang, C. Liu, W. Wang, R. Han, N. Ji, S. Zhang, Q. Liu, *ACS Catal* **2021**, *11*, 14224–14236.

[28] L. Yang, Y. Jiao, X. Xu, Y. Pan, C. Su, X. Duan, H. Sun, S. Liu, S. Wang, Z. Shao, *ACS Sustain Chem Eng* **2022**, *10*, 1899–1909.

[29] V. Fung, F. Polo-Garzon, Z. Wu, D. E. Jiang, *Catal Sci Technol* **2018**, *8*, 702–709.

[30] S. Royer, D. Duprez, F. Can, X. Courtois, C. Batiot-Dupeyrat, S. Laassiri, H. Alamdari, *Chem Rev* **2014**, *114*, 10292–10368.

[31] J. Wang, C. Cheng, B. Huang, J. Cao, L. Li, Q. Shao, L. Zhang, X. Huang, *Nano Lett* **2021**, *21*, 980–987.

[32] R. J. H. Voorhoeve, D. W. Johnson, J. P. Remeika, P. K. Gallagher, *Science (1979)* **1977**, *195*, 827–833.

[33] D. Kwon, I. Yang, S. An, J. Cho, J.-M. Ha, J. C. Jung, *Molecular Catalysis* **2021**, *506*, 111548.

[34] H. Hosono, K. Tanabe, E. Takayama-Muromachi, H. Kageyama, S. Yamanaka, H. Kumakura, M. Nohara, H. Hiramatsu, S. Fujitsu, *Sci Technol Adv Mater* **2015**, *16*, 033503.

[35] S. S. Acharyya, S. Ghosh, S. Adak, T. Sasaki, R. Bal, *Catal Sci Technol* **2014**, *4*, 4232–4241.

[36] Y. Yu, Z. Tang, J. Wang, R. Wang, Z. Chen, H. Liu, K. Shen, X. Huang, Y. Liu, M. He, *J Catal* **2020**, *381*, 96–107.

[37] M. W. Roberts, *Chem Soc Rev* **1989**, *18*, 451.

[38] J.-C. Dupin, D. Gonbeau, P. Vinatier, A. Levasseur, *Physical Chemistry Chemical Physics* **2000**, *2*, 1319–1324.

[39] A. S. A. Raj, V. Biju, *Mater Sci Semicond Process* **2017**, *68*, 38–47.

[40] R. K., P. N., V. C.P., T. S. Khan, S. Gupta, M. A. Haider, D. Jagadeesan, *Appl Catal B* **2021**, *297*, 120417.

[41] S. Gupta, C. Ciotonea, S. Royer, J.-P. Dacquin, C. P. Vinod, *Appl Mater Today* **2020**, *19*, 100586.

[42] Z. Zhang, X. Chen, X. Zhang, H. Lin, H. Lin, Y. Zhou, X. Wang, *Catal Commun* **2013**, *36*, 20–24.

[43] V. N. Popok, S. M. Novikov, Y. Yu. Lebedinskij, A. M. Markeev, A. A. Andreev, I. N. Trunkin, A. v. Arsenin, V. S. Volkov, *Plasmonics* **2021**, *16*, 333–340.

[44] B. P. Gangwar, V. Palakollu, A. Singh, S. Kanvah, S. Sharma, *RSC Adv.* **2014**, *4*, 55407–55416.

[45] M. Sukumar, L. J. Kennedy, J. J. Vijaya, B. Al-Najar, M. Bououdina, *New Journal of Chemistry* **2018**, *42*, 18128–18142.

[46] D. Manos, F. Papadopoulou, A. Margellou, D. Petrakis, I. Konstantinou, *Catalysts* **2022**, *12*, 187.

[47] J. Yuan, H. Dai, L. Zhang, J. Deng, Y. Liu, H. Zhang, H. Jiang, H. He, *Catal Today* **2011**, *175*, 209–215.

[48] K.-Y. A. Lin, Y.-C. Chen, Y.-F. Lin, *Chem Eng Sci* **2017**, *160*, 96–105.

[49] O. P. Taran, A. B. Ayusheev, O. L. Ogorodnikova, I. P. Prosvirin, L. A. Isupova, V. N. Parmon, *Appl Catal B* **2016**, *180*, 86–93.

[50] S. Mishra, R. Bal, R. K. Dey, *Molecular Catalysis* **2021**, *499*, 111310.

[51] T. Zhang, D. Zhang, X. Han, T. Dong, X. Guo, C. Song, R. Si, W. Liu, Y. Liu, Z. Zhao, *J Am Chem Soc* **2018**, *140*, 16936–16940.

[52] W. Chen, H. Jin, F. He, P. Cui, C. Cao, W. Song, *Nano Res* **2022**, *15*, 3017–3025.

[53] K. Tian, W.-J. Liu, S. Zhang, H. Jiang, *Green Chemistry* **2016**, *18*, 5643–5650.

[54] Y. Liu, Y. Zheng, P. Dong, W. Zhang, W. Wu, J. Mao, *ACS Appl Mater Interfaces* **2021**, *13*, 61047–61054.

[55] M. Ishida, Y. Masumoto, R. Hamada, S. Nishiyama, S. Tsuruya, M. Masai, *Journal of the Chemical Society, Perkin Transactions 2* **1999**, 847–854.

[56] C. A. Antonyraj, K. Srinivasan, *Catalysis Surveys from Asia* **2013**, *17*, 47–70.

[57] D. A. Nichela, A. M. Berkovic, M. R. Costante, M. P. Juliarena, F. S. García Einschlag, *Chemical Engineering Journal* **2013**, *228*, 1148–1157.

Chapter 2B

Shaped Perovskite Synthesis and Applications

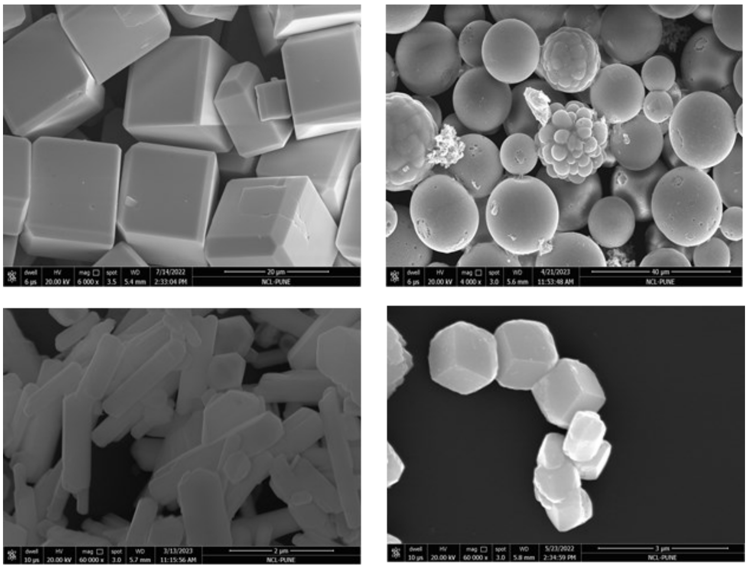

2B.1 Introduction

Facet engineering by creating specific shapes is an elegant route for modifying the physical, chemical, and electronic characteristics of a solid surface. [1–3] This approach offers an efficient method to enhance the performance of materials across various industries. Researchers in catalysis science are delving into the synthesis and activity of metal nanoparticles, focusing on controlling their shapes to optimize their properties.[4–8] As mentioned in Chapter 1, mixed metal oxides are investigated in catalysis due to the synergistic effect of combining two or more metals, enhancing the materials' activity. However, the influence of shape or facet-dependent synthesis and activity in mixed metal oxides remains largely unexplored. By tuning the active facet of these mixed metal oxides, numerous opportunities could emerge for their application within the scientific community. As discussed in Chapter 2A, the unique perovskite crystal structure, where a large cation (A) occupies the corners of the cubic lattice and a smaller cation (B) resides at the center, surrounded by an octahedron of oxygen anions, allows for extensive compositional variation.[9] This tunability makes perovskite oxides exceptionally versatile, enabling the fine-tuning of their physical properties to suit specific applications such as solid oxide fuel cells, photocatalysis, and environmental remediation. One of the most compelling aspects of perovskite oxides is their shape-dependent properties, which profoundly influence their catalytic performance. The morphology of these materials dictates the exposure of specific crystallographic facets, the distribution of active sites, and the overall surface area available for catalytic reactions. Each distinct shape offers unique catalytic behaviors, as the crystallographic facets often display different reactivities. For example, certain facets may preferentially adsorb reactants or intermediates, altering the reaction pathways and significantly enhancing catalytic efficiency.

The shape-dependent synthesis and relative catalytic properties are well explored in material science for mixed metal systems.[10–12] Still, only a handful of reports discuss the shape-dependent synthesis of perovskites.[13–15] The known methods are ineffective for obtaining large amounts of the mixed metal oxides. The reports also suffer from numerous drawbacks, such as the non-availability of simple chemical routes for controlling the single phase of the mixed metal oxides.

Therefore, there exists an interest in obtaining perovskite-based mixed metal oxides for facet engineering, which have various shapes, such that the numerous facets of the oxides are obtained for effective and optimal applications in the new technological domains.[16] There also exists an urgent need to provide a simple, efficacious process for preparing such perovskite-based mixed metal oxides cost-effectively.

The synthesized materials have been investigated for their catalytic activity in the oxidation of cyclohexane, an important source of cyclohexanone and cyclohexanol (KA oil) used in producing various industrial goods.[17] KA oil serves as a precursor to nylon-6 and nylon-6,6 polymers, with a global demand of approximately 10^6 tons per year. The oxidation of cyclohexane requires significant energy to break the C-H bonds, leading to harsh reaction conditions such as high temperatures (413-433 K) and pressures (1-2 MPa).[18] Numerous studies have investigated the use of heterogeneous catalysts for the one-step production of KA oil.[19–24]. However, only a few reports discuss the application of perovskite oxides in the oxidation of cyclohexane.[25,26] This research aims to elucidate the underlying principles governing perovskite-based catalysts' performance by exploring various morphologies and their corresponding catalytic activities. The insights gained from this work will contribute to the rational design of next-generation catalytic materials capable of achieving superior activity, selectivity, and stability in various industrially important processes.

2B.2 Experimental Section

2B.2.1 Materials and methods:

Lanthanum nitrate hexahydrate was purchased from Loba Chemie, Ferric nitrate nonahydrate and Citric acid monohydrate were purchased from Himedia, and Copper nitrate tetrahydrate, Manganese nitrate hexahydrate, Potassium hydroxide and Urea were purchased from Merck. All the chemicals were used without further purification.

2B.2.2 Synthesis

A hydrothermal synthesis method was applied to synthesize the shaped perovskite.[27] Equimolar aqueous solutions of all the metals were prepared in 10 mL water. Four mmol of each metal precursor was dissolved in 10 mL de-ionized water. The solutions were mixed by adding one solution to another dropwise under stirring to get solution A. Then, Solution A was vigorously stirred for 10-15 minutes. Then 2.5-5 g of urea was added to solution A and stirred for 5 minutes until complete mixing of the urea to get solution B. Then potassium hydroxide pallets (9-11 g) were introduced into solution B and stirred for 10 to 20 minutes to cool down the mixture. After cooling, the solution was transferred to the autoclave with a 50 mL capacity and packed using the metallic jacket. After that, the material was heated for 24-48 h at a temperature of 240 °C. Then, the material was cooled to room temperature and washed several times using water. The mixture was centrifuged and separated from the powder sample. The powder sample was dried at 60 °C for several hours in the final step. The powder sample was ground and characterized without any further treatment.

2B.2.3 Characterizations

The electron paramagnetic resonance (EPR) spectroscopy was conducted using an Elexsys E500 spectrometer to analyze the sample's magnetic properties. The measurement involved collecting 2048 data points, ensuring a high-resolution spectrum. To enhance the signal quality, 100 averaged scans were performed, allowing a more accurate representation of the sample's characteristics. The experiment focused on the first harmonic, which is crucial for detecting the resonance signals of paramagnetic species. Modulation was applied at a frequency of 99 kHz with a modulation amplitude of 0.5 G, optimizing the sensitivity and resolution of the spectral data. All measurements were carried out at room temperature, providing a stable environment for the analysis and facilitating the interpretation of the EPR signals. This setup enabled a comprehensive investigation of the electronic and structural properties of the sample under study.

Electron energy loss spectral (EELS) images were acquired using Tecnai with a Gatan imaging filter (GIF) detector (Gatan, Inc., Pleasanton, CA, USA). The TEM images and EELS data were processed using a Digital Micrograph plugin within the Gatan Microscopy Suite (GMS).

2B.2.4 Catalytic Activity Test

A liquid-phase oxidation of cyclohexane was conducted in a two-necked round-bottom flask with a condenser. The flask was charged with 0.5 mL of cyclohexane, 5 mL of acetonitrile as the solvent, 25 mg of catalyst, and 0.5 mL of H_2O_2 as the oxidant. The reaction took place at 60°C for 24 hours with continuous stirring. Upon completion, the catalyst was separated through simple centrifugation, and the products were analyzed using a ThermoScientific gas chromatography (GC) equipped with a DB624 column and flame ionization detector (FID). Product identification was done by comparing them with authentic samples using GC.

The catalytic activities of catalysts were also tested for the hydroxylation of benzene to phenol using H_2O_2 as an oxidizing agent. The reaction conditions are the same as optimized in Chapter 2A.

2B.3 Results and Discussion

2B.3.1 Electron Microscopy

The morphological details of the synthesized material were examined using electron microscopy. The process of morphology evolution was observed through time-dependent hydrothermal synthesis using 8g of KOH. Figure 2B.1 illustrates the progression of the cube-type morphology, which began to emerge after 24 hours of synthesis. Subsequently, at 36 hours, the cube-shaped $LaFeO_3$ oxides were observed alongside impurities of oval-shaped crystals. Finally, the material exhibited a perfect cube-shaped morphology with increased hydrothermal time to 48 hours. The nomenclature of the material $LaFeO_3$ is as follows: cube-shaped $LaFeO_3$ is denoted as LFOC while hexagonal rod and rectangular rod are named LFOHR and LFORR, respectively.

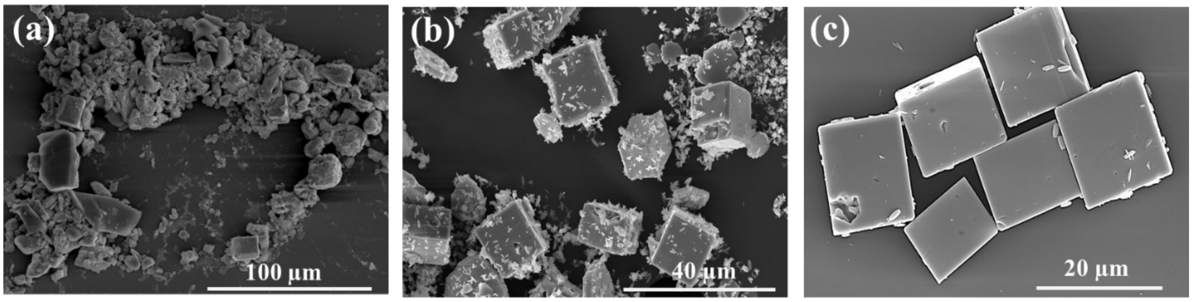

Figure 2B.1 FESEM images of $LaFeO_3$ with the different synthesis times 24 h (a), 36 h (b) and 48 h (c).

After optimizing the synthesis time for the morphology evolution, the amount of alkali source was varied. It was found that varying the KOH amount can result in the evolution of different morphologies of the $LaFeO_3$ (Table 2B.1), as confirmed by the SEM. When the KOH amount was varied from 9g to 11g, the hexagonal cube and the rectangular rod were observed in the case of 11 g of KOH (Table 2B.1 and Figure 2B.2).

Table 2B.1 Sample preparation conditions of various shapes of $LaFeO_3$.

$LaFeO_3$ (Shape)	Catalyst Code	Urea (g)	KOH (g)
Cube	LFOC	3	9
Rod (Hexagonal)	LFOHR	3	10
Rod (Rectangular)	LFORR	3	11

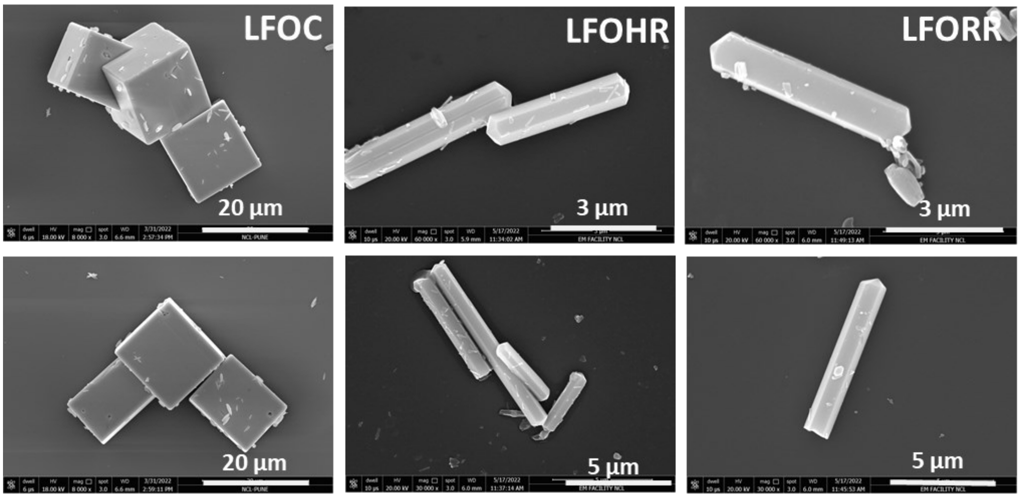

Figure 2B.2 FESEM images of various $LaFeO_3$ synthesized by varying KOH amounts

Table 2B.2 Morphological parameter of various shapes of $LaFeO_3$.

Catalyst Code	**Length (µm)**	**Width/Diameter (µm)**
LFOC	10-12	10-12
LFOHR	5-10	0.8-0.9
LFORR	8-12	0.8-1.3

EDS (Energy-Dispersive X-ray Spectroscopy) elemental mapping was used in conjunction with Scanning Electron Microscopy (SEM) to determine the distribution of elements within a sample. Figure 2B.3 shows the homogeneous distribution of the elements all over the material's surface for cube and rod-shaped $LaFeO_3$.

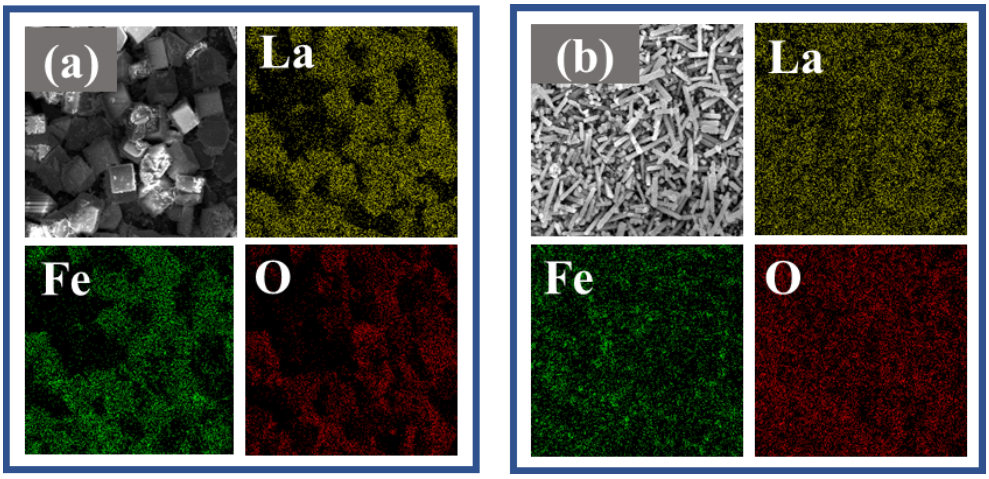

Figure 2B.3 EDS elemental mapping of LFOC cube (a), LFOHR (b).

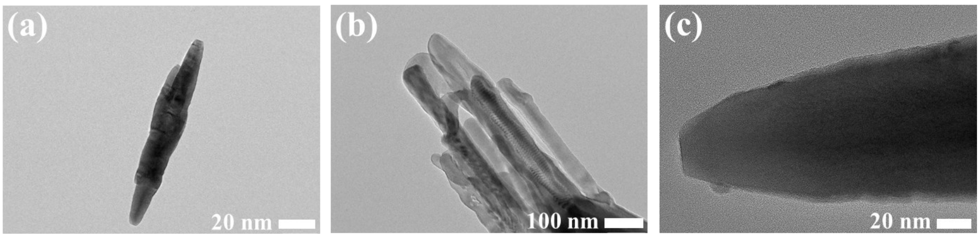

Figure 2B.4 HRTEM images of LFOC (a), LFOHR (b) and LFORR (c).

The synthesized material was examined at the atomic level using Transmission Electron Microscopy. It was observed that the cube is composed of smaller oval-shaped particles, while the rod-shaped particles were seen in the LFOHR and LFORR cases (Figure 2B.4). STEM elemental mapping was employed to gain insights at the atomic level distribution. It was found that all the elements (La, Fe and O) are homogeneously distributed all over the surface of the material (Figure 2B.5)

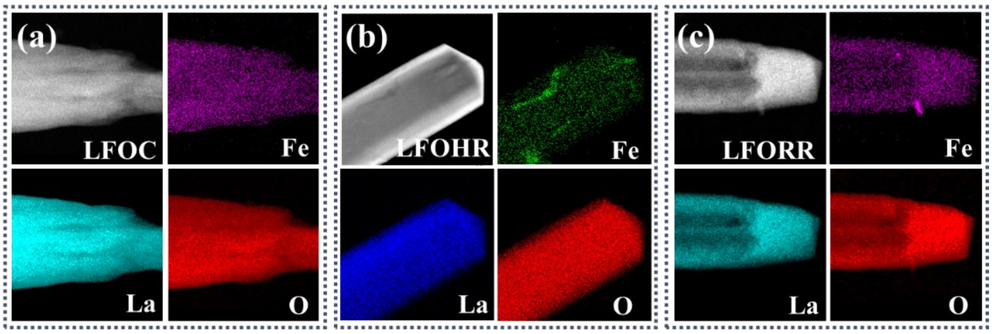

Figure 2B.5 Elemental mapping of LFOC cube (a), LFOHR (b) and LFORR (c).

In order to examine the impact of temperature on the characteristics of the synthesized material, the perovskite oxide was subjected to heating at 700 °C for 4 hours and then analyzed using electron microscopy. Figure 2B.6a illustrates that there was no change in the morphology of the cube following the high-temperature calcination. Similar trend was observed with the rod-shaped $LaFeO_3$. This analysis confirms the material's stability, retaining its shape at high temperatures, indicating its potential utility in high-temperature reactions where the specific exposed surface can exhibit high catalytic activity.

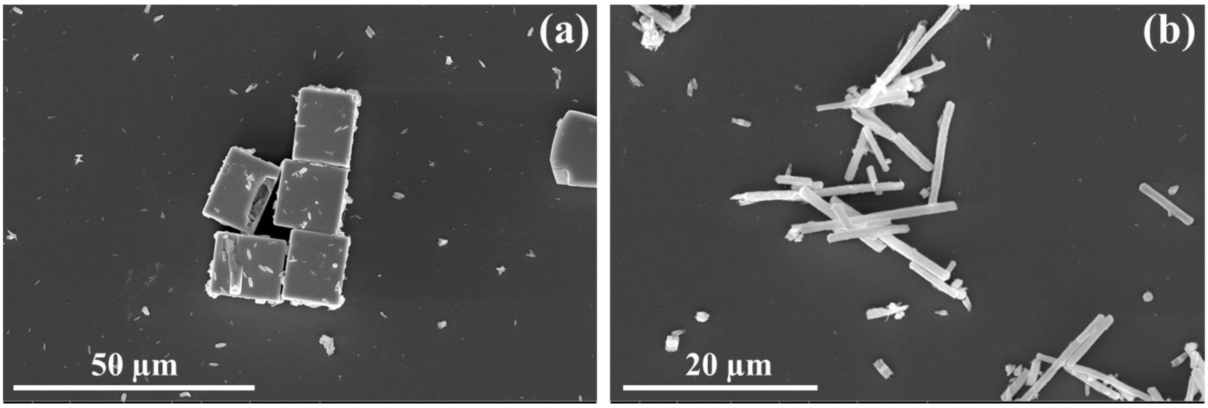

Figure 2B.6 FESEM images of various-shaped $LaFeO_3$ after heat treatment LFOC(a), LFOHR (b).

After successfully synthesizing various shapes of $LaFeO_3$, we aimed to investigate the effects of doping on the morphology of perovskite oxides. Specifically, by substituting 20% of La with Ba through A site doping, we observed changes in the morphology. During the synthesis process of the cube shape, we noted elongation when La was doped with barium in the perovskite lattice (Figure 2B.7 a-b). Similarly, we have also explored the effect of B site doping in the cube shape $LaFeO_3$. Substituting the Fe with 20% Cu results in the cube shape morphology only, but with the curvy edge, which was sharper in the case of $LaFeO_3$ (Figure 2B c-d). These results gave us insights to explore the system deeply.

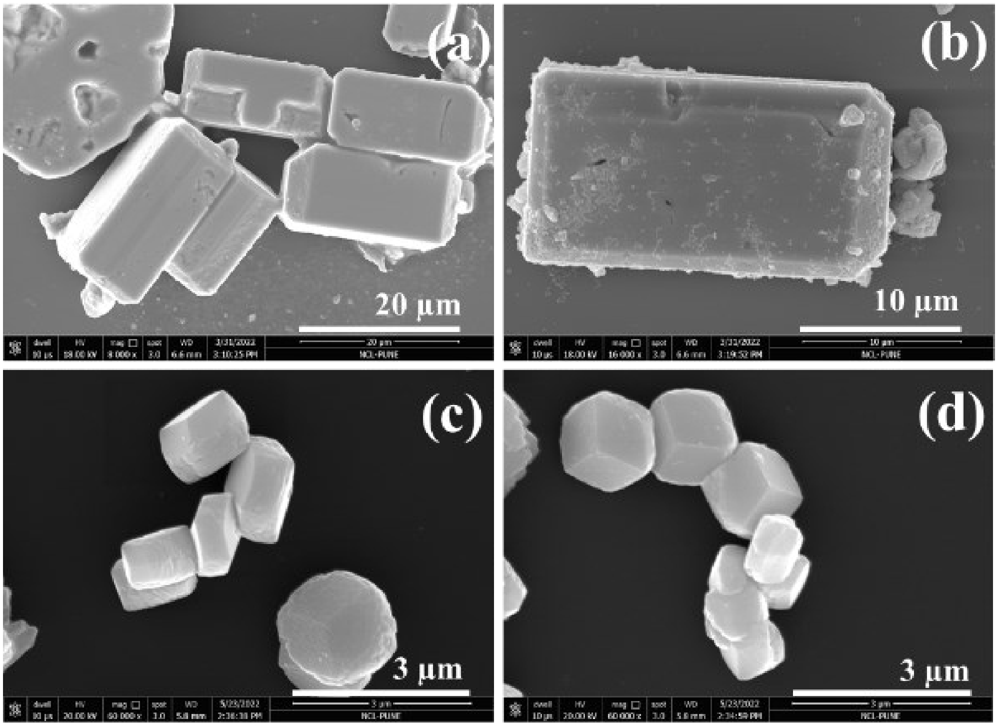

Figure 2B.7 FESEM images of A-site doped, i.e., La with Ba (a-b), and B-site doped, i.e., Fe with Cu (c-d), $LaFeO_3$.

After exploring the La-Fe-based perovskite material, we explored the various La-M (M= Mn, Co, Ni, Cu etc.) based perovskite materials. For this, we synthesized various perovskite oxides with different morphologies using the same synthesis method. As shown in Figure 2B.8, the La_2CuO_4, $LaMnO_3$, $LaCoO_3$ and $LaNiO_3$ adopt rod shape morphology when the synthetic process uses 8g KOH and 3g urea. Although the morphology was the same in the mentioned oxides, the dimensions were different in all cases.

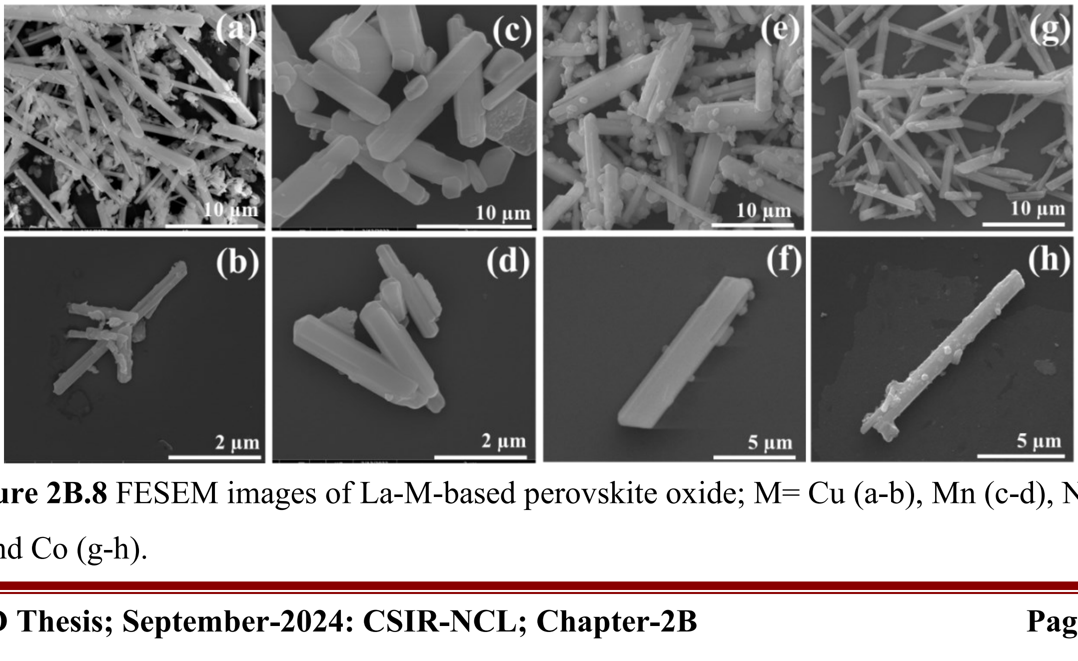

Figure 2B.8 FESEM images of La-M-based perovskite oxide; M= Cu (a-b), Mn (c-d), Ni (e-f) and Co (g-h).

2B.3.2 X-Ray Diffraction

The powder X-ray diffraction (XRD) pattern for different catalysts was obtained in the 2θ range of 10-80 degrees. Upon analyzing the reflection patterns of various shapes of La-Fe-based oxides, it is apparent that they share similarities with the $LaFeO_3$ (JCPDS01-074-2203), confirming the formation of perovskite oxide (Figure 2B.9). Although minor impurities of $La(OH)_3$ were noted in the synthesized material, this could be attributed to the lower synthesis temperature or time.

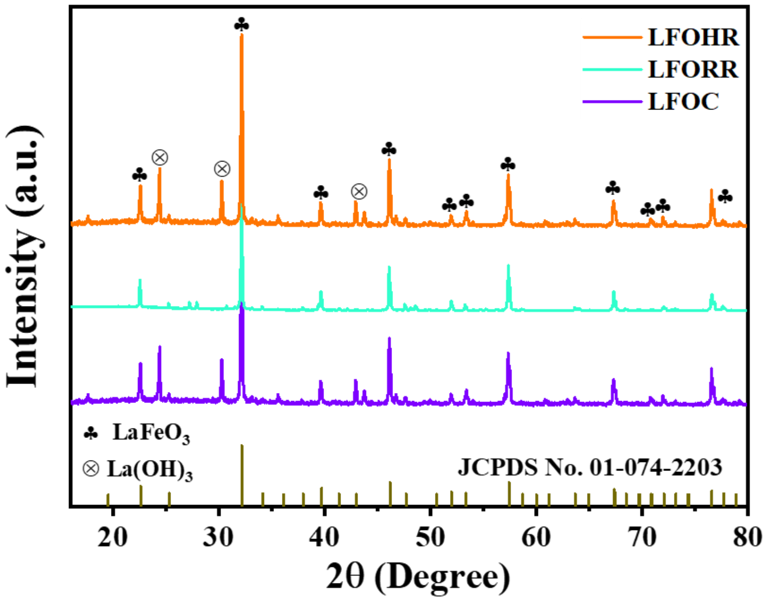

Figure 2B.9 XRD spectrum of various catalysts.

XRD tool was utilized to characterize other hydrothermally synthesized materials. In the case of La-Cu-based synthesized material, the pure perovskite phase of the La_2CuO_4 (JCPDS-01-074-2203) was observed. Two extra peaks (35.53° and 37.72°) of tenorite-CuO were observed along with the stable perovskite phase of La_2CuO_4 (Figure 2B.10). This is because of the equimolar amount of the copper used in the synthesis. This analysis indicated the efficiency of the developed hydrothermal process by which various perovskite oxides can be synthesized.

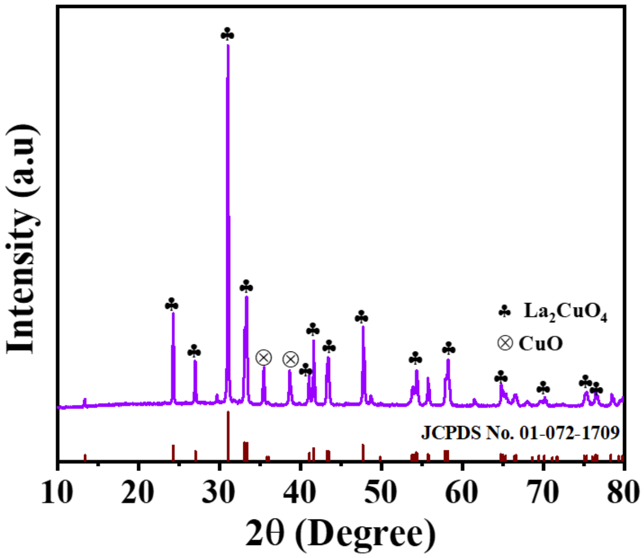

Figure 2B.10 XRD of La-Cu based perovskite.

2B.3.3 X-Ray Photoelectron spectroscopy

In the case of O 1s, XPS reveals the presence of various oxygen species. The peak in the range of 528-530 eV is indicative of lattice oxygen, whereas the peak from 531-533 eV corresponds to adsorbed oxygen species, and the peak at higher binding energy (>534 eV) corresponds to the adsorbed water species.[29] As explained in Chapter 2A, the adsorbed oxygen is linked to the presence of oxygen vacancies., which are well known for their high catalytic activity. The presence of the peaks in the 531-534 eV region gave us insights into the presence of oxygen vacancies, so it was worth investigating.

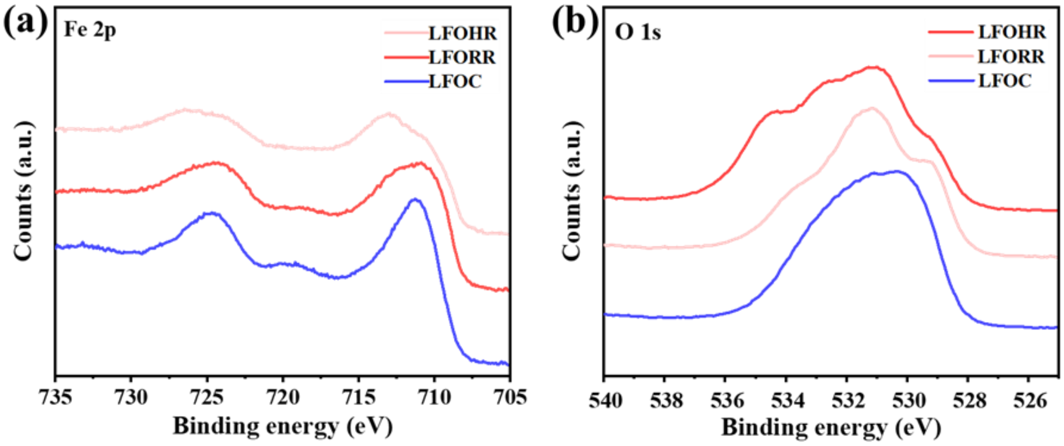

Figure 2B.11 Fe 2p (a), O 1s (b) XPS spectrum of various catalysts.

2B.3.4 Electron Paramagnetic Resonance

EPR studies were carried out to confirm the presence of oxygen vacancies in the synthesized material. Oxygen vacancies often create unpaired electrons in the material. These unpaired electrons are paramagnetic, meaning they can be detected by EPR. The presence of these paramagnetic centers indicates oxygen vacancies. The g-factor around 2.002 is often associated with electrons trapped at oxygen vacancies in oxides. The signal around 3500 G, associated with the polarons, has been observed in our synthesized material (Figure 2B.12). These Polarons are known to result from the formations of oxygen vacancies and are localized around the Fe d orbital.[30]

The sol-gel method-derived $LaFeO_3$ (LFO std.) was synthesized and tested for EPR studies for comparison purposes. In the case of LFO std., no signal associated with polarons was observed, confirming the absence of oxygen vacancies. This analysis indicated the presence of defects (oxygen vacancies) in the hydrothermally synthesized material.

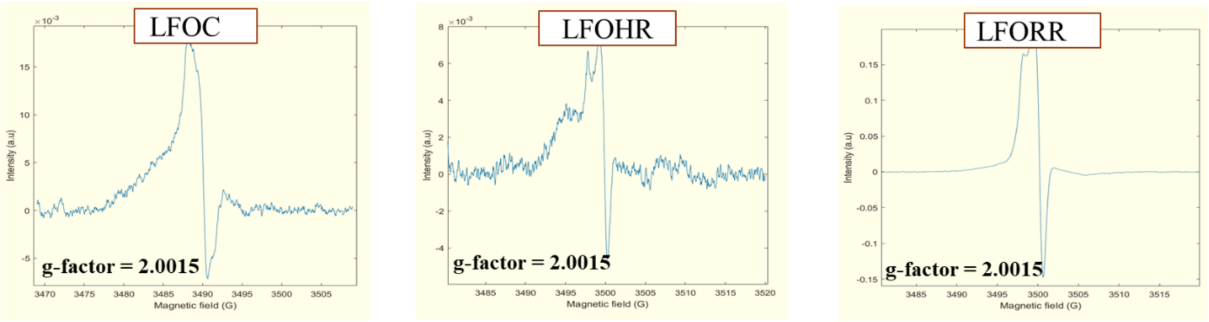

Figure 2B.12 EPR spectrum of various-shaped $LaFeO_3$.

2B3.5 Electron Energy Loss Spectra

The EELS technique was employed to discern the elements existing in the sample at the atomic level. For LFOC (Figure 2B.10a), the appearance of a peak at approximately 710 eV confirms the presence of iron in the sample, corresponding to the Fe $L_{2,3}$ edge. Additionally, a peak at around 840 eV corresponds to La $M_{4,5}$, indicating the presence of lanthanum in the sample. Similar peaks were also observed for LFORR and LFOHR, signifying the presence of both metals at the atomic level in the synthesized material.

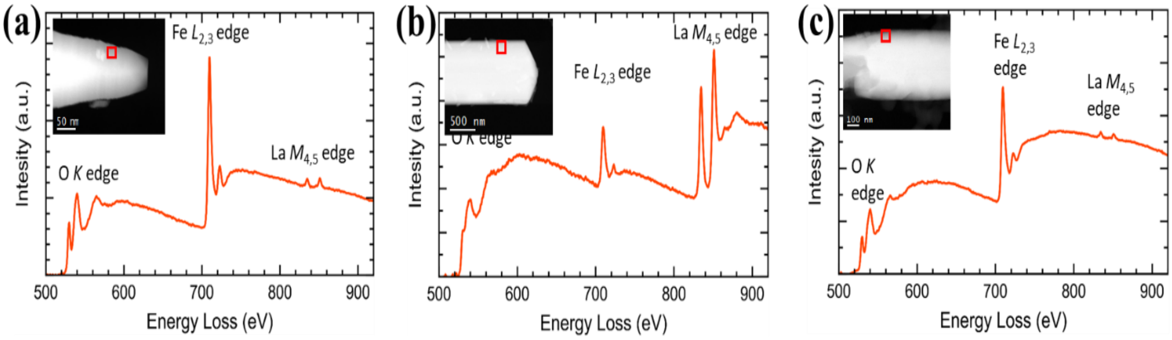

Figure 2B.13 EEL spectrum of various-shaped $LaFeO_3$: LFOC (a), LFOHR (b) and LFORR (c).

2B.3.6 N_2 sorption analysis

Nitrogen adsorption-desorption analysis was utilized to measure the BET surface area of the synthesized material. It has been found that the surface area of the La-Fe-based oxides is not so high <1 m^2/g. However, the doping in the perovskite system increases the area significantly.

The doping at the A site (BLFO) results in incrementing the surface area to a value of 1.2 m^2/g (almost four times compared to LFOC), while the B site doping increased the surface area much higher to a value of 5.5 m^2/g.

Table 2B.3 N_2 sorption analysis of various shapes of $LaFeO_3$.

Sr. No.	**Sample**	**BET Surface area (m^2/g)**
1	LFO	0.3
2	LFOC	0.5
3	LFOHR	0.4
4	LFORR	0.8
5	LCFO	5.5
6	BLFO	1.2

2B.3.7 Catalytic activity

The materials synthesized have been used for various catalytic reactions, including cyclohexane oxidation, benzene hydroxylation, water purification (methylene blue degradation) and C-C bond activation (Cyclohexene oxidation). The last two reactions are beyond the scope of the thesis and will not be discussed further.

During the oxidation of cyclohexane to KA oil, the primary product observed was cyclohexyl hydroperoxide. According to the reports, this can be converted to cyclohexanol using PPh_3. The La-Fe-based perovskite catalyst was found to selectively produce cyclohexanol as the main product after converting cyclohexyl hydroperoxide to cyclohexanol. A comparison between the synthesized perovskite and the standard $LaFeO_3$ (LFO) synthesized using the standard sol-gel method revealed that the activity of the latter was significantly low, allowing only a 5% conversion of cyclohexane oxidation during a 5h reaction. The cube-shaped $LaFeO_3$ catalyst was able to oxidize 13% of the cyclohexane to the desired products, while the rod-shaped $LaFeO_3$ catalyst exhibited much better activity, achieving 23% conversion with almost 95% selectivity towards cyclohexanol (Figure 2B.14). This activity correlates with the EPR studies as the presence of oxygen vacancy in the shaped perovskites result in the high activity for the cyclohexane oxidation.

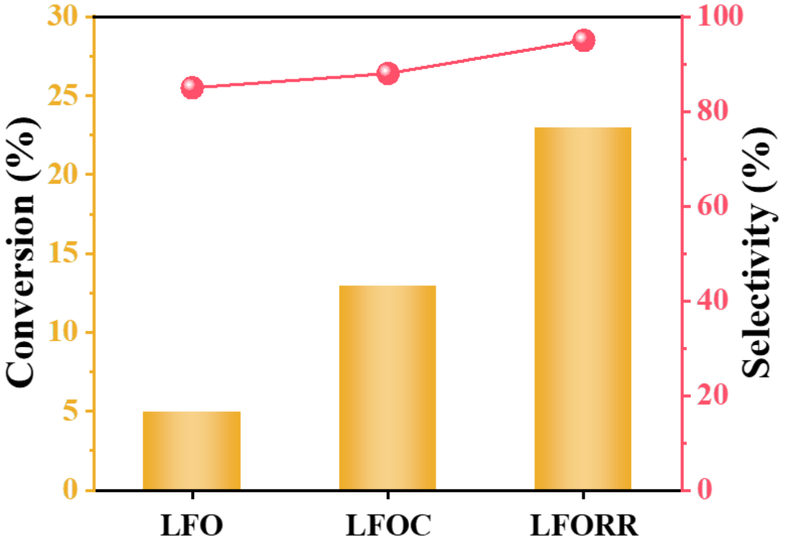

Figure 2B.14 Catalytic activity of various-shaped $LaFeO_3$.

Data are presented as mean ± standard deviation (SD) ‘1.2%’.

Reaction conditions: Cyclohexane 0.5 mL, Acetonitrile 0.5 mL (50% w/v), 5 h, 60 °C.

Table 2B.4 Catalytic activity of various catalysts for cyclohexane oxidation.

Catalyst	**Conversion (%)**	**Selectivity (%)**	
		Cyclohexanol	**Cyclohexanone**
LFO std	5	85	15
LFOC	13	88	12
LFORR	23	95	5
LCO std	10	82	18
LCORod	34	87	13
LMO std	6	92	8
LMORod	25	90	10
LNO std	11	79	21
LNORod	27	89	11

Reaction Conditions: Cyclohexane 0.5 mL, Acetonitrile 0.5 mL (50% w/v), H_2O_2 0.5mL, 5 h, 60 °C. Data are presented as mean ± standard deviation (SD) ‘1%’.

As discussed above, the effectiveness of hydrothermally synthesized shaped $LaFeO_3$ in the cyclohexane oxidation process was examined. Subsequently, other perovskite oxides were evaluated for the same reaction, with their respective perovskites being synthesized using the sol-gel method at higher temperatures. The results demonstrated that all hydrothermally synthesized materials exhibited significantly higher catalytic activity than the standard materials. In studying the optimization of reaction time for cyclohexane oxidation, it was observed that the substrate's conversion is directly related to the reaction time. Specifically, when the LFO rod was utilized for the said reaction, the conversion of cyclohexane increased from 23% to 28% when the reaction time was extended from 5 h to 12 h. Furthermore, a further increase to 24 hours resulted in a cyclohexane conversion of 33%. The selectivity of the cyclohexanol was maintained at more than 90% in all the cases.

Table 2B.5 Catalytic activity of LFORR for cyclohexane oxidation at different time intervals.

Catalyst	**Reaction Time (h)**	**Conversion (%)**	**Selectivity (%)**	
			Cyclohexanol	**Cyclohexanone**
LFORR	5	23	95	5
LFORR	12	28	92	8
LFORR	24	33	91	9

After utilizing the catalyst for cyclohexane oxidation, the benzene hydroxylation was tested utilizing the various shapes of the $LaFeO_3$. A similar type of trend was found in the one-step phenol production as the rod shape gave the best activity while the LFO standard and LFO cube showed lower conversion.

Table 2B.6 Catalytic activity of various catalysts for Benzene Oxidation.

Catalyst	**Benzene Conversion (%)**	**Phenol Selectivity (%)**
LFO std	5	99
LFOC	14	99
LFORR	31	99

Reaction Conditions: Benzene 0.5 mL, Acetonitrile 0.5 mL (50% w/v), H_2O_2 0.5mL, 5 h, 60 °C. Data are presented as mean ± standard deviation (SD) '1%'.

2B.4 Conclusions

In this study, we have successfully developed and utilized a hydrothermal method for synthesizing shaped perovskite oxides. This approach has been highly effective in creating perovskite materials with diverse morphologies, thereby broadening the potential applications of these materials. Advanced characterization techniques revealed structural defects in the synthesized perovskites compared to those produced using the traditional sol-gel method.

These defects significantly enhance the catalytic activity of the perovskites, making them especially effective for important industrial reactions such as cyclohexane oxidation and benzene oxidation. The noticeable improvement in catalytic performance in these reactions underscores the potential of hydrothermally synthesized perovskites in catalysis and emphasizes the importance of defect engineering in optimizing the properties of functional materials.

In summary, our exploration into the synthesis of shaped perovskites has yielded promising results, particularly in the realm of shaped metal nanoparticles. While the existing literature predominantly focuses on shaped metal nanoparticles and metal oxides, a notable gap exists regarding the synthesis and characterization of mixed metal oxides. Our successful synthesis of these shaped metal nanoparticles not only contributes to the growing body of knowledge in this field but also opens up new avenues for research and application.

This will not only bridge the existing knowledge gap but also pave the way for innovative solutions in catalysis and other fields. Our findings lay the groundwork for future studies, encouraging continued exploration and development in the synthesis of advanced materials.

2B.5 References

[1] A.-X. Yin, X.-Q. Min, Y.-W. Zhang, C.-H. Yan, *J Am Chem Soc* **2011**, *133*, 3816–3819.

[2] Y. Tang, X. Chi, S. Zou, X. Zeng, *Nanoscale* **2016**, *8*, 5771–5779.

[3] V. R. Stamenkovic, B. Fowler, B. S. Mun, G. Wang, P. N. Ross, C. A. Lucas, N. M. Marković, *Science (1979)* **2007**, *315*, 493–497.

[4] S. Sreedhala, V. Sudheeshkumar, C. P. Vinod, *Nanoscale* **2014**, *6*, 7496.

[5] G. A. Somorjai, D. W. Blakely, *Nature* **1975**, *258*, 580–583.

[6] Y. Xiong, B. J. Wiley, Y. Xia, *Angewandte Chemie International Edition* **2007**, *46*, 7157–7159.

[7] C. Li, M. Luo, Z. Xia, S. Guo, *Nano Materials Science* **2020**, *2*, 309–315.

[8] N. Tian, Z.-Y. Zhou, S.-G. Sun, Y. Ding, Z. L. Wang, *Science (1979)* **2007**, *316*, 732–735.

[9] P. K. Gallagher, D. W. Johnson, E. M. Vogel, F. Schrey, *Mater Res Bull* **1975**, *10*, 623–627.

[10] C. Xu, J. Xie, D. Ho, C. Wang, N. Kohler, E. G. Walsh, J. R. Morgan, Y. E. Chin, S. Sun, *Angewandte Chemie International Edition* **2008**, *47*, 173–176.

[11] S. E. Habas, H. Lee, V. Radmilovic, G. A. Somorjai, P. Yang, *Nat Mater* **2007**, *6*, 692–697.

[12] A.-X. Yin, X.-Q. Min, Y.-W. Zhang, C.-H. Yan, *J Am Chem Soc* **2011**, *133*, 3816–3819.

[13] K. Huang, L. Yuan, Y. Jiang, J. Zhang, Z. Geng, L. Luo, S. Feng, *Inorg Chem Front* **2018**, *5*, 732–738.

[14] H. Liu, C. Hu, Z. L. Wang, *Nano Lett* **2006**, *6*, 1535–1540.

[15] P. Chai, X. Liu, Z. Wang, M. Lu, X. Cao, J. Meng, *Cryst Growth Des* **2007**, *7*, 2568–2575.

[16] R. Hailili, Z.-Q. Wang, X.-Q. Gong, C. Wang, *Appl Catal B* **2019**, *254*, 86–97.

[17] *Ullmann's Encyclopedia of Industrial Chemistry*, Wiley, **2000**.

[18] R. Liu, H. Huang, H. Li, Y. Liu, J. Zhong, Y. Li, S. Zhang, Z. Kang, *ACS Catal* **2014**, *4*, 328–336.

[19] A. Ribeiro, L. Martins, S. Carabineiro, J. Figueiredo, A. Pombeiro, *Molecules* **2017**, *22*, 603.

[20] S. A. C. Carabineiro, L. M. D. R. S. Martins, M. Avalos-Borja, J. G. Buijnsters, A. J. L. Pombeiro, J. L. Figueiredo, *Appl Catal A Gen* **2013**, *467*, 279–290.

[21] S. A. C. Carabineiro, L. M. D. R. S. Martins, A. J. L. Pombeiro, J. L. Figueiredo, *ChemCatChem* **2018**, *10*, 1804–1813.

[22] A. SAKTHIVEL, P. SELVAM, *J Catal* **2002**, *211*, 134–143.

[23] E. Yuan, M. Gu, P. Jian, *Korean Journal of Chemical Engineering* **2020**, *37*, 1137–1148.

[24] S. Fu, K. You, Z. Chen, T. Liu, Q. Wang, F. Zhao, Q. Ai, P. Liu, H. Luo, *Front Chem Sci Eng* **2022**, *16*, 1211–1223.

[25] X. Li, S. Hao, Z. Chen, T. Huang, S. Fu, F. Zhao, K. You, H. Luo, *Ind Eng Chem Res* **2024**, *63*, 6087–6099.

[26] E. Muhumuza, P. Wu, T. Nan, L. Zhao, P. Bai, S. Mintova, Z. Yan, *Ind Eng Chem Res* **2020**, *59*, 21322–21332.

[27] F. Tong, Y. Zhao, M. Wang, *Micro Nano Lett* **2019**, *14*, 259–262.

[28] J.-C. Dupin, D. Gonbeau, P. Vinatier, A. Levasseur, *Physical Chemistry Chemical Physics* **2000**, *2*, 1319–1324.

[29] P. Kumar, A. Vijay Jagtap, S. Gupta, C. P. Vinod, *Chem Asian J* **2022**, DOI 10.1002/asia.202200788.

[30] T. Das, J. D. Nicholas, Y. Qi, *J Mater Chem A Mater* **2017**, *5*, 25031–25043.

Chapter 3

Continuous Flow Methane Oxidation to Methanol using H_2 and O_2

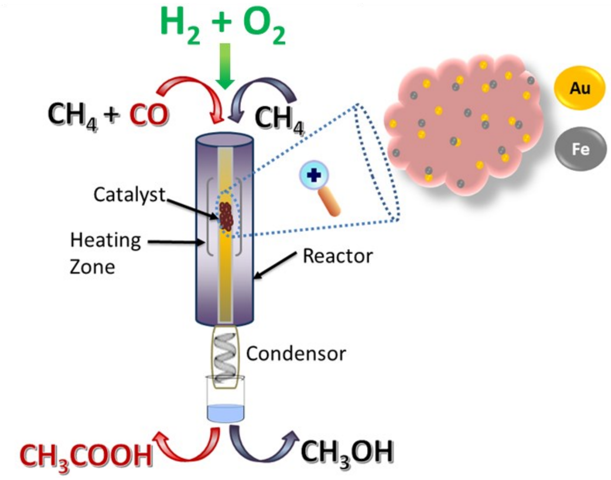

A part of this chapter is adapted from

Anuradha V Jagtap[$], **Pawan Kumar**[$], Sharad Gupta, N. Abharana, S.N. Jha, D. Bhattacharyya, T. G. Ajithkumar and C. P. Vinod, Atmospheric-Pressure Continuous-Flow Methane Oxidation to Methanol and Acetic Acid Using H_2O_2 over the Au–Fe Catalyst *ACS Sustainable Chem. Eng.* **2024**, 12, 8958-8967

[$] Equal contribution

Pawan Kumar, Anuradha V Jagtap, Nikhil S., S. Tanmay Ghosh, S. Krishnamurty and C. P. Vinod, Continuous Flow Methane Oxidation using *in-situ* H_2O_2 Generation at Ambient Pressure (Manuscript under preparation)

3.1 Introduction

To harness the plentiful methane as a fossil fuel, the challenges associated with storing and transportation is essential, necessitating the development of high-pressure infrastructure.[1,2] A potentially practical approach involves the transformation of methane into liquid substances like methanol.[3–5] Nonetheless, accomplishing the direct activation of methane in a single step poses challenges due to the need to break and activate the robust carbon-hydrogen (C-H) bonds for producing other value added products.[6–8] Methanol is a crucial foundational compound for producing olefins, aromatics, and other essential components to create fine chemicals.[9–12] As discussed in Chapter 1, the conventional approach for industrial synthesis involves an energy-consuming process where methane is reformed into syngas, which is then converted into methanol under high pressure.[13] A more attractive option would be the direct partial oxidation of methane to produce methanol. However, the strong carbon-hydrogen bond in methane poses a significant challenge for this method. Methane requires a substantial amount of energy to break this bond. Also, methane has a low electron affinity and minimal polarizability, further complicating the process.[14–16] Additionally, methanol is more prone to oxidation than the reactant molecule methane, often leading to methanol oxidation during the reaction. Attempts to overcome this challenge have explored the use of costly or hazardous oxidants, but these have not proven suitable for widespread commercial use.[7,17,18] Using inexpensive oxygen (O_2) as an oxidant remains an option, but it still suffers from suboptimal selectivity, primarily due to the favorable formation of carbon dioxide (CO_2).[19–21] Using H_2O_2 as an oxidant is environment-friendly and highly efficient because of the elevated oxygen content and green by-products. The new and cheaper technologies for producing H_2O_2 make any catalytically oxidative pathway this molecule might offer a boon or future. The existing method for producing hydrogen peroxide involves a series of hydrogenation and oxidation steps using alkyl anthraquinone, which is only cost-effective when done on a large scale.[22] However, most hydrogen peroxide applications require smaller quantities, leading to a notable discrepancy between production levels and actual usage needs. The problem with H_2O_2 is its stability, as it can readily convert into water and oxygen. To avoid the problem associated with the stability of H_2O_2, a promising strategy can be the utilization of *in-situ* generated H_2O_2 from H_2 and O_2 in the same vessel or reactor of the oxidation reaction. Generating hydrogen peroxide (H_2O_2) directly at the reaction site has been a long-standing objective in converting various chemical feedstocks into valuable products. Researchers have explored a wide range of selective oxidation reactions, such as the epoxidation of propene and styrene, the oxidation of alcohols, and the partial oxidation of methane, to achieve efficient and cost-effective processes.[23–27]. In this report, we developed a bimetallic catalyst over hydrophobic support to activate methane efficiently. We have synthesized an Au-Fe catalyst supported over hydrophobic silica to partially oxidize methane to methanol using *in-situ* generated hydrogen peroxide as an oxidant both in batch and continuous process. We also show that co-feeding CO with methane produces acetic acid in excellent yield. Zhu Jin et al. recently reported methane oxidation to methanol using *in-situ* generated H_2O_2 over Au-Pd catalyst in a batch reactor at 30 bar pressure.[28] The overall conversion achieved through the atmospheric pressure continuous process in the present work is the best reported, surpassing the high-pressure batch process for methanol and acetic acid.

3.2 Experimental Section

3.2.1 Materials

All chemicals were used without further purification. Metal precursors, Iron(III) nitrate nonahydrate, and hydrogen tetrachloroaurate(III) trihydrate were purchased from Alfa Aesar. Ammonium chloride and sodium hydroxide flakes were purchased from Merck. Silica source tetraethylorthosilicate (TEOS) and poly(methylhydrosiloxane) were purchased from Sigma Aldrich, and hydrogen peroxide (30% w/v) was purchased from Thomas Baker. Methane (99.999% pure), Carbon monoxide (99.999% pure), diluted hydrogen (5% H_2 + 95% N_2), and diluted oxygen (25% H_2 + 75% N_2) were purchased from Vadilal Chemical Limited.

3.2.2 Catalyst Synthesis

3.2.2.1 Synthesis of Hydrophobic Silica (HS)

Hydrophobic Silica (HS) was synthesized using the sol-gel technique. In a specific synthesis process, 4 g of P123 was completely dissolved in 300 mL of a 1.6 M HCl solution at 40 °C. An equal volume of TEOS and PMHS (4.3 mL of each) as sources of silica were simultaneously added to the solution above after stirring for 4 hours and then left to age for 24 h. This mixture was subsequently placed in a stainless-steel autoclave and subjected to hydrothermal treatment at 100 °C for 48 h under static conditions. Once it had cooled to ambient temperature, the white solid was separated by filtration, rinsed with deionized water, and dried at 80 °C for several hours. The template was then eliminated through calcination at 350 °C for 10 hours. TEOS was exclusively utilized as the silica source to synthesize unmodified silica (SBA-15), with all other procedures remaining the same.

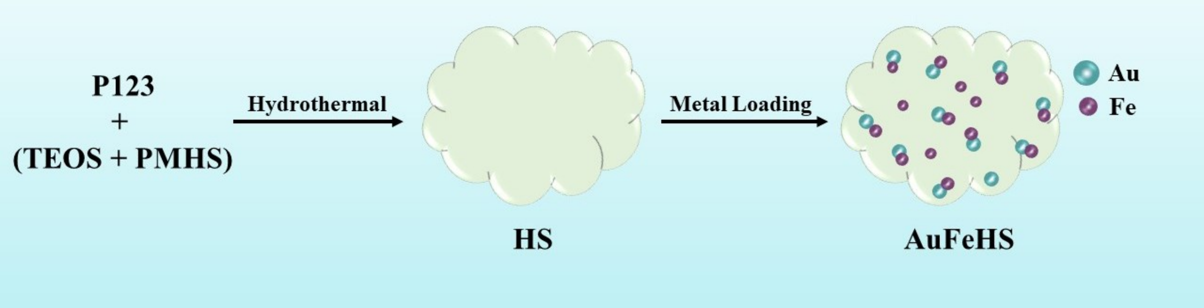

Figure 3.1 Schematic presentation of AFHS catalyst synthesis.

3.2.2.2 Synthesis of FeHS Catalyst

Iron (Fe) was deposited over hydrophobic silica using the well-known deposition precipitation method. In a typical procedure, 0.5 g of HS was typically dispersed in 50 mL millipore water, followed by sonication for 5-10 min. Subsequently, the pH of the solution was maintained between 9-10 using 0.1 M NaOH solution with continuous stirring. Afterward, the metal precursor's aqueous solution was gradually added to the mixture over 20-30 minutes, keeping the pH constant, and the mixture was kept undisturbed for 1 h. The resultant solid was separated by centrifugation, dried in a hot oven at 80 °C for several hours, and then calcined in static air at 350 °C for 4 h. The final powder catalyst, FeHS, was directly utilized in catalytic reactions without further processing.

3.2.2.3 Synthesis of AuHS and AuFeHS Catalyst

The deposition of Au over the FeHS catalyst was performed using the deposition precipitation method. Typically, 0.5 g of FeHS catalyst was dispersed in 50 mL millipore water, and a fixed amount of ammonium chloride (NH_4Cl) was added to the liquid solution as a modifier. In the next step, the aqueous solution of Au precursor was added to the resulting solution dropwise by maintaining the pH at 9.5 using 0.1M aq NaOH solution. The obtained precipitate was then centrifuged, washed with deionized water, and dried at 80 °C. The powder obtained was yellowish. The dried powder was calcined in static air at 350 °C for 4h, and the resulting powder (brown color) catalyst (AuFeHS) was used for the catalytic reactions without any post-treatment. For AuHS, Au was deposited over HS, and all other steps were kept constant.

3.2.3 Catalyst Characterization

Wide angle XRD analysis was recorded on Rigaku D MAX CuKα radiation with λ= 1.54 Ao from 10^o to 90^o at the scan rate of 2 ^{o}/min. The low-temperature liquid nitrogen adsorption and desorption method with a Quantachrome instrument measured the specific surface area of the catalyst. A quartz tube with 50 mg of the sample was dried and degassed for 3 h at 300 °C and under a 1 MPa vacuum. After the pretreatment, the adsorption and desorption experiments were carried out with N_2 as the adsorbed gas and He as the balance gas.

To prepare the specimen for TEM/STEM, the samples were dispersed in IPA by ultrasonication, and a drop of this dispersion was placed on a holey carbon grid and dried. Transmission electron microscopy analysis was done with a Tecnai (Model F30) operating at 300 kV acceleration voltage. AC-TEM/STEM analysis at 80 kV was performed on a Titan Cubed Themis 300 double corrected (probe and image) microscope equipped with a high brightness electron gun and monochromator; for high-resolution imaging, the JEOL F-200 HRTEM instrument was used.

Electron Energy Loss Spectral (EELS) images were acquired using Tecnai with a Gatan imaging filter (GIF) detector (Gatan, Inc., Pleasanton, CA, USA). The TEM images and EELS data were processed using a Digital Micrograph plugin within the Gatan Microscopy Suite (GMS).

X-ray photoelectron spectroscopy (XPS) measurements were conducted using a Thermo Scientific Kalpha+ spectrometer, employing micro-focused and monochromated Al Kα radiation at 1486.6 eV operating at a pass energy of 50 eV. Peak fitting for individual core levels was performed using Avantage software with a smart-type background.

IR Absorption analysis was done using a Bruker Vertex IR instrument equipped with an MCT detector.

Confirmation and quantification of the hydrophobicity were obtained from contact angle measurements.

Inductively Coupled Plasma-Optical Emission Spectrometry was used to measure the final wt % of the metal in the catalyst. SPECTROARCOS FHS12 was used for the analysis. In sample preparation, HF and freshly prepared aqua-regia were used to digest the sample. Catalyst amount was taken as required to make a 20-ppm concentrated (for each metal) solution of 25 mL for the analysis.

^{23}Na and ^{29}Si solid-state NMR experiments were performed on the JEOL-400 spectrometer, operating at a magnetic field strength of 9.4 T. Liquid product NMR was performed on the Bruker AV-500 instrument with a strength of 500 MHz.

XAS measurements have been carried out at the EnergyScanning EXAFS beamline (BL-9) at the Indus-2 Synchrotron Source (2.5 GeV, 100 mA) at Raja Ramanna Centre for Advanced Technology (RRCAT), Indore, India.

Experimental details of XAS analysis: An X-ray Absorption Spectroscopy (XAS) measurement, which comprises both X-ray Near Edge Structure (XANES) and Extended X-ray Absorption Fine Structure (EXAFS) techniques, has been carried out in Au-Fe catalysis samples. EXAFS measurements on the Au-Fe catalyst samples have been carried out at the Energy Scanning EXAFS beamline (BL-9) at Indus-2 Synchrotron source (2.5 GeV, 300 mA) at the Raja Ramanna Centre for Advanced Technology (RRCAT), Indore, India.[29,30] The beamline operates in the 4-25 KeV photon energy range. The beamline optics consists of a Rh/Pt coated collimating meridional cylindrical mirror used to collimate the beam. This mirror is also used before the DCM for the higher harmonic rejection. The collimated beam is monochromatized by a Si (111) (2d = 6.2709) based double crystal monochromator (DCM). The second crystal of the DCM is a sagittal cylindrical crystal, which is used for horizontal focusing of the beam, while another Rh/Pt coated bendable post mirror facing down is used for vertical focusing of the beam at the sample position. The rejection of the higher harmonics content in the incident X-ray beam was also performed by detuning the second crystal of the DCM using the piezo motor to an extent such that the flux of the beam at the outlet of the DCM is reduced to less than 30% of the flux at its inlet.

In the case of the present samples, the Fe K edge data of the samples have been recorded in fluorescence mode Au L_3 data, while the Fe standards and Fe K edge data of samples have been measured in transmission mode. For the transmission mode measurement, three ionization chambers (300 mm length each) have been used: one ionization chamber for measuring incident flux (I_0), the second one for measuring transmitted flux (I_t) and the third ionization chamber for measuring XAS spectrum of a reference metal foil for energy calibration. Appropriate gas pressure and gas mixtures have been chosen to achieve 10-20% absorption in the first ionization chamber and 70-90% absorption in the second ionization chamber to improve the signal-to-noise ratio. The absorption coefficient μ is obtained using the relation:

$$I_T = I_0 e^{-\mu x}$$

where x is the thickness of the absorber.

For the fluorescence mode, the sample is placed at 45° to the incident X-ray beam, and a fluorescence detector is placed at a right angle to the incident X-ray beam to collect the signal. One ionization chamber detector is placed before the sample to measure the incident flux (I0), and the fluorescence detector measures the fluorescence intensity (I_f). In this case, the X-ray absorption coefficient of the sample is determined by$\mu = I_f / I_0$. The spectrum was obtained as a function of energy by scanning the monochromator over the specified range.

To take care of the oscillations in the absorption spectra, $\mu(E)$ has been converted to an absorption function $\chi(E)$ defined as follows:

$$\chi(E) = \frac{\mu(E) - \mu_0(E)}{\Delta\mu_0(E_0)}$$

where E_0 is absorption edge energy, $\mu_0(E_0)$ is the bare atom background and $\Delta\mu_0(E_0)$ is the step in $\mu(E)$ value at the absorption edge. The energy-dependent absorption coefficient $\chi(E)$ has been converted to the wavenumber-dependent absorption coefficient $\chi(k)$ using the relation,

$$K = \sqrt{\frac{2m(E - E_0)}{\hbar^2}}$$

where m is the electron mass. $\chi(k)$ is weighted by k^2 to amplify the oscillation at high k and the $\chi(k)k^2$ functions are Fourier transformed in R space to generate the $\chi(R)$ versus R plots in terms of the real distances from the center of the absorbing atom. A set of EXAFS data analysis programs available within the Demeter software package have been used for EXAFS data analysis [31]. This includes background reduction, and Fourier transform to derive the$\chi(R)$ versus R spectra from the absorption spectra (using ATHENA software), and fitting of experimental data with the theoretical spectra using ARTEMIS software assuming a coordination shell. In the present case, we have restricted the fitting over the 1st major peak in the$\chi(R)$ versus R plot. During the fitting, bond distances, coordination numbers (including scattering amplitudes), and disorder (Debye-Waller) factors (σ^2), which give the mean square fluctuations in the distances, have been used as fitting parameters. The goodness of fit has been determined by the value of the R_{factor} defined by:

$$R_{factor} = \sum \frac{[Im(\chi_{dat}(r_i) - \chi_{th}(r_i)]^2 + [Re(\chi_{dat}(r_i) - \chi_{th}(r_i)]^2}{[Im(\chi_{dat}(r_i)]^2 + [Re(\chi_{dat}(r_i)]^2}$$

where, χ_{dat} and χ_{th} refer to the experimental and theoretical $\chi(r)$ values and Im and Re refer to the imaginary and real parts of the respective quantities.

$\chi(R)$ versus R plots generated at Fe K-edge using Fourier transform range of k =2.0-12 Å^{-1} from the $\mu(E)$ versus E spectra following the methodology described above at Fe K-edge. It should be mentioned here that the peak positions in the R space differs from the actual bond length values by a phase factor, which generally amounts to an increase of 0.3–0.5 Å from the peak position values, depending on the type of the nearest neighbor scatterer.

3.2.4 Catalytic Activity Test

Process for H_2O_2 production: The direct reaction of diluted H_2 and diluted O_2 gases (written as d-H_2 and d-N_2) was studied in a 50 mL stainless-steel Amar (Parr) reactor. A fixed amount of catalyst was dispersed in 10-20 mL of Millipore water. The autoclave was sealed and purged three times with d-O_2 gas at a pressure of 5 bar. It was then pressurized to a desired pressure of 10-30 bar of feed gas in various ratios of d-O_2:d-H_2. The solution was heated to the desired reaction temperature. Once the temperature reached the set value, the solution was vigorously stirred at approximately 950 rpm. The reaction was carried out for a fixed amount of time under constant circulation of ice-cold water to prevent the decomposition of the volatile product. After the reaction, the liquid samples were filtered using a syringe filter and analyzed using the ECO titrator instrument and Nuclear Magnetic Resonance Spectroscopy.

Process for methane oxidation using H_2O_2 in a batch reactor: In this process, 99.99% pure methane cylinder (CH_4), 99.99% carbon mono-oxide (CO), 30% (w/v) H_2O_2 and millipore water was used as reactant feed. The partial methane oxidation was performed in an Amar reactor of a stainless-steel autoclave with 100 mL capacity. A fixed amount of catalyst was dispersed in 20 mL of Millipore water, and then 50 µL 30% w/v diluted H_2O_2 was added. Then, the autoclave was sealed and purged thrice with methane (CH_4) gas at 5 bar pressure. It was then pressurized to the desired pressure (typically 15 bar) with CH_4 gas and then the 5 bar of CO was pressurized to a total reaction pressure of 20 bar. Then, the solution was heated to the desired reaction temperature (typically 50 °C). Once the temperature reached the set value, the solution was vigorously stirred at ca. 950 rpm for 30 min. After the completion of the reaction, the autoclave was subjected to cooling down below 10 °C in ice-cold water to minimize the loss of volatile products. The gas sample was collected in a gas bag after cooling the products. Liquid samples were collected after centrifugation and analyzed using gas chromatography and NMR techniques.

Process for methane oxidation using *in-situ* generated H_2O_2 in a batch reactor: Here, 99.9995 pure methane cylinder (CH_4), O_2 cylinder in which 25% O_2 or N_2 (denoted as d-O_2) and H_2 Cylinder 5% H_2 diluted with CO_2 or N_2 denoted as (d-H_2) and millipore water was used as reactant feed. For the Acetic acid production, CO was added to the reactant feed.

Direct oxidation of CH_4 with H_2 and O_2 gasses of all catalysts was evaluated in a 50 mL stainless-steel fixed bed reactor (a cylindrical reactor filled with catalyst pellets on the quartz wool). 50 mg of catalyst was dispersed in 20 mL of millipore water. Then, the autoclave was sealed and purged thrice with d-O_2 gas at 5 bar pressure. It was then pressurized to the desired pressure of 20 bar of feed gas in a ratio of 5:5:10::d-O_2:d-H_2:CH_4. Then, the solution was heated to the desired reaction temperature. Once the temperature reached the set value, the solution was vigorously stirred at ca. 950 rpm. The reaction was carried out for a fixed amount of time under the constant circulation of ice-cold water. After completion of the reaction, the gas sample was collected in a gas bag after cooling the products, and liquid samples were collected after the centrifugation. Products were analyzed using gas chromatography and the NMR technique. Acetic acid was produced using pure CO gas in feed with CH_4, d-H_2, and d-O_2.

Process for methane oxidation using H_2O_2 in a Continuous flow reactor: Catalytic performance was measured in a continuous flow cotton-plugged quartz reactor having a total length of 50 cm and an internal diameter of 8 mm. By providing the feed stream comprising methane (99.99% pure) and 30% (w/v) diluted H_2O_2 putting in contact with the catalyst in the temperature range of 30- 80 °C and under a pressure of 1 atm. CO was added to the reactant feed for acetic acid production, making other things the same. To avoid the loss of volatile products, methanol recovery from the effluents is done by an ice-cold condensation process below 10 °C. In the feed stream, an aqueous solution of hydrogen peroxide, typically 15% w/v, was controlled by a syringe pump, and both methane and CO flow were controlled by a mass flow controller (Alicat). Both were fed down through the layers of the pelletized catalyst bed. Liquid and gaseous products were separated in a coiled gas condenser and collected periodically for analysis for a 7 h period. The reaction was carried out for a fixed amount of time under the constant circulation of ice-cold water. After the reaction, the gas sample was collected after the products had cooled, and liquid samples were collected following centrifugation. Products were analyzed using gas chromatography and the NMR technique.

Process for methane oxidation using *in-situ* generated H_2O_2 in a Continuous flow reactor: The process is the same as methane oxidation in a continuous flow reactor using H_2O_2. However, in this process, peroxide was generated *in-situ* and utilized simultaneously by diluting hydrogen and oxygen gases with methane. The flow of gases was maintained using a mass flow controller, water was used to liquefy the products, and the flow was controlled by a syringe pump. The flow of d-H_2 and d-O_2 was maintained at 30 mL/min, while the methane flow was 20 mL/min. In the case of acetic acid production, the CO flow was maintained at 5 mL/min.

Product quantification

Qualitative product analysis was done using gas chromatography and NMR techniques. ^{1}H & ^{13}C NMR were recorded in H_2O+D_2O (90:10) solvent using Bruker Avance DRX 500 spectrometer. 630 µL of the reaction mixture was added to the 70 µL of D_2O and transferred to the NMR tube for the analysis. The GC technique was utilized for the quantitative analysis using the response factor method. A defined amount of products was calibrated using this method and calibration curves were plotted. The yield calculation of the product was done using the area under the curve.

The yields of products and selectivity of liquid oxygenates were calculated using the following equations:

$$Yields\ of\ products\ (\mu mol g_{metal}{}^{-1}) = \frac{Products\ yield\ (\mu mol)}{Amount\ of\ the\ metal\ (g)}$$

$$^{*}Selectivity\ of\ MeOH = \frac{Amount\ of\ MeOH}{Total\ amount\ of\ oxygenates} \times 100$$

$$^{*}Selectivity\ of\ CH_3COOH = \frac{Amount\ of\ CH_3COOH}{Total\ amount\ of\ oxygenates} \times 100$$

*The oxygenates have gaseous products (CO, CO_2) and liquid oxygenates, which are included in the selectivity calculations.

Qualitative and quantitative analysis of H_2O_2 production was confirmed using titration. The reaction mixture was titrated against $KMnO_4$ in the Eco titrator instrument.

3.3 Result and Discussion

The significance of a hydrophobic backing in oxidation reactions utilizing H_2O_2 lies in its ability to promote the proximity of peroxide molecules to the active sites of Au and Fe. This proximity enhances the efficiency of the reaction between incoming methane and peroxide. Notably, the active sites become obstructed under hydrophilic conditions, where moisture is present. Additionally, in aqueous conditions, the size of Au particles is known to increase, further diminishing the catalyst's activity. The synthesis of hydrophobic support involved modifying silica by adding a methyl chain through a sol-gel method, which enhances the desorption of methanol from its surface and minimizes excessive oxidation. Following this modification, iron (Fe) and gold (Au) were deposited onto the silica support using a specialized deposition precipitation method. Our group has explored deep insights into the deposition of small Au NPs using this method. Here, we have explored the deposition and synergistic effect of Au and Fe supported over HS, which is confirmed and discussed using various spectroscopic techniques.

3.3.1 Contact Angle

At first, the contact angle analysis was utilized to confirm the modification of the silica, hence the formation of hydrophobic silica. Here, the contact angle is the angle at which the water droplet meets the solid surface of the silica.

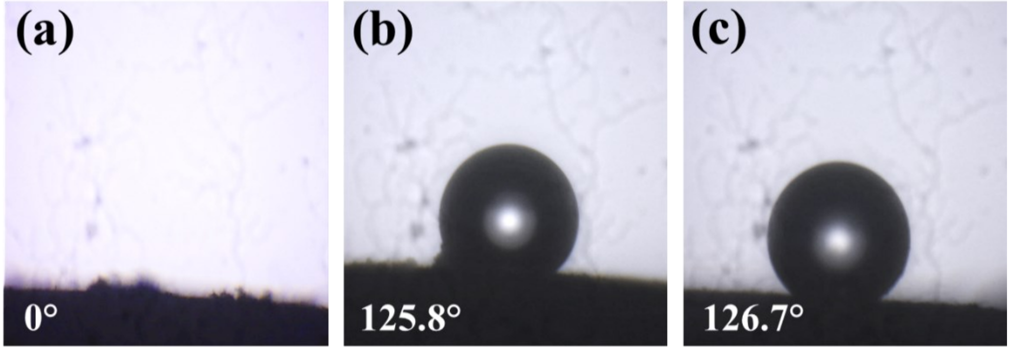

Figure 3.2 Contact angle measurement of SBA-15 (a), HS (b), and AuFeHS (c).

Generally, the surface can be considered hydrophilic if the contact angle is near zero, while the surface is hydrophobic if the contact angle is more than 90°. From the analysis of SBA-15

(Figure 3.2a), it is clear that the silica surface is hydrophilic with a contact angle of nearly 0°. In the case of HS (Figure 3.2b), the contact angle was observed as 125.8°, indicating the hydrophobicity generation over the surface. The further deposition of the metals on the silica surface has not affected the hydrophobicity of the silica, as confirmed by the contact angle of 126.7° (Figure 3.2c).

3.3.2 FTIR Spectroscopy

FTIR spectroscopy was utilized further to confirm the modification of the silica. For SBA-15, no peak was observed in the region of C-H vibration. However, in the case of HS, the stretching vibration at ~2975 cm^{-1} in the infrared region confirms the C-H functionalization of the silica, hence hydrophobicity (Figure 3.3).

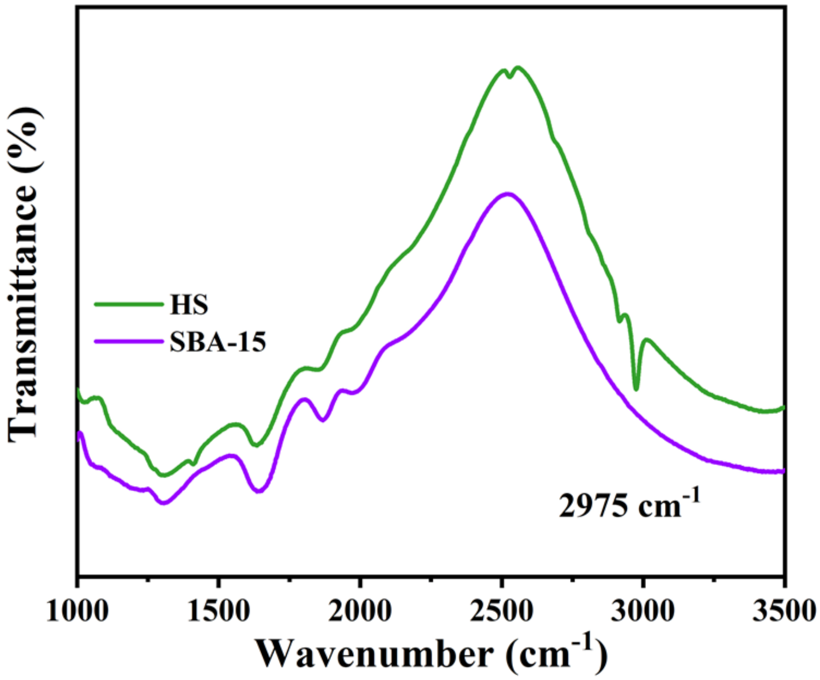

Figure 3.3 FTIR analysis of SBA-15 and HS.

Diffuse Reflectance Infrared Fourier Transform Spectroscopy (DRIFT) was also utilized to confirm the *in-situ* production of H_2O_2. The peak generation in the OH stretching region confirms the formation of H_2O_2 (Figure 3.4). The AFHS 0 min corresponds to the FTIR spectrum of the catalyst when the H_2 and O_2 gas flow was not switched on. After flowing the gases for 5 min (AFHS 5 min), the intensity of the spectrum in the region of 3250-4000 cm^{-1} increases, which indicates the increment in the OH species. Along with the broad spectrum, peaks were noticed for the isolated OH species in between the region of 3600-3700 cm^{-1} region (Figure 3.4b).

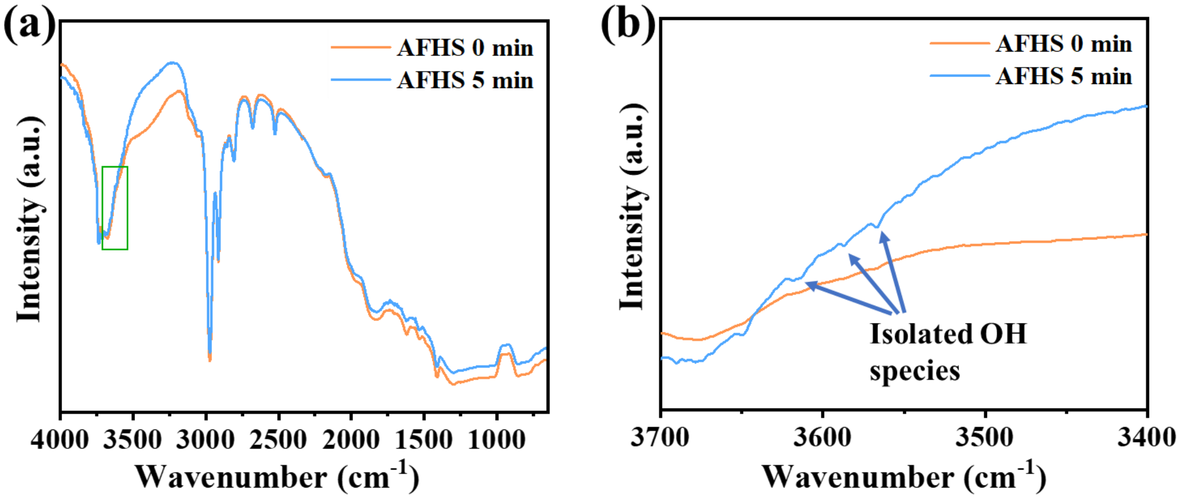

Figure 3.4 DRIFT spectrum of AuFeHS catalyst treated with H_2 and O_2 gases.

3.3.3 X-Ray Diffraction

XRD analysis of the catalysts confirms the amorphous nature of the material. After the deposition of Au and Fe, the absence of any diffraction pattern other than silica in the AuFeHS further confirms the excellent dispersion of the metals in the silica matrix (Figure 3.5).

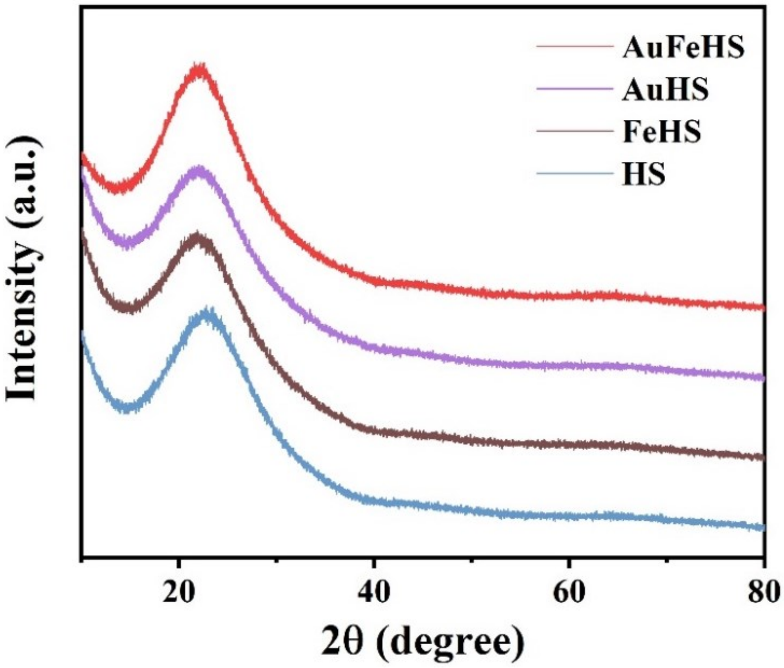

Figure 3.5 XRD patterns of various catalysts.

3.3.4 N_2 sorption analysis

The surface area measurements using the BET method were examined through the N_2 adsorption-desorption isotherms of HS and AuFeHS (Figure 3.6). The physicochemical properties of the materials analyzed following the surface area evaluation are detailed in Table 3.1.

Table 3.1 N_2 adsorption-desorption analysis data of HS and AuFeHS.

Catalyst	BET Surface area (m^2/g)	Pore volume (cm^3/g)	Peak pore diameter (nm)
HS	571	0.53	3.8
AuFeHS	564	0.78	3.8

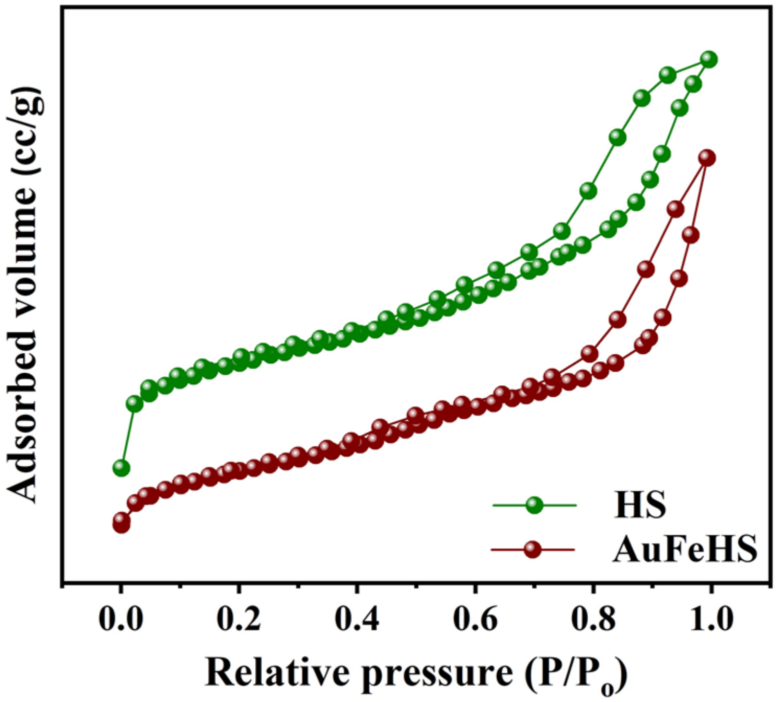

Figure 3.6 N_2 sorption isotherm of HS and AuFeHS

3.3.5 Electron Microscopy

Electron microscopy was utilized to examine the morphological details of the synthesized material. It reveals the absence of the channels in HS compared to the SBA-15, confirming the successful modification of SBA-15 (Figure 3.7).

After the deposition of Au and Fe over the support, High Resolution- Transmission Electron Microscopy probed the presence of small-size Au nanoparticles highlighted using yellow circles (Figure 3.8a). The morphology of the nanoparticles is spherical and hexagonal (Figure 3.8b). The d spacing of 0.21 nm further confirms the presence of Au nanoparticles (Figure 3.8c). The size of the Au nanoparticles is between 1.5 and 4.5 nm (Figure 3.8d calculated from Fig. 3.8a).

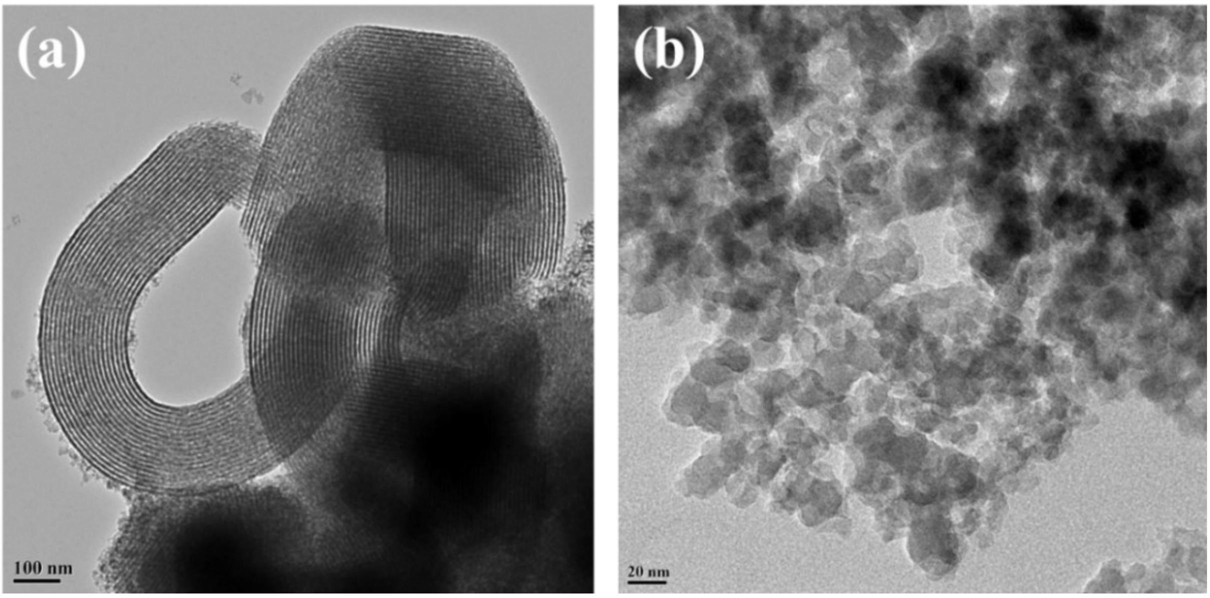

Figure 3.7 TEM images of SBA-15 (a) and HS (b).

Aberration-corrected high-angle annular dark-field scanning transmission electron microscopy (HAADF-STEM) was utilized to reveal the morphology and structure information of AuFeHS catalysts. The Au nanoparticle can easily be visualized over the surface of AuFeHS catalysts. The energy-dispersive X-ray spectroscopy (EDS) elemental maps confirm the high dispersive nature of metal particles over the HS (Figure 3.9).

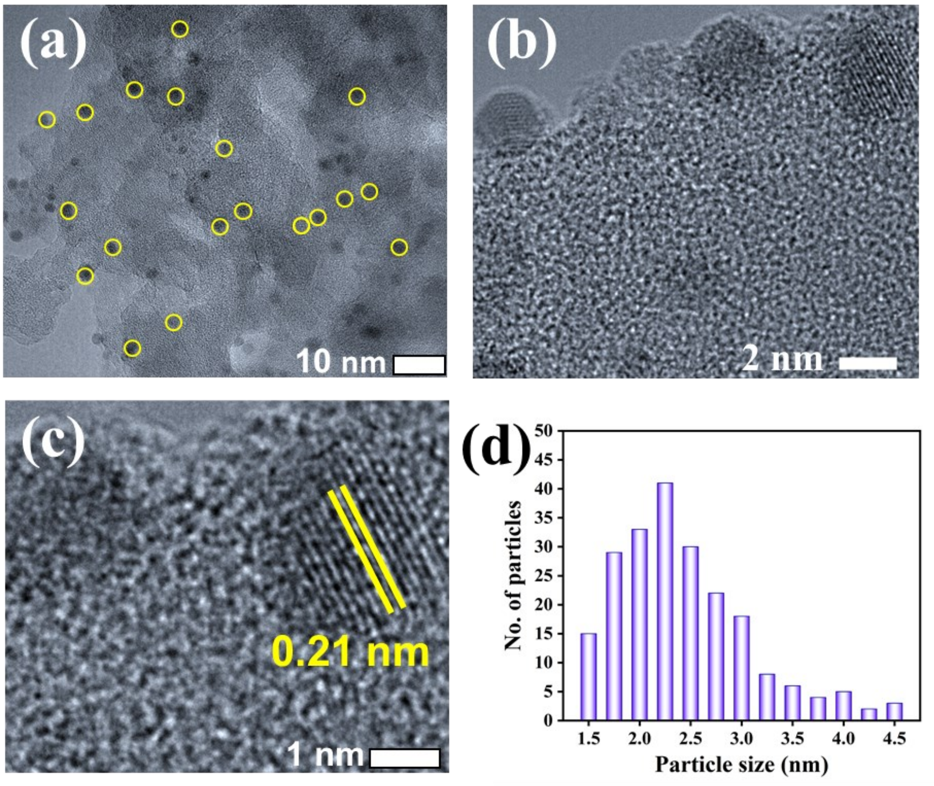

Figure 3.8 HR-TEM analysis of AFHS (a-c) and particle size histogram (d).

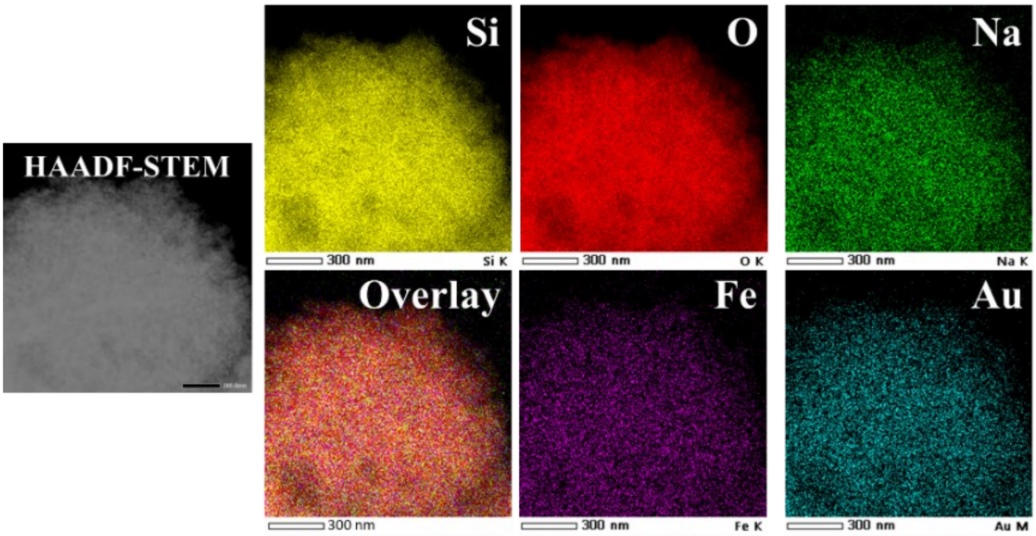

Figure 3.9 Elemental mapping of AuFeHS.

As in the case of FeHS and AuFeHS, the Fe particle could not be visualized because of the small size of Fe and the contrast difference between Au and Fe. To confirm the presence of the Fe particles over the surface, Electron Energy-Loss Spectroscopy (EELS) was utilized. The spectra were recorded from the different regions of the surface of the AuFeHS. These spectra show the presence of Fe $L_{2,3}$ edges (L_3 = 710 eV and L_2 = 722 eV), confirming the existence of Fe in the sample.

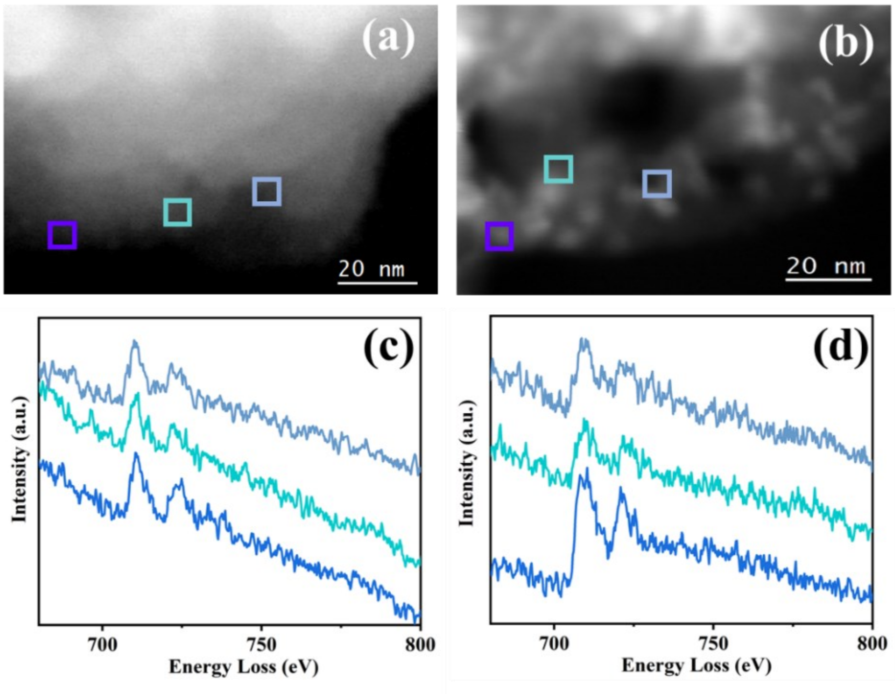

Figure 3.10 STEM-HAADF image of FeHS (a) and AuFeHS (b), Electron Energy Loss Spectra of FeHS and AuFeHS (c and d respectively).

After the successful deposition of Au and Fe over the silica support, it is worth exploring if there was any interaction between them. So, we have utilized the line analysis of STEM to confirm the interaction, which resulted in the synergistic effect for the enhanced catalytic activity (will be discussed later). The STEM line analysis of AuFeHS reveals that both the metals (Au and Fe) are present in the neighborhood of each other and have a direct interaction (Figure 3.11).

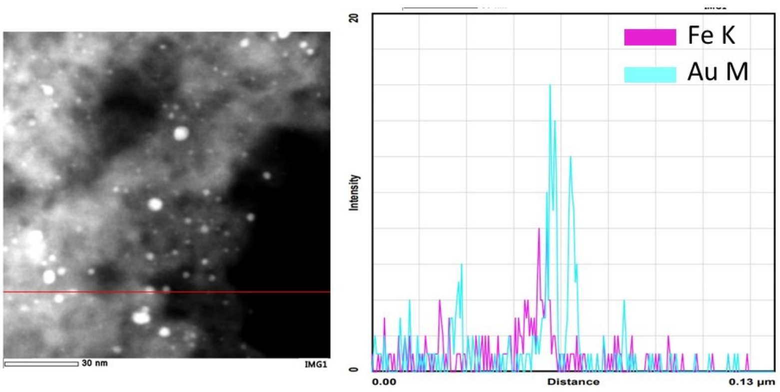

Figure 3.11 STEM Line analysis of AuFeHS catalyst.

3.3.6 Solid-State NMR Spectroscopy

Solid-state NMR spectroscopy (^{23}Na, ^{29}Si) enabled us to probe materials' molecular structure and dynamics. As NaOH was used as the precipitating agent in synthesizing the catalytic material, the *in-situ* modification of the silica by Na atoms was probed. For the HS, ^{29}Si (Figure 3.12a) confirmed the presence of Q^2, Q^3, Q^4, and T^2, T^3 states.[32,33] It was observed that when iron (Fe) was deposited using sodium hydroxide (NaOH), sodium (Na) atoms were integrated into the silica matrix, forming a Si-O-Na framework. This was confirmed by the decrease in Q^3 and Q^2 states, as shown in Figure 3.12b. Additionally, a further reduction in Q^3 and Q^2 states was observed after the deposition of gold (Au) on FeHS assisted by NaOH (Figure 3.12d).

In the ^{23}Na NMR spectrum (Figure 3.13), no peak for the ^{23}Na was observed in the case of HS, confirming the absence of any Na in the support. While examining the metal-loaded catalyst, 7.32 ppm and -1.59 ppm peaks confirmed the presence of the Si-O-Na framework in the case of FeHS, AuHS and AuFeHS.[34]

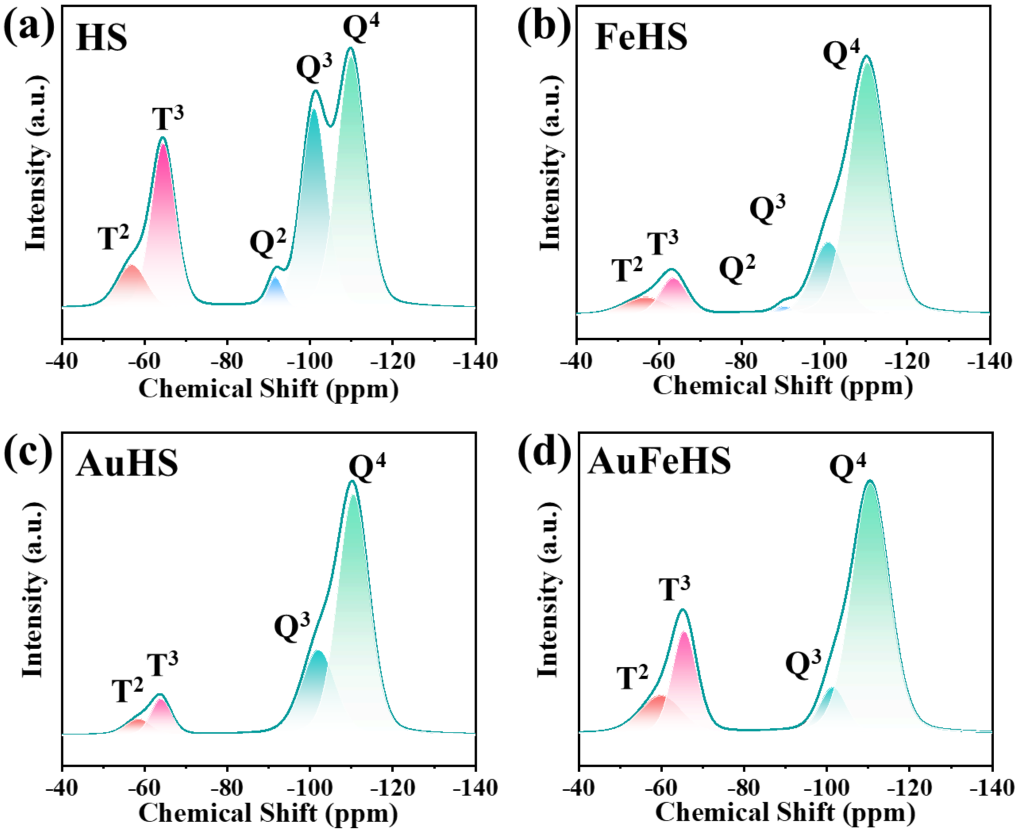

Figure 3.12 ^{29}Si MAS spectrum of various catalysts.

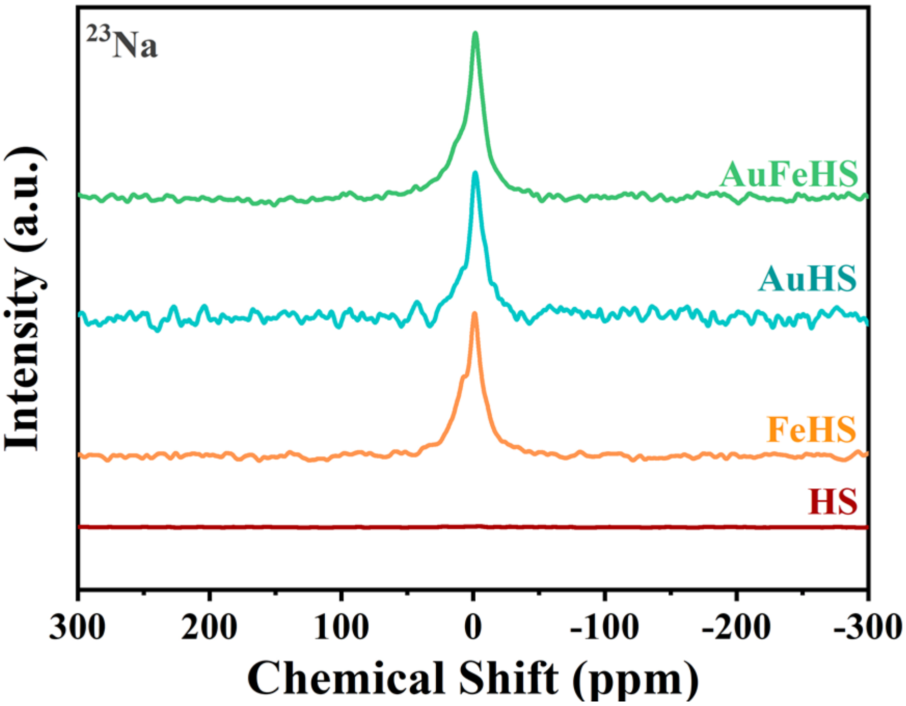

Figure 3.13 ^{23}Na MAS spectrum of various catalysts.

3.3.7 X-ray photoelectron spectroscopy

X-ray photoelectron spectroscopy (XPS) was employed to validate the oxidation states of the elements, shedding light on the altered electronic environment surrounding the Fe species. No charge correction was necessary, as an electron flood gun was employed during data acquisition, and the binding energy (BE) values were reported as recorded.

In Figure 3.14a, the Fe 2p spectra of FeHS revealed a peak at 710.5 eV, confirming the presence of Fe^{3+} species. In comparison, a peak at around 712.7 eV corresponded to FeOOH species on the catalyst surface, as reported previously.[35] For the AuFeHS catalyst, the Fe 2p spectra showed a binding energy of 711 eV, indicating the presence of Fe^{3+} species (Figure 3.14b). A lower binding energy at 709.7 eV was observed, confirming that low-valent $Fe^{3-\delta+}$ species were identified as critical Fe sites in methane activation.[36,37] These low-valent Fe sites are known to play a significant role in hydrogen peroxide activation by providing the OH moiety to activate methane to form CH_3OH.[38,39] Notably, the low-valent $Fe^{3-\delta+}$ at 709.7 eV was absent over the FeHS catalyst, reflected in its poorer catalytic performance (discussed later).

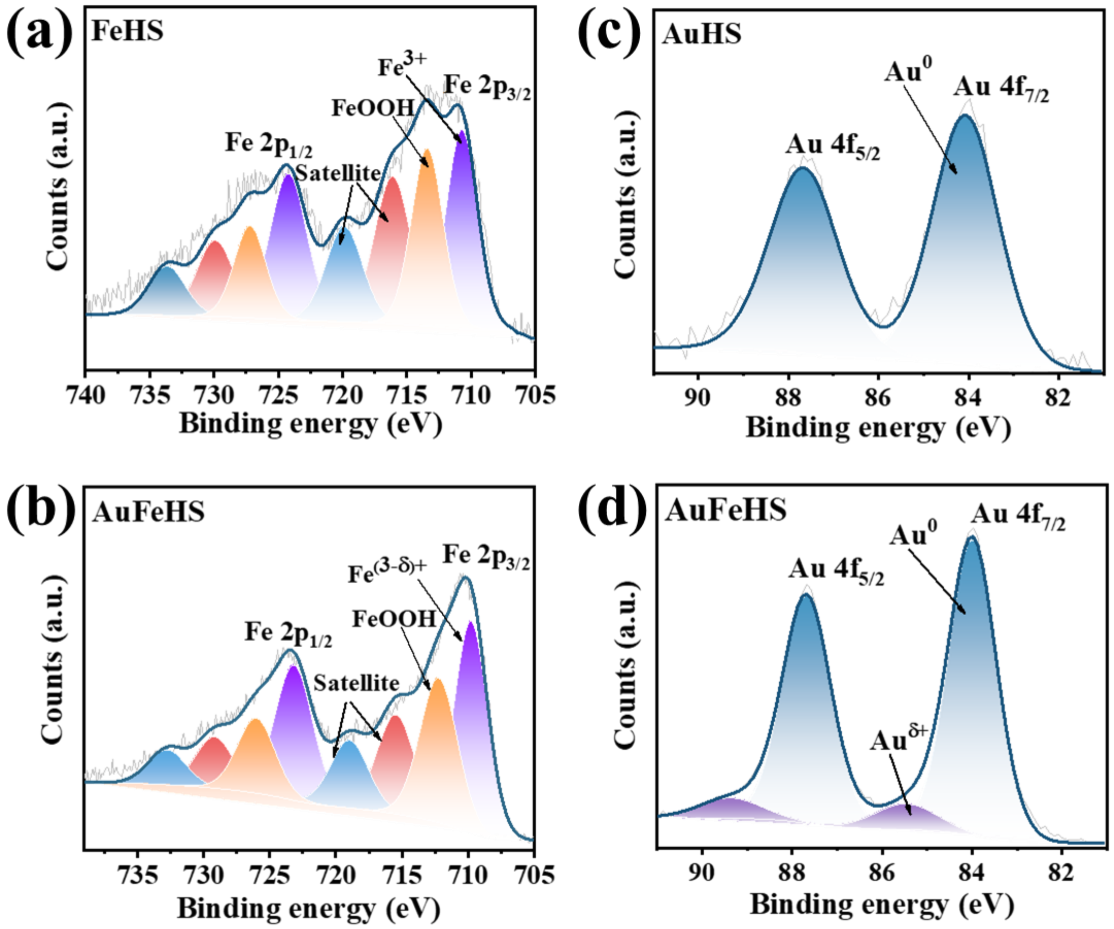

Figure 3.14 Fe 2p XPS spectrum of FeHS (a), AuFeHS (b), Au 4f XPS spectrum of AuHS (c), AuFeHS (d).

In Figure 3.14d, the Au 4f XPS spectra of AuFeHS displayed two peaks centered at 84.0 eV (Au $4f_{7/2}$) and 87.7 eV (Au $4f_{5/2}$), with a spin-orbit splitting difference of 3.7 eV, indicative of the binding energy of elemental gold (Au^0). An additional peak at a higher binding energy (~85 eV, $4f_{7/2}$) suggested the presence of cationic ($Au^{\delta+}$) species, indicating a possible charge donation and stabilization of the $Fe^{3-\delta+}$ species. Based on the relative peak areas, their respective atomic percentages were estimated as 85% for Au^0 and 15% for $Au^{\delta+}$. Notably, no significant change was observed in the case of the Au (both fresh and spent) catalyst. It is important to mention that the cationic Au species was absent in the AuHS catalyst (Figure 3.14c). Besides Au and Fe, sodium (Na) was also detected in the catalyst, which will be discussed in more detail later. The Na 1s XPS spectrum confirmed the interaction of the Si-O-Na (Figure 3.15) environment.[40,41]

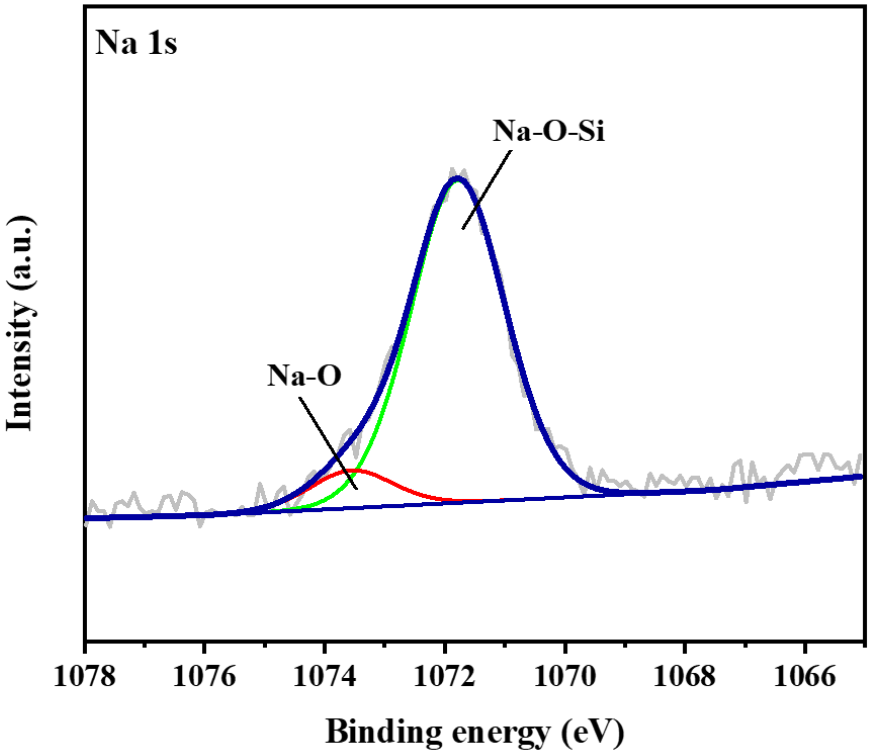

Figure 3.15 Na 1s XPS spectrum of AuFeHS.

3.3.8 X-ray Absorption Spectroscopy (XAS)

The normalized XANES spectra were measured at the Fe K-edge in the presence of Fe standards (Figure 3.16a). The absence of Fe-Fe interaction in the samples indicates that the Fe species in the catalysts are single atoms. The FeHS sample's Fe absorption edge aligns with the Fe_2O_3 standard, meaning that Fe exists in the +3 oxidation state within the sample. In contrast, the AuFeHS catalyst reveals the presence of low-valent iron species. Analyzing the radial distribution functions at the Fe K-edge for all samples (Figure 3.16c), the first peak occurs at approximately 1.5 Å, a notably lower value than that of elemental Fe foil. This finding corroborates that the Fe in the sample is not elemental, which is consistent with the XANES data discussed earlier.

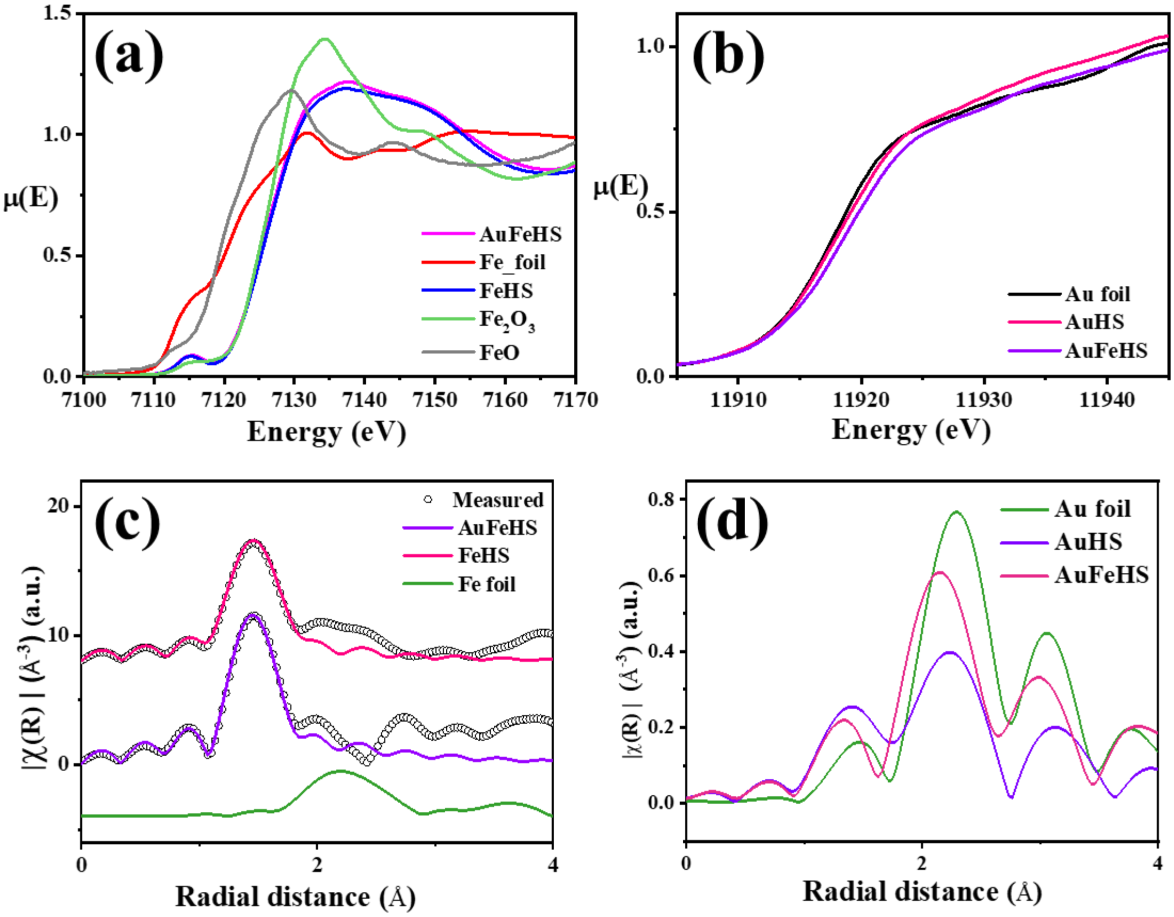

Figure 3.16 Normalized XANES spectra at Fe K-edge and Au L_3-edge of various catalysts, (a,b) respectively. Experimental χ(R) vs. R data of Au-Fe catalyst measured at Fe K-edge and Au L-edge respectively (c,d), along with best fit theoretical plots (Open circles: experimental data, solid line: theoretical best fit).

The best-fit χ(R) versus R plots for all the samples, covering a fitting range of R = 0-4 Å. The peak at ~1.5 Å corresponds to two neighboring O shells with a coordination number of 3, located at 1.94 Å and 2.11 Å. Linear combination fitting (LCF) of the AuFeHS sample indicates that it comprises 72% Fe_3O_4 and 28% FeO.

Figure 3.16b presents the normalized XANES spectra measured at the Au L_3-edge compared to Au foil. Most samples exhibit an Au absorption edge identical to that of Au foil, signifying the presence of elemental Au in all of them. Nonetheless, the AuFeHS sample displays a slightly higher L_3 edge than the Au metal edge, potentially indicating some charge transfer, as also supported by XPS data. At the Au L_3-edge, the radial distribution functions or χ(R) versus R plots for all the samples are displayed in Figure 3.16d. In contrast to the Fe edge data, the first significant peak here is situated beyond 2 Å, closely resembling the Au foil data. This indicates that the nearest neighbors of Au in these samples are predominantly Au atoms, confirming that the samples are primarily in their elemental form. However, the first peak for AuFeHS is marginally shifted to a lower R-value, likely attributable to some degree of charge transfer, as elucidated by XANES and XPS data.

3.3.9 Catalytic Activity

The synthesized catalysts were tested for methane oxidation to methanol and Acetic acid.

3.3.9A Methane Oxidation to Methanol

From a commercialization aspect, the oxidation reactions involving H_2O_2 are attractive if an onsite production of H_2O_2 can be achieved during the POM catalytic process. There are several reports on the efficacy of Au nanoparticles in the heterogeneous catalytic production of H_2O_2 from H_2 and O_2.[10,23,28,42] The presence of Au in the catalyst prompted us to check POM activity in the presence of *in-situ* generated H_2O_2. We have already explored the utilization of H_2O_2 for the effective methane oxidation to methanol and acetic acid and the optimum temperature and methane pressure under the batch process were found to be 60 °C and 10 bar. So, the same optimizations were used for *in-situ* generated H_2O_2. With the AuHS catalyst, the methanol yield was 11.3 µmol with 95% methanol selectivity. As shown in Figure 3.17a, with no sites available for H_2O_2 synthesis, the FeHS catalyst was inactive for *in-situ* peroxide production and methanol synthesis.

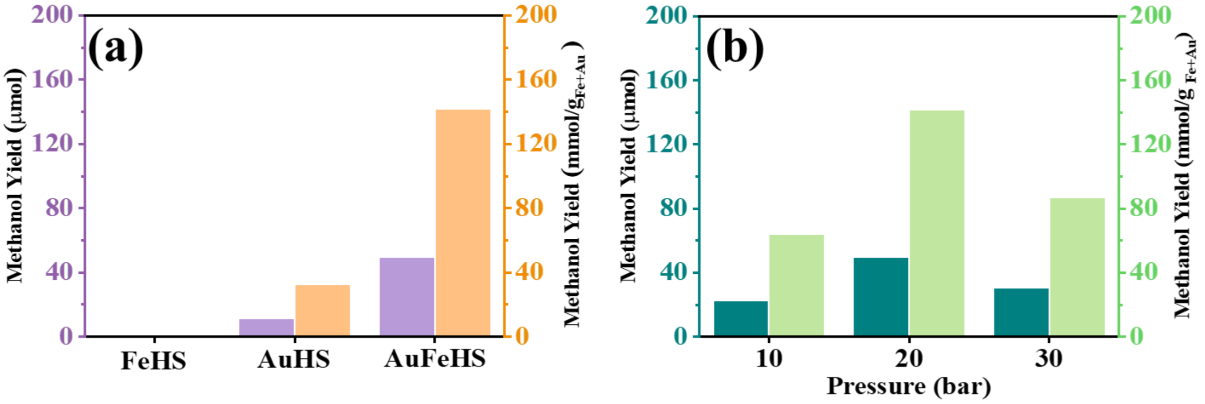

Figure 3.17 Catalytic activity of various catalysts (a), AuFeHS under different reaction pressures (b), in the batch process. Data are presented as mean ± standard deviation (SD) '1.2%'.Reaction Conditions: 50 mg Catalyst, 60 °C, 0.5 h, 20 mL H_2O, 900 rpm.

Table 3.2 Catalytic activity of various catalysts under batch process.

Sr. No.	Catalyst	Reaction conditions	MeOH µmol	MeOH mmol/g_{Fe+Au}	MeOH µmol/g_{cat}
1	FeHS	20 bar (1:1:2::d-O_2:d-H_2:CH_4)	0	0	0
2	AuHS	20 bar (1:1:2::d-O_2:d-H_2:CH_4)	11.33	32.38	226
3	AuFeHS	20 bar (1:1:2::d-O_2:d-H_2:CH_4)	49.60	141	991
4	AuFeHS	10 bar (3:3:4::d-O_2:d-H_2:CH_4)	22.29	63.60	445
5	AuFeHS	30 bar (7:7:16::d-O_2:d-H_2:CH_4)	32.12	91.70	642
6	AuFeHS[a]	20 bar (1:1:2::d-O_2:d-H_2:CH_4)	2.60	7.50	52
7	AuFeHS	15 bar (1:1:1::d-O_2:d-H_2:CH_4)	20.83	59.50	416

Reaction Conditions: 50 mg Catalyst, 0.5 h, 20 mL H_2O, 60 °C, 900 rpm. [a] Room Temp.

Under the same conditions, the AuFeHS catalyst produced a 49 µmol (141 mmol/g_{Fe+Au}) of methanol. Reaction conditions were optimized, revealing that 20 bar pressure (1:1:2::d-O_2:d-H_2:CH_4) at 60°C was the best for the batch process (Figure 3.17b & Table 3.2, Entry 3).

Methane partial oxidation at room temperature over AuFeHS catalyst under similar conditions showed very low product formation, confirming the difficulty in methane activation at low temperatures.

Along with the GC, ^{1}H NMR spectroscopy was utilized to confirm the products. As shown in Figure 3.18, the presence of a peak (3.3 ppm) corresponding to methanol is the only liquid product observed on the reaction mixture confirming the highly selective production of methanol. The peak around 4.7 ppm corresponds to water (solvent).

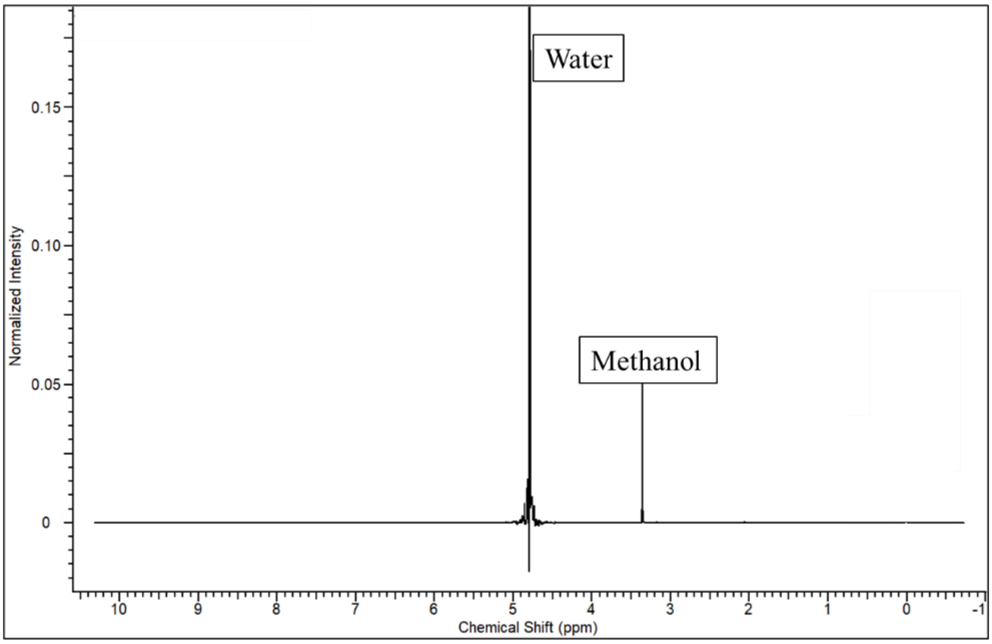

Figure 3.18 ^{1}H NMR profile of reaction mixture in H_2O+D_2O for qualitative analysis (batch process). 50 mg Catalyst, 20 bar (1:1:2::d-O_2:d-H_2:CH_4), 0.5 h, 60 °C, 20 mL H_2O, 900 rpm.

For the confirmation of the production of *in-situ* H_2O_2, NMR and potentiometric titration were utilized. The catalyst (AuFeHS) was subjected to react with H_2 and O_2 for 0.5 h at 60 °C, and then the reaction mixture was investigated using NMR in DMSO-d6 using DMF as an internal standard (Figure 3.19).

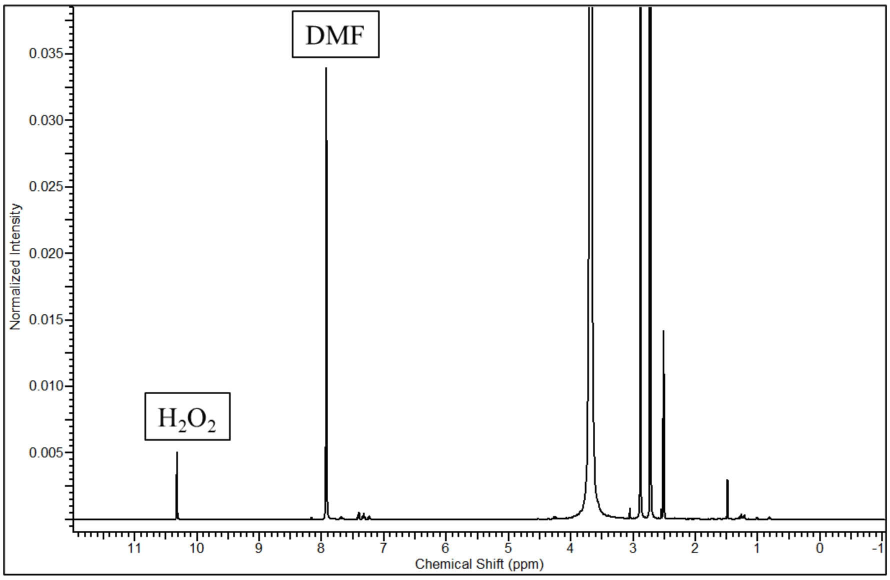

Figure 3.19 ^{1}H NMR profile of reaction mixture in DMSO-d6 for H_2O_2 qualitative analysis. Reaction Conditions: 50 mg Catalyst, 10 bar (1:1::d-O_2:d-H_2), 0.5 h, 60 °C, 20 mL H_2O, 900 rpm.

An ECO titrator instrument further confirms the *in-situ* H_2O_2 synthesis by titrating the reaction mixture against $KMnO_4$ solution (Figure 3.20).

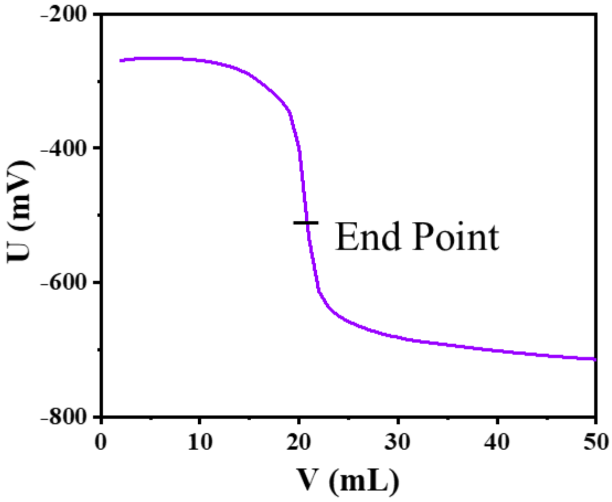

Figure 3.20 Potentiometric titration curve of methane partial oxidation in batch process.

Further, the AuFeHS catalyst was tested for the continuous oxidation of methane to methanol through the *in-situ* generated H_2O_2, using hydrogen and oxygen gases. The reaction was monitored for up to 7 h (Figure 3.21) and showed a steady increase up to 4 h with a methanol yield reaching 17.4 mmol/g_{Fe+Au}.

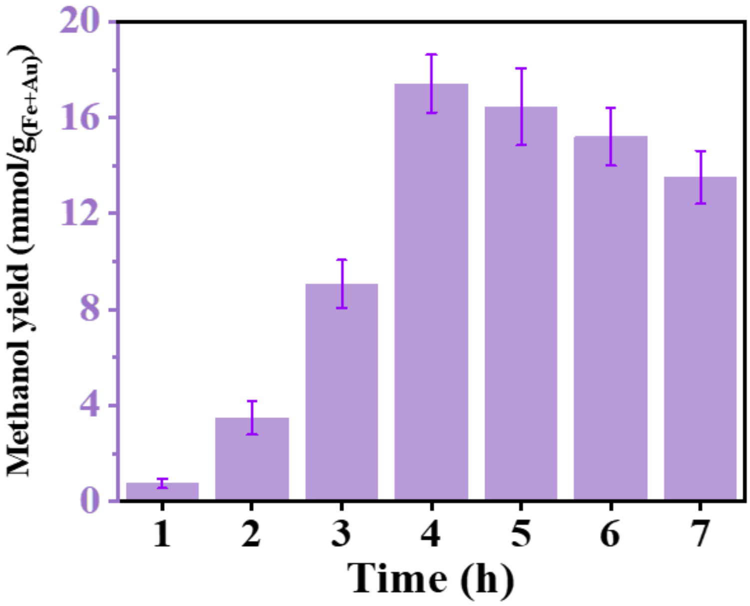

Figure 3.21 Catalytic activity of AuFeHS in the continuous flow process under atmospheric conditions.

3.3.9B Methane Oxidation to Acetic Acid

When CO was introduced with the methane into the reaction feed in a batch process using H_2O_2 as an oxidant, selective acetic acid production was observed with 3403 µmol/g_{cat} with 90% selectivity at 50 °C with an AuFeHS catalyst. The increase in temperature resulted in a decrease in the production of liquid oxygenate and an increase in CO_2 production as an overoxidized product (Figure 3.22).

Further, the catalysts were tested for acetic acid production using H_2O_2 in a continuous flow process. The catalytic activity of the AuFeHS in the reaction confirms that the Au and Fe synergistic effect is also effective for acetic acid production at atmospheric conditions. The catalyst produced 648 µmol/g_{cat} of the acetic acid with a very high selectivity of 96% among the liquid oxygenates after 4 h of the reaction time. The lower conversion in the case of CH_4 + CO in the reactant feed compared to CH_4 alone is because of the lower amount of the oxidant used in the reaction and overoxidation of the CO to the CO_2 as a competitive reaction.

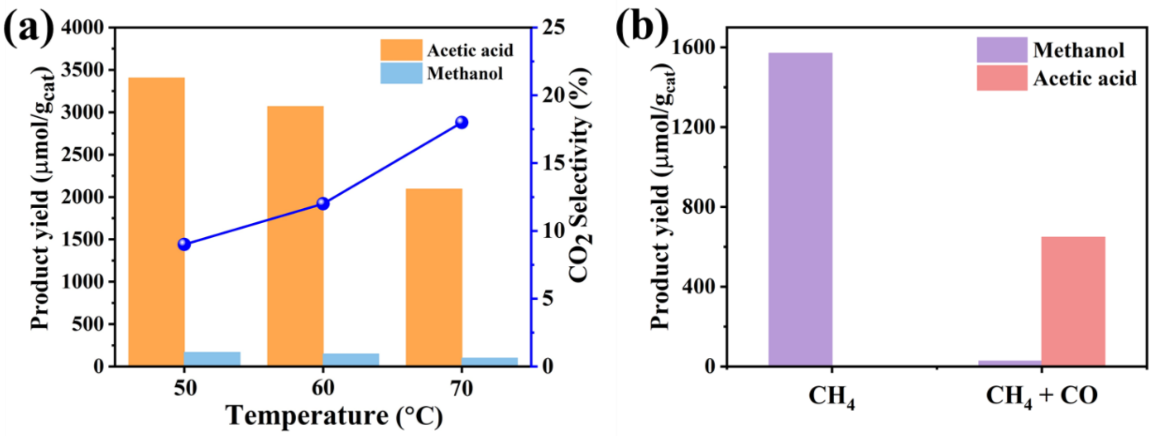

Figure 3.22 Catalytic activity of AuFeHS at various reaction temperatures in a batch process (a), in the continuous flow process (b).

Moving ahead to utilize the *in-situ* produced H_2O_2 for acetic acid production, the reaction was first tested for the batch process. With a total reaction pressure of 25 bar, there was no production of any liquid oxygenates in the case of FeHS. At the same time, the AuFeHS was efficiently able to produce acetic acid and methanol as the major products.

In the controlled experiments, using N_2 instead of methane resulted in no product formation, confirming the methane as a carbon source (Table 3.3 entry 5). No products were detected when methane was only used in the reaction feed without any oxidants, which confirms the mixture of O_2 and H_2 as OH sources for methanol formation. At the same time, the labeling experiments have also proved the same in the previous report.[43]

Table 3.3 Catalytic activity of various catalysts under batch process.

Sr. No.	Catalyst	Reaction conditions	MeOH mmol/g_{cat}	Acetic acid µmol/g_{cat}
1	FeHS	25 bar (1:1:12::d-O_2:d-H_2:CO:CH_4)	-	-
2	AuFeHS	20 bar (1:1:2::d-O_2:d-H_2:CH_4)	991	-
3	AuFeHS	25 bar (1:1:1:2::CO:d-O_2:d-H_2:CH_4)	641	362
4	AuFeHS	25 bar (1:1:1:2::d-O_2:d-H_2:CO:N_2)	-	-
5	AuFeHS	25 bar (CH_4)	-	-

Reaction Conditions: 50 mg Catalyst, 10 bar (1:1::d-O_2:d-H_2), 0.5 h, 60 °C, 20 mL H_2O, 900 rpm.

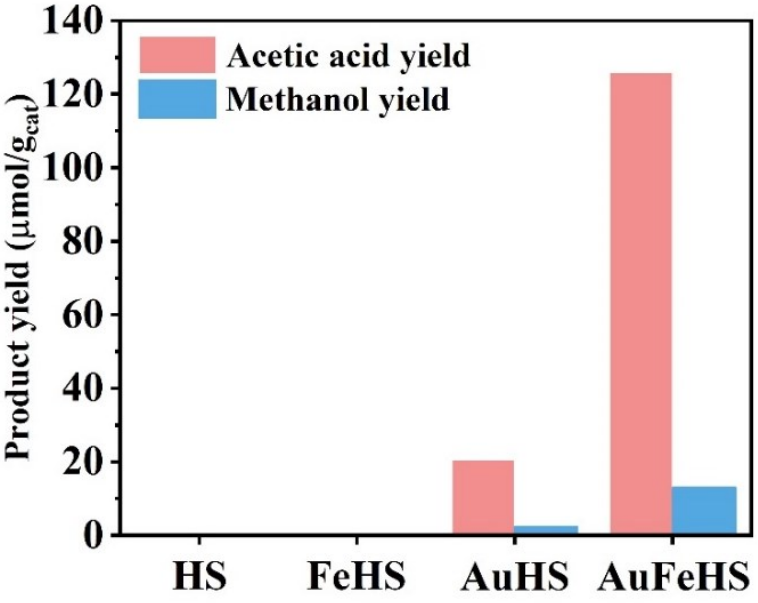

Figure 3.23 Catalytic activity of various catalysts under continuous flow process.

A step further into the process, the catalysts were tested for acetic acid production at atmospheric conditions under the continuous flow process utilizing the *in-situ* generated H_2O_2. In the reaction period of 7 h, the best activity was observed up to 4 h, similar to when only methane was in the feed (discussed above). HS and FeHS could not produce any liquid oxygenates, while AuHS produced 22.8 µmol/g_{cat}. Under the same reaction conditions, the AuFeHS catalyst catalyzed the methane and CO, producing 139 µmol/g_{cat} in the 4h of reaction time (Figure 3.23).

NMR spectroscopy also confirms the presence of Acetic acid and Methanol in the reaction mixture when CO was co-feeded in the reaction feed (Figure 3.24). The peaks at 2.0 and 3.3 ppm correspond to Acetic acid and Methanol, respectively.

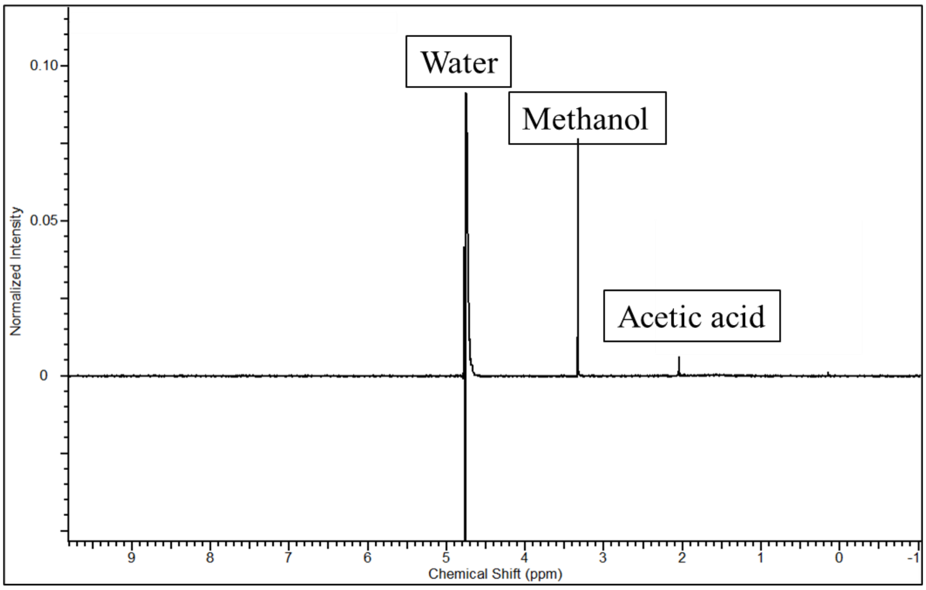

Figure 3.24 ^{1}H NMR profile of reaction mixture in H_2O+D_2O for qualitative analysis (batch process). 50 mg Catalyst, 20 bar (15 bar CH_4 + 5 bar CO), 1 h, 60 °C, 0.025 M H_2O_2 (20 mL), 900 rpm.

3.3.10 Spent Catalyst Analysis

The spent catalyst was analyzed after 7h of the continuous flow reaction to understand why the catalytic activity decreased after 4h of the reaction time. This decrease was because of the Au particle size increase in the presence of H_2O_2 and the blockage of the active sites by the reactant and product molecules. The TEM image of the AuFeHS spent catalyst shows that the Au NP's size was increased (Figure 3.25).

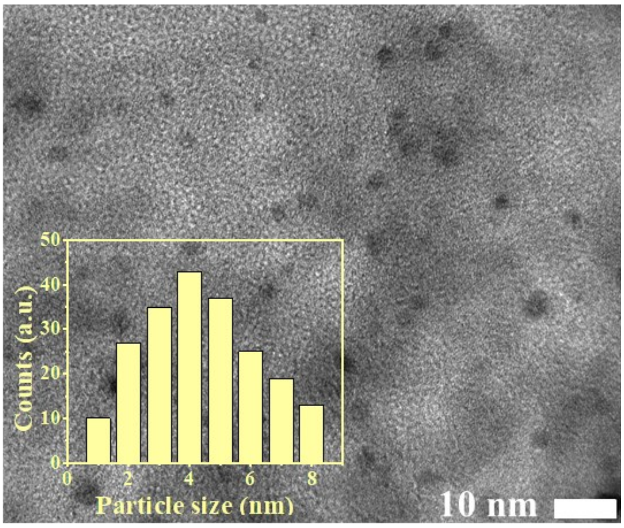

Figure 3.25 HR-TEM image of AuFeHS spent catalyst and particle size histogram (inset).

3.4 Theoretical Studies

3.4.1 Computational Details

All geometry optimizations and energy calculations for the surfaces and methane to methanol conversion mechanisms were carried out using the Kohn-Sham Generalized DFT method, incorporating Grimme's DFT-D3 corrections for van der Waals interactions, as implemented in the Vienna Ab initio Simulation Package (VASP).[44–46] The exchange-correlation energy was treated with the Perdew-Burke-Ernzerhof (PBE) functional within the generalized gradient approximation,[47] and electron-ion interactions were modeled using the Projector Augmented Wave (PAW) method.[48] A plane wave basis set with a kinetic energy cutoff of 520 eV was employed. For geometry and frequency calculations, a 3 x 3 x 1 Monkhorst-Pack k-point grid was used, with a 20 Å vacuum along the all axis to prevent structural interactions.[49–51] Electronic properties, such as Density of States (DOS) and Charge Density Difference (CDD), were computed using an 8 x 8 x 1 Monkhorst-Pack k-point scheme. Convergence criteria for ion relaxation were set at 10^{-6} eV for energy and 10^{-5} eV/atom for forces. Vaspkit 1.3.3 was used to calculate free energy and DOS,[52] while VESTA software was utilized for surface modeling.[53] The Gibbs free energy (ΔG) of the intermediates in the methane to methanol conversion process was determined accordingly

$$\Delta G = E_{ads} + \Delta E_{ZPE} - T\Delta S$$

where Eads is the adsorption energy of the intermediate, ΔEZPE is the zero-point energy difference between the adsorption state and gas state, T is the temperature, and ΔS is the entropy variation between the adsorption and gas phase.

3.4.2. Density Functional Theory Computations

Initially, the geometry of the catalyst surface was modeled and optimized to ensure that the simulated structure closely represents the actual material surface, providing a reliable foundation for further electronic and catalytic analyses. To mimic the experimental catalyst, we utilized an amorphous Hydrophobic Silica (HS) surface onto which a single Fe atom-doped Au cluster (AuFe) was deposited, as shown in Figure 3.26. This configuration served as the basis for all subsequent mechanistic investigations.

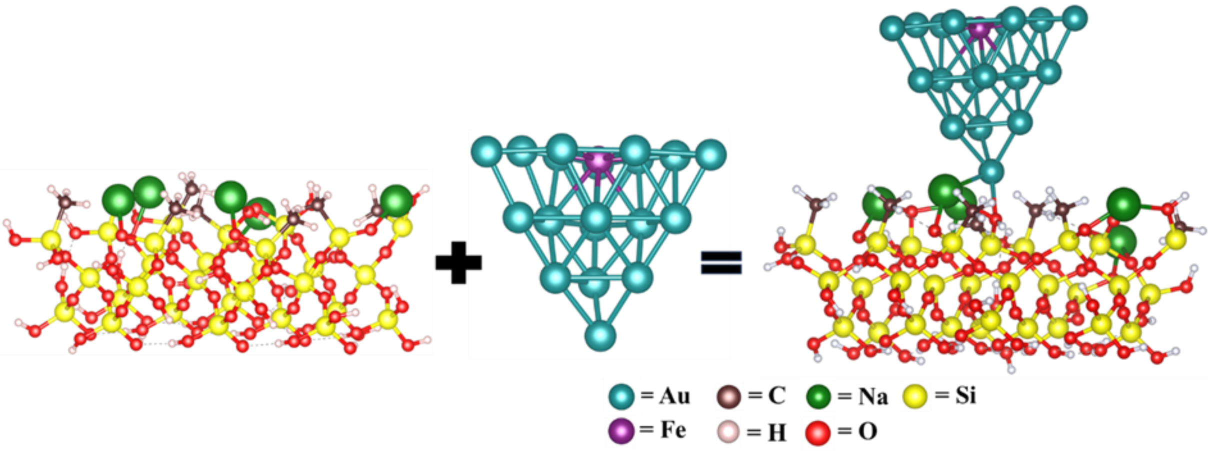

Figure 3.26 Optimized ground state structure of the AuFeHS catalyst formed by depositing a Fe-doped Au cluster onto an amorphous hydrophobic silica surface.

To explore the electronic structure in detail, d-band centre and Total Density of States (TDOS) calculations were performed from the surface. The d-band centre, a key indicator of catalytic activity, was found to be -3.4 eV, revealing significant insights into the interaction strength with adsorbates, which directly impacts the catalytic efficiency, as shown in Figure 3.27.

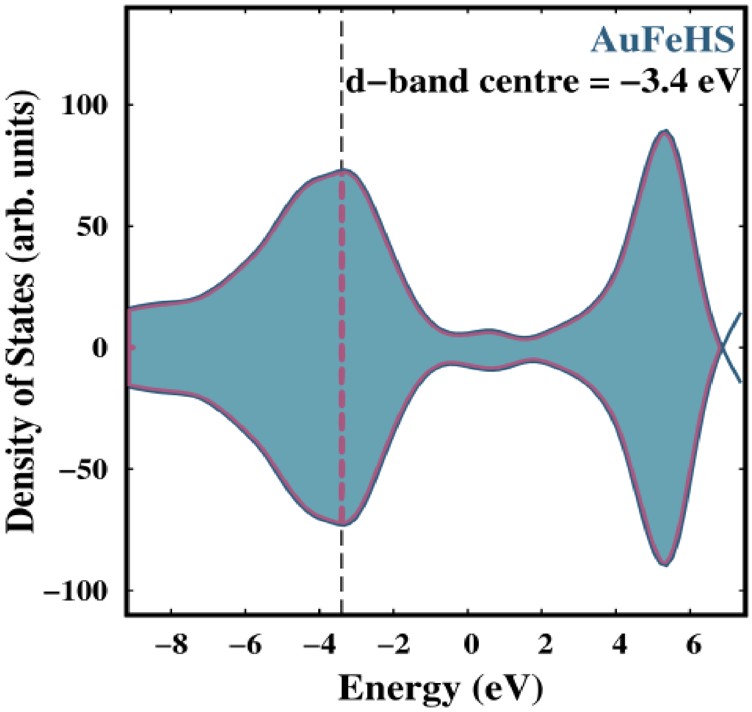

Figure 3.27 Density of States (DOS) of AuFeHS structure.

The adsorption steps of the methane-to-methanol conversion mechanism were simulated on this surface, focusing on each intermediate step: *OH-*OH, *OH-*CH_4-*OH, *CH_3-H_2O-*OH, *CH_3-*OH, and *CH_3OH, as shown in Figure 3.28. Gibbs free energies (ΔG) were calculated for each intermediate and plotted accordingly, as shown in Figure 3.28. The ΔG values across the reaction pathway indicate that each step of the methane-to-methanol conversion is kinetically favorable on this catalyst (Figure 3.28). The elementary step with the highest energy barrier, identified as the potential rate-determining step (PDS), occurs between the second and third elementary steps (*OH-*CH_4-*OH to CH_3-H_2O-OH), with a Potential determining step (PDS) value of approximately 2.3 eV. This step serves as a critical point in evaluating the feasibility of the methane-to-methanol conversion reaction, with the low energy barrier demonstrating the catalyst's effectiveness in promoting this complex reaction sequence. Insights from the free energy diagram provided a comprehensive understanding of the catalytic process, clearly demonstrating the catalyst’s potential to facilitate the conversion of methane to methanol. The identification of the PDS and the associated energy barrier further underscores the effectiveness of the catalyst in this conversion process.

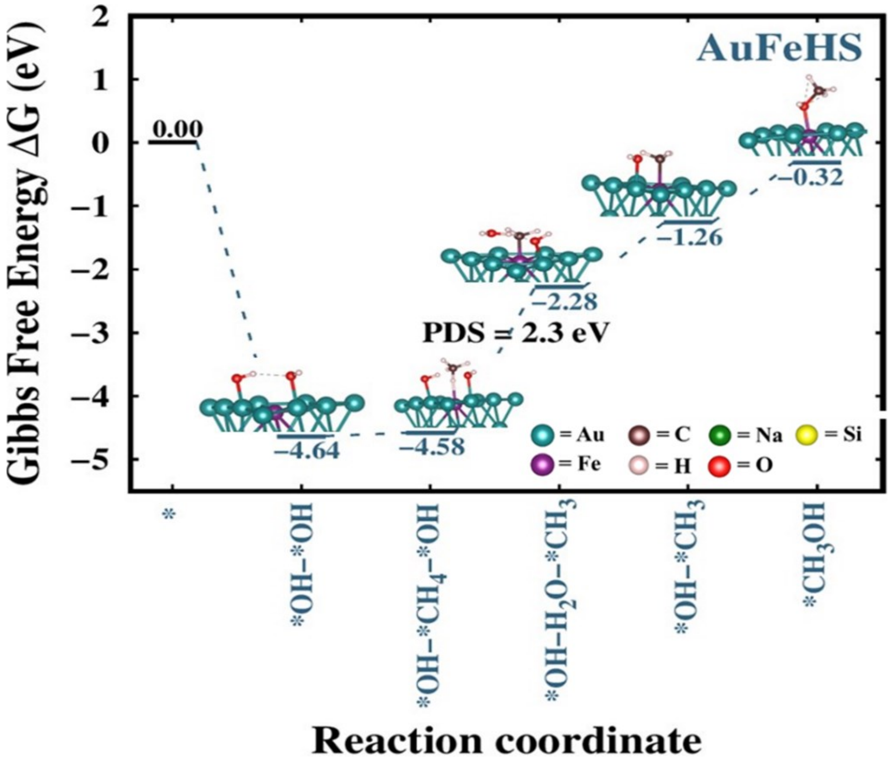

Figure 3.28 Free energy diagrams depicting the methane to methanol pathways on AuFeHS catalyst.

To investigate the synergistic effect of Fe-doped Au clusters on CH_4 activation, we performed Density Functional Theory (DFT) calculations on three systems: a pristine Au_{20} cluster, a $FeAu_{19}$ cluster, and a single Fe atom anchored on a hydrophobic silica (HS) surface. We calculated the Gibbs free energy (ΔG) to assess the feasibility of the CH_4 activation reaction on these catalysts. Table 3.4 clearly indicates that CH_4 activation is most favorable on the AuFeHS catalyst. This finding highlights the significant role of the synergistic effect between gold and iron in enhancing CH_4 activation.

Table 3.4 ΔG calculation for CH_4 activation of various catalysts.

Sr. No.	**Catalyst**	**ΔG (in eV)**
1	AuFeHS-CH_4	-0.59
2	AuHS-CH_4	-0.03
3	FeHS-CH_4	-0.14
4	AuFe/SBA15-CH_4	+1.98

3.5 Conclusions

Designing catalysts for methane activation at low pressure and temperature presents a challenge, mainly due to the need to protect the active species from potential deactivation by reactive oxidants such as O_2, H_2O_2, or H_2O.[54] In our particular approach, we successfully generate and maintain the stability of low-valence $Fe^{\delta+}$ species, which can activate CH_4, H_2 and O_2 simultaneously, by employing gold (Au). The catalytic data confirmed that the hydrophobicity of the material and synergistic effect among Au and Fe results in high activity for the partial oxidation of methane under mild conditions. The close and mutually beneficial relationship between the iron (Fe) and gold (Au) components in the catalyst is demonstrated through STEM line analysis. The presence of O_2 and H_2 in the reaction media results in the formation of H_2O_2, which is further used as an oxidant, confirmed by the potentiometric titration. Along with titration, FTIR was used to confirm OH species in the reaction media using FTIR technique. By flowing the H_2 and O_2 gases over the catalyst, the generation of peaks in the OH stretching region further confirms the on-site formation of OH species used for the methanol formation.[55,56] Hence, the synergistic effect among the atomically distributed Fe and Au nanoparticles activated the methane utilizing the *in-situ* generated H_2O_2. The DFT-based study successfully highlighted the catalytic potential of the AuFeHS surface for methane to methanol conversion. The optimized geometry, favorable d-band center position, detailed insights from TDOS, and the free energy diagram collectively emphasize the catalyst's enhanced performance and efficiency in this vital chemical transformation.

This pioneering report on methane partial oxidation utilizing *in-situ* generated hydrogen peroxide in a continuous flow system at ambient pressure marks a significant advancement in catalytic processes. This represents a significant advancement over previous literature reports focusing solely on high-pressure reaction conditions. Operating at ambient pressure makes the process more energy-efficient and scalable. Using *in-situ* generated H_2O_2 avoids the need for separate H_2O_2 storage and handling, further simplifying the process. The successful demonstration of this innovative approach highlights the potential for enhanced efficiency and selectivity in methane conversion and underscores the viability of using hydrogen peroxide as a green oxidant. The findings pave the way for further exploration and optimization of this method, offering promising implications for sustainable energy production and environmental benefits.

In summary, we have developed a strategy for partial methane oxidation using *in-situ* generated H_2O_2. The synergistic effect of Au and Fe in the bimetallic system enhances the activity proficiently. Uniquely, the high catalytic activity under the atmospheric conditions and continuous flow reactor demonstrates the presence of highly active sites over the catalyst's surface. This study opens the doors for researchers to solve this recognized problem of methane partial oxidation.

3.6 References

[1] N. D. Parkyns, C. I. Warburton, J. D. Wilson, *Catal Today* **1993**, *18*, 385–442.

[2] M. Álvarez, P. Marín, S. Ordóñez, *Ind Eng Chem Res* **2021**, *60*, 9409–9417.

[3] B. Wu, T. Lin, Z. Lu, X. Yu, M. Huang, R. Yang, C. Wang, C. Tian, J. Li, Y. Sun, L. Zhong, *Chem* **2022**, *8*, 1658–1672.

[4] X. Cui, H. Li, Y. Wang, Y. Hu, L. Hua, H. Li, X. Han, Q. Liu, F. Yang, L. He, X. Chen, Q. Li, J. Xiao, D. Deng, X. Bao, *Chem* **2018**, *4*, 1902–1910.

[5] X. Tang, L. Wang, B. Yang, C. Fei, T. Yao, W. Liu, Y. Lou, Q. Dai, Y. Cai, X.-M. Cao, W. Zhan, Y. Guo, X.-Q. Gong, Y. Guo, *Appl Catal B* **2021**, *285*, 119827.

[6] V. Fung, F. Polo-Garzon, Z. Wu, D. E. Jiang, *Catal Sci Technol* **2018**, *8*, 702–709.

[7] R. A. Periana, O. Mironov, D. Taube, G. Bhalla, C. Jones, *Science (1979)* **2003**, *301*, 814–818.

[8] S. A. Ikbal, C. Colomban, D. Zhang, M. Delecluse, T. Brotin, V. Dufaud, J.-P. Dutasta, A. B. Sorokin, A. Martinez, *Inorg Chem* **2019**, *58*, 7220–7228.

[9] G. A. Olah, *Angewandte Chemie International Edition* **2005**, *44*, 2636–2639.

[10] M. H. Ab Rahim, M. M. Forde, R. L. Jenkins, C. Hammond, Q. He, N. Dimitratos, J. A. Lopez-Sanchez, A. F. Carley, S. H. Taylor, D. J. Willock, D. M. Murphy, C. J. Kiely, G. J. Hutchings, *Angewandte Chemie International Edition* **2013**, *52*, 1280–1284.

[11] J. Yuan, W. Zhang, X. Li, J. Yang, *Chemical Communications* **2018**, *54*, 2284–2287.

[12] L. Luo, J. Luo, H. Li, F. Ren, Y. Zhang, A. Liu, W.-X. Li, J. Zeng, *Nat Commun* **2021**, *12*, 1218.

[13] S. Hamzehlouia, S. A. Jaffer, J. Chaouki, *Sci Rep* **2018**, *8*, 8940.

[14] L. Sun, Y. Wang, N. Guan, L. Li, *Energy Technology* **2020**, *8*, DOI 10.1002/ente.201900826.

[15] T. Yu, Z. Li, W. Jones, Y. Liu, Q. He, W. Song, P. Du, B. Yang, H. An, D. M. Farmer, C. Qiu, A. Wang, B. M. Weckhuysen, A. M. Beale, W. Luo, *Chem Sci* **2021**, *12*, 3152–3160.

[16] W. Huang, S. Zhang, Y. Tang, Y. Li, L. Nguyen, Y. Li, J. Shan, D. Xiao, R. Gagne, A. I. Frenkel, F. F. Tao, *Angewandte Chemie International Edition* **2016**, *55*, 13441–13445.

[17] R. L. Lieberman, A. C. Rosenzweig, *Nature* **2005**, *434*, 177–182.

[18] S. H. Morejudo, R. Zanón, S. Escolástico, I. Yuste-Tirados, H. Malerød-Fjeld, P. K. Vestre, W. G. Coors, A. Martínez, T. Norby, J. M. Serra, C. Kjølseth, *Science (1979)* **2016**, *353*, 563–566.

[19] G. Qi, T. E. Davies, A. Nasrallah, M. A. Sainna, A. G. R. Howe, R. J. Lewis, M. Quesne, C. R. A. Catlow, D. J. Willock, Q. He, D. Bethell, M. J. Howard, B. A. Murrer, B. Harrison, C. J. Kiely, X. Zhao, F. Deng, J. Xu, G. J. Hutchings, *Nat Catal* **2022**, *5*, 45–54.

[20] X. Zhang, Y. Wang, K. Chang, S. Yang, H. Liu, Q. Chen, Z. Xie, Q. Kuang, *Appl Catal B* **2023**, *320*, 121961.

[21] J. Mao, H. Liu, X. Cui, Y. Zhang, X. Meng, Y. Zheng, M. Chen, Y. Pan, Z. Zhao, G. Hou, J. Hu, Y. Li, G. Xu, R. Huang, L. Yu, D. Deng, *Nat Catal* **2023**, DOI 10.1038/s41929-023-01030-2.

[22] J. M. Campos-Martin, G. Blanco-Brieva, J. L. G. Fierro, *Angewandte Chemie International Edition* **2006**, *45*, 6962–6984.

[23] R. J. Lewis, K. Ueura, X. Liu, Y. Fukuta, T. E. Davies, D. J. Morgan, L. Chen, J. Qi, J. Singleton, Jennifer. K. Edwards, S. J. Freakley, C. J. Kiely, Y. Yamamoto, G. J. Hutchings, *Science (1979)* **2022**, *376*, 615–620.

[24] C. M. Crombie, R. J. Lewis, R. L. Taylor, D. J. Morgan, T. E. Davies, A. Folli, D. M. Murphy, J. K. Edwards, J. Qi, H. Jiang, C. J. Kiely, X. Liu, M. S. Skjøth-Rasmussen, G. J. Hutchings, *ACS Catal* **2021**, *11*, 2701–2714.

[25] S. J. Freakley, S. Kochius, J. van Marwijk, C. Fenner, R. J. Lewis, K. Baldenius, S. S. Marais, D. J. Opperman, S. T. L. Harrison, M. Alcalde, M. S. Smit, G. J. Hutchings, *Nat Commun* **2019**, *10*, 4178.

[26] Q. Chen, E. J. Beckman, *Green Chemistry* **2008**, *10*, 934.

[27] J. Lyu, L. Niu, F. Shen, J. Wei, Y. Xiang, Z. Yu, G. Zhang, C. Ding, Y. Huang, X. Li, *ACS Omega* **2020**, *5*, 16865–16874.

[28] Z. Jin, L. Wang, E. Zuidema, K. Mondal, M. Zhang, J. Zhang, C. Wang, X. Meng, H. Yang, C. Mesters, F.-S. Xiao, *Science (1979)* 2**020**, *367*, 193–197.

[29] S. Basu, C. Nayak, A. K. Yadav, A. Agrawal, A. K. Poswal, D. Bhattacharyya, S. N. Jha, N. K. Sahoo, *J Phys Conf Ser* **2014**, *493*, 012032.

[30] A. K. Poswal, A. Agrawal, A. K. Yadav, C. Nayak, S. Basu, S. R. Kane, C. K. Garg, D. Bhattachryya, S. N. Jha, N. K. Sahoo, **2014**, pp. 649–651.

[31] M. Newville, B. Ravel, D. Haskel, J. J. Rehr, E. A. Stern, Y. Yacoby, *Physica B Condens Matter* **1995**, *208–209*, 154–156.

[32] I. S. Protsak, Y. M. Morozov, W. Dong, Z. Le, D. Zhang, I. M. Henderson, *Nanoscale Res Lett* **2019**, *14*, 160.

[33] R. Gadzała-Kopciuch, M. Kluska, M. Wełniak, B. Buszewski, *Mater Chem Phys* **2005**, *89*, 228–237.

[34] H. Koller, G. Engelhardt, A. P. M. Kentgens, J. Sauer, *J Phys Chem* **1994**, *98*, 1544–1551.

[35] T. Yang, L. Meng, S. Han, J. Hou, S. Wang, X. Wang, *RSC Adv* **2017**, *7*, 34687–34693.

[36] M. C. Simons, S. D. Prinslow, M. Babucci, A. S. Hoffman, J. Hong, J. G. Vitillo, S. R. Bare, B. C. Gates, C. C. Lu, L. Gagliardi, A. Bhan, *J Am Chem Soc* **2021**, *143*, 12165–12174.

[37] J. G. Vitillo, A. Bhan, C. J. Cramer, C. C. Lu, L. Gagliardi, *ACS Catal* **2019**, *9*, 2870–2879.

[38] S. Sun, A. J. Barnes, X. Gong, R. J. Lewis, N. F. Dummer, T. Bere, G. Shaw, N. Richards, D. J. Morgan, G. J. Hutchings, *Catal Sci Technol* **2021**, *11*, 8052–8064.

[39] Á. Szécsényi, G. Li, J. Gascon, E. A. Pidko, *ACS Catal* **2018**, *8*, 7961–7972.

[40] A. Mekki, D. Holland, C. F. McConville, M. Salim, *J Non Cryst Solids* **1996**, *208*, 267–276.

[41] B. Dong, Y. Xu, S. Lin, X. Dai, *Sci Rep* **2015**, *5*, 17274.

[42] C. M. Crombie, R. J. Lewis, D. Kovačič, D. J. Morgan, T. E. Davies, Jennifer. K. Edwards, M. S. Skjøth-Rasmussen, G. J. Hutchings, *Catal Letters* **2021**, *151*, 164–171.

[43] A. V. Jagtap, P. Kumar, S. Gupta, A. Nagendra, S. N. Jha, D. Bhattacharyya, T. G. Ajithkumar, C. P. Vinod, *ACS Sustain Chem Eng* **2024**, DOI 10.1021/acssuschemeng.4c02993.

[44] J. Moellmann, S. Grimme, *The Journal of Physical Chemistry C* **2014**, *118*, 7615–7621.

[45] L. Goerigk, in *Non-Covalent Interactions in Quantum Chemistry and Physics*, Elsevier, **2017**, pp. 195–219.

[46] J. A. Pople, P. M. W. Gill, B. G. Johnson, *Chem Phys Lett* **1992**, *199*, 557–560.

[47] J. Hafner, *J Comput Chem* **2008**, *29*, 2044–2078.

[48] K. F. Garrity, J. W. Bennett, K. M. Rabe, D. Vanderbilt, *Comput Mater Sci* **2014**, *81*, 446–452.

[49] R. A. Evarestov, V. P. Smirnov, *Phys Rev B* **2004**, *70*, 233101.

[50] H. J. Monkhorst, J. D. Pack, *Phys Rev B* **1976**, *13*, 5188–5192.

[51] P. Wisesa, K. A. McGill, T. Mueller, *Phys Rev B* **2016**, *93*, 155109.

[52] V. Wang, N. Xu, J.-C. Liu, G. Tang, W.-T. Geng, *Comput Phys Commun* **2021**, *267*, 108033.

[53] K. Momma, F. Izumi, *J Appl Crystallogr* **2008**, *41*, 653–658.

[54] Y. Tang, Y. Li, F. (Feng) Tao, *Chem Soc Rev* **2022**, *51*, 376–423.

[55] F. Dai, Q. Zhuang, G. Huang, H. Deng, X. Zhang, *ACS Omega* **2023**, *8*, 17064–17076.

[56] C. Apostolidou, *Adv Theory Simul* **2020**, *3*, DOI 10.1002/adts.202000174.

Chapter 4

Oxidation of Methane to Formic Acid under Mild Conditions

Pawan Kumar, Iqraa, Srishti Kesarwani, Rajashri Urkude, Nita R. Patil, Prashant Niphadkar, Vijay V. Bokade, M. Ali Haider, C P Vinod Direct Conversion of Methane to Formic Acid over Au-Fe- Na- ZSM-5 at Ambient Pressure using H_2O_2 (Manuscript under preparation)

4.1 Introduction

Methane conversion to C_1 oxygenates is the best way to utilize this greenhouse gas, but it is challenging since over-oxidation by combustion to CO_2 and H_2O is thermodynamically preferred.[1,2] It is proposed that a wide range of chemical products can be derived from methane.[3] One significant product is formic acid, which can serve as a feedstock chemical and a fuel. Formic acid is a versatile and renewable building block for various chemical applications. It is used as a preservative, a disinfectant, a pH regulator, and a reducing agent.[4,5] Formic acid is produced globally at a rate of approximately 800,000 tons per year through the combination of methanol and carbon monoxide with a strong base. It is utilized in various applications, including the textile industry, cleaning, and preservation. The demand for formic acid may rise significantly due to the advancement of efficient formic acid dehydrogenation catalysts, which could have widespread use in developing a hydrogen economy.[6] Aside from fossil fuels, practical hydrogen storage systems rely on pressurized containers or cryogenic conditions.[7] However, formic acid (HCOOH), with its volumetric hydrogen density of 53 g of H_2 per litre, low toxicity, and liquid state under ambient conditions, presents itself as an ideal hydrogen storage material for specific applications.[8] Thus, converting methane to formic acid can mitigate greenhouse gas emissions and transition toward a more sustainable and environmentally friendly chemical industry.

Extensive research has been dedicated to directly converting methane to formic acid in a single step. However, this process is hampered by either diminished activity or the requirement for stringent reaction conditions.[5,9] Fe-MOR catalysts are reported for formic acid production but suffer from high temperature and pressure reaction conditions in the zeolite-supported catalyst.[10] Bimetallic catalysts are also known for methane partial oxidation, whereas Ir-Fe catalysts have shown a synergistic effect on the production of formic acid.[4] In a recent work, researchers explored the role of Na in methane activation and utilization.[11] Taking the cue, we developed a bimetallic catalyst supported over the Na-ZSM to explore the methane partial oxidation towards formic acid production in an efficient way. As Fe and Au are known for the catalytic oxidation of methane individually, we tried to incorporate both metals on the zeolite support using an easy synthesis route (deposition precipitation). As discussed in Chapter 3, tuning the active site on the catalyst surface where the electronic interaction among the two metals can effectively participate in methane activation. The oxidation and stabilization of the product formic acid have been extensively studied using the DFT models. The novelty of this work lies in designing the bimetallic catalyst with the interaction between Au, Fe, and Na for methane activation. The Au and Fe particle sizes have been observed at ~5nm. The synergistic effect of the metals (Au and Fe) governs the high activity of methane partial oxidation. The continuous flow process at ambient pressure conditions presents an effective way toward the industrialization of the holy grail of catalysis.

4.2 Experimental Section

4.2.1 Materials

All chemicals were used without further purification. Metal precursors, Iron(III) nitrate nonahydrate, and hydrogen tetrachloroaurate(III) trihydrate were purchased from Alfa Aesar. Tetrapropylammonium bromide 98 % (TPABr), Aluminium sulphate (99%), and sulphuric acid (98%) were purchased from Lobachemie. Ammonium chloride and sodium hydroxide flakes were purchased from Merck. Methane (99.99% pure) was purchased from Vadilal Chemical Limited.

4.2.2 Catalyst Synthesis

4.2.2.1 Synthesis of NZ

The support Na-ZSM-5 (NZ) was prepared using a molar gel composition of $SiO_2/0.0125Al_2O_3/0.3Na_2O/0.1TPABr/36\ H_2O$ as per the previous reports.[12,13] Typically, 7.86 g of TPABr and 30.0 g of DI water were dissolved with stirring to produce Solution A. Solution B was prepared separately by mixing 62.60 g sodium silicate (28 % SiO_2 & 8 % Na_2O) in 30.0 g water with vigorous stirring. Then, solution B was slowly added to solution A, referred to as solution C. 2.43 g of aluminum sulfate was carefully mixed in an acidic solution containing 5.13 g of Sulfuric acid and 10.0 g of water. This alumina solution (solution D) was then slowly added to solutions C and E, stirring for 2 h. Finally, 69.5 g of water was added to solution E with stirring for 1 h to produce a final gel, and the pH was maintained at 10.0 ± 0.2. The final gel was transferred to a Stainless steel autoclave and subjected to hydrothermal crystallization at 160 °C for 48 h. After hydrothermal crystallization, the gel was separated into a wet cake by vacuum filtration, then dried at 120 °C and calcined in a muffle furnace at 550 °C for 10 h to obtain a ZSM-5 composite in Na-form.

4.2.2.2 Synthesis of FeNZ catalyst

Iron (Fe) was deposited over NZ using the well-known deposition precipitation method. Typically, 0.5 grams of NZ were dispersed in 50 mL of Millipore water with sonication for 5 to 10 minutes. For the deposition of metal over support, the pH of the solution was adjusted to a range of 9 to 10 using a 0.1 M NaOH solution while stirring. The aqueous solution containing the metal precursor was slowly added drop by drop to the above solution for 20 to 30 minutes, maintaining the pH. The mixture was then aged for 1 h. A solid powder was obtained after centrifugation and drying in a hot air oven at 80 °C for several hours. This powder was calcined in static air at 350 °C for 4 h. The resulting powder catalyst (xFeNZ, x = wt % of Fe) was utilized for catalytic reactions without undergoing additional post-treatment.

4.2.2.3 Synthesis of AuNZ catalyst

Gold (Au) was deposited over NZ using the well-known deposition precipitation method. 0.5 g of NZ was typically dispersed in 50 mL of Millipore water with sonication for 5 to 10 minutes. For the deposition of metal over support, the pH of the solution was adjusted to a range of 9 to 10 using a 0.1 M NaOH solution while stirring. To this solution, a required amount of NH_4Cl (typically 108 mg) was added. The aqueous solution containing the metal precursor was slowly added drop by drop to the above solution for 20 to 30 minutes, maintaining the pH. The mixture was then aged for 1 h. After centrifugation and drying in a hot air oven at 80 °C, a solid powder was obtained for several hours. This powder was calcined in static air at 350 °C for 4 h. The resulting powder catalyst (yAuNZ, y = wt % of Au) was utilized for catalytic reactions without undergoing additional post-treatment

4.2.2.4 Synthesis of AuFeNZ catalyst

Deposition of Au onto the FeNZ catalyst was also carried out using the deposition-precipitation method. Typically, 0.5 grams of FeNZ catalyst were dispersed in 50 mL of Millipore water, and a fixed quantity of ammonium chloride was introduced into the solution as a modifier. Subsequently, the aqueous solution containing the Au precursor was slowly added dropwise to the resulting solution while maintaining the pH at 9.5 with a 0.1 M aqueous NaOH solution. The resulting precipitate was centrifuged, washed with deionized water, and dried at 80 °C. The dried powder was further calcined in static air at 350 °C for 4 h, yielding the resulting powder catalyst (xAuyFeNZ, x and y = wt % of Fe and Au respectively), which was utilized for catalytic reactions without any additional post-treatment.

4.2.3 Characterizations

The ex-situ X-ray diffraction (XRD) experiments were carried out on a Rigaku miniflex 2200PC diffractometer with a graphite monochromator and Cu Kα radiation ($\lambda = 1.5418$ Å).

N_2 physisorption isotherms were recorded at -196 °C on a Micromeritics Tristar II automated gas sorption system. Before analysis, the samples were outgassed under a dynamic vacuum at 350 °C for 3 h. Textural properties were calculated from the adsorption/desorption isotherms using Tristar II software version 1.55. The specific surface area was determined using the multipoint BET algorithm in the P/P_0 range from 0.10 to 0.25.

The microstructure and morphology of the products were characterized using a transmission electron microscope (TEM, Tecnai F20) with an accelerating voltage of 200 kV, a high-resolution transmission electron microscope (HRTEM, JEM-2100) with an accelerating voltage of 200 kV and a scanning electron microscope (SEM, JEOL-TEM) equipped with energy-dispersive X-ray spectroscopy (EDS) with an accelerating voltage of 200 kV.

X-ray photoelectron spectroscopy (XPS) measurements were carried out using a Thermo Scientific Kalpha+ spectrometer. The peak fitting of the individual core levels was done using Avantage software with a smart-type background.

^{23}Na and ^{29}Si solid-state NMR experiments were performed on the JEOL-400 spectrometer, operating at a magnetic field strength of 9.4 T. Liquid product NMR was performed on Bruker AV-500 instrument with a strength of 500 MHz.

The Fe K-edge (7112 eV) and Au L_3-edge (11919 eV), X-ray absorption spectra were recorded at Scanning EXAFS Beamline (BL-09) of INDUS-2 Synchrotron Source, Raja Ramanna Centre for Advanced Technology (RRCAT), Indore.

Experimental details of XAS

The beamline is equipped with a Si (111) based double crystal monochromator for energy selection and a meridional cylindrical mirror (Rh/Pt coated) for collimation. The data was collected when the synchrotron source 2.5 GeV ring was operated at 120 mA injection current. XAFS (XANES and EXAFS) measurements were carried out at room temperature in fluorescence mode. An ion chamber was filled with N_2, He, and Ar for Fe and Au foil and for the samples. The second crystal of the monochromator was 60% detuned during the data collection to suppress the higher harmonic components. The energy calibration was performed using Fe and Au metal foil as a reference. The standard normalization and background subtraction procedures were executed using the ATHENA software version 0.9.26 to obtain normalized XANES spectra.[14] Fourier transformed (FT) of EXAFS oscillations were calculated to observe the $|\chi(R)|$ vs R space spectra, and its fitting was done using ARTEMIS software version 0.9.26 which uses FEFF6 and ATOMS[15] programs to simulate the theoretical scattering paths according to crystallographic structure.

4.2.4 Catalytic activity for methane partial oxidation to formic acid

Process for methane oxidation using H_2O_2 in a batch reactor: The partial oxidation of methane was performed in an Amar (Parr) reactor of a stainless-steel autoclave with 100 mL capacity. A fixed amount of catalyst was dispersed in 20 mL of Millipore water, and a desired amount of 50% w/v H_2O_2 was added. Then, the autoclave was sealed and purged three times with methane (CH_4) gas at 5 bar pressure. It was then pressurized to the desired pressure (typically 10 bar) with CH_4 gas, and the solution was heated to the desired reaction temperature (usually 60 °C). Once the temperature reached the set value, the solution was vigorously stirred at ca. 950 rpm for a fixed amount. After the completion of the reaction, the autoclave was subjected to cooling down below 10 °C in ice-cold water to minimize the loss of volatile products. The gas sample was collected in a gas bag after cooling the products. Liquid samples were collected after centrifugation and analyzed using gas chromatography (GC) and NMR.

Process for methane oxidation using H_2O_2 in a continuous flow reactor: The catalytic performance was evaluated in a continuous flow cotton-plugged quartz reactor with a total length of 50 cm and an internal diameter of 8 mm. The feed stream, consisting of 99.99% pure methane and 30% w/v diluted H_2O_2, was brought into contact with the catalyst within a temperature range of 30-80 °C and at a pressure of 1 atm. Methanol recovery from the effluents was achieved through an ice-cold condensation process maintained below 10 °C to prevent the loss of volatile products. The feed stream, containing a 15% w/v aqueous solution of hydrogen peroxide, was regulated using a syringe pump, while the methane flow was controlled by a mass flow controller (Alicat). Both gases were passed through the layers of the pelletized catalyst bed. Liquid and gaseous products were separated in a coiled gas condenser and collected periodically for analysis for a 7 h period. The reaction was conducted for a fixed duration with continuous circulation of ice-cold water. Following completion of the reaction, gas samples were collected after cooling, and liquid samples were collected after centrifugation. The products were analyzed using gas chromatography and NMR techniques.

Product Quantification

The solution comprised liquid products filtered from catalyst powder, yielding a clean liquid that included acetic acid, methanol, formic acid, methyl peroxide, and other compounds. This liquid was quantitatively analyzed using proton nuclear magnetic resonance (^{1}H-NMR) spectroscopy, with potassium hydrogen phthalate (KHP) dissolved in a D_2O and H_2O mixture serving as the calibration standard. Gaseous products such as carbon monoxide (CO) and carbon dioxide (CO_2) were measured using gas chromatography with a flame ionization detector (FID). A sample was collected in a bag and manually injected into the gas chromatography sampling valve for the gas analysis. The study on methane conversion to various liquid products utilized ^{1}H NMR spectroscopy on a Bruker AV-NEO400 spectrometer operating at 400 MHz. After the reaction, 0.5 mL of the reaction mixture was combined with 0.08 mL of deuterium oxide and 0.02 mL of KHP, which was used as the internal standard at a concentration of 1 mM in an NMR tube. The concentration of the liquid products generated in the catalytic experiments was determined using the following formula:

$$\frac{n_x}{n_y} = \frac{I_x}{I_y} \times \frac{N_y}{N_x}$$

In this context, n_x denotes the molar concentration of KHP, while I_x refers to the integral area observed in the ^{1}H NMR spectra for KHP. Additionally, N_x represents the number of nuclei corresponding to the four equivalent protons of KHP that appear at 7.25 ppm. Likewise, n_y is derived using the same formula for the liquid product. I_y indicates the integral area of the resulting product, and N_y signifies the number of nuclei linked to the respective peak. During the NMR measurements, a solvent suppression program was run to minimize the signal originating from H_2O. Each catalysis experiment generated a 20 ml solution of left H_2O_2 and liquid products (methanol, formic acid, methyl peroxide, acetic acid). Ratios of peak areas of methanol, formic acid, or methyl peroxide to the peak area of KHP were calculated.

4.3 Result and Discussion

4.3.1 X-Ray Diffraction

The XRD spectrum of the zeolite well matches with the standard spectrum of Na-ZSM5 (JCPDS- 00-048-0135). With the loading of Au and Fe (0.1 wt% Fe and 0.1 wt% Au) over the catalyst surface, no changes were observed in the reflection pattern of the material, confirming the structural stability (Figure 4.1a). The absence of any extra peak other than the support confirms the good dispersion of the metals over the catalyst surface.

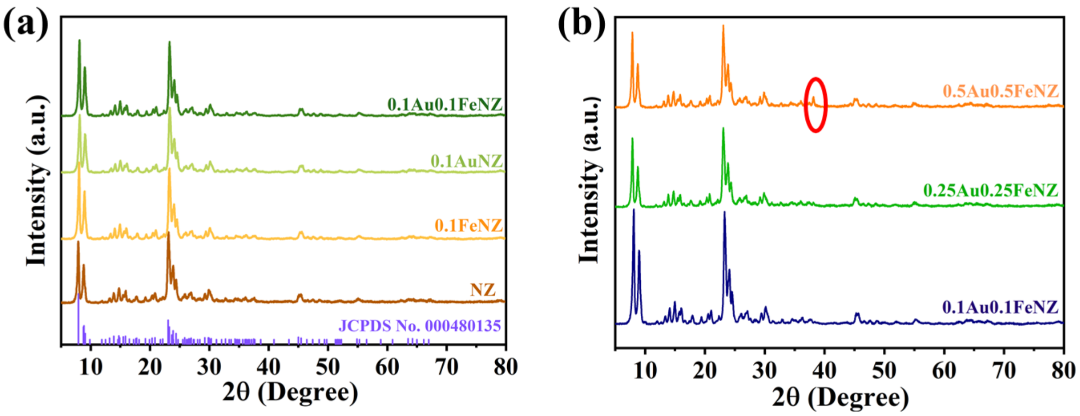

Figure 4.1 XRD spectrum of various catalysts.

Then, the amount of metal loading (Au and Fe) was investigated using the powder XRD. The XRD pattern of the 0.1Au0.1FeNZ does not contain any extra reflection than the support confirming the dispersion of the same over the catalyst surface. When the amount of each metal increased from 0.1 wt.% each to 0.25 wt.%, no change was observed in the reflection pattern of the material, indicating high stability. With a further increase in the metal loading, an extra peak was observed along with the zeolite peaks at 38.3° corresponding to Au metal. The peak generation is probably because of the increased size of the Au metal. However, no peak was observed for Fe metal or oxide.

4.3.2 Electron microscopy

Electron microscopy was utilized to investigate the morphological details of the synthesized material. The transmission electron microscopic images reveal the cubic morphology of the support. On the deposition of the material, no change in the morphology of the particles was observed, which confirms the material's stability under the synthesis conditions (Figure 4.2a-d).

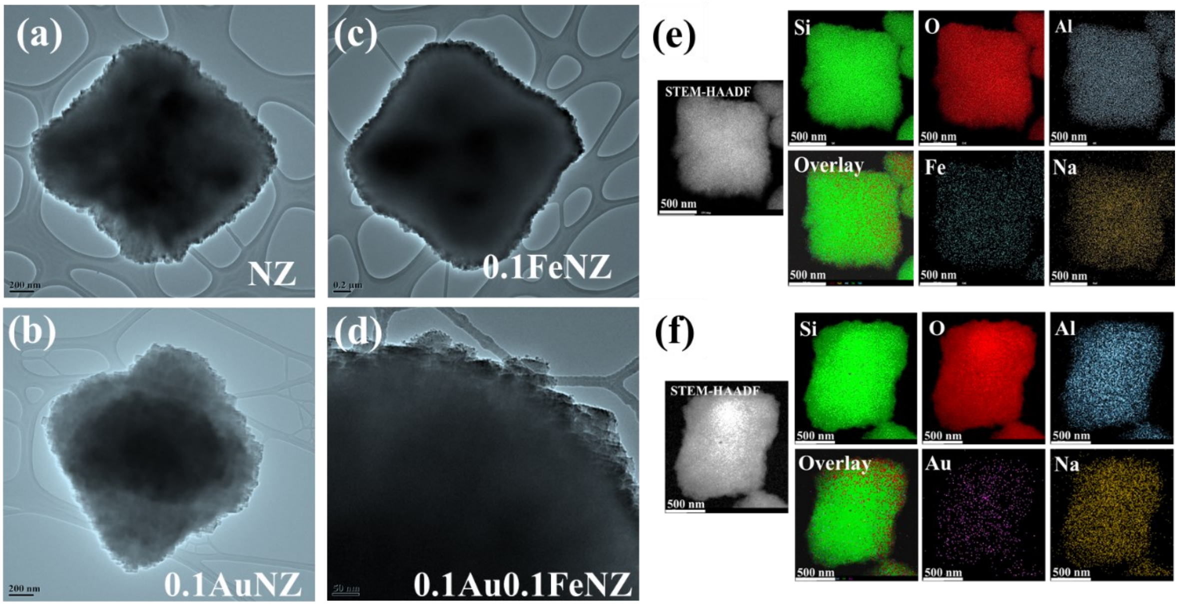

Figure 4.2 FESEM images of various catalysts (a-d), Elemental mapping of 0.1FeNZ (e), and 0.1AuNZ (f).

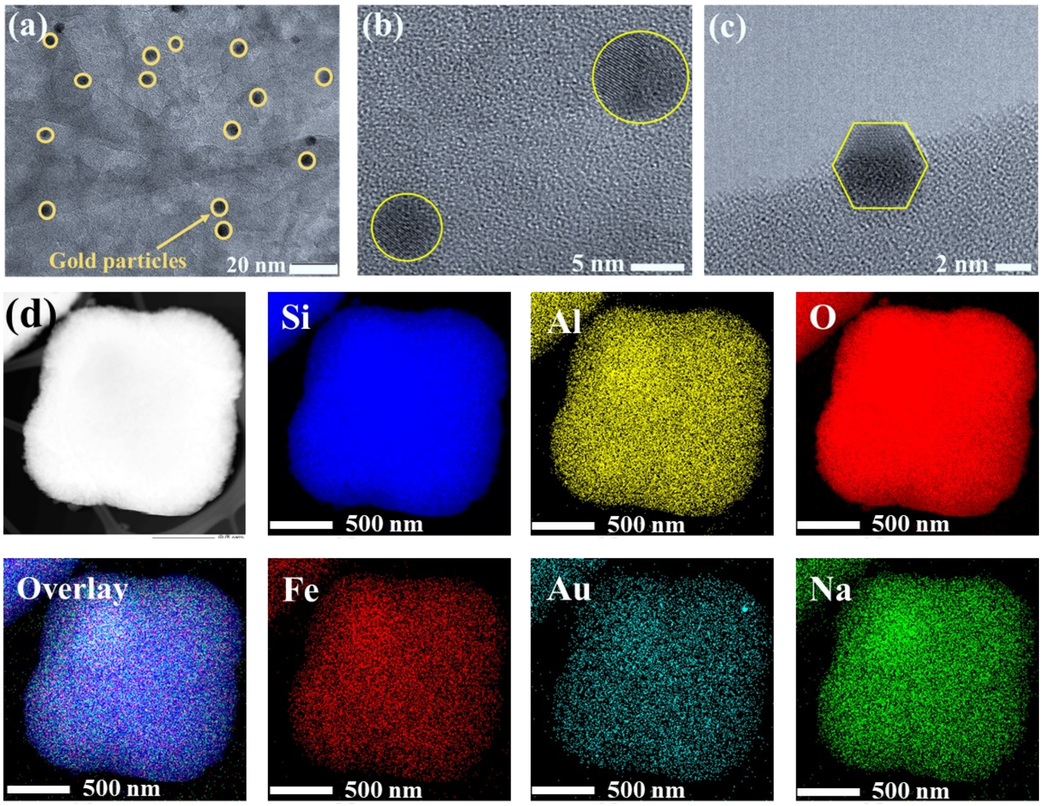

Figure 4.3 High resolution-TEM images of the 0.1Au0.1FeNZ (a-c), Elemental mapping of 0.1Au0.1FeNZ (d).

The elemental mapping of the monometallic catalysts indicated the absence of any cluster formation of Au and Fe on the catalyst's surface and confirmed the homogeneous distribution of the elements over the surface of zeolites (Figures 4.2e and 4.2f) The high-resolution TEM was utilized to visualize the small nanoparticles.

In the bimetallic catalyst (AuFeNZ), analysis reveals small Au nanoparticles (spherical and hexagonal) present on the surface of the zeolite support (Figures 4.3a-c). The presence of Fe was not observed due to the small size and the contrast difference between Au and Fe. The average size of the Au particles was observed to be 4-6 nm. STEM elemental mapping was further used to confirm the presence of the metals on the zeolite support. Figure 4.3d confirms the uniform distribution of the metals on the zeolite support in bimetallic catalysts.

As the presence of the Au and Fe was observed over the surface of the zeolite, it is worth exploring the interaction between the two, and the STEM line analysis was utilized for the same (Figure 4.4). The presence of signals from Au and Fe in the same position suggests a direct interaction between the two elements. This discovery has motivated us to further explore this interaction and determine whether it can result in a synergistic effect that enhances catalytic activity.

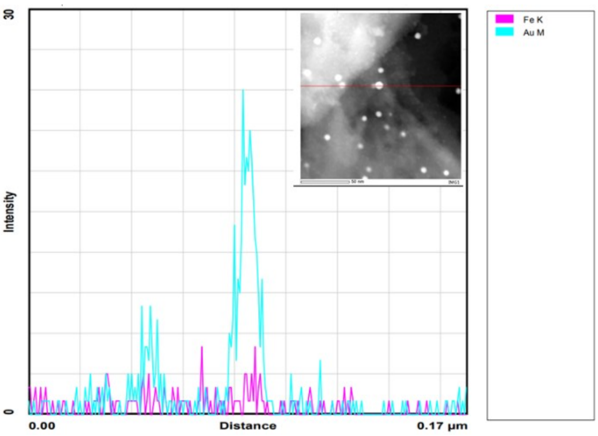

Figure 4.4 STEM line analysis of 0.1Au0.1FeNZ.

4.3.3 X-ray photoelectron spectroscopy

XPS is one of the best tools for investigating the oxidation state and electronic environment of the species on the material's surface. The XPS analysis of the monometallic and bimetallic catalysts was done to explore the active phase of the metals for methane oxidation (Figures 4.5 a and b). In the case of monometallic catalysts (0.1FeNZ), the Fe spectrum shows the peak at 711.5 eV and 714.6 eV corresponding to Fe $2p_{3/2}$, confirming the presence of Fe as 3+. In the case of a bimetallic catalyst (0.1Au0.1FeNZ), the peak shift to a lower binding energy value of 710.7 eV and 713.7 eV, indicating the electronic interaction between the Au and Fe over the catalyst surface, supporting the STEM line analysis.

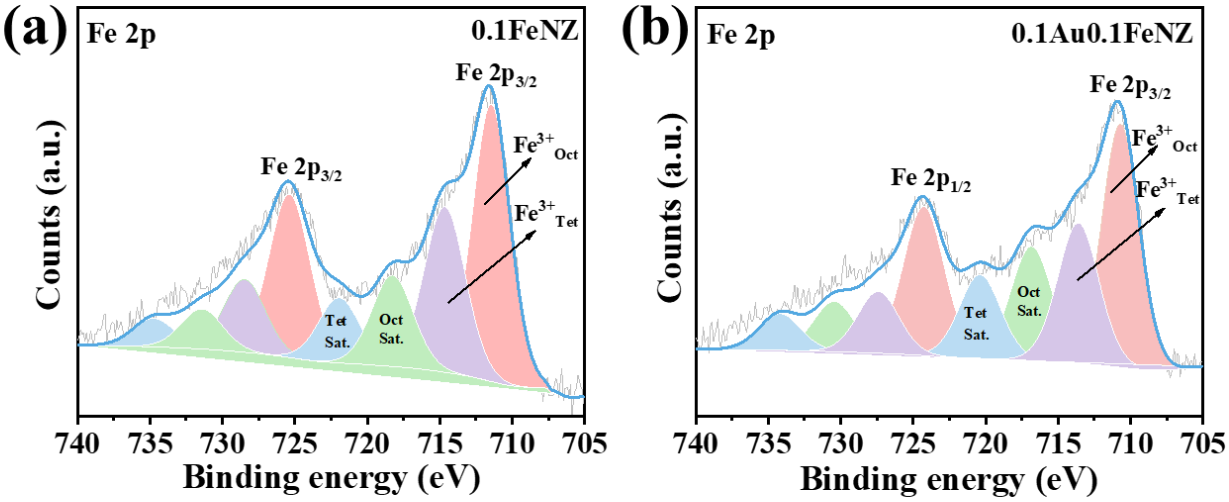

Figure 4.5 Fe 2p XPS spectrum of 0.1FeNZ (a), and 0.1Au0.1FeNZ (b) catalysts.

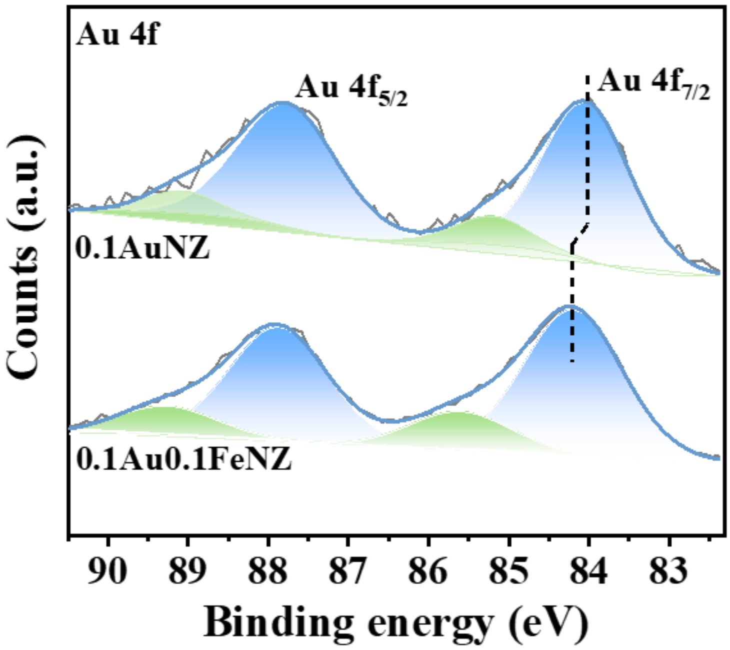

Figure 4.6 Au 4f XPS spectrum of 0.1AuNZ and 0.1Au0.1FeNZ catalysts.

In the case of Au 4f XPS analysis, the 0.1AuNZ, which showed the peak at 84.0 eV, indicates the metallic nature of the Au species in the material (Figure 4.6). In the case of a bimetallic catalyst, the Au $4f_{7/2}$ shifts to a higher binding energy value of 84.3 eV, indicating the charge transfer from the metal Au to Fe, further supporting the Fe 2p XPS analysis's electronic interaction analysis.

4.3.4 X-Ray Absorption Spectroscopy

X-ray absorption analysis was utilized to examine the local geometric and electronic environment of Fe over the catalyst surface. In the normalized XANES spectra (Figure 4.7a), the monometallic catalyst (0.1FeNZ, 0.5FeNZ) Fe absorption edge aligns with the Fe_2O_3 standard, confirming that the Fe in the sample is in the +3 oxidation state. In the case of bimetallic catalysts (0.1Au0.1FeNZ and 0.5Au0.5FeNZ), the Fe absorption edge also aligns with the Fe_2O_3 standard. However, the intensity shift between the monometallic and bimetallic catalysts indicated the interaction between the Au and Fe. A very small contribution from the Fe-Fe interaction was observed in the samples, revealing the single atomic nature of Fe species (majorly) in the catalysts.

Table 4.1 EXAFS fitting parameters for Fe K-edge.

Sample	Bond	N	R (Å)	σ^2	ΔE_0	R-factor
0.1FeNZ	Fe-O_1	6	1.840 +/- 0.011	0.003 +/- 0.002	-1.783 +/- 1.206	0.016
	Fe-Fe	6	3.117 +/- 0.138	0.035 +/- 0.027		
	Fe-O_2	6	3.467 +/- 0.027	0.003 +/- 0.002		
0.5FeNZ	Fe-O_1	6	1.933 +/- 0.017	0.003 +/- 0.004	-3.785 +/- 1.614	0.021
	Fe-Fe	6	2.913 +/- 0.031	0.011 +/- 0.005		
	Fe-O_2	6	3.559 +/- 0.017	0.003 +/- 0.004		
0.1Au0.1FeNZ	Fe-O_1	6	1.980 +/- 0.020	0.019 +/- 0.004	-1.749 +/- 1.521	0.017
	Fe-Fe	6	3.006 +/- 0.082	0.063 +/- 0.018		

	Fe-O$_2$	6	3.625 +/- 0.082	0.063 +/- 0.018		
0.5Au0.5FeNZ	Fe-O$_1$	6	1.875 +/- 0.010	0.004 +/- 0.002	-9.012 +/- 1.280	0.010
	Fe-Fe	6	2.937 +/- 0.028	0.005 +/- 0.004		
	Fe-O$_2$	6	2.596 +/- 0.021	0.007 +/- 0.002		
0.1Au0.1FeNZ	Fe-O$_1$	6	1.995 +/- 0.018	0.017 +/- 0.004	2.237 +/- 1.310	0.018
	Fe-Fe	6	3.102 +/- 0.048	0.035 +/- 0.008		
	Fe-O$_2$	6	3.850 +/- 0.634	0.132 +/- 0.183		

N: coordination number; *R*: bond distance; σ^2: Debye-Waller factor; ΔE_0: the inner potential correction. *R* factor: goodness of fit.

In the case of Figure 4.7b, it can be seen that with the lower content of Fe in the catalyst (0.1FeNZ and 0.1Au0.1FeNZ), the contribution from Fe-Fe is negligible, which increases with the higher weight loading (0.5FeNZ and 0.5Au0.5FeNZ) catalyst. However, a detailed analysis is needed for the complete picture of the same.

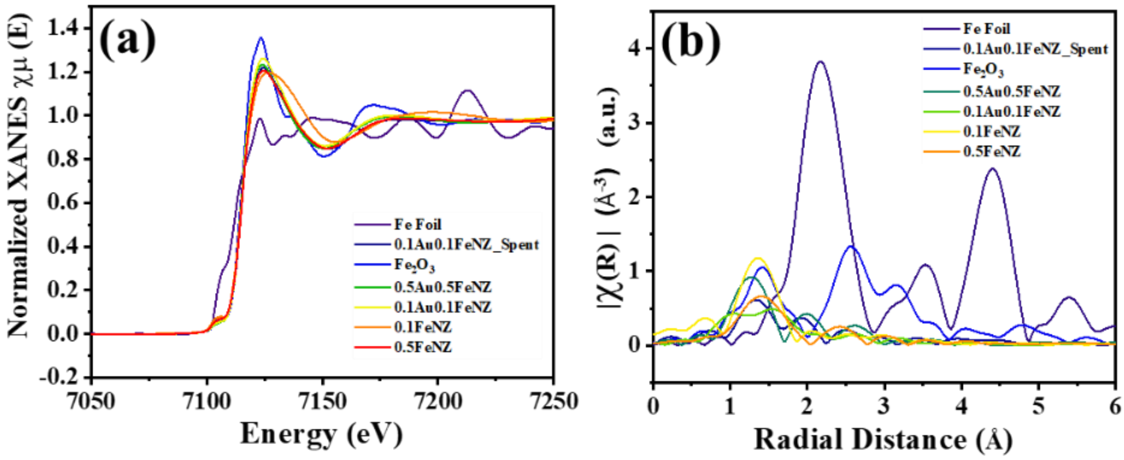

Figure 4.7 Normalized XANES spectra at Fe K-edge of various catalysts (a), Experimental χ(R) vs. R data of Au-Fe catalyst measured at Fe K-edge (b).

4.3.5 Solid-state NMR

^{29}Si and ^{23} Na solid state analysis was utilized to investigate the effect of metal deposition over the surface of Na-containing zeolite support. The resulting ^{29}Si spectrum shows three main resonances; specifically, the signals at −115 ppm and −112 ppm were attributed to two tetrahedral Si(0Al) sites, which are non-equivalent from a crystallographic standpoint, while the signal at −105 ppm was indicative of Si(1Al) structural units.[16–18] No significant changes were observed in the spectrum with the metal deposition (monometallic and bimetallic), indicating the structure stability of the material (Figure 4.8).

In the ^{23}Na NMR spectrum, no extra peak was observed after the metal deposition, confirming a similar geometric environment to the Na in the support and the metal-supported catalyst (Figure 4.9). ^{23}Na MAS confirms the presence of Na in the catalytic material, known for efficient methane activation, and will be discussed later in the theoretical section.

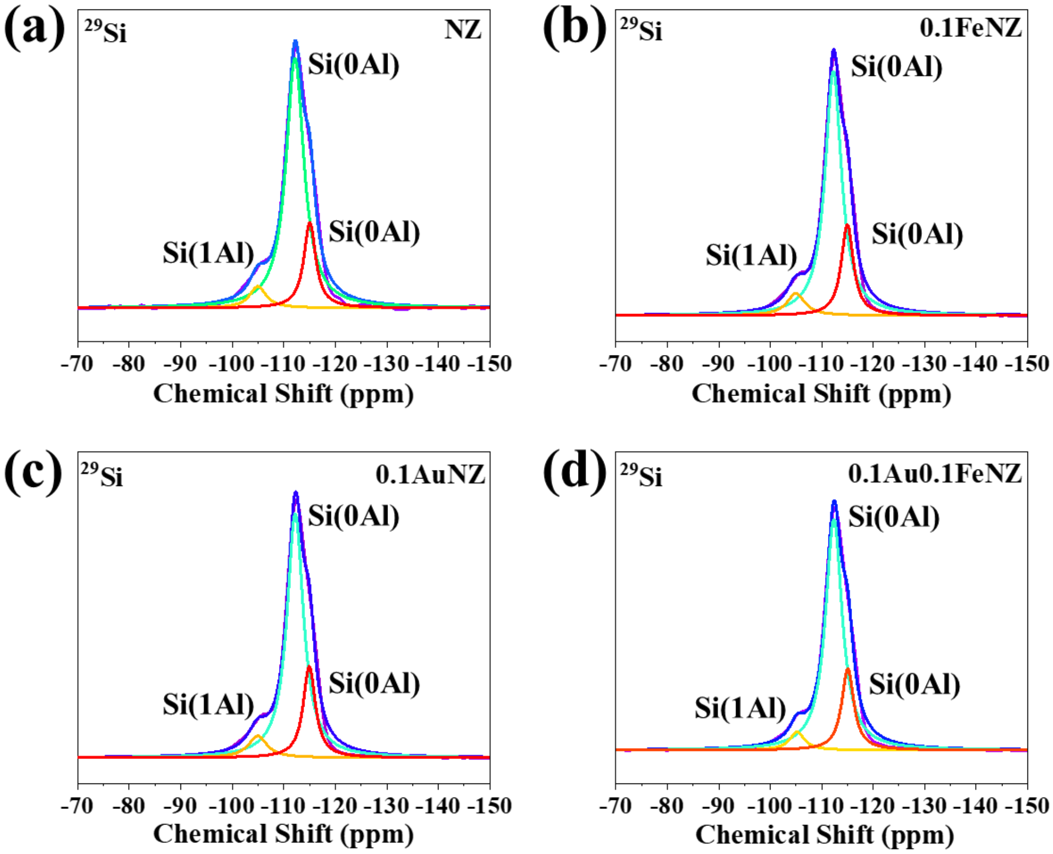

Figure 4.8 ^{29}Si MAS spectrum of various catalysts: NZ (a), 0.1FeNZ (b), 0.1AuNZ, (c), and 0.1Au0.1FeNZ (d).

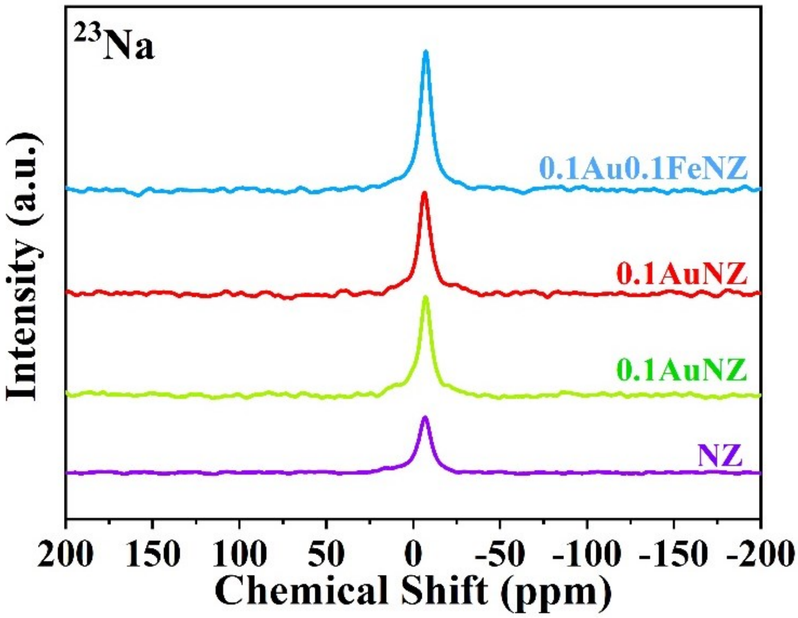

Figure 4.9 ^{23}Na MAS spectrum of various catalysts.

4.3.6 N_2 sorption analysis

The textural properties of the catalysts were assessed through surface area analysis. Figure 4.10 displays the N_2 adsorption/desorption isotherm for the different catalysts, all of which exhibited a type IV hysteresis loop, indicating the presence of mesopores in the material. The surface area of the zeolite support (NZ) was measured at 445 m^2/g. Minimal surface area reduction was observed following the deposition of the metals. The peak pore diameter was found to be less than 2 nm in all the materials (Table 4.2).

Table 4.2 N_2 adsorption-desorption analysis data of various catalysts.

Catalyst	BET Surface area (m^2/g)	Pore volume (cm^3/g)	Peak pore diameter (nm)
NZ	445	0.23	1.47
0.1FeNZ	431	0.22	1.47
0.1AuNZ	408	0.22	1.47
0.1Au0.1FeNZ	418	0.21	1.47

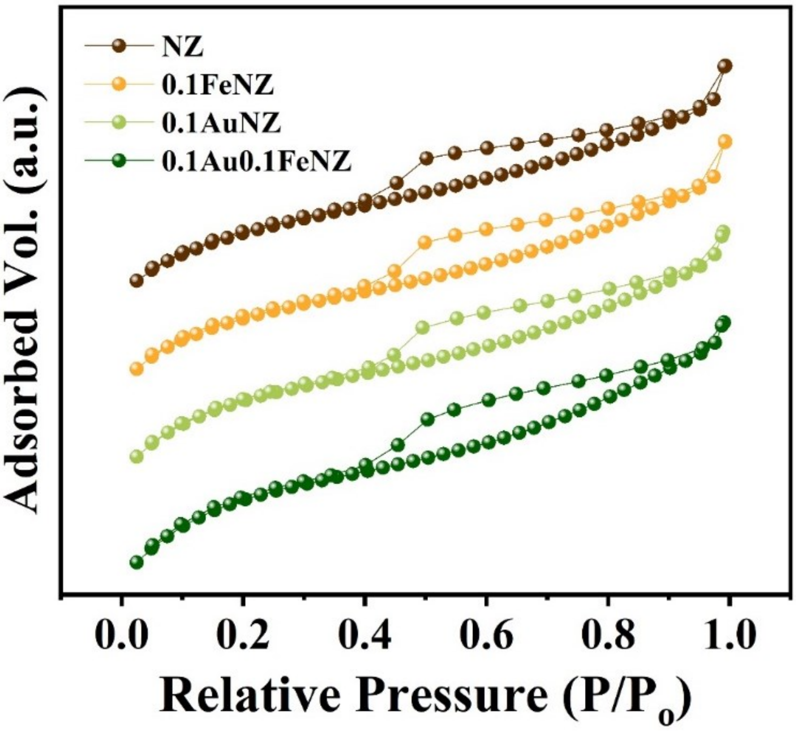

Figure 4.10 N_2 adsorption-desorption isotherm of various catalysts.

4.3.7 Methane oxidation to Formic acid

The activity comparison of various catalysts (Figure 4.11a) found that the support (NZ) only produced 331 µmol of the oxygenates because of the presence of Al and Na in the material. When Fe was deposited over the NZ, it was used for methane oxidation, which produced 701 µmol of the oxygenates. While 0.1AuNZ produced 541 µmol of the oxygenate, 0.1Au0.1FeNZ produced 4264 µmol of the oxygenates within 30 minutes of the reaction with 95% selectivity for the liquid oxygenates (Figure 4.12a). Selectivity for the formic acid increased from 60 to 89% in the case of 0.1Au0.1FeNZ when compared to NZ. The activity is higher than reported so far under the same reaction condition. The highly dispersed Au nanoparticles interact with Fe atoms and result in higher activity because of the synergistic effect of the two metals. Rising temperatures initially boost productivity from 50 to 60 °C (Figure 4.11b), but further increases lead to a decline due to the decomposition of H_2O_2 (Figure 4.12b). Additionally, higher temperatures promote the production of gaseous by-products, compromising formic acid selectivity.

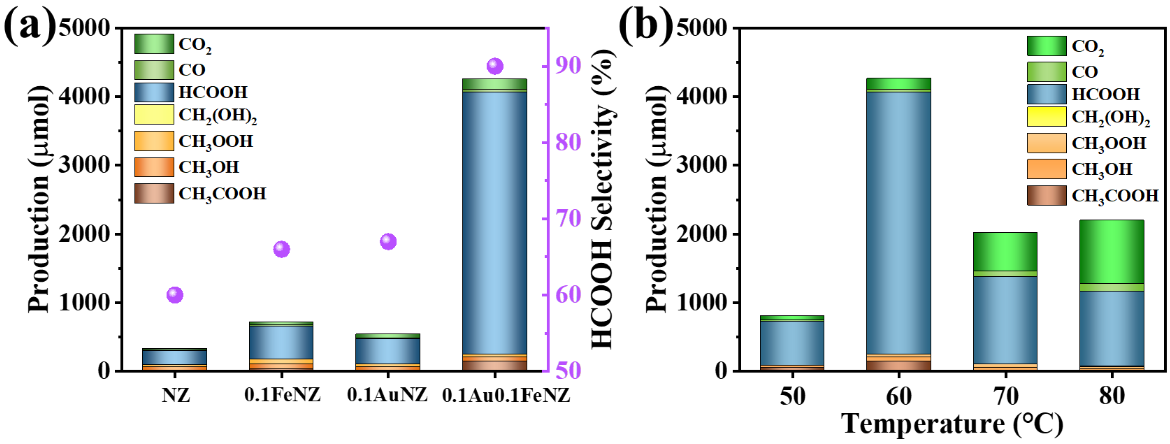

Figure 4.11 Catalytic activity of, various catalysts (a), and 0.1Au0.1FeNZ at 50-80 °C (b), in batch process. Reaction Conditions: 50 mg catalyst,10 bar CH_4, 0.5 h, 900 rpm, 5 M H_2O_2 (20 mL)

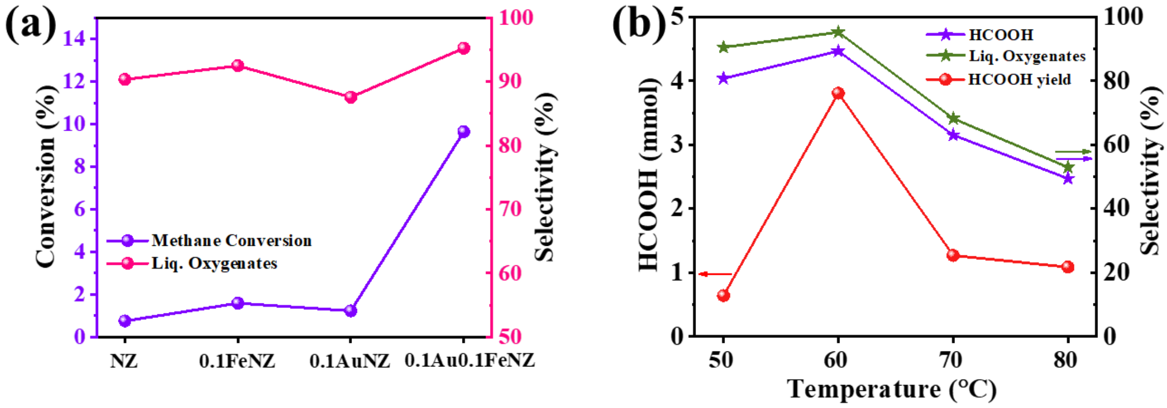

Figure 4.12 Catalytic activity: of various catalysts (a) and of 0.1Au0.1FeNZ at 50-80 °C (b). Reaction Conditions: 50 mg catalyst, 10 bar CH_4, 0.5 h, 900 rpm, 5 M H_2O_2 (20 mL)

The pressure optimization confirms the 10 bar as the best-suited pressure for this one-step methane oxidation reaction (Figure 4.13a). However, the oxidant amount analysis affirms that productivity correlates directly with the quantity of oxidant in the system and the cost-effectiveness of peroxide utilization (Figure 4.13b). Moreover, the substantial production of oxygenates from greenhouse gases through this method presents opportunities for researchers to harness methane effectively.

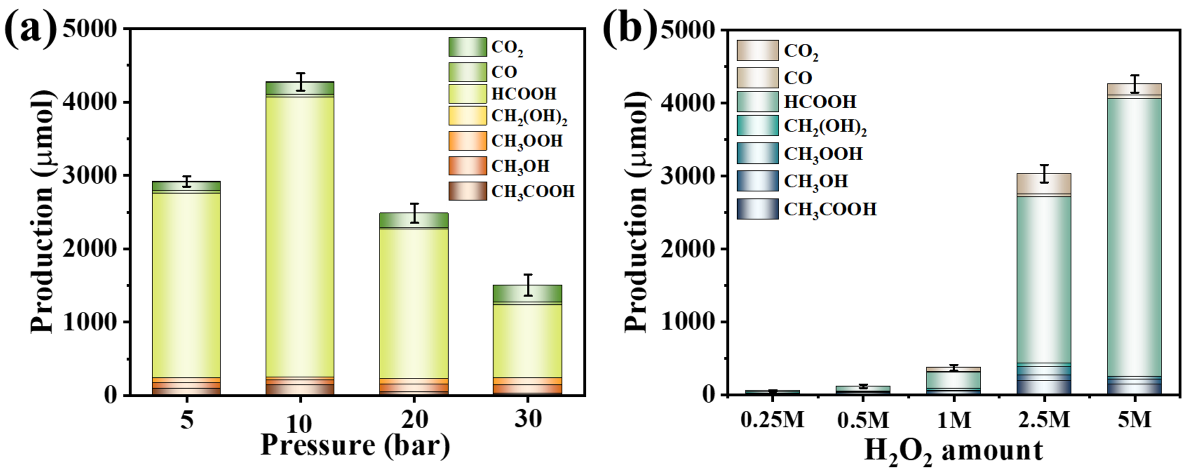

Figure 4.13 Catalytic activity of various catalysts at different reaction conditions in the batch process. Reaction Conditions: 50 mg catalyst. 0.5 h, 60 °C, 900 rpm.

Controlled experiments demonstrate that negligible conversion occurred when no catalyst was employed. Moreover, the absence of H_2O_2 resulted in no observable oxygenate production during the reaction, affirming peroxide as a critical oxidant in the product formation. Similarly, when methane was not introduced in the reaction, no product was detected (Table 4.3).

Table 4.3 Catalytic activity of various catalysts under controlled experiments.

S. No.	Catalyst	Reaction feed	Products (µmol)
1	0.1Au0.1FeNZ	CH_4+H_2O_2	4264.0
2	0.1Au0.1FeNZ	N_2+H_2O_2	0
3	0.1Au0.1FeNZ	CH_4+No oxidant	0
4	No Catalyst	CH_4+H_2O_2	0

Reaction Conditions: 50 mg catalyst, 10 bar CH_4, 0.5 h, 900 rpm, 5 M H_2O_2 (20 mL)

From Figure 4.12 it is clear that the catalytic activity is driven by the synergistic effect of Au and Fe supported over the zeolite surface. Altering the weight loading of gold (Au) and iron (Fe) on the NZ catalyst demonstrates that achieving an equal amount of Au and Fe yields the optimal outcome, as indicated in Table 4.4.

Table 4.4 Catalytic activity data of various catalysts in batch process.

S. No.	**Catalyst**	**Products (µmol)**								**HCOOH Sel. (%)**
		CH_3COOH	**CH_3OH**	**CH_3OOH**	**$CH_2(OH)_2$**	**HCOOH**	**CO**	**CO_2**	**Total**	
1	NZ	2.1	2.3	3.2	4	23	2.5	3.3	40.4	56.9
2	0.1Au0.1FeNZ	7.3	6.5	7.4	11.1	105.8	2.3	8.1	148.5	71.2
3	0.25Au0.25FeNZ	25.3	13.7	7.1	15.9	154.8	2.5	11.2	230.5	67.2
4	0.25Au0.5FeNZ	14.3	11.5	3.9	5.8	65.2	7.1	53.1	160.9	40.5
5	0.5Au0.25FeNZ	11.7	11.0	3.8	20.1	95.1	2.8	14.4	158.9	59.9
6	0.5Au0.5FeNZ	12.9	12.2	3.5	13	121	8.7	47.4	218.7	55.3

Reaction Conditions: 50 mg catalyst. 0.5 h, 60 °C, 10 bar CH_4, 0.25 M H_2O_2 (20 mL).

When the metal loading increased (Table 4.4), productivity was enhanced, leading to a decrease in specific yield (mmol/g_{Au+Fe}). This suggests that finding the right balance between the two metals is crucial for maximizing efficiency. The presence of highly dispersed Au nanoparticles interacting with Fe atoms results in a higher activity due to the synergistic effect between the two metals, contributing to the observed performance improvements.

The catalytic activity was examined by the NMR spectroscopy. Figure 4.14 shows the spectrum of the reaction mixture of the batch process comprising the liquid oxygenates discussed above.

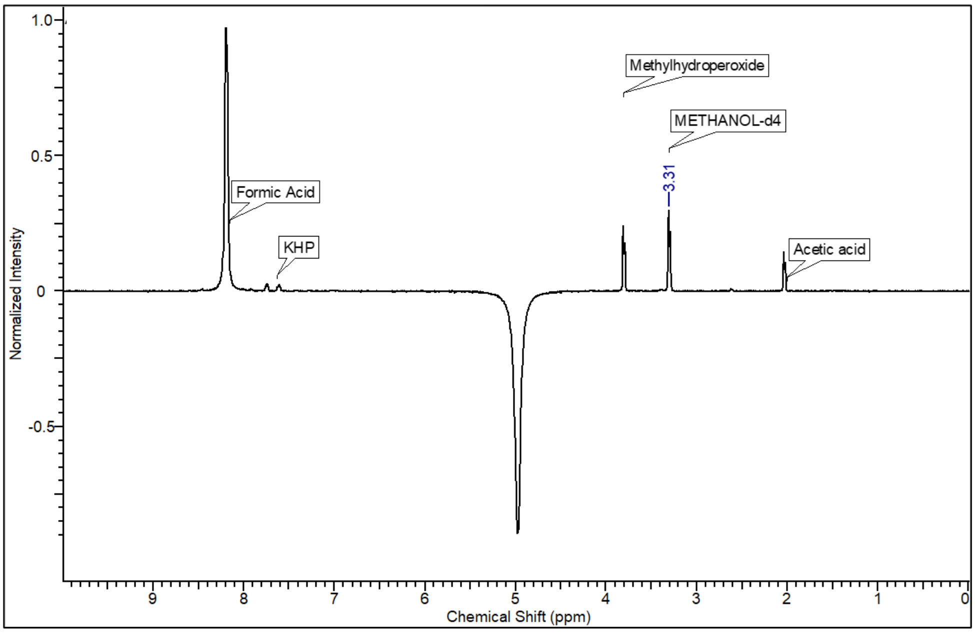

Figure 4.14 ^{1}H NMR profile of reaction mixture in H_2O+D_2O (NMR solvent) using KHP as internal standard. Reaction conditions: 50 mg 0.1Au0.1FeNZcatalyst. 0.5 h, 60 °C, 5 M H_2O_2 (20 mL). Chemical Shift (ppm) 2.0 (Acetic acid), 3.3 (Methanol), 3.8 (Methylhydroperoxide), 7.6 (KHP) and 8.3 (Formic acid)

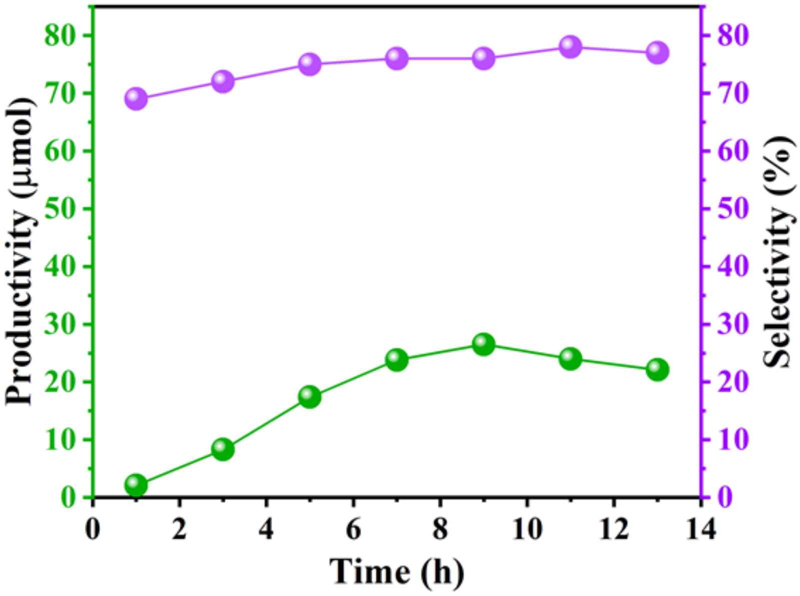

Figure 4.15 Catalytic activity of 0.1Au0.1FeNZ in the continuous flow process.

The entire catalysis process was transformed into a continuous flow system operating under ambient pressure conditions. We achieved a significant production of formic acid by applying the reaction conditions from our recent work.[19] The production increased steadily for up to 9 h of the reaction but then experienced a slight decrease, possibly due to product accumulation on the catalyst surface (Figure 4.15). Nonetheless, the sustained activity over the 9 h indicates the stability of the active sites in the synthesized catalytic material is phenomenal, considering the benign condition of the methane oxidation process. The comparison of our activity data with existing literature clearly demonstrates that our synthesized catalyst yields the best results under mild conditions (Table 4.5).

Table 4.5 Literature comparison of methane conversion under mild conditions using H_2O_2 as oxidants.

Catalyst	**Selectivity (%)**		**Products amounts (µmol)**					**Reaction conditions**				**Ref.**
	Oxy.	**HCOOH**	**CH_3OH**	**CH_3OOH**	**HCOOH**	**CO_2**	**Oxy.**	**t (h)**	**P (bar)**	**T (°C)**	**H_2O_2 (M)**	
Pd_1O_4/ZSM-5	96.2	56	7.39	39.4	60.8	4.2	107.6	0.5	30	50	0.5	[20]
	87.9	96	10.9	1.74	338.4	48.2	351.1	0.5	30	95	0.5	
Fe/MOR	~91	~20	~40	~25	~100	~25	~240	1	30	50	0.5	[10]
	~88	~80	~25	~5	~250	~40	~280	1		100		
0.03wt.% Fe/ZSM-5(66)	94	86	295	83	3832	268	4210	0.5	30	80	5	[5]
	95.1	84.4	6.9	51.1	457	26.4	515	0.5	30	80	0.5	
Fe-ZIF-8-0.28	96.8	96.8	0.1	1.0	32.6	-	33.7	0.5	30	50	0.5	[21]
0.1Au0.1FeNZ	95.2	89.3	63.2	42	3808	159	4264	0.5	10	60	5	**This Work**
0.1Au0.1FeNZ	97	79	1	1.2	18.8	-	21	9	1	80	9	**This Work**

4.3.8 Spent Catalyst Analysis

After the batch reaction, the catalyst was dried and analyzed using various characterization techniques. In this case of XRD, the spectrum resembles the fresh catalyst as no loss of the peaks was observed in the same (Figure 4.16a). It confirms no deformation in the material's structure, indicating the catalyst's stability. The XPS was utilized to examine the electronic environment of the active species over the catalyst surface after the reaction (Figure 4.16b-c). XPS also confirmed the presence and retention of the material in the active sites. These analyses represents the bimetallic catalyst's high stability and durability resulting from active site regeneration.

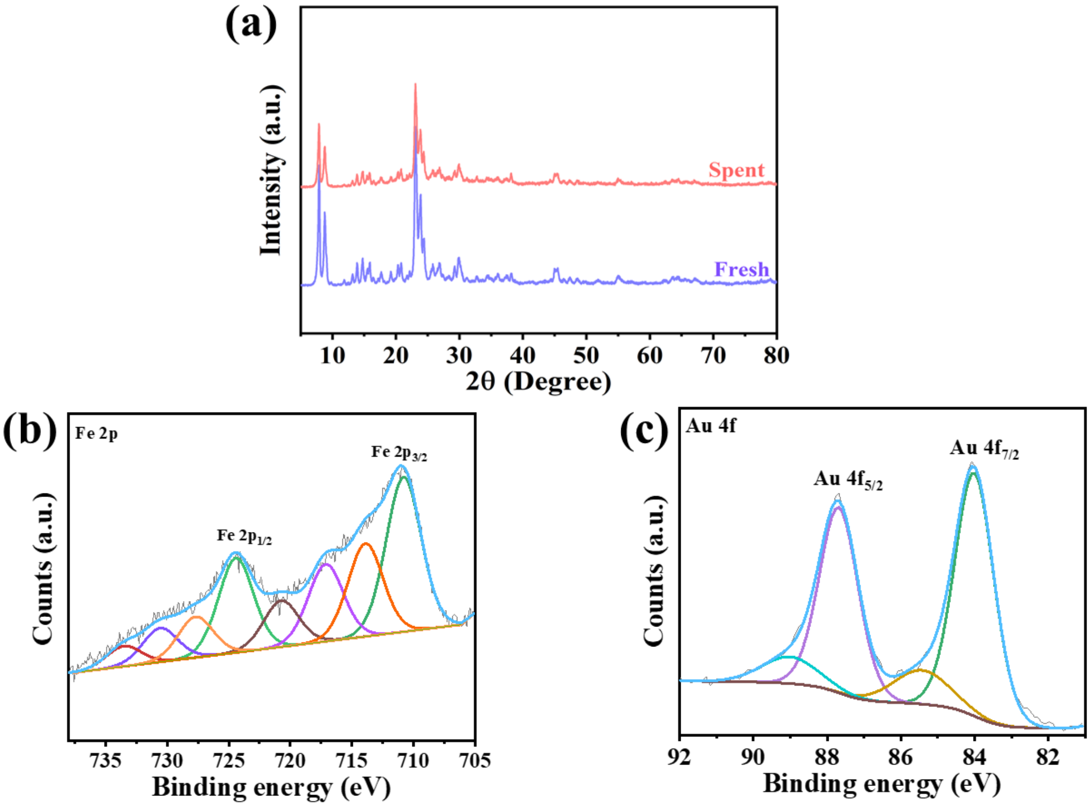

Figure 4.16 XRD spectrum (a), Fe 2p XPS spectrum (b), Au4f spectrum of spent 0.1Au0.1FeNZ (c).

4.4 Theoretical Calculations

Methodology

Fractional coordinates of the MFI zeolite structure were obtained from the Materials Studio 2020 (Biovia, San Diego) database with unit cell parameters: a = 20.022 Å, b = 19.899 Å, c = 13.383 Å and $\alpha = \beta = \gamma = 90°$). From the 96 T sites of the zeolite, two silicon (Si^{4+}) atoms were replaced from the T7 and T12 sites to introduce Aluminium (Al^{3+}) atoms into the framework [22], with charge compensation by the addition of Na^+ positioned in the main 10-membered ring (MR) referred as Na' and the other at a relatively stable position (I2, referred as Na'') connected to the 10 MR ring (Figure 4.16a) as suggested by Zhen et al. and Petr Nachtigall et al.[21,22] The proposed active site for methane oxidation consists of a mononuclear iron-oxide and cationic gold (Au^+ZSM-5) species anchored within the MFI framework.[22,24,26] In this, the iron cluster and Au^+ ion are anchored on the framework Al position at T7 and T12, respectively (Figure 4.16b). First principal calculations were performed using the periodic plane-wave Density Functional Theory (DFT) code available in the Vienna Ab initio Simulation Package (VASP, version 6.2.2).[27,28] The plane wave basis set was expanded to an energy cutoff value of 400 eV, and the exchange-correlation function was described using the Perdew-Burke-Ernzerhof (PBE) functional with generalized gradient approximation (GGA). Core electron potentials are approximated with the projector augmented wave (PAW) pseudopotential.[29,30] For the Fe atom, Hubbard U correction is applied in the DFT+U framework, wherein U-J = 4 was set for Fe, as suggested by Rohrbach et al.[31] To account for Van der Waals interactions, the Grimme DFT-D3 method was implemented.[32] For geometry optimization, force and energy convergence criteria were set at 0.05 eV/Å and 10^{-6} eV, respectively, and a single k-point was employed. All calculations were performed spin polarised with a Gaussian smearing of 0.02 eV. Transition state (TS) structures on the reaction coordinate are identified using the climbing image nudged elastic band (CI-NEB) method.[33,34] and applying the same force and energy convergence criteria. Activation energy and reaction energy were calculated as the difference between the TS and initial reactant state structures and the difference between the reactant and product state structures, respectively.

Au (111) surface is modeled with four metal layers and a vacuum of 15 Å in the perpendicular z-direction. The top two layers of the surface model are allowed to relax to mimic the surface relaxation process, while the bottom two are fixed to the bulk lattice coordinates. A Monkhorst-Pack k-point mesh 3x3x1 is used to sample the irreducible Brillouin zone.[35] The rest of the method follows the same parameters of pseudopotential, energy cutoff, force and energy convergence criteria, and TS search as described for the zeolite structure.

Additionally, we considered Au_{38} nanoparticles as catalytic species to explore their catalytic properties in methane oxidation and activation of hydrogen peroxide.

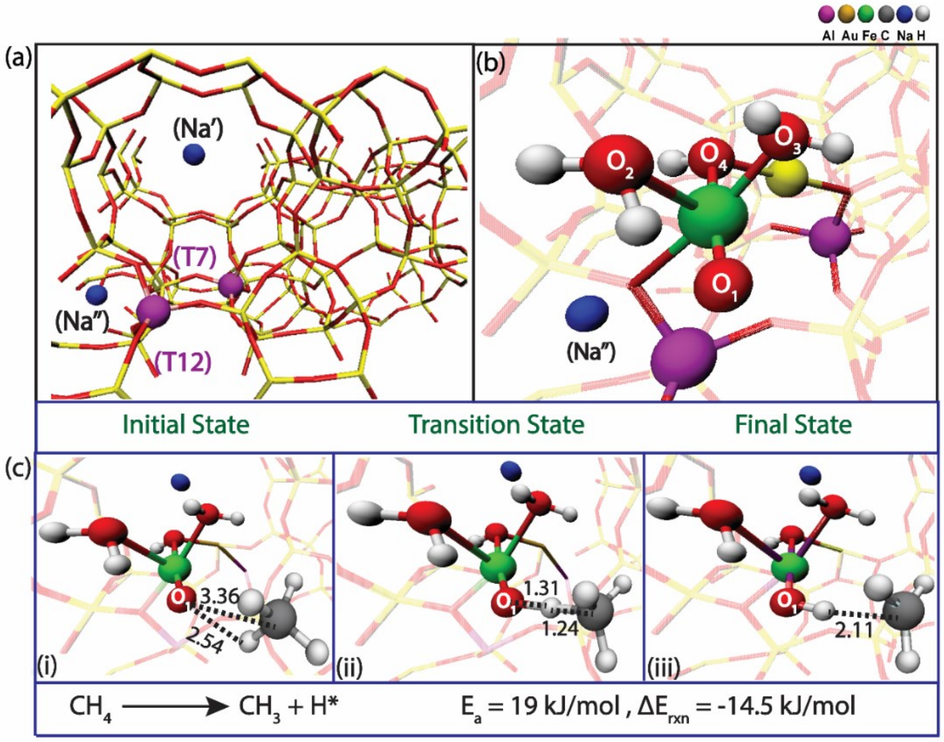

Figure 4.17 Structure of Na-ZSM-5 (a), Fe-oxide cluster along with cationic gold species anchored on Al sites within the zeolite framework (b), The DFT-simulated pathway over the AuFeNZ for methane activation (c), (i) optimized initial state (ii) transition state, and (iii) final state.

Result and discussion

Methane oxidation reaction to produce formic acid could take place on a bi-functional active site within the zeolite pore. This could be a mononuclear Fe cluster anchored on the Al-O acidic site, as suggested by Weckhuysen and co-workers,[22] which lies in close vicinity of cationic gold species (AuFeNZ) as modeled in Figure 4.17b. The active centre (Fe-O) on the iron oxide cluster consists of a coordinatively unsaturated oxygen atom, O_1 (Figure 4.17b), available for methane activation. The active site is generated during the oxidation process with hydrogen peroxide, as described by Weckhuysen and co-workers.[22,25] DFT simulations estimated 19 kJ/mol activation energy with -14.5 kJ/mol exothermicity in the methane activation step (Figure 4.17c).

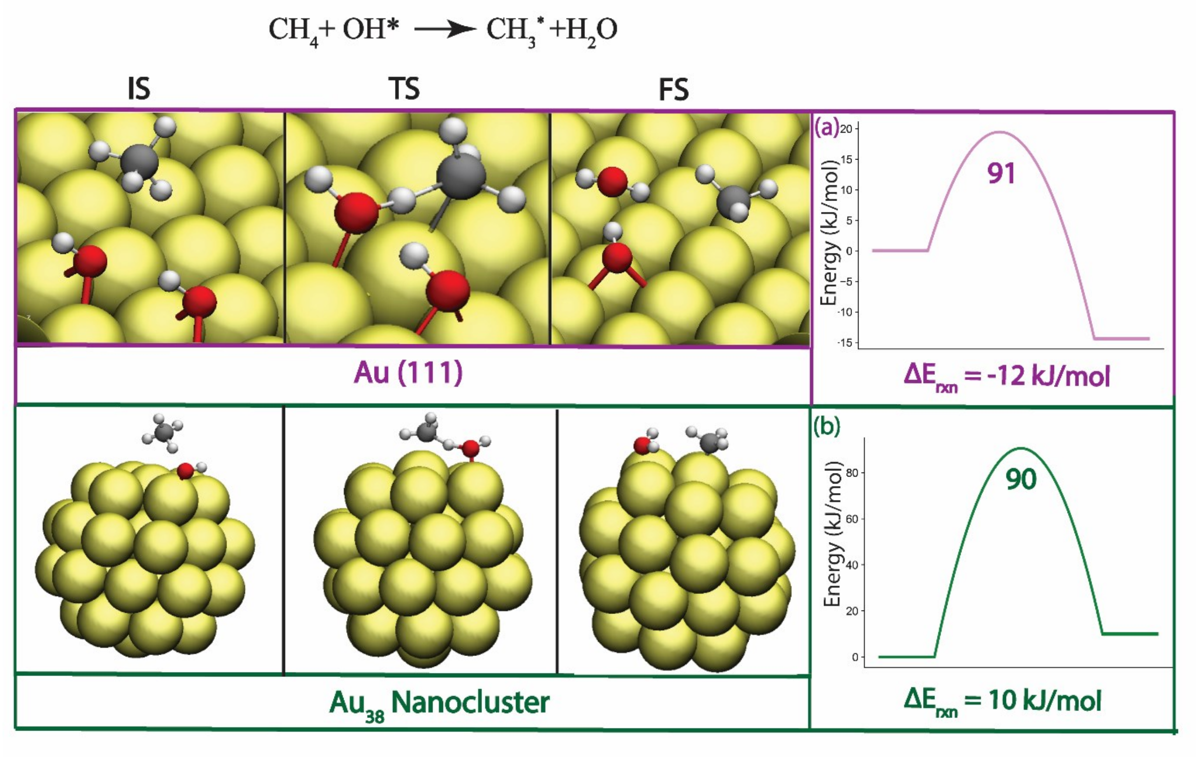

Figure 4.18 The DFT-simulated pathway over the Au (111) (a) and Au_{38} nanoparticle (b) for the C-H bond activation in methane to CH_3 radical.

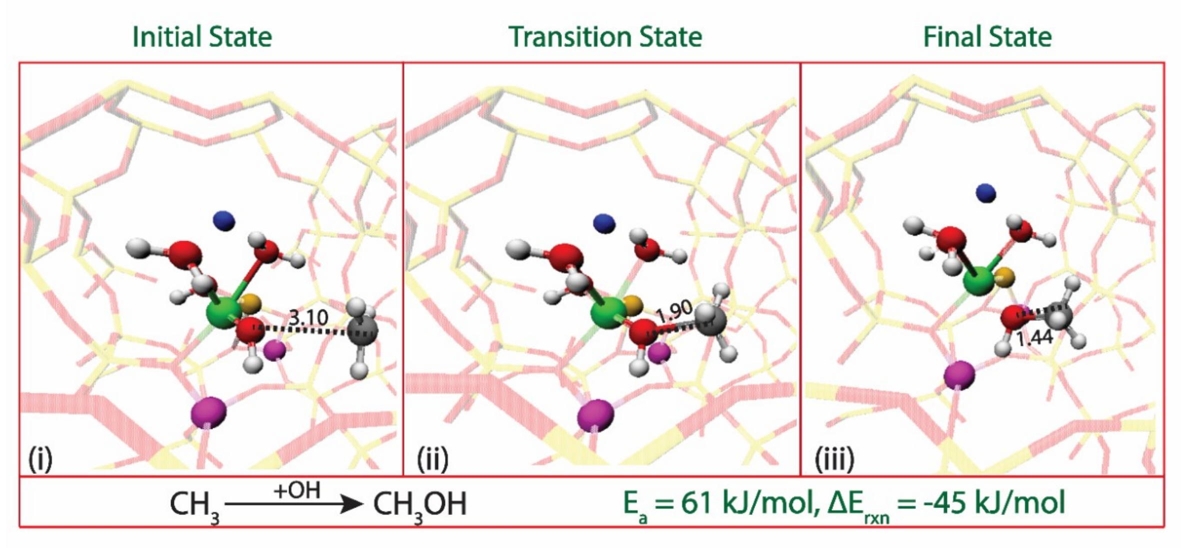

Figure 4.19 The DFT-simulated pathway for methanol formation in AuFeNZ catalyst.

Alternatively, Au nanoparticles in HZM-5 could also activate methane, as suggested by Hutching and co-workers.[26] However, methane activation on Au (111) and Au_{38} nanoparticles has a significantly higher barrier (E_a = 91 and 90 kJ/mol, respectively), as represented in Figure 4.18.

Since Fe-O sites are available for methane activation, it is more likely to be the active centre. Post activation on the Fe-O site, a methyl radical (CH_3) is produced, which may combine with the available hydroxyl radical (OH) generated from hydrogen peroxide decomposition.[36,37] This is likely to be a barrierless step, as also suggested in the work of Weckhuysen and co-workers in methane conversion to methanol on Cu-Fe/ZSM-5 catalyst in the presence of hydrogen peroxide.[22] CH_3OH can also be produced in zeolite pores by combining the generated CH_3 radical with OH*. After the desorption of methanol, the proposed active site O_1 can be regenerated again.

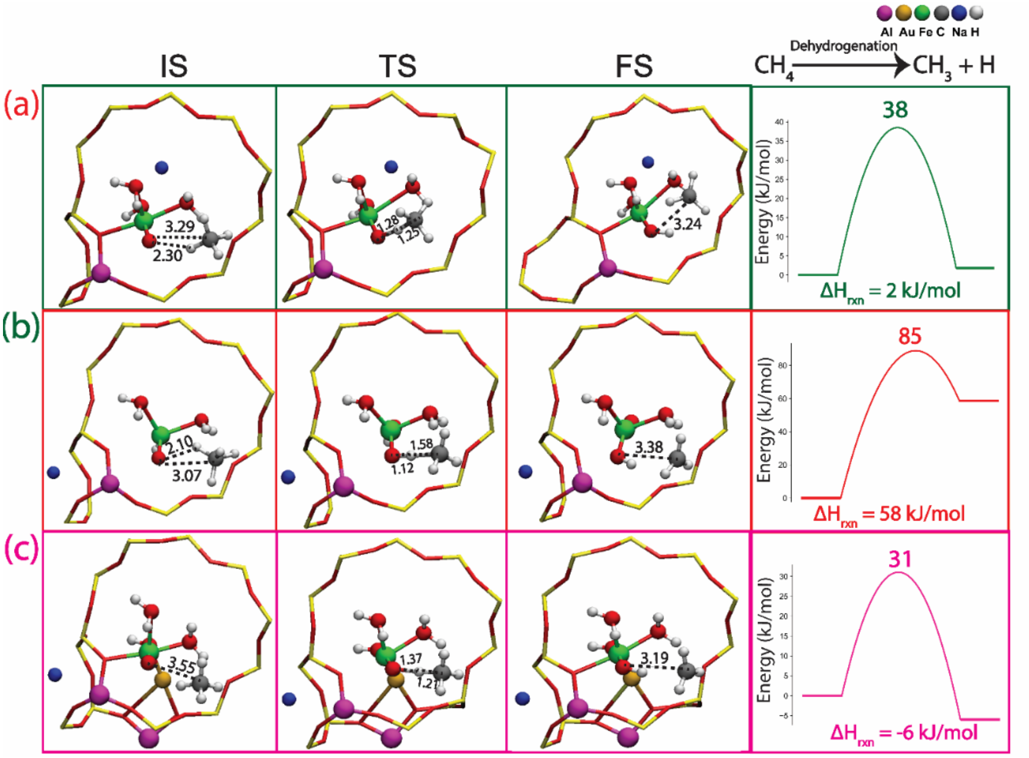

Figure 4.20 The DFT-simulated calculation for the C-H bond activation of the CH_4 over the mononuclear Fe species anchored in zeolite: The optimized initial state (IS), transition state (TS), and final state (FS) for methane activation in Fe Na'-ZSM-5 (a), within zeolite framework of Fe Na''-ZSM-5 (b), within zeolite Au/Fe Na''-ZSM-5 (c). For clarity, only the active sites and the zeolite ring are depicted.

The electronic effects of Na and Au in the vicinity of the active site are expected to greatly influence this methane activation at O_1. Figure 4.20 shows three different sets of calculations by removing the Au atom, changing the position of Na' to Na'', and/or removing the Na atom. In all three cases, the methane activation barrier at the O_1 site varies from 31 to 85 kJ/mol.

Thus, the synergistic interaction between the Au and Na atoms facilitates methane activation, resulting in a methyl radical and hydroxyl group attached to the Fe center.

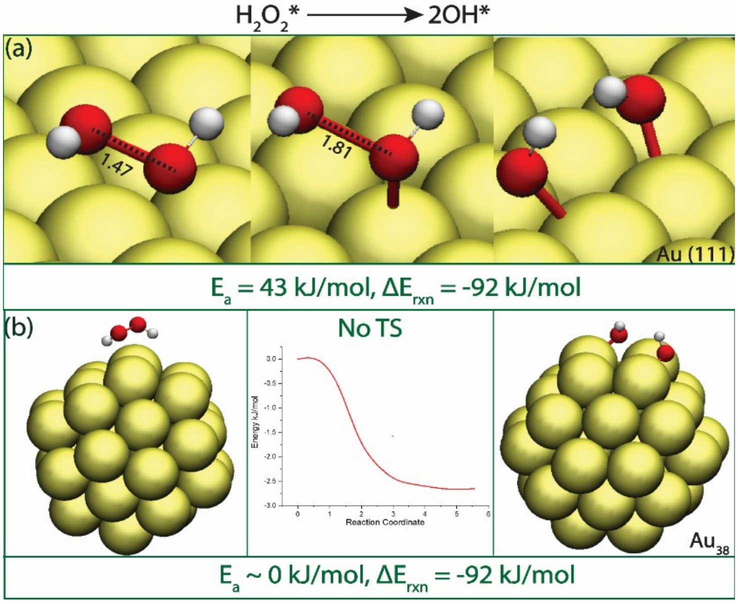

Figure 4.21 The DFT-simulated calculation for the H_2O_2 dissociation into OH radicals: The optimized initial state (IS), transition state (TS), and final state (FS) over the slab Au (111) (a), Radical (OH) formation Au_{38} nanoparticle (b).

Following the formation of methanol, there are two available sites to produce formic acid: on the iron oxide cluster itself or on the surface of Au nanoclusters. Hydrogen peroxide decomposition is likely to produce OH species on the surface of Au nanoparticles, as suggested by Davis and co-workers.[38] DFT simulations suggested a barrierless path for H_2O_2 decomposition to form surface hydroxyls on Au_{38} nanoclusters, as shown in Figure 4.21.

Surface hydroxyl on the Au surface will likely facilitate O-H and C-H activation reactions in methanol to form formic acid,[38–41] Figure 4.22. Interestingly, all steps leading to formic acid formation are highly exothermic, with activation barriers of less than 30 kJ/mol on the Au (111) surface, Figure 4.23a and Figure 4.22. Thus, a path exists for formic acid production from methanol on Au nanoparticles. Alternatively, as shown in Figures 4.23b and c, methanol could yield formic acid on iron oxide clusters. Methanol decomposes to hydrated methane diol $CH_2(OH)_2$ in two elementary steps with activation energies <30 kJ/mol. Methane diol is spontaneously transformed into formaldehyde,[42] which is subsequently oxidized (E_a <10 kJ/mol) to HCOOH by the O_1 species on the iron oxide cluster, Figure 4.23c.

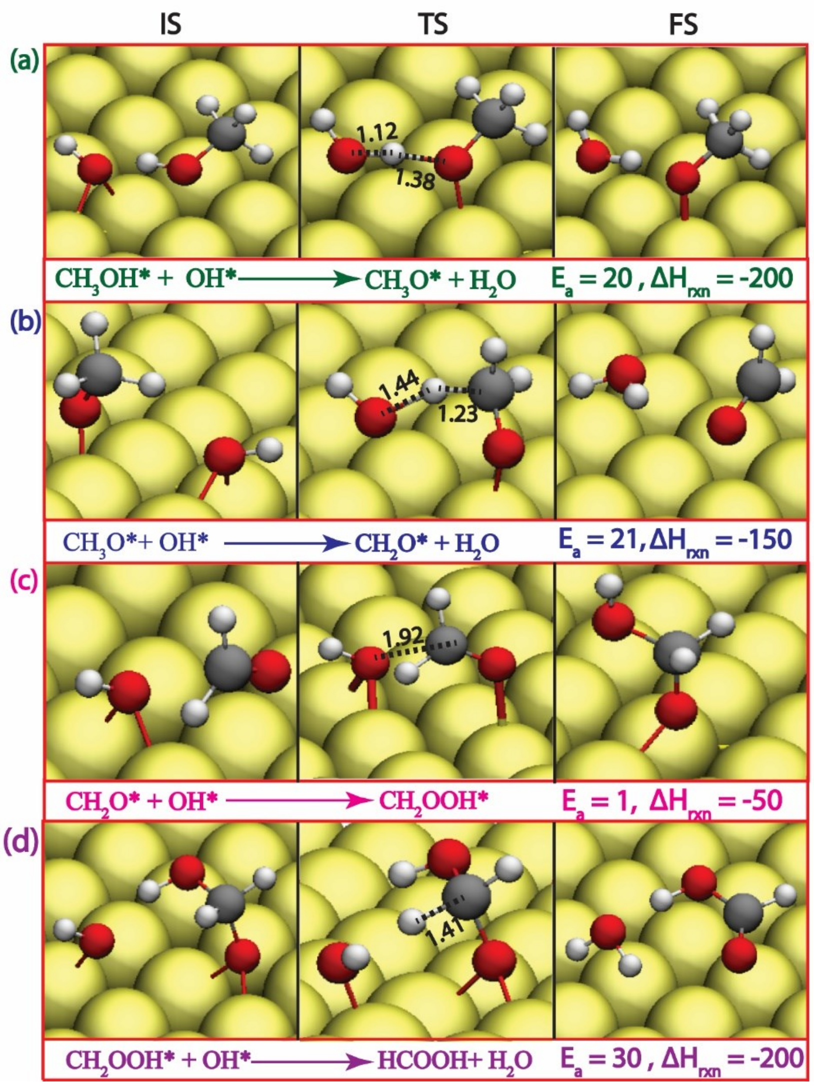

Figure 4.22 The DFT-simulated pathway over the Au (111) for the oxidation of CH_3OH to HCOOH using H_2O_2 as the oxidant (a-d). For clarity, only the top layer of metal is depicted.

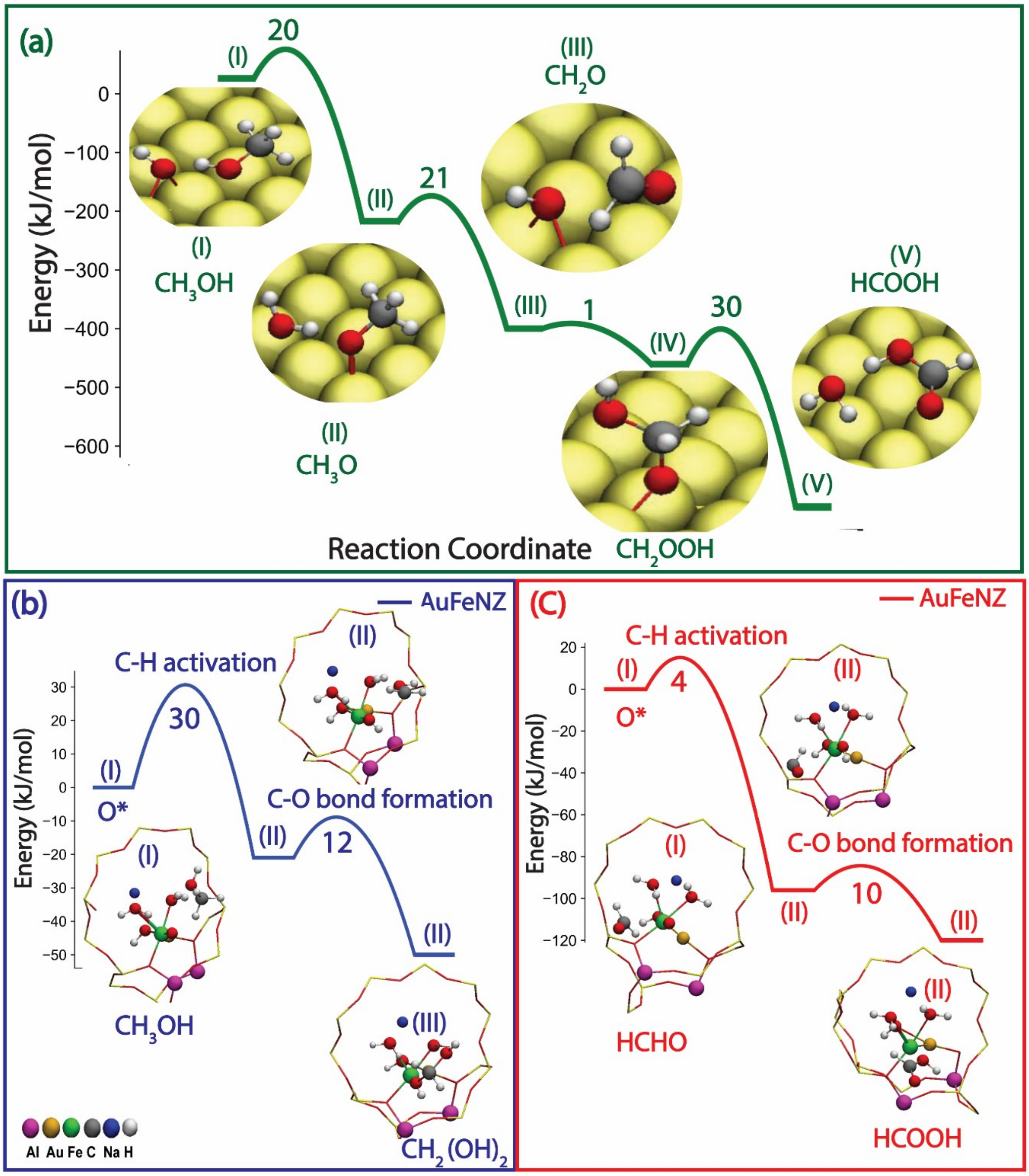

Figure 4.23 The DFT-simulated pathway over the Au (111) for directly oxidizing CH_3OH to HCOOH using H_2O_2 as the oxidant (a). Proposed reaction scheme of reaction pathway for methanol activation (b) and formaldehyde activation to formic acid in AuFeNZ (c). (activation energy in kJ/mole)

4.5 Conclusions

This chapter presents the successful design and development of a highly efficient bimetallic catalyst for the one-step conversion of methane to formic acid. The catalyst, composed of gold (Au) and iron (Fe), influences the synergistic interaction between the two metals to achieve exceptional catalytic performance. Detailed characterization using Transmission Electron Microscopy (TEM), X-ray Photoelectron Spectroscopy (XPS), and X-ray Absorption Spectroscopy (XAS) confirmed the structural and electronic properties that contribute to this enhanced activity. Complementary theoretical studies revealed that the catalyst exhibits a low activation barrier for the critical steps in methane activation, which is essential for driving the conversion process efficiently.

Under mild reaction conditions in a batch process, the 0.1Au0.1FeNZ catalyst produced 4264 µmol of oxygenates with 89% selectivity towards formic acid. Furthermore, in a continuous flow process under atmospheric conditions, the catalyst maintained its activity, producing 26.5 µmol of oxygenates. The results demonstrate the viability of the 0.1Au0.1FeNZ catalyst in practical applications and set the stage for future innovations in catalytic methane conversion. By carefully designing multicomponent catalysts and studying their performance, insights into the synergistic effects and their impact on catalytic activity and selectivity were gained. These findings highlight the potential of the catalyst for methane valorization, offering both high efficiency and selectivity under mild and novel process conditions, indicating the significant scalability prospects for industrial applications. By refining reactor designs and optimizing operational parameters, it may be feasible to deploy this catalyst in larger-scale methane conversion processes, thereby advancing sustainable chemical production from the plentiful resources of methane

4.6 References

[1] T. Yu, Z. Li, L. Lin, S. Chu, Y. Su, W. Song, A. Wang, B. M. Weckhuysen, W. Luo, *ACS Catal* **2021**, *11*, 6684–6691.

[2] P. Xie, J. Ding, Z. Yao, T. Pu, P. Zhang, Z. Huang, C. Wang, J. Zhang, N. Zecher-Freeman, H. Zong, D. Yuan, S. Deng, R. Shahbazian-Yassar, C. Wang, *Nat Commun* **2022**, *13*, 1375.

[3] L. Sun, Y. Wang, N. Guan, L. Li, *Energy Technology* **2020**, *8*, DOI 10.1002/ente.201900826.

[4] X. Yu, B. Wu, M. Huang, Z. Lu, J. Li, L. Zhong, Y. Sun, *Energy & Fuels* **2021**, *35*, 4418–4427.

[5] K. Zhu, S. Liang, X. Cui, R. Huang, N. Wan, L. Hua, H. Li, H. Chen, Z. Zhao, G. Hou, M. Li, Q. Jiang, L. Yu, D. Deng, *Nano Energy* **2021**, *82*, 105718.

[6] L. Schlapbach, A. Züttel, *Nature* **2001**, *414*, 353–358.

[7] A. F. Dalebrook, W. Gan, M. Grasemann, S. Moret, G. Laurenczy, *Chemical Communications* **2013**, *49*, 8735.

[8] F. Joó, *ChemSusChem* **2008**, *1*, 805–808.

[9] A. K. Md. L. Rahman, M. Kumashiro, T. Ishihara, *Catal Commun* **2011**, *12*, 1198–1200.

[10] Z. Fang, H. Murayama, Q. Zhao, B. Liu, F. Jiang, Y. Xu, M. Tokunaga, X. Liu, *Catal Sci Technol* **2019**, *9*, 6946–6956.

[11] Y. K. Krisnandi, D. A. Nurani, D. V. Alfian, U. Sofyani, M. Faisal, I. R. Saragi, A. Z. Pamungkas, A. P. Pratama, *Heliyon* **2021**, *7*, e08305.

[12] V. P. Shiralkar, P. N. Joshi, M. J. Eapen, B. S. Rao, *Zeolites* **1991**, *11*, 511–516.

[13] S. B. Kulkarni, V. P. Shiralkar, A. N. Kotasthanc, R. B. Borade, P. Ratnasamy, *Zeolites* **1982**, *2*, 313–318.

[14] B. Ravel, M. Newville, *J Synchrotron Radiat* **2005**, *12*, 537–541.

[15] B. Ravel, *J Synchrotron Radiat* **2001**, *8*, 314–316.

[16] M. Popova, Á. Szegedi, M. Oykova, H. Lazarova, N. Koseva, M. R. Mihályi, P. Shestakova, *Molecules* **2021**, *26*, 3576.

[17] M. Hunger, in *Zeolite Chemistry and Catalysis*, Springer Netherlands, Dordrecht, **2009**, pp. 65–105.

[18] B. Grahovski, R. Velinova, P. Shestakova, A. Naydenov, H. Kolev, I. Yordanova, G. Ivanov, K. Tenchev, S. Todorova, *Catalysts* **2023**, *13*, 834.

[19] A. V. Jagtap, P. Kumar, S. Gupta, A. Nagendra, S. N. Jha, D. Bhattacharyya, T. G. Ajithkumar, C. P. Vinod, *ACS Sustain Chem Eng* **2024**, DOI 10.1021/acssuschemeng.4c02993.

[20] W. Huang, S. Zhang, Y. Tang, Y. Li, L. Nguyen, Y. Li, J. Shan, D. Xiao, R. Gagne, A. I. Frenkel, F. F. Tao, *Angewandte Chemie* **2016**, *128*, 13639–13643.

[21] L. Lin, G. Zhang, L. Kang, T. Yu, Y. Su, G. Zeng, S. Chu, W. Luo, *ChemCatChem* **2023**, *15*, DOI 10.1002/cctc.202201234.

[22] T. Yu, Z. Li, L. Lin, S. Chu, Y. Su, W. Song, A. Wang, B. M. Weckhuysen, W. Luo, *ACS Catal* **2021**, *11*, 6684–6691.

[23] Z. K. Chu, G. Fu, X. Xu, in *Catal Today*, **2011**, pp. 112–119.

[24] J. Kučera, P. Nachtigall, *Physical Chemistry Chemical Physics* **2003**, *5*, 3311–3317.

[25] T. Yu, Z. Li, W. Jones, Y. Liu, Q. He, W. Song, P. Du, B. Yang, H. An, D. M. Farmer, C. Qiu, A. Wang, B. M. Weckhuysen, A. M. Beale, W. Luo, *Chem. Sci.* **2021**, *12*, 3152–3160.

[26] G. Qi, T. E. Davies, A. Nasrallah, M. A. Sainna, A. G. R. Howe, R. J. Lewis, M. Quesne, C. R. A. Catlow, D. J. Willock, Q. He, D. Bethell, M. J. Howard, B. A. Murrer, B. Harrison, C. J. Kiely, X. Zhao, F. Deng, J. Xu, G. J. Hutchings, *Nat Catal* **2022**, *5*, 45–54.

[27] G. Kresse, J. Furthmüller, *Comput Mater Sci* **1996**, *6*, 15–50.

[28] G. Kresse, J. Furthmüller, *Phys Rev B* **1996**, *54*, 11169–11186.

[29] J. P. Perdew, K. Burke, M. Ernzerhof, *Phys Rev Lett* **1996**, *77*, 3865–3868.

[30] M. Ernzerhof, G. E. Scuseria, *Journal of Chemical Physics* **1999**, *110*, 5029–5036.

[31] A. Rohrbach, J. Hafner, G. Kresse, *Phys Rev B* **2004**, *70*, 125426.

[32] S. Grimme, S. Ehrlich, L. Goerigk, *J Comput Chem* **2011**, *32*, 1456–1465.

[33] D. Sheppard, R. Terrell, G. Henkelman, *Journal of Chemical Physics* **2008**, *128*, DOI 10.1063/1.2841941.

[34] G. Henkelman, B. P. Uberuaga, H. Jónsson, *Journal of Chemical Physics* **2000**, *113*, 9901–9904.

[35] H. J. Monkhorst, J. D. Pack, *Phys Rev B* **1976**, *13*, 5188–5192.

[36] N. F. Dummer, D. J. Willock, Q. He, M. J. Howard, R. J. Lewis, G. Qi, S. H. Taylor, J. Xu, D. Bethell, C. J. Kiely, G. J. Hutchings, *Chem Rev* **2023**, *123*, 6359–6411.

[37] K. Zhu, S. Liang, X. Cui, R. Huang, N. Wan, L. Hua, H. Li, H. Chen, Z. Zhao, G. Hou, M. Li, Q. Jiang, L. Yu, D. Deng, *Nano Energy* **2021**, *82*, DOI 10.1016/j.nanoen.2020.105718.

[38] M. S. Ide, R. J. Davis, *Acc Chem Res* **2014**, *47*, 825–833.

[39] S. E. Davis, M. S. Ide, R. J. Davis, *Green Chemistry* **2013**, *15*, 17–45.

[40] B. N. Zope, D. D. Hibbitts, M. Neurock, R. J. Davis, *Science (1979)* **2010**, *330*, 74–78.

[41] D. Hibbitts, M. Neurock, *Surf Sci* **2016**, *650*, 210–220.

[42] X. Cui, H. Li, Y. Wang, Y. Hu, L. Hua, H. Li, X. Han, Q. Liu, F. Yang, L. He, X. Chen, Q. Li, J. Xiao, D. Deng, X. Bao, *Chem* **2018**, *4*, 1902–1910

Chapter 5

Summary and Conclusions

The thesis provides an in-depth exploration of the synthesis and application of heterogeneous catalysts for C-H activation, focusing on their remarkable capabilities in various catalytic processes, particularly the oxidation of benzene, cyclohexane and methane.

In ***Chapter 2A,*** the research begins with synthesizing La-Cu-based oxides through the sol-gel method, specifically highlighting the perovskite structure of La_2CuO_4. This catalyst exhibited an impressive ability to selectively hydroxylate benzene to phenol, achieving a conversion rate of 51% with an exceptional selectivity exceeding 99% within a 5h reaction period using hydrogen peroxide as the oxidant. The chapter emphasizes the catalyst's exceptional efficiency, further supported by advanced characterization techniques that provide valuable insights into the material's structural and electronic properties. The findings of this chapter suggest a promising alternative to traditional hydroxylation methods, positioning perovskite materials as significant players in the field of catalysis.

Chapter 2B delves into developing a hydrothermal method for synthesizing perovskite oxides with various morphologies, an area not explored in mixed metal oxides. This innovative approach proved to be highly effective in creating materials with diverse shapes that exhibited shape-dependent catalytic activity. The chapter discusses how advanced characterization techniques revealed the presence of structural defects in the hydrothermally synthesized perovskites, which significantly improved their catalytic performance in critical industrial reactions, such as cyclohexane and benzene oxidation. This exploration underscores the importance of defect engineering in optimizing the properties of functional materials. It contributes to the broader understanding of perovskite synthesis methods, opening new avenues for their application in industrial catalysis.

Chapter 3 focuses on the challenges of designing catalysts to activate methane at low pressure and temperature. The research highlights a novel approach that successfully generates and stabilizes low-valence $Fe^{\delta+}$ species capable of simultaneously activating methane, hydrogen, and oxygen, with gold nanoparticles playing a crucial role in this process. The chapter details how the hydrophobicity of the catalyst and the synergistic interactions between the gold and iron components lead to remarkable catalytic activity for the partial oxidation of methane under mild conditions. The study comprehensively analyses the catalyst's performance through various characterization techniques, revealing the close relationship between the iron and gold components. This chapter emphasizes the potential of this novel catalyst design and process conditions to address the grave challenges in methane valorization under industrially suitable conditions.

Chapter 4 presents the successful design and development of a highly efficient bimetallic catalyst composed of gold and iron for the one-step conversion of methane to formic acid. The chapter details how the synergistic interaction between the two metals results in exceptional catalytic performance, supported by extensive characterization using techniques such as Transmission Electron Microscopy (TEM), X-ray Photoelectron Spectroscopy (XPS), and X-ray Absorption Spectroscopy (XAS). The findings reveal that the catalyst exhibits a low activation barrier for critical steps in methane activation, essential for efficiently driving the conversion process. Under mild reaction conditions, the 0.1Au0.1FeNZ catalyst produced a substantial yield of 4264 µmol of oxygenates with 89% selectivity toward formic acid. Moreover, in a continuous flow process under atmospheric conditions, the catalyst maintained its activity, producing 26.5 µmol of oxygenates. These results highlight the potential of this material as a next-generation catalyst for methane valorization, demonstrating both high efficiency and selectivity at benign conditions that have not been reported so far in the literature.

Conclusions

In conclusion, this thesis presents ground-breaking strategies for synthesizing and utilizing heterogeneous catalysts in selective oxidation reactions. The research advances the understanding of catalyst design and performance and sets the stage for practical applications in industrial catalysis, particularly in the context of sustainable chemical processes. The findings underscore the critical role of synthesis methods and defect engineering in optimizing catalyst properties, offering new insights into the vast potential of perovskite materials in catalytic applications. This work opens new pathways for researchers to explore innovative solutions to the challenges associated with methane and benzene oxidation, ultimately contributing to developing more efficient and environmentally friendly chemical processes.

ABSTRACT

Name of the Student: Pawan Kumar
Registration No.: 10CC20A26080
Faculty of Study: Chemical Sciences
Year of Submission: 2024
AcSIR academic centre/CSIR Lab: CSIR-National Chemical Laboratory, Pune
Name of the Supervisor(s): Dr. Vinod C. Prabhakaran

Title of the thesis: Studies on Novel Catalyst Designs for C-H Activation

---

This thesis delves into the development of heterogeneous catalysts for the C-H activation. ***Chapter 1*** discusses the general introduction of C-H activation strategies and the important reactions targeted by the industry. ***Chapter 2*** has two sections. Section ***2A*** focuses on the design and synthesis of perovskite materials for applications in heterogeneous catalysis. The material synthesized through the sol-gel route demonstrates promising catalytic activity in the one-step conversion of benzene to phenol using H_2O_2 as an oxidant. Chapter 2B focuses on the design and synthesis of shape-dependent perovskite catalysts, a grey area in nanomaterial synthesis, and their demonstrations in the facet-dependent reactivity for industrially significant cyclohexane to KA oil reaction. The synthesis process developed enables the incorporation of various transition metals at the B site, with La occupying the A site to produce the shaped perovskites.

In ***Chapter 3***, SBA-15 is subjected to hydrophobic modification, followed by the deposition of Au and Fe onto the silica surface. The resulting catalyst is demonstrated to partially oxidize methane to methanol through in-situ generated H_2O_2 with high activity and selectivity. Advanced characterization techniques and theoretical studies offer valuable insights into plausible reasons for the efficient methane conversion utilizing the *in-situ* generated H_2O_2. The single atomic nature of the Fe, which is electronically modified through the interaction with Au nanoparticles, affirms the high activity. The ability to produce methanol continuously at ambient pressure presents promising prospects for the industrialization of this holy grail catalytic problem. In ***Chapter 4***, a bimetallic catalyst was synthesized and tested for the efficient conversion of methane to formic acid. The catalyst consisted of Au and Fe deposited on the surface of Na-ZSM5. The synergistic effect between Au and Fe, facilitated by Na, led to high activity and selectivity in producing formic acid under mild reaction conditions in both batch and continuous processes. XAS studies provide information about the local geometrical and electronic structure of the material. Theoretical studies offered in-depth insights into the synergistic effect and the lower energy barriers for the efficient production of formic acid. Chapter 5 summarizes the conclusions drawn from the investigation into the design of various catalytic systems for C-H activation. The role of active sites, the synergistic effects between metals, and the support modification all play crucial roles in achieving efficient conversion and selectivity through C-H activation.

List of Publications Emanating from the Thesis work

1. **P. Kumar**, A. Vijay Jagtap, S. Gupta, C. P. Vinod, La−Cu based heterogeneous perovskite catalyst for highly selective benzene hydroxylation under mild conditions. *Chem Asian J.* **2022,** 17, e202200788
2. **Pawan Kumar**, Anuradha V Jagtap, N. Abharana, S.N. Jha, D. Bhattacharyya, and C. P. Vinod, Atmospheric-Pressure Continuous-Flow Methane Oxidation to Methanol and Acetic Acid Using H_2O_2 over the Au–Fe Catalyst. *ACS Sustainable Chem. Eng.* **2024,** 12, 8958-8967
3. **Pawan Kumar**, Anuradha V Jagtap, Nikhil S., S. Tanmay Ghosh, S. Krishnamurty and C. P. Vinod, Continuous Flow Methane Oxidation using *in-situ* H_2O_2 Generation at Ambient Pressure *(Manuscript under preparation)*
4. **Pawan Kumar**, Iqraa, Srishti Kesarwani, Prashant Niphadkar, Vijay Bokade, M. Ali Haider, C. P. Vinod, Highly efficient conversion of methane to formic acid with Au-Fe decorated Na containing zeolite under mild conditions. *(Manuscript under preparation)*
5. **Pawan Kumar**, Mithra K. M., S. Royer, J. P. Dacquin, J. Dhainaut and C. P Vinod, Shaped Perovskite synthesis and their application. *(Manuscript under preparation)*

List of Publications Non-Emanating from the Thesis Work

1. Indra Narayan Chakraborty, Vanshika Jain, Pradyut Roy, **Pawan Kumar**, Chathakudath P. Vinod, and Pramod P. Pillai Photocatalytic Regeneration of Reactive Cofactors with InP Quantum Dots for the Continuous Chemical Synthesis. *ACS Catal.* ***2024***, 14, 6740–6748

Patent, Poster and Conferences

Patents-

1. ‘A catalyst for partial oxidation of substrate to value-added products under ambient conditions - Provisional No.- 202211057120
2. ‘Shaped metal oxides (perovskites) and process for preparation thereof’ - Provisional No. 202311033445
3. ‘Na-based support containing catalyst for partial oxidation of substrate to value-added products’ - Provisional No. 202311059066

List of Posters presented with details

1. Indo-French Seminar on Catalysts for Sustainability held on 10-13 Dec 2023 at IISER Thiruvananthapuram, Kerla

Title: Morphology-controlled perovskites synthesis and application

Abstract: Shape-controlled synthesis and activity of the metal nanoparticles are well explored in material science. In the same scenario, mixed metal oxides are also explored in the field of catalysis, where synergistic effects among two metals play roles in the activity of the materials. Shape- or facet-dependent synthesis and activity have yet to be explored for mixed metal oxides. It can open several ways for the scientific community to apply the mixed metal oxide material.

We have synthesized the shaped perovskites with the combination of Lanthanum and transition metal (Fe, Cu, Mn etc.) using the hydrothermal method with various morphology. The poster presentation will discuss shape-dependent catalysis (Oxidation/reduction).

List of Oral presentation

Annual Students Conference – NCL Research Foundation held at CSIR-NCL, 29th-30th Nov. **2022**.

List of Conference attended

Annual Students Conference – NCL Research Foundation held at CSIR-NCL, 30th Nov.-1st Dec. **2023**.

ACES Asian Chemical Editorial Society
doi.org/10.1002/asia.202200788
CHEMISTRY AN ASIAN JOURNAL Research Article
www.chemasianj.org

Special Collection

La–Cu based heterogeneous perovskite catalyst for highly selective benzene hydroxylation under mild conditions

Pawan Kumar,[a, b] Anuradha Vijay Jagtap,[a, b] Sharad Gupta,[a] and Chathakudath P. Vinod*[a, b]

Abstract: Direct hydroxylation of benzene towards phenol with high conversion and selectivity remains a great challenge. We report herein an efficient La_2CuO_4 perovskite catalyst for one-step oxidation of benzene using hydrogen peroxide under mild conditions. The catalyst was characterized using XRD, TEM, XPS, TG-DTA, and other advanced techniques. The one-pot hydroxylation reaction carried out at 60 °C under optimum reaction conditions in the presence of catalytic material shows benzene to phenol transformation with 51% conversion with $>99\%$ selectivity with 65 percent peroxide efficiency, respectively. The influence of reaction conditions such as temperature, amount of oxidant, reaction time and mode of addition of the oxidant was crucial in selectivity optimization.

Introduction

Production of industrially important fine chemicals and feedstocks from inexpensive and naturally abundant petroleum-derived hydrocarbons is one of the hot research topics, yet, a long-standing challenge remains[1,2]. Due to stringent environmental regulations, the development of new catalytic technologies operating under benign conditions is intensely explored by the community. In this regard, benzene to phenol via direct C–H activation attracts genuine scientific interest among researchers worldwide. It is well known that phenol is a critical feedstock in the chemical industry for the diverse production of several key products/chemicals/intermediates such as resins, fungicides, pesticides, preservatives, pharmaceuticals, caprolactam, and adipic acid[3–5]. Currently, the Cumene process for industrial phenol production suffers from several drawbacks like poor yield, production of explosive by-products such as cumene hydroperoxide, and a multi-step reaction scheme. This has given enough scope for improving this process[6] and developing a one-step heterogeneous process for converting benzene into phenol using H_2O_2 as an oxidant with high conversion and selectivity is of great interest[7,8]. Heterogeneous catalysts are advantageous because of the easy separation/recovery of solid catalytic material from the process leading to a greener pathway and lesser pollution[9,10]. Recently, novel heterogeneous catalysts, such as zeolites[11,12], noble metal-based catalysts[9,13–15] and transition metal nanomaterials (especially Cu, Fe and V)[10,16–22] have been developed for this reaction. A recent report shows ~71% benzene conversion with 91% selectivity for phenol using Cu_1-N_2/HCNS single-atom catalyst[17]. Supported metal oxides are also explored where Cu/Fe-SBA-15 shows ~35% benzene conversion with 90% phenol selectivity[19]. A lot of research has been done using different catalytic systems, but most of them suffer from low stability, tedious synthesis methods, and the usage of excess expensive oxidants.

Perovskites are a class of inorganic materials that have attracted considerable attention in other areas of materials chemistry but have not been much explored in catalysis[23–25]. They are well known for stability and, with easy and scalable preparation routes, are the ideal choice as catalysts for fine chemical synthesis. Perovskite oxides have a general chemical formula of $ABO_{3,}$ where A is a rare-earth metal, alkaline metal, or other ions with a large radius, B represents a transition metal, and O is oxygen. In these materials, the A sites hold the structure and the B sites account for the catalytic activity[26]. Recently, perovskite nanomaterials were used as catalysts for methane activation, CO_2 reduction, epoxidation reaction, etc.[26–31]. In comparison with mixed metal oxide materials, perovskite-type catalysts have higher thermal stability, flexible valence states of transition metal ions in their structure, and redox properties[32]. Also, A or B site cations are usually coordinated by other ions like oxygen, producing defects like oxygen vacancy sites that fine-tune the catalyst's performance. Generally, perovskite exists in various structural forms, among which the A_2BO_4 class is known as layered perovskite[33].

Herein, we report a perovskite oxide of La_2CuO_4 as an efficient catalyst for a one-step hydroxylation of benzene to phenol under mild conditions. La_2CuO_4 has an orthorhombic distortion with a tetragonal K_2NiF_4 structure[34] where the CuO_2 layer and a rock salt LaO layer are stacked [Figure 1]. Each Cu atom is surrounded by six oxygen atoms forming CuO_6 octahedral coordination leading to an apex angle interconnected octahedron perovskite. The structure will have a CuO_2 layer sandwiched between two LaO layers. This unique structural configuration of La_2CuO_4 perovskite is expected to provide variable oxidation states for the B site cation which is Cu in our catalyst material. We envisage that such defect centers can play a pivotal role in benzene hydroxylation as reported on supported Cu-based catalysts[17,35].

---

[a] P. Kumar, A. Vijay Jagtap, Dr. S. Gupta, Prof. C. P. Vinod
Catalysis and Inorganic Chemistry Division
CSIR-National Chemical Laboratory
Dr. Homi Bhabha Road, 411008 Pune, Maharashtra (India)
E-mail: cp.vinod@ncl.res.in

[b] P. Kumar, A. Vijay Jagtap, Prof. C. P. Vinod
Academy of Scientific and Innovative Research (AcSIR),
201002 Ghaziabad (India)

Supporting information for this article is available on the WWW under https://doi.org/10.1002/asia.202200788

This manuscript is part of a joint special collection highlighting the chemistry research from CSIR Institutes in India

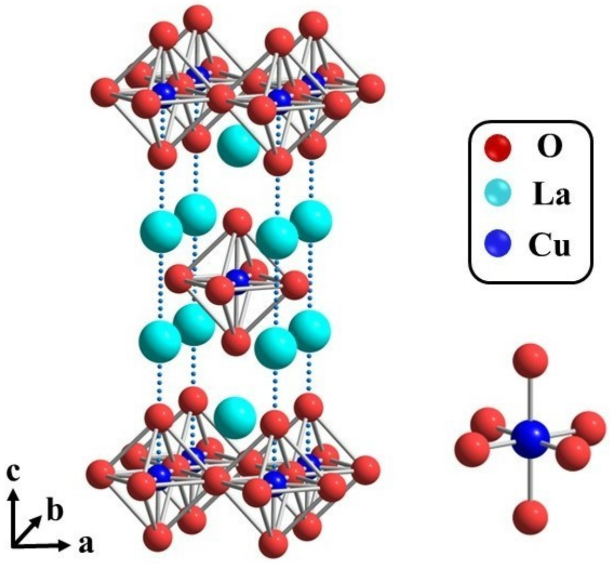

Figure 1. Structure of La_2CuO_4 perovskite.

Results and Discussion

X-ray diffraction patterns for various La–Cu based catalysts synthesized using the sol-gel method and calcined at 800 °C were collected and shown in Figure 2(a). The XRD spectrum of 50LCO shows a single perovskite phase (La_2CuO_4) with an orthorhombic structure (space group Fmmm) and the results agree with the standard pattern of La_2CuO_4 (JCPDS 038-0709)[36]. Interestingly, when the copper molar ratio was less than 1:0.5, lanthanum formed different phases in the form of hydroxide, oxide and carbonate. When the Cu: La molar ratio was 1:1, two additional reflections appeared (35.5° and 37.7°) of tenorite-CuO, which was confirmed by the JCPDS matching file (00-048-1548) [Figure S1]. XRD profiles of spent catalyst were also recorded to ensure structural stability [Figures S2, S3 and S4] and a detailed discussion is followed later. XRD patterns of various La–M (M=Ni, Co and Fe) based perovskite were also recorded to compare the active facets [Figure S5]. Materials were named xLCO, where x is the molar ratio of Cu metal with respect to La metal × 100. For example, if the Cu: La molar ratio is 0.5:1, the sample is named 50LCO; if it is 1:1, it is named 100LCO.

XPS is an excellent tool for investigating the surface states of catalyst materials[37]. Figure 2(b), (c) and (d) are the deconvoluted XPS spectra of Cu 2p, O 1s and La 3d of the as-

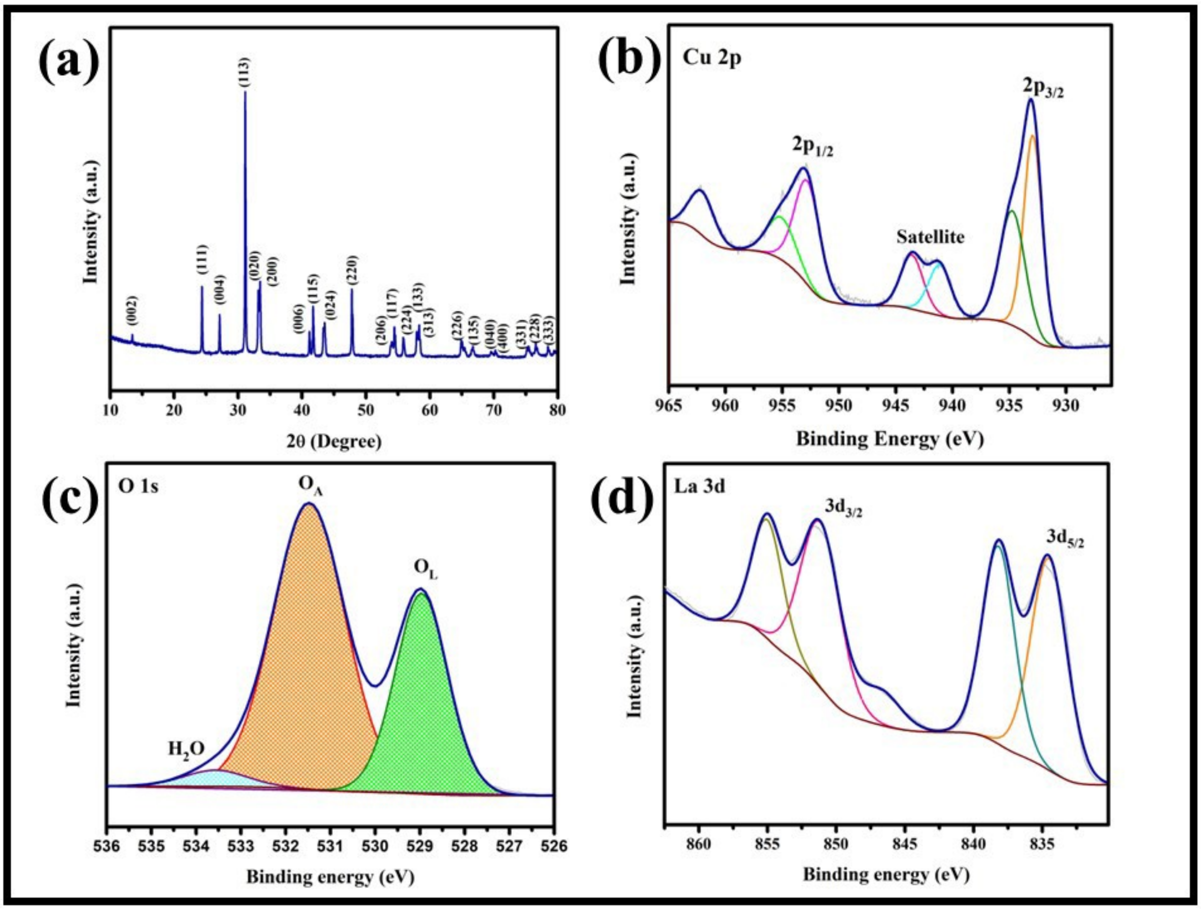

Figure 2. XRD profile of 50LCO (a), XPS spectrum of Cu 2p of 50LCO (b), XPS spectrum of O 1s of 50LCO (c) and XPS spectrum of La 3d of 50LCO (d).

synthesized 50LCO catalyst, respectively. The curve-fitting of the core levels was used to make qualitative and quantitative analyses. The O 1s spectrum could be deconvoluted into three components at binding energy (BE) = 528.8, 531.4, and 533.8 eV [Figure 2c], attributable to the surface lattice oxygen species (O_L), adsorbed oxygen (O_A) species, and molecularly adsorbed water species, respectively[38]. It should be noted that the adsorbed oxygen is associated with oxygen vacancy, and its significant presence in the O 1s spectrum is indicative of abundant surface defects[39–42].

For Cu 2p XPS spectra of the catalyst, the binding energy corresponding to Cu $2p_{3/2}$ is observed at 933 and 934.3 eV, confirming the presence of Cu^{1+} and Cu^{2+} species [Figure 2b]. It should be noted that the metallic Cu(0) appears at the same binding energy of 933 eV as that of Cu(1+). To further confirm the presence of Cu(1+), Cu LMM Auger was measured, which gave a broad kinetic energy peak centered around 917.3 eV with no signature for Cu(0) at 918.6 eV, establishing the presence of both Cu(1+) and Cu(2+) in the sample[43] [Figure S6]. The presence of shake-up satellite peaks at BE = 940.9 and 943.3 eV are the signature of Cu(2+)[44]. La 3d XPS spectrum shows two broad peaks with significant doublets at 830–840 eV and 847–857 eV, corresponding to La $3d_{5/2}$ and La $3d_{3/2}$ [Figure 2d]. Specifically, the peaks at 833.6, 837.7, 850.5 and 854.6 eV can all be assigned to La^{3+}, confirming that the valence state of La in 50LCO is largely +3.

The morphology details of the catalyst materials were revealed using electron microscopy [Figure 3]. The macroporous nature of the material is confirmed by the FESEM [Figure 3(a)], where large pores of approx 1–2 μm were visible on the surface.

TEM analysis confirmed that metal particles were not of specific shape or size [Figure 3(b)] and can be best classified into flake-type morphology. A detailed HRTEM analysis [Figure 3(c) and 3(d)] further supports the XRD results. With regard to the La_2CuO_4 system in Figure 3(d), the lattice spacing (d = 0.288 nm) matches the La_2CuO_4 (113) plane[36]. The homogeneous distribution of all the elements (La, Cu and O) is confirmed by color mapping, and EDAX establishes the elemental percentage, which matches the theoretical loading [Figure S7]. The morphological information of the 100LCO system and Fast Fourier Transformation (FFT) image confirms the presence of the orthorhombic phase of the bilayer system in both 50LCO and 100LCO [Figure S8].

Figure 4a shows the FTIR spectra of the 50LCO perovskite. The two prominent bands at 678 and 511 cm^{-1} correspond to La–O and Cu–O stretching modes of the orthorhombic La_2CuO_4 phase[45]. For 100LCO catalyst, in addition to 678 and 511 cm^{-1} bands, the presence of bands at 593 cm^{-1} (related to Cu–O stretching mode) confirms the presence of CuO as an additional second phase because of the higher molar ratio of Cu to La (1:1)[46]. The FTIR spectrum of 2LCO, 5LCO and 10LCO [Figure S9] reveals a sharp band at 3609 cm^{-1}, which is attributed to the bulk hydroxyl groups originating from $La(OH)_3$. Also, the peaks at 1477 cm^{-1} and 1384 cm^{-1} are the stretching modes of carbonate. This confirms the presence of phase-separated La_2O_3 species, expected to produce surface carbonate[47]. The FTIR data also indicates the phase purity of the 50LCO catalyst.

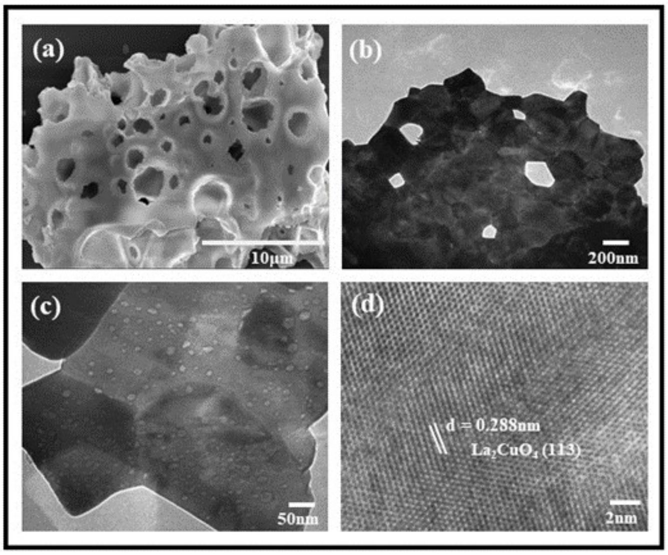

Figure 3. Electron microscopy images of 50LCO: FESEM image (a), TEM image (b) and HRTEM image (c and d).

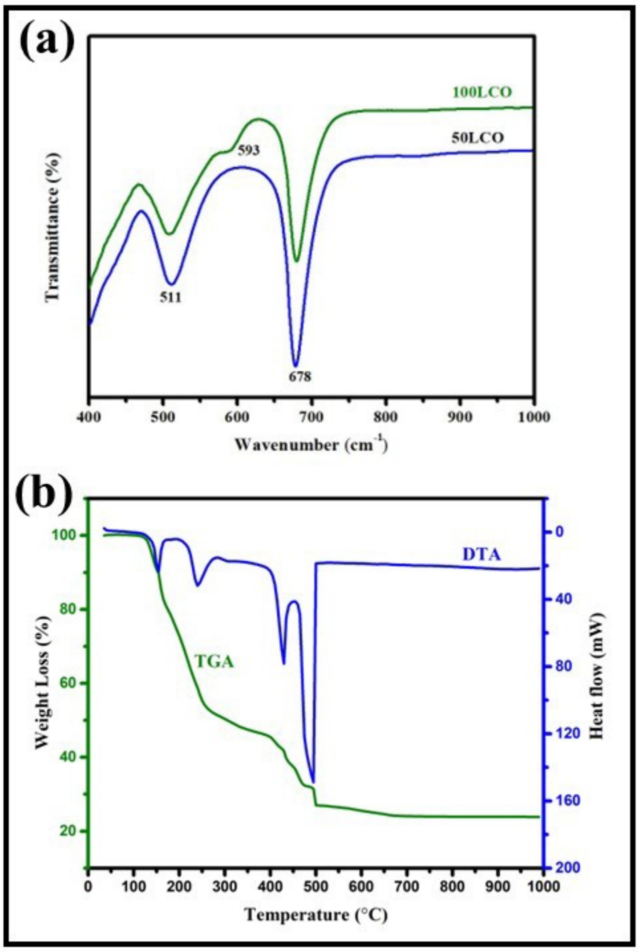

Figure 4. FTIR spectrum of 50LCO and 100LCO (a), TG-DTA curve of 50LCO (b).

Further insight into the thermal stability of the prepared material is given by thermogravimetric analysis (TGA). Figure 4(b) is the TG-DTA data from the dried sample of 50LCO. The dehydration and decomposition of solvent water, crystal water, and citrate in the gel were observed from the TG curve at 100–270 °C[48]. The TG-DTA curves show considerable weight loss between 300–520 °C. This is due to the oxidative combustion of citric acid or its decomposition products. There was no observable weight loss after 700 °C. The TG-DTA experiments indicate that the catalyst calcination temperature should be above 700 °C.

Nitrogen adsorption-desorption isotherms at 77 K for material revealed that the specific surface area was 65 m^2/g for 50LCO catalyst [Figure S10]. The average pore size distribution for the material was 24 A°. To the best of our knowledge, there are no reports in the literature for the surface area as high as La_2CuO_4 material in the present study, possibly due to mesopores and macropores in the structure[44,49,50].

Benzene Hydroxylation Activity of La–Cu-based catalyst

Effect of Cu molar ratio: While comparing the various copper lanthanum-based oxide systems, we found that the Cu molar ratio of 1:0.02 to La gave 38% conversion of benzene. With an increase in a molar ratio to 1:0.5, the benzene conversion increased to 51% with high phenol selectivity of $>99\%$ [Figure 5(a)]. From here, we can say that catalytic activity might depend on copper content in the system. But a further increase in the metal molar ratio to 1:1 did not produce an increment in the activity. So, it is clear that the monophasic La_2CuO_4 system shows the best activity compared to other La–Cu-based oxide systems. Although the turnover no. will be high in low Cu molar ratio catalysts, the recyclability test was not promising for this catalyst. Different sets of catalysts were tested for recyclability [Figure S11] and there was a noticeable decrement in the activity after each cycle in the case of a low Cu content catalyst. The reason behind the decrement is the leaching of the active phase from the catalyst, which is discussed in the later part. But the activity was maintained for 50LCO and 100LCO, over each cycle proving the catalyst's sustainability. After three cycles of catalyst testing, the structural integrity of the catalytic material was further confirmed by XRD [Figure S2]. Activity comparison with other perovskite oxides also confirms that La_2CuO_4 was the best among the present catalyst series [Figure S12]. Analysis of gaseous products confirmed that CO and CO_2 are present as gaseous by-products, but their contribution in conversion and selectivity was less than 0.01% and was neglected. Based on the recyclable stability of the perovskite catalysts, 50 LCO catalyst was utilized for further reaction optimizations.

Effect of Reaction parameters: The benzene conversion was investigated in a temperature range between room temperature to 70 °C, maintaining the same reaction conditions [Figure S13]. With an increase in the temperature, the benzene conversion increases but at the expense of phenol selectivity. The optimum activity with the best conversion and selectivity was noted at 60 °C.

In any catalytic reaction, kinetics is a yardstick for the catalyst's performance. A steady state or a decrease in the phenol yield with time points that either the radical chain reaction is brought to an end or the further oxidation of the phenol.

The effect of reaction time on benzene hydroxylation was tested in the range of 1–24 h and presented in Table S1. Gas chromatograms of the substrate, product and side products are provided in the supporting information [Figure S14–S21]. The obtained data reveals that the benzene conversion increase with the reaction time, reaching a maximum value of 51% after 5 h of benzene hydroxylation. Beyond this time, benzene conversion increases, but the phenol selectivity decreases resulting in a decrement in the yield of phenol. Consequently, the use of the extended time of benzene hydroxylation has a

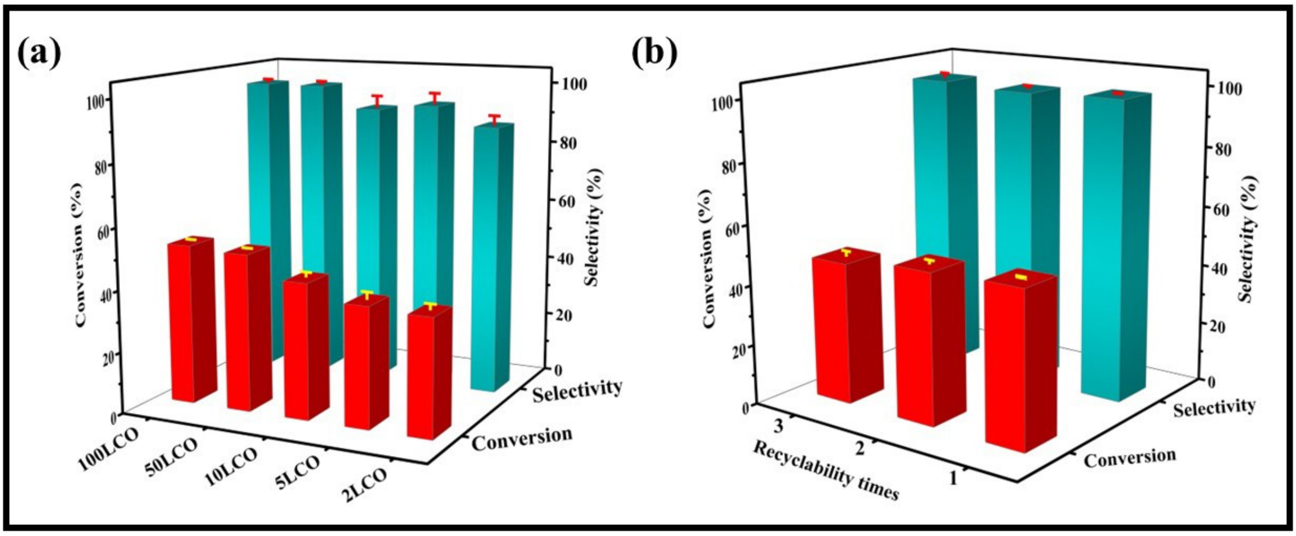

Figure 5. Catalytic activity of various catalysts (a) and recyclability test of 50LCO catalyst(b). Reaction conditions : benzene (0.5 mL), catalyst (20 mg), water (1 mL), acetonitrile (0.5 mL), H_2O_2 (0.5 mL), 60 °C, 5 h.

negative effect on the phenol yield because the produced phenol undergoes further oxidation, producing hydroquinone and catechol as side products as confirmed by GC through standard injection of side products [Figure S14–S17]. Thus, it can be inferred that beyond 5 h of benzene oxidation, a significant portion of the generated peroxide radical species react with the produced phenol molecules instead of activating the benzene molecules. In comparison to the previously reported data[51–53], a high benzene conversion with excellent phenol selectivity even with a 5 h of benzene hydroxylation time highlights the efficacy of 50LCO and can be attributed to the presence of abundant surface sites in 50LCO in activating the H_2O_2 molecules.

An increase in the H_2O_2 amount from 1:1 to 1:2 resulted in a marginal increment in the benzene conversion, meaning that the overall H_2O_2 efficiency is compromised [Figure S22]. Also, an increment in the H_2O_2 amount decreases the phenol selectivity due to the over-oxidation products. Interestingly, further experiments proved that the mode of adding H_2O_2 also influences the conversion as well as phenol selectivity. When H_2O_2 was added sequentially, reactivity data was markedly different. When the reaction time was 1 h, 500 μL/h of H_2O_2 was added upfront (Table S1 entry 2), which led to fast decomposition of H_2O_2, resulting in lower phenol selectivity (86%) and conversion (41%). This would imply a competition of the excess amount of OH radicals formed, taking either a decomposition pathway to form water or over oxidizing the formed phenol to polyphenols. In the case of a 3 h reaction, H_2O_2 addition was around 166 μL/h which leads to an increase in conversion (44%) as well as selectivity (92%). But when the reaction was carried out for 5 h (Table S1 entry 4) with sequential every hour addition of H_2O_2 (100 μL/h), an optimum for benzene hydroxylation was observed. When the H_2O_2 (500 μL) was added initially, and the reaction was carried out for 5 h (Table S1 entry 8), lower conversion and selectivity were observed, similar to the 1 h experiment discussed above [Table S1]. Following the sequential addition protocol with increased oxidant amount was also not beneficial (Table S1 entry 9) as 8 h reaction data showed 60% conversion with 74% selectivity. This implies that increasing the time and peroxide amount improves the conversion, but the large excess of peroxide in the reaction mixture produces over-oxidized products. The overall hydrogen peroxide efficiency was 64.9% for a 1:1 system for a 5 h sequential addition reaction, which is very high for any benzene hydroxylation reaction attempted using H_2O_2 as an oxidant[52–55]. To the best of our knowledge, the peroxide efficiency reported is exceptional from the literature point. From table 1, it is clear that when no catalyst was present, only 0.9% of benzene was converted to phenol which confirms that the reaction is catalytic. Benzene oxidation was tested with other oxidants like molecular oxygen and tert-butyl hydroperoxide (Table 1). Molecular oxygen was unable to insert the oxygen atom in the C–H bond of benzene resulting in low activity. In the case of TBHP, selectivity was not up to the mark because of the faster decomposition of peroxide. The use of H_2O_2 governs a greener pathway and high catalytic activity.

Catalyst Recovery and Reuse: To check the durability of the La–Cu based catalysts, several experiments were carried out using the recovered catalyst under the same conditions employed previously. After each catalytic run, the catalyst was recovered by centrifugation, washed multiple times with acetonitrile, dried at 60 °C for 12 h and used for the catalytic reaction without further pre-treatment. The results show a negligible decrease in the benzene conversion and phenol selectivity after the 3rd cycle using a 50LCO catalyst [Figure 5b]. Catalyst 100LCO also shows retention of activity [Figure S23]. Thus, it can be inferred that the 50LCO catalyst can endure the harsh reaction conditions of the benzene hydroxylation reaction, but it was not the same in the case of a lower Cu content catalyst [Figure S11]. The perovskite phase of the recovered catalyst (50LCO) was investigated using XRD analysis, and the fresh and recovered catalyst XRD profiles are compared in Figure S2. The obtained XRD pattern of the recovered catalyst reveals that no phase transformation was observed during benzene hydroxylation; however, a slight decrease in the peak intensity was observed. But, in the case of the lower Cu molar ratio, the material undergoes structural changes during the reaction, which can be the reason for lower activity after each cycle [Figure S4]. Similar to 50LCO, 100LCO catalyst did not undergo any phase transformation after the catalytic reaction, which confirms structural stability [Figure S3]. XPS analysis confirms that the proportion of Cu(2+) species was lower in the case of spent catalyst, which confirms the involvement of lattice oxygen and a slight shift toward lower binding energy was also observed in the case of the XPS spectrum of La after the reaction [Figure S6]. When the O 1s spectra were investigated, we found that, compared with the fresh one, the proportion of O_L decreased while that of the O_A increased in the used catalyst [Figure S24]. It was observed that the consumption of lattice oxygen would produce relatively weakly-bound surface oxygen species and oxygen vacancies. The decrement in the Cu^{2+} species in the spent catalyst points to the reduction

Table 1. Reaction data at various conditions.

Substrate/Catalyst/Oxidant	Time (h)	Conversion [%]	Phenol selectivity [%]	Other oxygenates selectivity [%]
Benzene/No catalyst/H_2O_2	5	0.9	100	0
Benzene/50LCO/No oxidant	5	0.7	100	0
Benzene/50LCO/H_2O_2	5	51	>99	<1
Benzene/50LCO/O_2	5	0.5	100	0
Benzene/50LCO/TBHP	5	56	65	35

Reaction conditions: benzene (0.5 mL), catalyst (20 mg), water (1 mL), acetonitrile (0.5 mL), oxidant (0.5 mL), 60 °C.

of lattice oxygen[56]. Compared with other La–Cu perovskite systems, the proportion of lattice oxygen was significantly higher than adsorbed oxygen in the case of La–Co-based perovskite [Figure S25]. This can be the reason for the lower activity of Co-based perovskite, i.e., 9% only [Figure S12]. This study also confirms that oxygen vacancies play a vital role in this reaction. It is not fair to compare the results in the present work with the previously reported systems in literature because of different reaction parameters. As per our knowledge, perovskite oxides have not been explored much for the benzene oxidation reaction. While most of the heterogeneous catalyst-based system for benzene hydroxylation uses large excess of H_2O_2, the perovskite catalyst used in this study clearly has an edge with superior peroxide efficiency. The easy route of synthesis and scalability of catalyst is best envisaged for industrial applications.

Mechanistic Aspect

From the above experimental observations, it is clear that copper act as the active site for benzene hydroxylation in the LCO catalyst system. Based on the previous studies and our own evidence, a plausible mechanism for benzene hydroxylation is proposed for the La–Cu based perovskite catalyst[57,58] [Figure 6]. It has been reported that Cu(I) in an aqueous solution may behave as a "Fenton-like" catalyst because of the redox behavior of Cu^{1+}/Cu^{2+}[59]. So, in the 1st step of the reaction, H_2O_2 gets activated over the catalyst surface and forms $OH^{\bullet}$ and OH^- species resulting in the conversion of Cu^{1+} to Cu^{2+}. Then the $OH^{\bullet}$ reacts with benzene and forms hydroxycyclohexadienyl radical. The formed radical species undergo self-destruction to form phenol and release electrons and H^+ ions[58]. The liberated H^+ reacts with OH^- to form water molecule and the released electron is captured by the catalyst resulting in the conversion of Cu^{2+} to Cu^{1+}.

Conclusions

In summary, we have reported La–Cu based oxides for benzene oxidation. La_2CuO_4 perovskite shows selective hydroxylation of benzene to phenol with a conversion of 51%, and high selectivity of >99% within 5 h using H_2O_2 as an oxidant. A high peroxide efficiency of 64.9% was achieved for the given system. The present study is an imperative strategy that can be an alternative to conventional supported heterogeneous catalysts for the selective hydroxylation of benzene.

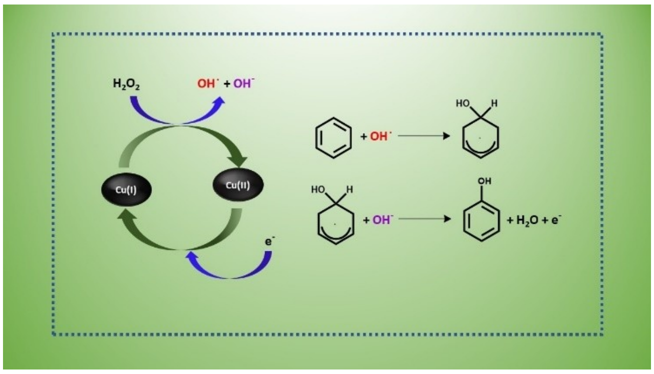

Figure 6. Proposed mechanism of benzene oxidation at the catalyst surface.

Experimental Section

Materials

All chemicals were used without further purification. Copper (II) nitrate trihydrate and citric acid monohydrate were purchased from Himedia and Lanthanum nitrate hexahydrate was purchased from Loba Chemie Pvt. Ltd. Benzene was purchased from Sigma Aldrich and HPLC grade acetonitrile and hydrogen peroxide (30% w/v) were purchased from Thomas Baker.

Synthesis of La–Cu based oxides. All samples with different Lanthanum-Copper ratios were prepared by the citrate sol-gel method, which allows the formation of amorphous citrates of metals with broad flexibility of compositions[40]. In this method, lanthanum metal precursor $La(NO_3)_3 \cdot 6H_2O$ and Cu metal precursor $Cu(NO_3)_2 \cdot 3H_2O$ were mixed with the desired mole ratio in 20 mL distilled water (18 MΩ cm) under stirring at 70 °C for 1 h. Citric acid was added to the metal salts at a molar ratio of 1:2 (total metal ion/citric acid) to ensure the complete complexation of metal ions. The resulting solution was stirred at 70 °C to form a gel. The gel was then dried at 70–100 °C for 12 h to remove the remaining water. The hygroscopic material was calcined in 2 steps, first at 400 °C for 4 h followed by 800 °C for 4 h. In a typical synthesis batch, 1 gm of catalyst was made with phase purity. Materials were named xLCO, where x is the molar ratio of Cu metal with respect to La metal ×100. For example, if the Cu: La molar ratio is 0.5:1, the sample is named 50LCO; if it is 1:1, it is named 100LCO. Other perovskite materials $LaFeO_3$, $LaNiO_3$ and $LaCoO_3$, were also prepared for catalysis comparison using the same method. All the synthesized catalysts were tested for benzene hydroxylation reaction.

Activity test. The catalytic activities were tested for the hydroxylation of benzene to phenol using H_2O_2 as the oxidizing agent. The reaction was carried out in a batch reactor process using a 25 mL two-necked flask equipped with a condenser and the reaction temperature was adjusted by immersing the flask in a thermally controlled oil bath. Benzene (0.5 mL), acetonitrile (0.5 mL), water (1 mL) and desired amount of catalyst were fed into a two-necked flask. After this step, a calculated amount of H_2O_2 (30% w/v) was introduced sequentially to the stirring mixture. In a typical standardized reaction, a total of 500 μL of H_2O_2 was used for the overall reaction, and this was added sequentially at intervals of every hour to a maximum of 4 h and then the reaction was left to proceed for another hour (total 5 h). The catalytic activity was evaluated at a reaction temperature of 30–70 °C and at a reaction time of 0.5–24 h. After the completion of the reaction, the mixture was centrifuged to remove the solid catalyst, and the liquid product was collected and analyzed using a NUCON GC equipped with a Db6 column and flame ionization detector. Gaseous product analysis was done using a methanizer in the FID detector.

Catalyst Characterization

The X-ray diffraction (XRD) patterns of the samples were recorded on a powder X-ray diffractometer (Rigaku Miniflex 2200PC), using

Cu–Kα radiation ($\lambda = 0.15418$ nm) in the 2θ range of 10–80° at a scanning rate of 3° min^{-1}.

The specific surface area of the catalyst was measured by the low-temperature liquid nitrogen adsorption and desorption method with a Quantachrome instrument. A quartz tube with 50 mg of the sample was dried and degassed for 10 h at 250 °C and under 1 MPa vacuum. After the pretreatment, the adsorption and desorption experiment was carried out with N_2 as the adsorbed gas and He as the balance gas.

Thermogravimetry differential thermal analysis (TG-DTA, Pyris Diamond) was used to analyze the formation mechanism and crystallization temperature of the material.

Fourier transform infrared (FT-IR) absorbance spectra were obtained in the wavenumber range between 4000 and 400 cm^{-1} using a Perkin Elmer Infrared Spectrometer.

Electron microscopy was used to find out the morphological details of the material. Field emission scanning electron microscopy (FESEM) characterization was carried out on a NOVA NANO SEM field emission scanning electron microscope. Transmission electron microscopy (TEM) analysis was performed over the TECNAI-20ST instrument. The samples for TEM analysis were prepared in isopropyl alcohol and dried completely before analysis. For high-resolution transmission electron microscopy (HRTEM) imaging, JEOL F-200 HRTEM instrument was used.

X-ray photoelectron spectroscopy (XPS) measurements were carried out using a Thermo Scientific Kalpha + spectrometer using micro-focused and monochromated Al Kα radiation with an energy of 1486.6 eV. The pass energy for the spectral acquisition was kept at 50 eV for individual core levels. The electron flood gun was utilized for providing charge compensation during data acquisition. The peak fitting of the individual core levels was done using Avantage software with a smart-type background.

Acknowledgments

P. K. thanks CSIR-UGC for the research fellowship. C. P. V. thanks Director CSIR-NCL and the Council of Scientific and Industrial Research (CSIR) for funding through in-house grant MLP030626.

Conflict of Interest

The authors declare no conflict of interest.

Data Availability Statement

Research data are not shared.

Keywords: benzene oxidation · heterogeneous · hydrogen peroxide efficiency · phenol · perovskite

[1] C. Shan, L. Zhu, L.-B. Qu, R. Bai, Y. Lan, *Chem. Soc. Rev.* **2018**, *47*, 7552–757.
[2] J. A. Leitch, C. G. Frost, *Chem. Soc. Rev.* **2017**, *46*, 7145–7153.
[3] Y. Gu, Q. Li, D. Zang, Y. Huang, H. Yu, Y. Wei, *Angew. Chem. Int. Ed.* **2021**, *60*, 13310–13316.
[4] W. Wang, N. Li, L. Shi, Y. Ma, X. Yang, *Appl. Catal. A* **2018**, *553*, 117–125.
[5] R. Meimani, Z. Aghajani, G. R. Najafi, *Res. Chem. Intermed.* **2018**, *44*, 3947–3958.
[6] R. J. Schmidt, *Appl. Catal. A* **2005**, *280*, 89–103.
[7] G. Ding, W. Wang, T. Jiang, B. Han, H. Fan, G. Yang, *ChemCatChem* **2013**, *5*, 192–200.
[8] T. Tsuji, A. A. Zaoputra, Y. Hitomi, K. Mieda, T. Ogura, Y. Shiota, K. Yoshizawa, H. Sato, M. Kodera, *Angew. Chem. Int. Ed.* **2017**, *56*, 7779–7782; *Angew. Chem.* **2017**, *129*, 7887–7890.
[9] K. Tian, W.-J. Liu, S. Zhang, H. Jiang, *Green Chem.* **2016**, *18*, 5643–5650.
[10] S. S. Acharyya, S. Ghosh, S. Adak, T. Sasaki, R. Bal, *Catal. Sci. Technol.* **2014**, *4*, 4232–4241.
[11] R. Bal, M. Tada, T. Sasaki, Y. Iwasawa, *Angew. Chem. Int. Ed.* **2006**, *45*, 448–452; *Angew. Chem.* **2006**, *118*, 462–466.
[12] H. Xin, A. Koekkoek, Q. Yang, R. van Santen, C. Li, E. J. M. Hensen, *Chemical Communications* **2009**, 7590.
[13] Z. Hou, L. Dai, Y. Liu, J. Deng, L. Jing, W. Pei, R. Gao, Y. Feng, H. Dai, *Appl. Catal. B* **2021**, *285*, 119844, DOI 10.1016/j.apcatb.2020.119844.
[14] S. M. Hosseini, M. Ghiaci, S. A. Kulinich, W. Wunderlich, B. H. Monjezi, Y. Ghorbani, H. S. Ghaziaskar, A. Javaheri Koupaei, *Appl. Surf. Sci.* **2020**, *506*, 144644, DOI 10.1016/j.apsusc.2019.144644.
[15] X. Ma, R. Dang, Z. Liu, F. Yang, H. Li, T. Guo, J. Luo, *Chem. Eng. Sci.* **2020**, *211*, 115274, DOI 10.1016/j.ces.2019.115274.
[16] J. Xu, Y. Hong, M. J. Cheng, B. Xue, Y. X. Li, *Microporous Mesoporous Mater.* **2019**, *285*, 223–230.
[17] T. Zhang, X. Nie, W. Yu, X. Guo, C. Song, R. Si, Y. Liu, Z. Zhao, *iScience* **2019**, *22*, 97–108.
[18] H. Zhou, Y. Zhao, J. Gan, J. Xu, Y. Wang, H. Lv, S. Fang, Z. Wang, Z. Deng, X. Wang, P. Liu, W. Guo, B. Mao, H. Wang, T. Yao, X. Hong, S. Wei, X. Duan, J. Luo, Y. Wu, *J. Am. Chem. Soc.* **2020**, *142*, 12643–12650.
[19] Y. Wu, X. Zhang, F. Wang, Y. Zhai, X. Cui, G. Lv, T. Jiang, J. Hu, *Ind. Eng. Chem. Res.* **2021**, *60*, 8386–8395.
[20] P. R. Makgwane, S. S. Ray, *J. Mol. Catal. A* **2015**, *398*, 149–157.
[21] Y. Dong, X. Zhan, X. Niu, J. Li, F. Yuan, Y. Zhu, H. Fu, *Microporous Mesoporous Mater.* **2014**, *185*, 97–106.
[22] N. S. Sanjini, S. Velmathi, *J. Porous Mater.* **2016**, *23*, 1527–1535.
[23] X. Du, J. Li, G. Niu, J. H. Yuan, K. H. Xue, M. Xia, W. Pan, X. Yang, B. Zhu, J. Tang, *Nat. Commun.* **2021**, *12*, 3348, DOI 10.1038/s41467-021-23788-4.
[24] F. Ali, C. Roldán-Carmona, M. Sohail, M. K. Nazeeruddin, *Adv. Energy Mater.* **2020**, *10*, 2002989, DOI 10.1002/aenm.202002989.
[25] Y. Hu, T. Niu, Y. Liu, Y. Zhou, Y. Xia, C. Ran, Z. Wu, L. Song, P. Müller-Buschbaum, Y. Chen, W. Huang, *ACS Energy Lett.* **2021**, *6*, 2917–2943.
[26] L. Yang, Y. Jiao, X. Xu, Y. Pan, C. Su, X. Duan, H. Sun, S. Liu, S. Wang, Z. Shao, *ACS Sustainable Chem. Eng.* **2022**, *10*, 1899–1909.
[27] L. He, Y. Zhang, Y. Zang, C. Liu, W. Wang, R. Han, N. Ji, S. Zhang, Q. Liu, *ACS Catal.* **2021**, *11*, 14224–14236.
[28] L. Yang, Y. Jiao, X. Xu, Y. Pan, C. Su, X. Duan, H. Sun, S. Liu, S. Wang, Z. Shao, *ACS Sustainable Chem. Eng.* **2022**, *10*, 1899–1909.
[29] V. Fung, F. Polo-Garzon, Z. Wu, D. E. Jiang, *Catal. Sci. Technol.* **2018**, *8*, 702–709.
[30] S. Royer, D. Duprez, F. Can, X. Courtois, C. Batiot-Dupeyrat, S. Laassiri, H. Alamdari, *Chem. Rev.* **2014**, *114*, 10292–10368.
[31] J. Wang, C. Cheng, B. Huang, J. Cao, L. Li, Q. Shao, L. Zhang, X. Huang, *Nano Lett.* **2021**, *21*, 980–987.
[32] R. J. H. Voorhoeve, D. W. Johnson, J. P. Remeika, P. K. Gallagher, *Science* **1977**, *195*, 827–833.
[33] D. Kwon, I. Yang, S. An, J. Cho, J.-M. Ha, J. C. Jung, *Molecular Catalysis* **2021**, *506*, 111548.
[34] H. Hosono, K. Tanabe, E. Takayama-Muromachi, H. Kageyama, S. Yamanaka, H. Kumakura, M. Nohara, H. Hiramatsu, S. Fujitsu, *Sci. Technol. Adv. Mater.* **2015**, *16*, 033503.
[35] S. S. Acharyya, S. Ghosh, S. Adak, T. Sasaki, R. Bal, *Catal. Sci. Technol.* **2014**, *4*, 4232–4241.
[36] J. Wang, C. Cheng, B. Huang, J. Cao, L. Li, Q. Shao, L. Zhang, X. Huang, *Nano Lett.* **2021**, *21*, 980–987.
[37] A. F. Lee, V. Prabhakaran, K. Wilson, *Chem. Commun.* **2010**, *46*, 3827.
[38] M. W. Roberts, *Chem. Soc. Rev.* **1989**, *18*, 451.
[39] J.-C. Dupin, D. Gonbeau, P. Vinatier, A. Levasseur, *Phys. Chem. Chem. Phys.* **2000**, *2*, 1319–1324.
[40] A. S. A. Raj, V. Biju, *Mater. Sci. Semicond. Process.* **2017**, *68*, 38–47.
[41] K. Rajendran, N. Pandurangan, C. P. Vinod, T. S. Khan, S. Gupta, M. A. Haider, D. Jagadeesan, *Appl. Catal. B* **2021**, *297*, 120417.
[42] S. Gupta, C. Ciotonea, S. Royer, J.-P. Dacquin, C. P. Vinod, *Appl Mater Today* **2020**, *19*, 100586.

[43] V. N. Popok, S. M. Novikov, Y. Yu. Lebedinskij, A. M. Markeev, A. A. Andreev, I. N. Trunkin, A. v. Arsenin, V. S. Volkov, *Plasmonics* **2021**, *16*, 333–340.
[44] Z. Zhang, X. Chen, X. Zhang, H. Lin, H. Lin, Y. Zhou, X. Wang, *Catal. Commun.* **2013**, *36*, 20–24.
[45] M. Sukumar, L. J. Kennedy, J. J. Vijaya, B. Al-Najar, M. Bououdina, *New J. Chem.* **2018**, *42*, 18128–18142.
[46] D. Manos, F. Papadopoulou, A. Margellou, D. Petrakis, I. Konstantinou, *Catalysts* **2022**, *12*, 187.
[47] B. P. Gangwar, V. Palakollu, A. Singh, S. Kanvah, S. Sharma, *RSC Adv.* **2014**, *4*, 55407–55416.
[48] J. Yuan, H. Dai, L. Zhang, J. Deng, Y. Liu, H. Zhang, H. Jiang, H. He, *Catal. Today* **2011**, *175*, 209–215.
[49] K.-Y. A. Lin, Y.-C. Chen, Y.-F. Lin, *Chem. Eng. Sci.* **2017**, *160*, 96–105.
[50] O. P. Taran, A. B. Ayusheev, O. L. Ogorodnikova, I. P. Prosvirin, L. A. Isupova, V. N. Parmon, *Appl. Catal. B* **2016**, *180*, 86–93.
[51] S. Mishra, R. Bal, R. K. Dey, *Molecular Catalysis* **2021**, *499*, 111310.
[52] T. Zhang, D. Zhang, X. Han, T. Dong, X. Guo, C. Song, R. Si, W. Liu, Y. Liu, Z. Zhao, *J. Am. Chem. Soc.* **2018**, *140*, 16936–16940.
[53] W. Chen, H. Jin, F. He, P. Cui, C. Cao, W. Song, *Nano Res.* **2022**, *15*, 3017–3025.
[54] K. Tian, W.-J. Liu, S. Zhang, H. Jiang, *Green Chem.* **2016**, *18*, 5643–5650.
[55] Y. Liu, Y. Zheng, P. Dong, W. Zhang, W. Wu, J. Mao, *ACS Appl. Mater. Interfaces* **2021**, *13*, 61047–61054.
[56] H. Chen, Y. Xu, K. Zhu, H. Zhang, *Appl. Catal. B* **2021**, *284*, 119732.
[57] M. Ishida, Y. Masumoto, R. Hamada, S. Nishiyama, S. Tsuruya, M. Masai, *J. Chem. Soc. Perkin Trans. 2* **1999**, 847–854.
[58] C. A. Antonyraj, K. Srinivasan, *Catal. Surv. Asia* **2013**, *17*, 47–70.
[59] D. A. Nichela, A. M. Berkovic, M. R. Costante, M. P. Juliarena, F. S. García Einschlag, *Chem. Eng. J.* **2013**, *228*, 1148–1157.

Manuscript received: July 28, 2022
Revised manuscript received: September 19, 2022
Version of record online: ■■, ■■■

RESEARCH ARTICLE

An efficient La_2CuO_4 perovskite catalyst for one-step oxidation of benzene using hydrogen peroxide under mild conditions is reported. The one-pot hydroxylation reaction, carried out at 60 °C under optimum reaction conditions in the presence of catalytic material, shows conversion of benzene to phenol with 51% conversion with $>$99% selectivity with 65 percent peroxide efficiency, respectively.

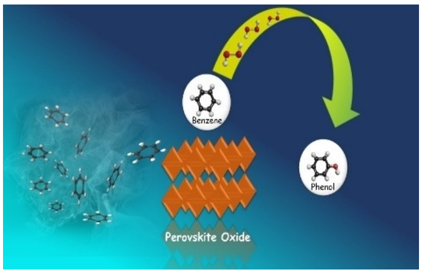

*P. Kumar, A. Vijay Jagtap, Dr. S. Gupta, Prof. C. P. Vinod**

1 – 9

La–Cu based heterogeneous perovskite catalyst for highly selective benzene hydroxylation under mild conditions

ACS Sustainable Chemistry & Engineering

pubs.acs.org/journal/ascecg

Research Article

Atmospheric-Pressure Continuous-Flow Methane Oxidation to Methanol and Acetic Acid Using H_2O_2 over the Au−Fe Catalyst

Anuradha V. Jagtap,[⊥] Pawan Kumar,[⊥] Sharad Gupta, Abharana Nagendra, Shambhu Nath Jha, D. Bhattacharyya, Thalasseril G. Ajithkumar, and C. P. Vinod*

Cite This: https://doi.org/10.1021/acssuschemeng.4c02993

Read Online

ABSTRACT: An enormous value proposition exists when molecules such as acetic acid and methanol are derived from natural gas. With abundant worldwide resources, the conversion of methane to methanol (M2M) by partial oxidation or to acetic acid through C-insertion is considered one of the most enterprising chemical transformations in catalysis. Methane partial oxidation using H_2O_2 as the oxidant is reported at high-pressure conditions with an excess of oxidant. In this work, significant catalytic challenges successfully tackled are the continuous partial oxidation of methane to methanol and acetic acid at atmospheric pressure. Under continuous flow and at atmospheric pressure, a modified silica-supported bimetallic (AuFeHS) catalyst catalyzed the conversion of methane to methanol using H_2O_2 with an impressive yield of 224 mmol/g_{Fe+Au}. Cofeeding of CO in the stream produces acetic acid, demonstrating a selectivity switch from methanol with an overall yield of 92 mmol/g_{Fe+Au}.

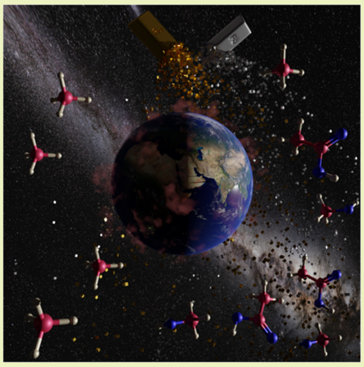

KEYWORDS: *methane, methanol, acetic acid, continuous flow oxidation, Au−Fe silica catalysts, synergistic effect*

INTRODUCTION

Methane is one of the major constituents of natural gas, and its presence in waste landfills and manure feedstocks adds to the potential list of chemicals contributing to global warming.[1] Methane has a high calorific value and can be directly used as fuel, but its storage and transportation are not practical, as it needs to be compressed to 10−100 atm for commercial utility. Alternatively, CH_4 is converted into chemicals using an indirect route involving synthesis gas ($CO + H_2$).[2] Methane is envisaged to have tremendous potential to be a raw material that can be converted to various high-value chemicals. One of the biggest obstacles in this direction is the activation of nonpolar methane with a central carbon atom surrounded by four hydrogen atoms forming a regular tetrahedron, thereby requiring harsh reaction conditions.[3] A more significant challenge is the partial oxidation of methane (POM) to methanol or any other useful platform molecules, as thermodynamics suggests that an activated C−H bond is so reactive that it readily undergoes complete oxidation to CO_2. Direct conversion of methane to value-added liquid fuels and chemicals such as methanol, olefins, hydrogen, and aromatics has thus become an important research topic attracting interest from the industry and academia.[4,5] Indeed, direct partial oxidation of methane to methanol is considered a holy grail problem in catalysis and is a dream reaction that still eludes the catalysis community.[5−8] In general, molecular oxygen and H_2O_2, the two green oxidants, are targeted because of their better commercialization scope, and if successful, catalytic technologies can be developed through these routes. While molecular oxygen is the ideal solution for this problem, the yields reported so far for methanol and other oxygenates are so poor that any commercialization scope is far in sight. Future developments in new and cheaper technologies for producing H_2O_2 could make any catalytically oxidative pathway involving this molecule highly advantageous.[9]

The development of active materials for this conversion in a high-pressure batch process has been explored on various supported metal sites and metal alloys.[10−14] Wang and co-workers reported the conversion of methane over oxo dicopper anchored on carbon nitride with a methanol production of 129.7 mmol/g_{Cu}·h.[10] Hutchings and co-workers reported the production of 7.02 μmol of oxygenates in 30 min of using AuPdCu supported on titania.[14] Most of the reports suffer from a low product yield and high-temperature (70−80 °C) and high-pressure (20−30 bar) reaction conditions, limiting the use of the catalyst at the commercial level.

Early reports on single-site catalysts for methane partial oxidation have interested researchers because the highly dispersed metal particles on various supports significantly modify their chemical and electronic properties in the

Received: April 10, 2024
Revised: May 15, 2024
Accepted: May 15, 2024

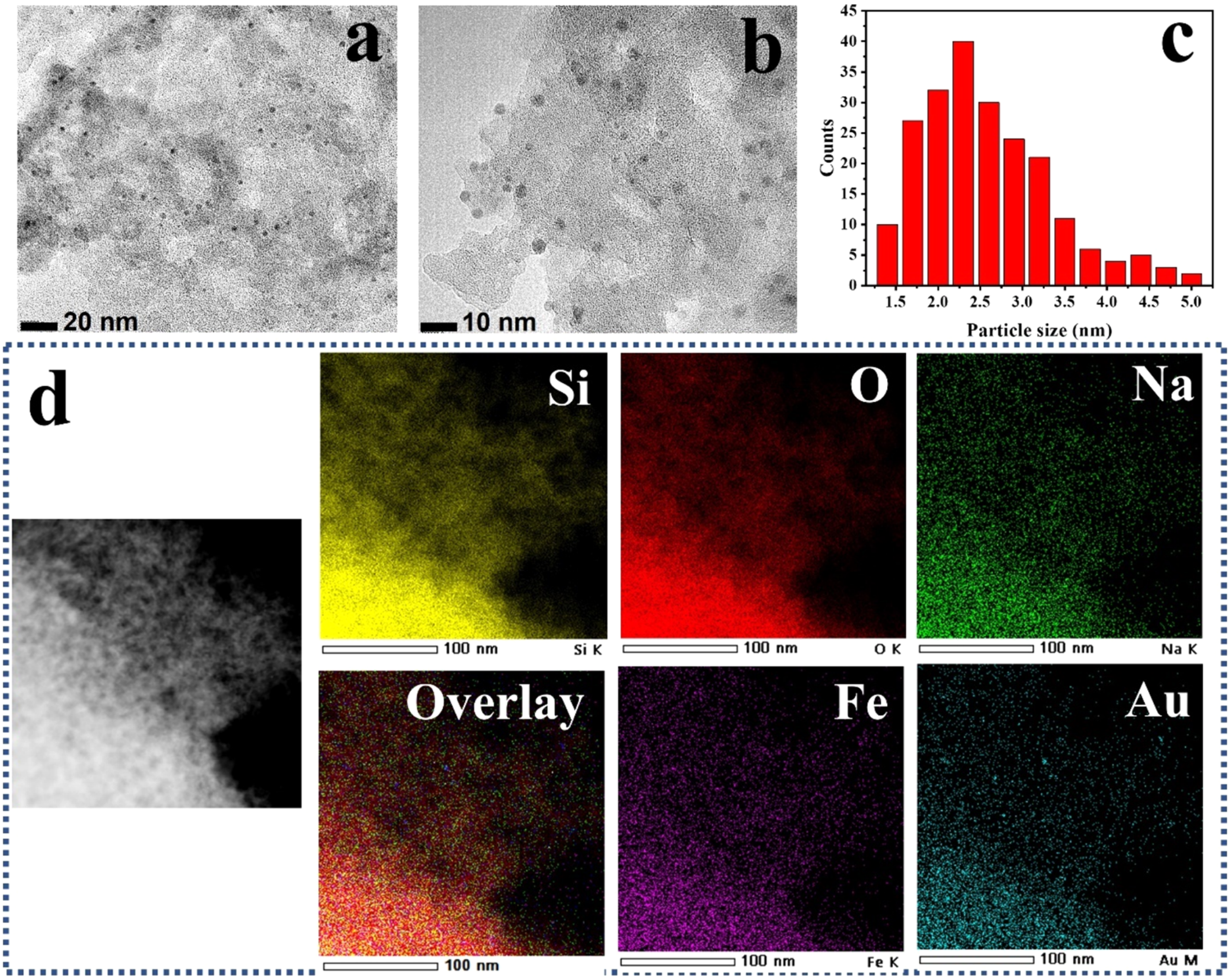

Figure 1. (a, b) High-resolution TEM images of AuFeHS (scale—20 and 10 nm, respectively). (c) Particle size distribution histogram of AuFeHS determined from TEM analysis. (d) Elemental mapping of AuFeHS.

materials.[15−25] Bao and co-workers explored the various transition metals supported on graphene, confirming that the graphene-confined iron single-atom catalyst can activate the methane at room temperature and 20 bar pressure. In this report, the FeN_4/GN-2.7 catalyst catalyzed methane partial oxidation, producing approximately 114 μmol of C1 oxygenates in 10 h.[18] Song and co-workers produced synergistic catalysts with single chromium atoms supported on TiO_2 nanoparticles for direct methane oxidation to C1 oxygenated products, yielding 43.9 μmol.[17] In another report, ZSM-5-supported single Cu atoms were shown to be active and selective for methane partial oxidation with a yield for C1 oxygenates of 4800 μmol/g_{cat} within 30 min.[22] The literature suggests that most catalysts employed for methane activation suffer from low methanol selectivity, harsh reaction conditions, and poor material stability.

There are only limited reports on the POM to methanol in a continuous flow reactor,[8,27−29] with most reports being on using molecular oxygen as the oxidant with frugal conversion to methanol. For example, Narsimhan et al. reports the production of 1.81 μmol/ g_{cat}·h methanol using O_2 as an oxidant at 210 °C.[8] Hutchings and co-workers recently reported POM reaction in a high-pressure continuous process using H_2O_2 as an oxidant.[26] The yield obtained was 0.081 $mol_{Product}/kg_{cat}$·h at 20 bar pressure. Considering the importance of this reaction, it is highly desirable to construct a catalyst material that can activate methane at mild conditions and selectively produce the desired oxygenates. In this report, we disclose a Au−Fe catalyst supported over hydrophobic silica to partially oxidize methane to methanol using H_2O_2 as an oxidant both in a batch process (10 bar) and in a continuous process (atmospheric pressure) with high selectivity. We also show that cofeeding CO with methane produces acetic acid in excellent yield. The overall conversion achieved through the atmospheric pressure continuous process in the present work is the best reported, surpassing the high-pressure batch process for methanol and acetic acid.

RESULTS AND DISCUSSION

A modified deposition precipitation (DP) method was used to disperse atomic clusters of Fe onto hydrophobic silica (HS) support.[30] The best-performing catalyst (0.2Au0.5FeHS, further written as AuFeHS) had an optimum Fe concentration of 0.46 wt % and an Au concentration of 0.23 wt %, confirmed by inductively coupled plasma-optical emission spectrometry (ICP-OES). Hydrophobic support is important in oxidation

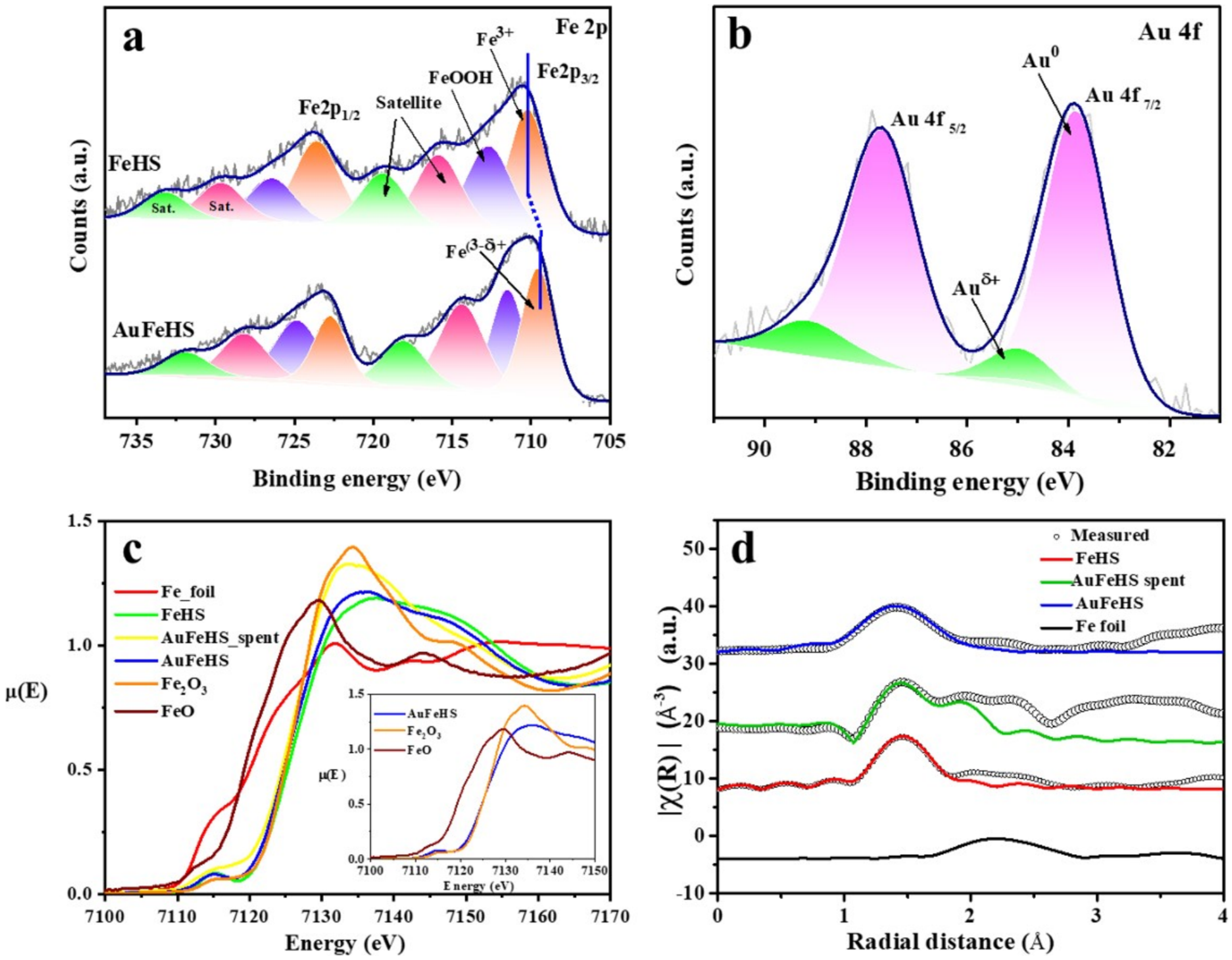

Figure 2. Characterization of various catalysts: (a, b) XPS spectrum of Fe 2p and Au 4f of AuFeHS, respectively. (c) Normalized XANES spectra at the Fe K-edge of various catalysts. (d) Experimental $\chi(R)$ vs R data of the Au−Fe catalyst measured at the Fe K-edge along with best-fit theoretical plots (open circles: experimental data; solid line: theoretical best fit).

reactions involving H_2O_2 because it helps peroxide to be close to the active sites of Au and Fe, where incoming methane can react with peroxide efficiently.[31,32] Further, it is known that the active sites get blocked in the hydrophilic conditions because of the presence of moisture, and it is also known that the Au particle size increases in the aqueous conditions, which further lowers the activity of the catalyst.[33−35] A hydrophobic environment also facilitates easy desorption of the methanol from the surface, preventing overoxidation.[36,37] The hydrophobicity of silica was confirmed by contact angle analysis with an observed angle of 118° (Figures S1 and S2). The C−H vibration from silica confirmed hydrophobic functionalization from HS (Figure S3). The absence of characteristic reflections of Au and Fe from powder XRD confirms a fine dispersion of metals over the AuFeHS catalyst (Figure S4). This observation was expected with a low loading of the metals on the silica support. FeHS images obtained from HRTEM did not show any contrast difference to characterize Fe particles (Figure S7a). Atomic dispersion of Fe over the silica surface with extremely low loading could be the reason for this. However, small Au nanoparticles were observed in AuFeHS (Figure 1a,b). Such nanoparticle formation of Au is expected even at small loadings because of the higher surface energy of gold, which tends to stabilize in a larger size.[38,39] The elemental mapping further shows that the Au nanoparticles are finely dispersed over FeHS, resulting in a strongly interfaced AuFeHS catalyst (Figures 1d and S5−S7). The particle size distribution for Au on FeHS was in the range of 1.2−5.0 nm (Figure 1c). A specific surface area of 392 m^2/g was observed for the AuFeHS catalyst by using the present synthesis method (Figure S8 and Table S1). X-ray photoelectron spectroscopy confirmed the oxidation state of the elements, which also gave insights into the perturbed electronic environment surrounding the Fe species. The C 1s spectrum recorded from both samples showed the main peak at ∼285 eV corresponding to C−C and C−H fragments from the modified silica support (Figure S9). Since the electron flood gun was used during data acquisition, charge correction was not required, and the BE values were reported as recorded. In Figure 2a, the Fe 2p spectra of FeHS show the presence of a peak at 710.3 eV, confirming the presence of Fe^{3+} species, while the peak around 712.5 eV corresponds to FeOOH species on the catalyst surface.[40] The Fe 2p spectra of AuFeHS showed the binding energy at 710.6 eV corresponding to the Fe^{3+} species (Figure 2a), and a lower binding energy (709.5 eV) confirms the presence of a low-valent $Fe^{3-\delta+}$ species, which is identified as an important Fe

https://doi.org/10.1021/acssuschemeng.4c02993

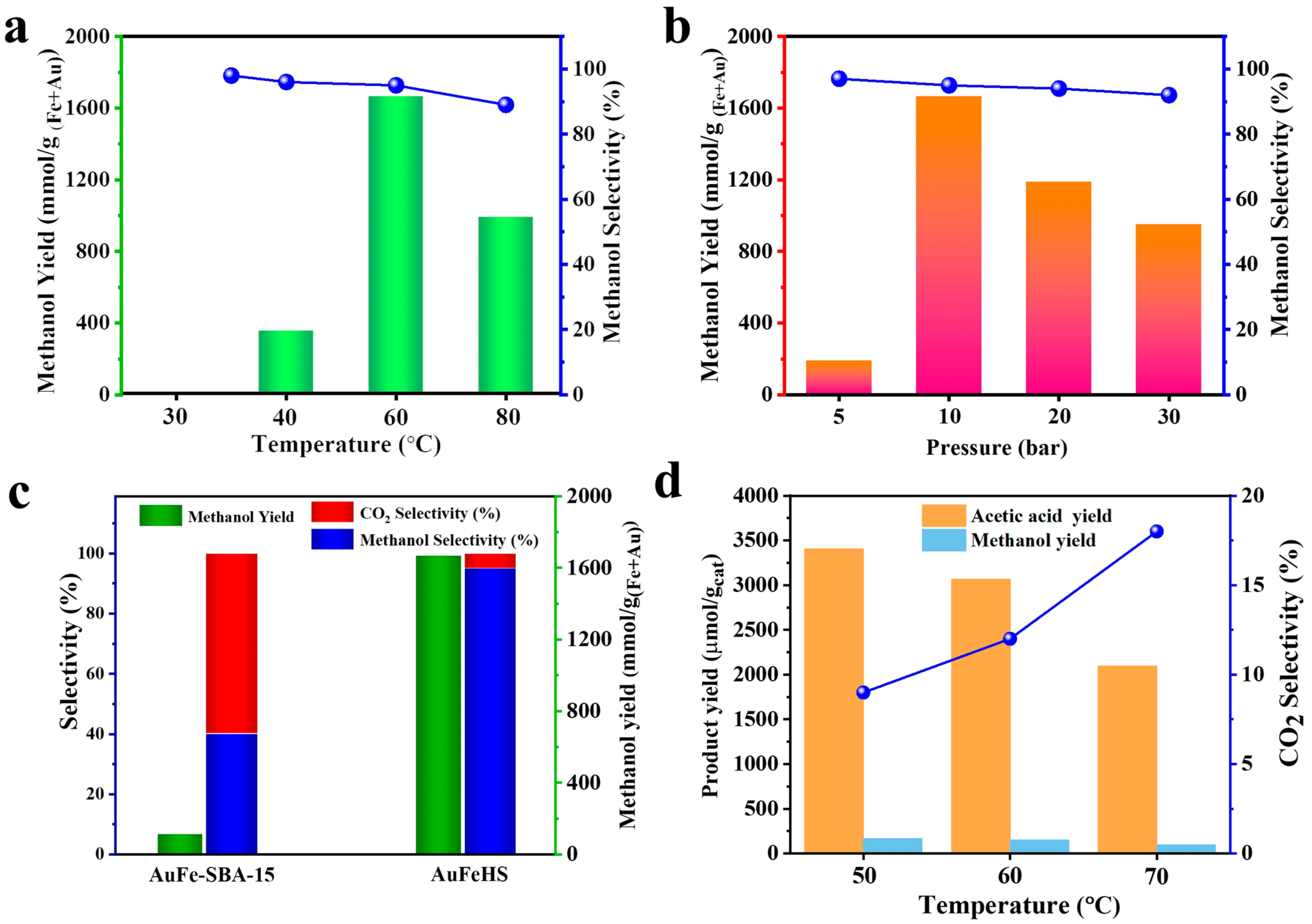

Figure 3. Catalytic activity analysis in the batch process. (a) Catalytic activity of AuFeHS at various temperatures: reaction conditions 25 mg of catalyst, 30 min, 10 bar methane, 0.5 mL of H_2O_2 (30% w/v), 20 mL of H_2O, 30−80 °C, 950 rpm. (b) Catalytic activity of AuFeHS at various pressures: reaction conditions 25 mg of catalyst, 30 min, 60 °C, 0.5 mL of H_2O_2 (30% w/v), 20 mL of H_2O, methane 5−30 bar, 950 rpm. (c) Catalytic activity of various catalysts: reaction conditions 25 mg of catalyst, 30 min, 10 bar methane, 0.5 mL of H_2O_2 (30% w/v), 20 mL of H_2O, 60 °C, 950 rpm. (d) Catalytic activity of AuFeHS at various temperatures: reaction conditions 50 mg of catalyst, 1 h, 15 bar methane, 5 bar CO, 0.05 mL of H_2O_2 (30% w/v), 20 mL of H_2O, 50−70 °C, 950 rpm.

site in methane activation.[41,42] The low-valent Fe sites are also reported to be the sites for hydrogen peroxide activation by providing the OH moiety to the activated methane molecule for the formation of CH_3OH.[43,44] Over the FeHS catalyst, the low-valent $Fe^{3-\delta+}$ at 709.5 eV was absent and reflected in their poor catalysis (Figure 2a). The Au 4f XPS spectra of AuFeHS (Figure 2b) showed two peaks centered at 83.9 eV (Au $4f_{7/2}$) and 87.6 eV (Au $4f_{5/2}$) with the spin−orbit splitting difference of 3.7 eV corresponding to the binding energy of elemental gold Au0. A higher binding energy peak ~85 eV ($4f_{7/2}$) establishing the cationic ($Au^{\delta+}$) species shows a possible charge donation and stabilization of the $Fe^{3-\delta+}$ species. Based on relative peak areas, their respective atomic percentages were estimated as 85% for Au^0 and 15% for $Au^{\delta+}$ peaks. No considerable change was observed in the case of the Au (fresh and spent) catalyst.

The cationic Au species was absent in the case of the AuHS catalyst (Figure S10). Apart from Au and Fe, Na was also present in the catalyst, and the details are given in a later discussion.

Figure 2c shows the normalized XANES spectra measured at the Fe K-edge along with Fe standards. No Fe−Fe interaction was observed in the samples, revealing the single atomic nature of Fe species in the catalysts. The Fe absorption edge of the FeHS sample coincides with that of the Fe_2O_3 standard, indicating that Fe is present in the +3 oxidation state in the sample, while the low-valent species of iron was observed in the AuFeHS catalyst. For the AuFeHS sample, by linear combination fitting (LCF), we could see that it has a 72% contribution of Fe_2O_3 and 28% FeO (Figure S11). Figures S12 and S13 show the full EXAFS ($\mu(E)$ vs E) spectra of Au−Fe catalyst samples for the Fe edge and the Au edge, respectively. Figure S14 shows the normalized XANES spectra measured at the Au L_3-edge and that of the Au foil. The Au absorption edge of most samples coincides with that of the Au foil, showing that Au is in an elemental state in all of the samples. However, AuFeHS has an L_3 edge slightly higher than the Au metal edge, possibly due to some charge transfer, which is also evident as Au in the cationic form as inferred from XPS. From the radial distribution functions of all samples at the Fe K-edge, as shown in Figure 2d, the first peak appears at ~1.5 Å, which is at an appreciably lower value compared to that of the Fe foil. This shows that Fe is not in the elemental Fe state in the sample, as also demonstrated by the XANES data discussed above (also shown in Figure 2c). The peak at ~1.5 Å corresponds to two neighboring O shells with C.N. of 3 at 1.94 and 2.11 Å. The

https://doi.org/10.1021/acssuschemeng.4c02993

best fit $\chi(R)$ versus R plots (fitting range R = 0−4 Å) of all of the samples are shown in Figure 2d, and the best-fit values are shown in Table S2.

The radial distribution functions $\chi(R)$ versus R plots of all of the samples at the Au L_3-edge are shown in Figure S15. Contrary to the Fe edge data, here, the first major peak lies above 2 Å and close to that of the Au foil data, showing that the nearest neighbor of Au in these samples is Au itself and all samples are mostly in the elemental form. However, the first peak of AuFeHS is marginally shifted to a lower R, probably due to some charge transfer, as explained by XANES and XPS.

The presence of isolated metal atoms on the surface is probed through in situ IR spectroscopy (Figure S16).[45,46] The support shows no or little interaction with the CO molecules. The adsorption of CO on Au metal atoms shows different signals for various oxidation states. There were two detectable signals in the case of Au and Fe-loaded silica near 2105 and 2175 cm^{-1}. The signal centered at 2105 cm^{-1} is assigned to terminally adsorbed Au^0-CO, whereas the signal at 2175 cm^{-1} is assigned to $Au^{\delta+}$-CO.[47,48]

Catalytic Activity and Selectivity of Au−Fe Catalysts for Methane Oxidation

The initial screening of all of the catalysts for the partial oxidation of methane (POM) was carried out in a batch reactor at 10 bar methane pressure. The catalytic activity of hydrophobic silica (HS), monometallic Fe-HS, Au-HS, and bimetallic Au-Fe hydrophobic silica-supported catalysts was investigated. According to previous reports, an Fe loading of less than 1 wt % is found to be optimum for efficient methane activation, so we fixed the amount of Fe as 0.5 wt % in the catalyst and varied the Au loading.[49,50] The screening of bimetallic metal loadings was carried out, and the optimum was found to be 0.5 wt % Fe and 0.2 wt % of Au (Table S3). No product was detected for the reaction over the support (HS) (Figure S17). The FeHS catalyst gave a yield of 285 mmol/g_{Fe} with a methanol selectivity of 82% from the catalyst. Under a similar reaction condition, the AuFeHS catalyst gave a remarkable yield reaching 1666 mmol/g_{Fe+Au} with a selectivity of 95%, one of the highest selectivities reported yet.[10,43] The other component of the catalyst, AuHS, was also tested, and the yield was only 47.6 mmol/g_{Au} methanol, showing synergistic effects. CO_2 was observed as a side product with a selectivity of around 5%, showing 95% selectivity for the liquid oxygenates. Certainly, the optimal reaction conditions in a batch process involve maintaining a temperature of 60 °C and a methane pressure of 10 bar. During temperature optimization, initially raising the temperature enhances the catalyst's activity. However, further temperature escalation leads to diminished productivity due to the decomposition of H_2O_2 at higher temperatures. It is clear from Figure 3a that the AuFeHS catalyst exhibits peak performance at 60 °C, yielding 1666 mmol/g_{Fe+Au}.

Likewise, varying the methane pressures (ranging from 5 to 30 bar) in the reaction revealed optimal activity at a 10 bar methane pressure. The initial increase in activity can be attributed to the greater availability of methane reactant molecules. However, beyond 10 bar, the excess methane molecules obstruct the active sites responsible for H_2O_2 oxidation, thereby reducing reactivity (Figure 3b). The role of the hydrophobic support can be differentiated through the activity comparison of the supports, as Au and Fe supported on SBA-15 gave only 111 mmol/g_{Fe+Au} methanol under optimized conditions (Figure 3c) (detailed comparison in Table S4). A comparison of the catalytic activity data from the Au−Fe catalyst with the best reports in the literature shows the impressive performance of this catalyst. The better yields than the presented data are from Au−Pd colloidal particles[6] and on $Cu_2@C_3N_4$[10]-supported catalysts but suffer from poor (initial) selectivity and high-pressure conditions than those reported in this work (Table S6). The control experiments performed (Table S4, entries 1−3) showed that no product was detected without methane flow, oxidant, and catalyst.

Stephanolpolous and co-workers showed an elegant pathway for producing acetic acid during the partial oxidation of methane by introducing CO as a coreactant.[25] Zhong and co-workers recently reported the production of 3323 μmol/g_{cat} total oxygenate products, with 60% acetic acid selectivity, using CO in the reactant feed.[4]

Taking a cue from these reports, we carried out methane partial oxidation in the presence of CO, and the results are shown in Figure 3d. As intuited, there was a selectivity switch and acetic acid was formed as the main product with a yield of 3403 μmol/g_{cat} within 1 h of the reaction at 50 °C in the batch process with a total gas pressure of 20 bar (15 bar CH_4:5 bar CO). Methanol was observed as the only other liquid oxygenate product formed, with a yield of 166 μmol/g_{cat}. An increment in the gaseous product (CO_2) was observed with an increase in the reaction temperature (Figure 3d). In the case of the AuFeHS catalyst, the CO_2 selectivity was 10% when CO was added to the feed (Figure 3d) at 50 °C, while it was 5−6% when methane was only in the reactant feed under standardized conditions (Figure 3b). Gas chromatography (GC) and NMR confirmed product formation, and the yield was quantified by GC using standard calibrations. A representative NMR spectrum from the reaction mixture is attached in the Supporting Information (Figure S18), where the peaks corresponding to CH_3OH (δ = 3.3), dissolved CH_4 (δ = 0.15), and acetic acid (δ = 2.0) were observed in the NMR.

Following the batch process, where excellent yield and selectivity were demonstrated for methanol and acetic during the partial oxidation of methane, we extended the POM reaction in a continuous reactor. The scheme showing the partial oxidation reaction carried out in a fixed-bed reactor in a continuous flow process at atmospheric pressure is shown in Scheme 1. The continuous flow process at atmospheric

Scheme 1. Schematic Illustration of the Catalytic Reaction

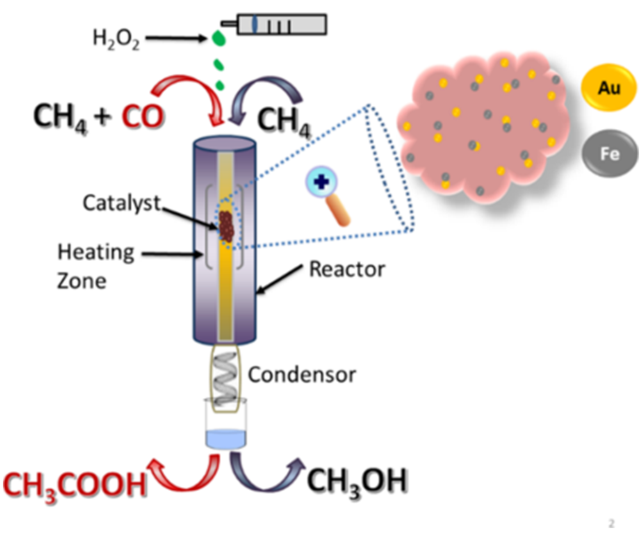

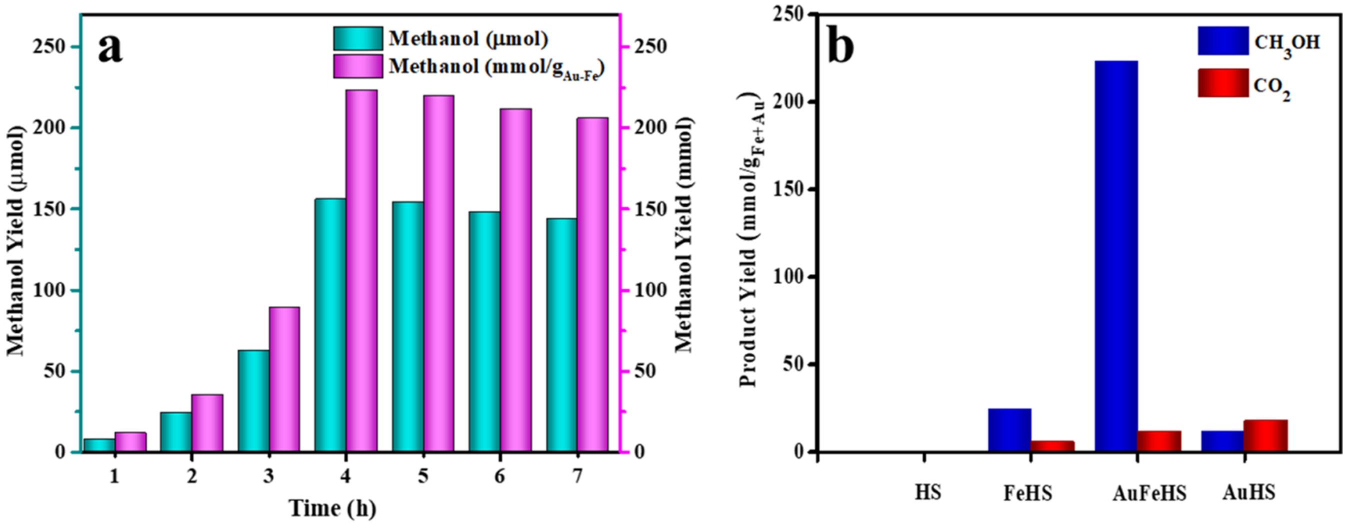

Figure 4. Catalytic activity of the various catalysts. (a) Catalytic activity of AuFeHS in a continuous flow reactor up to 7 h: reaction conditions: 100 mg of catalyst, 80 °C, 2 mL/h H_2O_2 (15% w/v) flow, methane flow 20 mL/min. (b) Catalytic activity of various catalysts in a continuous flow reactor: reaction conditions 100 mg of catalyst, 80 °C, 2 mL/h H_2O_2 (15% w/v) flow, methane flow 20 mL/min, 4 h.

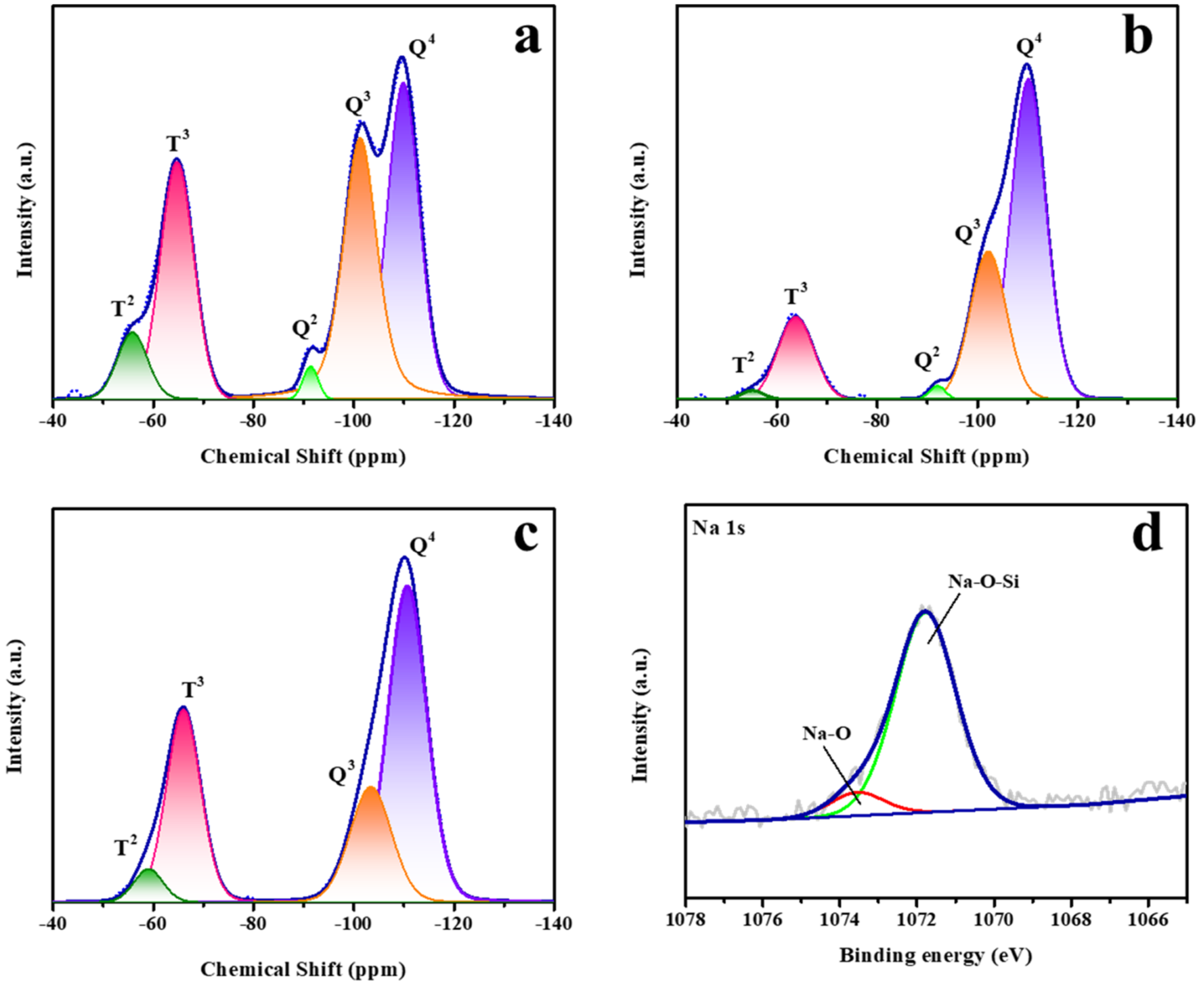

Figure 5. Characterizations of the various catalysts. (a) ^{29}Si MAS NMR spectrum of HS. (b) ^{29}Si MAS NMR spectrum of FeHS. (c) ^{29}Si MAS NMR spectrum of AuFeHS. (d) Na 1s XPS spectrum of AuFeHS.

pressure for up to 7 h showed steady methanol production (Figure 4a). The product yield reached a maximum at 4 h (157 μmol) under the optimized conditions. In the case of the HS catalyst, no product was observed, while methanol was observed as the main product when metal was deposited over HS. The FeHS catalyst produced 24.2 mmol/g_{Fe} methanol, while an outstanding product yield of 224 mmol/g_{Fe+Au} was reported in the case of AuFeHS. For the AuHS catalyst, 12 mmol/g_{Au} was the productivity within 4 h of the reaction (Figure 4b). The remarkable methanol yield of 422 μmol/h g_{cat} or 0.42 $mol_{methanol}/kg_{catalyst}$ h (for 4 h) from the AuFeHS catalyst is better than the reported value of 1.81 μmol/h g_{cat} methanol using O_2 as an oxidant at 210 °C[8] and 0.081 $mol_{Product}/kg_{catalyst}$ h under 20 bar pressure using H_2O_2 as an oxidant.[26] It is also exemplary because of the benign conditions (atmospheric pressure) used to carry out the POM to methanol. The introduction of CO to the reactant feed results in acetic acid formation as the main product, with methanol and CO_2 as side products. 648 μmol/g_{cat} acetic acid formed within 4 h of the reaction (Table S5, entry 2). The temperature optimization confirms that 80 °C is the best condition for the effective conversion of methane at atmospheric pressure (Table S5).

The background reaction from organic groups from the catalyst, which impart hydrophobicity to the catalyst, was ruled out by carrying out the isotope (CD_4) labeling experiments on the AuFeHS catalyst. The peak at 3.3 ppm showed multiplets in the ^1H NMR spectra, confirming that the methyl group in the alcohol originated from CD_4 rather than any other ligands from the support (Figure S19). The ^2H and ^{13}C NMR spectra further confirmed the presence of labeled methanol (Figure S20). Using nitrogen gas as a feed instead of methane resulted in no products, supporting the above experiment (Table S5, entry 3). Finally, a comparison with the recent literature values for the partial oxidation of methane to methanol using H_2O_2 as an oxidant is given (Table S6). Clearly, the AuFeHS catalyst catalyzed the partial oxidation of methane to methanol or acetic acid with exceptional yields at previously considered unfavorable conditions.

The unprecedented activity of the AuFeHS catalyst for the highly selective partial oxidation of methane to methanol and acetic acid under benign conditions could be largely understood based on the synergy between Fe and Au, which are individually known to catalyze this reaction with H_2O_2 at high-pressure conditions. The synergistic effects between Au and Fe are also evident in the case of SBA-15 as the production of methanol (0.78 mmol/g_{cat}) was observed in the case of AuFe deposited over SBA-15 using the same synthesis method (Table S4, entry 9). Fe-SBA-15 and Au-SBA-15 were able to produce only 0.30 and 0.15 mmol/g_{cat} methanol, respectively (Table S4, entries 7 and 8). Thus, the hydrophobicity of silica and the synergistic effect are key for enhanced activity for the POM reaction. One of the challenges in designing low-pressure, low-temperature methane activation catalysts is stabilizing the active species, which are easily poisoned by reacting oxidants like O_2, H_2O_2, or H_2O.[51] In our case, low-valent $Fe^{\delta+}$, which can simultaneously activate both CH_4 and H_2O_2, is generated and stabilized by Au. The intimate interaction between Fe and Au in the catalyst was evident from STEM line analysis (Figure S21). Solid-state NMR revealed the atomic environment of the disordered structure of hydrophobic silica. For the HS, ^{29}Si (Figure 5a) confirmed the presence of Q^2, Q^3, Q^4, and T^2, T^3 states.[52,53] When Fe was deposited using NaOH, Na atoms were incorporated in the silica matrix by making the Si−O−Na framework, confirmed by the decrement in the Q^3 and Q^2 states (Figure 5b). A further decrease in the Q^3 and Q^2 states was seen after the NaOH-assisted Au deposition (Figure 5c). The Na 1s XPS spectrum confirmed the interaction of the Si−O−Na (Figure 5d) environment.[54,55] In the ^{23}Na NMR spectrum, 7.32 ppm and −1.59 ppm peaks confirmed the presence of the Si−O−Na framework[56] (Figures S22 and S23). XPS and EDAX analyses supported the data. The pyridine-adsorbed FT-IR spectrum of the AuFeHS catalyst exhibits characteristic bands in the region 1400−1500 cm^{-1} (Figure S24). The band at 1449 cm^{-1} is assigned to Lewis acid sites bonded to pyridine.[57,58] The band at ∼1640 cm^{-1} is observed due to the −OH deformation vibrations and the physisorbed water molecules onto the surface of the materials.[59] It should be noted that the amount of physisorbed water over the hydrophobic catalyst was much less compared with SBA-15 (Figure S3). The acidic sites on the bimetallic catalysts are crucial here and are well-known for the C−H sigma complex for methane activation[60] and help in the regeneration of $Fe^{\delta+}$ sites.[61] The activated C−H sigma complex is converted to the CH_3 radical on the low-valent $Fe^{3-\delta+}$ sites. Once the CH_3 and OH radicals are formed, methanol formation, facile CO insertion, and generation of acetic acid become easy. It is imperative to conclude that Au nanoparticles, being excellent CO oxidation catalysts, provide low-energy activation sites for the adsorption of CO.[62] Even though we have optimized the catalysts based on bimetallic compositions, the role of Na and Lewis acid sites in the overall POM reaction is worth exploring and is beyond the scope of this study.

CONCLUSIONS

In summary, we have reported AuFeHS, a bimetallic catalyst supported on modified sodium containing silica (HS), for the continuous flow oxidation of methane to value-added products at ambient pressure and mild temperatures using H_2O_2 as an oxidant. The highly selective conversion of methane to methanol (>95%) with a yield of 1666 mmol/$g_{(Au+Fe)}$ within 30 min in the batch process indicates the presence of highly active sites in the material, and the production of methanol in a continuous flow process with a yield of 224 mmol/$g_{(Fe+Au)}$ opens the doors for the activation of methane at atmospheric conditions. While the synergistic effect between Au and Fe metals with sufficient acidic sites over the silica support catalyzes the production of a high amount of methanol and acetic acid under benign conditions, care should be taken to prepare the support, which helps keep the peroxide radical close to the active metal sites. We believe that tuning active Fe species through bimetallic modulation is a clever way to achieve the catalytic conversion of lower alkanes to oxygenates, opening the scope for the commercialization of M2O (methane to oxygenates) technologies.

ASSOCIATED CONTENT

Supporting Information

The Supporting Information is available free of charge at https://pubs.acs.org/doi/10.1021/acssuschemeng.4c02993.

Synthesis of HS, FeHS, and AuFeHS; material characterization methods; procedure and optimizations of the catalytic reactions; product calculation and XAS calculations; and activity data figures and tables (PDF)

AUTHOR INFORMATION

Corresponding Author

C. P. Vinod − *Catalysis and Inorganic Chemistry Division, CSIR-National Chemical Laboratory, Pune 411008, India; Academy of Scientific and Innovative Research (AcSIR), Ghaziabad 201002, India;* orcid.org/0000-0001-9857-4907; Phone: +91-20-2590-2086; Email: cp.vinod@ncl.res.in

Authors

Anuradha V. Jagtap − *Catalysis and Inorganic Chemistry Division, CSIR-National Chemical Laboratory, Pune 411008, India; Academy of Scientific and Innovative Research (AcSIR), Ghaziabad 201002, India*

Pawan Kumar − *Catalysis and Inorganic Chemistry Division, CSIR-National Chemical Laboratory, Pune 411008, India; Academy of Scientific and Innovative Research (AcSIR), Ghaziabad 201002, India;* orcid.org/0000-0002-2206-0210

Sharad Gupta − *Catalysis and Inorganic Chemistry Division, CSIR-National Chemical Laboratory, Pune 411008, India;* orcid.org/0000-0003-4368-8338

Abharana Nagendra − *Atomic and Molecular Physics Division, Bhabha Atomic Research Centre (BARC), Mumbai 400085, India*

Shambhu Nath Jha − *Atomic and Molecular Physics Division, Bhabha Atomic Research Centre (BARC), Mumbai 400085, India*

D. Bhattacharyya − *Atomic and Molecular Physics Division, Bhabha Atomic Research Centre (BARC), Mumbai 400085, India;* orcid.org/0000-0002-1657-1858

Thalasseril G. Ajithkumar − *Physical and Materials Chemistry Division and Central NMR Facility, CSIR-National Chemical Laboratory, Pune 411008, India;* orcid.org/0000-0002-9217-2138

Complete contact information is available at:
https://pubs.acs.org/10.1021/acssuschemeng.4c02993

Author Contributions

$^{\perp}$A.V.J. and P.K. contributed equally to this work. C.P.V. conceptualized the project; A.V.J., P.K., and S.G. carried out the investigation; C.P.V. obtained funding acquisition; C.P.V., T.G.A. (NMR), S.N.J., and D.B. (EXAFS) performed the supervision; C.P.V., P.K., A.V.J., and S.G. wrote the original draft; and C.P.V., T.G.A. (NMR), S.N.J. (EXAFS), and D.B. (EXAFS) performed the final writing, review and editing.

Notes

The authors declare no competing financial interest.

ACKNOWLEDGMENTS

AVJ and PK thank CSIR and CSIR-UGC for the research fellowship. CPV thanks the Director CSIR-NCL and the Council of Scientific and Industrial Research (CSIR) for funding through in-house grant MLP030626. The authors thank Ms. N. Patil for solid state NMR data collection and Dr. Sapna Ravindranathan for useful discussions regarding isotope NMR experiments.

REFERENCES

(1) Luo, L.; Luo, J.; Li, H.; Ren, F.; Zhang, Y.; Liu, A.; Li, W.-X.; Zeng, J. Water Enables Mild Oxidation of Methane to Methanol on Gold Single-Atom Catalysts. *Nat. Commun.* **2021**, *12* (1), No. 1218, DOI: 10.1038/s41467-021-21482-z.

(2) Hamzehlouia, S.; Jaffer, S. A.; Chaouki, J. Microwave Heating-Assisted Catalytic Dry Reforming of Methane to Syngas. *Sci. Rep.* **2018**, *8* (1), No. 8940, DOI: 10.1038/s41598-018-27381-6.

(3) Latimer, A. A.; Kulkarni, A. R.; Aljama, H.; Montoya, J. H.; Yoo, J. S.; Tsai, C.; Abild-Pedersen, F.; Studt, F.; Nørskov, J. K. Understanding Trends in C−H Bond Activation in Heterogeneous Catalysis. *Nat. Mater.* **2017**, *16* (2), 225−229.

(4) Wu, B.; Lin, T.; Lu, Z.; Yu, X.; Huang, M.; Yang, R.; Wang, C.; Tian, C.; Li, J.; Sun, Y.; Zhong, L. Fe Binuclear Sites Convert Methane to Acetic Acid with Ultrahigh Selectivity. *Chem* **2022**, *8* (6), 1658−1672.

(5) Qi, G.; Davies, T. E.; Nasrallah, A.; Sainna, M. A.; Howe, A. G. R.; Lewis, R. J.; Quesne, M.; Catlow, C. R. A.; Willock, D. J.; He, Q.; Bethell, D.; Howard, M. J.; Murrer, B. A.; Harrison, B.; Kiely, C. J.; Zhao, X.; Deng, F.; Xu, J.; Hutchings, G. J. Au-ZSM-5 Catalyses the Selective Oxidation of CH_4 to CH_3OH and CH_3COOH Using O_2. *Nat. Catal.* **2022**, *5* (1), 45−54.

(6) Agarwal, N.; Freakley, S. J.; McVicker, R. U.; Althahban, S. M.; Dimitratos, N.; He, Q.; Morgan, D. J.; Jenkins, R. L.; Willock, D. J.; Taylor, S. H.; Kiely, C. J.; Hutchings, G. J. Aqueous Au-Pd Colloids Catalyze Selective CH_4 Oxidation to CH_3OH with O_2 under Mild Conditions. *Science* **2017**, *358* (6360), 223−227.

(7) Xie, J.; Jin, R.; Li, A.; Bi, Y.; Ruan, Q.; Deng, Y.; Zhang, Y.; Yao, S.; Sankar, G.; Ma, D.; Tang, J. Highly Selective Oxidation of Methane to Methanol at Ambient Conditions by Titanium Dioxide-Supported Iron Species. *Nat. Catal.* **2018**, *1* (11), 889−896.

(8) Narsimhan, K.; Iyoki, K.; Dinh, K.; Román-Leshkov, Y. Catalytic Oxidation of Methane into Methanol over Copper-Exchanged Zeolites with Oxygen at Low Temperature. *ACS Cent. Sci.* **2016**, *2* (6), 424−429.

(9) Jin, Z.; Wang, L.; Zuidema, E.; Mondal, K.; Zhang, M.; Zhang, J.; Wang, C.; Meng, X.; Yang, H.; Mesters, C.; Xiao, F.-S. Hydrophobic Zeolite Modification for in Situ Peroxide Formation in Methane Oxidation to Methanol. *Science* **2020**, *367* (6474), 193−197.

(10) Xie, P.; Ding, J.; Yao, Z.; Pu, T.; Zhang, P.; Huang, Z.; Wang, C.; Zhang, J.; Zecher-Freeman, N.; Zong, H.; Yuan, D.; Deng, S.; Shahbazian-Yassar, R.; Wang, C. Oxo Dicopper Anchored on Carbon Nitride for Selective Oxidation of Methane. *Nat. Commun.* **2022**, *13* (1), No. 1375, DOI: 10.1038/s41467-022-28987-1.

(11) Ni, F.; Richards, T.; Smith, L. R.; Morgan, D. J.; Davies, T. E.; Lewis, R. J.; Hutchings, G. J. Selective Oxidation of Methane to Methanol via In Situ H_2O_2 Synthesis. *ACS Org. Inorg. Au* **2023**, 3, 177.

(12) Zhao, W.; Shi, Y.; Jiang, Y.; Zhang, X.; Long, C.; An, P.; Zhu, Y.; Shao, S.; Yan, Z.; Li, G.; Tang, Z. Fe-O Clusters Anchored on Nodes of Metal−Organic Frameworks for Direct Methane Oxidation. *Angew. Chem., Int. Ed.* **2021**, *60* (11), 5811−5815.

(13) Zhou, H.; Liu, T.; Zhao, X.; Zhao, Y.; Lv, H.; Fang, S.; Wang, X.; Zhou, F.; Xu, Q.; Xu, J.; Xiong, C.; Xue, Z.; Wang, K.; Cheong, W.; Xi, W.; Gu, L.; Yao, T.; Wei, S.; Hong, X.; Luo, J.; Li, Y.; Wu, Y. A Supported Nickel Catalyst Stabilized by a Surface Digging Effect for Efficient Methane Oxidation. *Angew. Chem.* **2019**, *131* (51), 18559−18564.

(14) Ab Rahim, M. H.; Armstrong, R. D.; Hammond, C.; Dimitratos, N.; Freakley, S. J.; Forde, M. M.; Morgan, D. J.; Lalev, G.; Jenkins, R. L.; Lopez-Sanchez, J. A.; Taylor, S. H.; Hutchings, G. J. Low Temperature Selective Oxidation of Methane to Methanol Using Titania Supported Gold Palladium Copper Catalysts. *Catal. Sci. Technol.* **2016**, *6* (10), 3410−3418.

(15) Yuan, J.; Zhang, W.; Li, X.; Yang, J. A High Performance Catalyst for Methane Conversion to Methanol: Graphene Supported Single Atom Co. *Chem. Commun.* **2018**, *54* (18), 2284−2287.

(16) Wang, A.; Li, J.; Zhang, T. Heterogeneous Single-Atom Catalysis. *Nat. Rev. Chem.* **2018**, *2*, 65−81, DOI: 10.1038/s41570-018-0010-1.

(17) Shen, Q.; Cao, C.; Huang, R.; Zhu, L.; Zhou, X.; Zhang, Q.; Gu, L.; Song, W. Single Chromium Atoms Supported on Titanium

Dioxide Nanoparticles for Synergic Catalytic Methane Conversion under Mild Conditions. *Angew. Chem.* **2020**, *132* (3), 1232−1235.

(18) Cui, X.; Li, H.; Wang, Y.; Hu, Y.; Hua, L.; Li, H.; Han, X.; Liu, Q.; Yang, F.; He, L.; Chen, X.; Li, Q.; Xiao, J.; Deng, D.; Bao, X. Room-Temperature Methane Conversion by Graphene-Confined Single Iron Atoms. *Chem* **2018**, *4* (8), 1902−1910.

(19) Osadchii, D. Y.; Olivos-Suarez, A. I.; Szécsényi, Á.; Li, G.; Nasalevich, M. A.; Dugulan, I. A.; Crespo, P. S.; Hensen, E. J. M.; Veber, S. L.; Fedin, M. V.; Sankar, G.; Pidko, E. A.; Gascon, J. Isolated Fe Sites in Metal Organic Frameworks Catalyze the Direct Conversion of Methane to Methanol. *ACS Catal.* **2018**, *8* (6), 5542−5548.

(20) Bai, S.; Liu, F.; Huang, B.; Li, F.; Lin, H.; Wu, T.; Sun, M.; Wu, J.; Shao, Q.; Xu, Y.; Huang, X. High-Efficiency Direct Methane Conversion to Oxygenates on a Cerium Dioxide Nanowires Supported Rhodium Single-Atom Catalyst. *Nat. Commun.* **2020**, *11* (1), No. 954, DOI: 10.1038/s41467-020-14742-x.

(21) Antil, N.; Chauhan, M.; Akhtar, N.; Newar, R.; Begum, W.; Malik, J.; Manna, K. Metal−Organic Framework-Encaged Monomeric Cobalt(III) Hydroperoxides Enable Chemoselective Methane Oxidation to Methanol. *ACS Catal.* **2022**, *12* (18), 11159−11168.

(22) Tang, X.; Wang, L.; Yang, B.; Fei, C.; Yao, T.; Liu, W.; Lou, Y.; Dai, Q.; Cai, Y.; Cao, X. M.; Zhan, W.; Guo, Y.; Gong, X. Q.; Guo, Y. Direct Oxidation of Methane to Oxygenates on Supported Single Cu Atom Catalyst. *Appl. Catal., B* **2021**, *28* (5), No. 119827, DOI: 10.1016/j.apcatb.2020.119827.

(23) Grundner, S.; Markovits, M. A. C.; Li, G.; Tromp, M.; Pidko, E. A.; Hensen, E. J. M.; Jentys, A.; Sanchez-Sanchez, M.; Lercher, J. A. Single-Site Trinuclear Copper Oxygen Clusters in Mordenite for Selective Conversion of Methane to Methanol. *Nat. Commun.* **2015**, *6*, No. 7546, DOI: 10.1038/ncomms8546.

(24) Huang, W.; Zhang, S.; Tang, Y.; Li, Y.; Nguyen, L.; Li, Y.; Shan, J.; Xiao, D.; Gagne, R.; Frenkel, A. I.; Tao, F. F. Low-Temperature Transformation of Methane to Methanol on Pd_1O_4 Single Sites Anchored on the Internal Surface of Microporous Silicate. *Angew. Chem.* **2016**, *128* (43), 13639−13643.

(25) Shan, J.; Li, M.; Allard, L. F.; Lee, S.; Flytzani-Stephanopoulos, M. Mild Oxidation of Methane to Methanol or Acetic Acid on Supported Isolated Rhodium Catalysts. *Nature* **2017**, *551* (7682), 605−608.

(26) Xu, J.; Armstrong, R. D.; Shaw, G.; Dummer, N. F.; Freakley, S. J.; Taylor, S. H.; Hutchings, G. J. Continuous Selective Oxidation of Methane to Methanol over Cu- and Fe-Modified ZSM-5 Catalysts in a Flow Reactor. *Catal. Today* **2016**, *270*, 93−100.

(27) Álvarez, M.; Marín, P.; Ordóñez, S. Harnessing of Diluted Methane Emissions by Direct Partial Oxidation of Methane to Methanol over Cu/Mordenite. *Ind. Eng. Chem. Res.* **2021**, *60* (26), 9409−9417.

(28) Xu, R.; Liu, N.; Dai, C.; Li, Y.; Zhang, J.; Wu, B.; Yu, G.; Chen, B. H $_2$ O-Built Proton Transfer Bridge Enhances Continuous Methane Oxidation to Methanol over Cu-BEA Zeolite. *Angew. Chem., Int. Ed.* **2021**, *60* (30), 16634−16640.

(29) Yang, G. S.; Kang, J.; Park, E. D. Aqueous-Phase Partial Oxidation of Methane over Pd−Fe/ZSM-5 with O_2 in the Presence of H_2. *ChemCatChem* **2023**, *15* (7), No. e202201630, DOI: 10.1002/cctc.202201630.

(30) Soni, Y.; Pradhan, S.; Bamnia, M. K.; Yadav, A. K.; Jha, S. N.; Bhattacharyya, D.; Khan, T. S.; Haider, M. A.; Vinod, C. P. Spectroscopic Evidences for the Size Dependent Generation of Pd Species Responsible for the Low Temperature CO Oxidation Activity on Pd-SBA-15 Nanocatalyst. *Appl. Catal., B* **2020**, *272*, No. 118934.

(31) Wang, H.; Xin, W.; Wang, Q.; Zheng, X.; Lu, Z.; Pei, R.; He, P.; Dong, X. Direct Methane Conversion with Oxygen and CO over Hydrophobic DB-ZSM-5 Supported Rh Single-Atom Catalyst. *Catal. Commun.* **2022**, *162*, No. 106374.

(32) Carter, J. H.; Lewis, R. J.; Demetriou, N.; Williams, C.; Davies, T. E.; Qin, T.; Dummer, N. F.; Morgan, D. J.; Willock, D. J.; Liu, X.; Taylor, S. H.; Hutchings, G. J. The Selective Oxidation of Methane to Methanol Using *in Situ* Generated H_2O_2 over Palladium-Based Bimetallic Catalysts. *Catal. Sci. Technol.* **2023**, *13* (20), 5848−5858.

(33) Daté, M.; Haruta, M. Moisture Effect on CO Oxidation over Au/TiO_2 Catalyst. *J. Catal.* **2001**, *201* (2), 221−224.

(34) Daté, M.; Okumura, M.; Tsubota, S.; Haruta, M. Vital Role of Moisture in the Catalytic Activity of Supported Gold Nanoparticles. *Angew. Chem., Int. Ed.* **2004**, *43* (16), 2129−2132.

(35) Sun, G.; Jin, Y.; Zhang, Z.; Wang, Z.; Chai, P.; Xiong, F.; Huang, W. The Double-Edged Sword Effect of Water in the Low-Temperature CO Oxidation on Pt(111) Surface. *J. Phys. Chem. C* **2018**, *122* (39), 22530−22537.

(36) Ikbal, S. A.; Colomban, C.; Zhang, D.; Delecluse, M.; Brotin, T.; Dufaud, V.; Dutasta, J.-P.; Sorokin, A. B.; Martinez, A. Bioinspired Oxidation of Methane in the Confined Spaces of Molecular Cages. *Inorg. Chem.* **2019**, *58* (11), 7220−7228.

(37) Claveau, E. E.; Sader, S.; Jackson, B. A.; Khan, S. N.; Miliordos, E. Transition Metal Oxide Complexes as Molecular Catalysts for Selective Methane to Methanol Transformation: Any Prospects or Time to Retire? *Phys. Chem. Chem. Phys.* **2023**, *25* (7), 5313−5326.

(38) Liu, J.-C.; Wang, Y.-G.; Li, J. Toward Rational Design of Oxide-Supported Single-Atom Catalysts: Atomic Dispersion of Gold on Ceria. *J. Am. Chem. Soc.* **2017**, *139* (17), 6190−6199.

(39) Zhang, H.; Liu, G.; Shi, L.; Ye, J. Single-Atom Catalysts: Emerging Multifunctional Materials in Heterogeneous Catalysis. *Adv. Energy Mater.* **2018**, *8* (1), No. 1701343.

(40) Yang, T.; Meng, L.; Han, S.; Hou, J.; Wang, S.; Wang, X. Simultaneous Reductive and Sorptive Removal of Cr(<scp > vi</Scp>) by Activated Carbon Supported *β*-FeOOH. *RSC Adv.* **2017**, *7* (55), 34687−34693.

(41) Simons, M. C.; Prinslow, S. D.; Babucci, M.; Hoffman, A. S.; Hong, J.; Vitillo, J. G.; Bare, S. R.; Gates, B. C.; Lu, C. C.; Gagliardi, L.; Bhan, A. Beyond Radical Rebound: Methane Oxidation to Methanol Catalyzed by Iron Species in Metal−Organic Framework Nodes. *J. Am. Chem. Soc.* **2021**, *143* (31), 12165−12174.

(42) Vitillo, J. G.; Bhan, A.; Cramer, C. J.; Lu, C. C.; Gagliardi, L. Quantum Chemical Characterization of Structural Single Fe(II) Sites in MIL-Type Metal−Organic Frameworks for the Oxidation of Methane to Methanol and Ethane to Ethanol. *ACS Catal.* **2019**, *9* (4), 2870−2879.

(43) Sun, S.; Barnes, A. J.; Gong, X.; Lewis, R. J.; Dummer, N. F.; Bere, T.; Shaw, G.; Richards, N.; Morgan, D. J.; Hutchings, G. J. Lanthanum Modified Fe-ZSM-5 Zeolites for Selective Methane Oxidation with H $_2$ O $_2$. *Catal. Sci. Technol.* **2021**, *11* (24), 8052−8064.

(44) Szécsényi, Á.; Li, G.; Gascon, J.; Pidko, E. A. Mechanistic Complexity of Methane Oxidation with H_2O_2 by Single-Site Fe/ZSM-5 Catalyst. *ACS Catal.* **2018**, *8* (9), 7961−7972.

(45) Meunier, F. C. Relevance of IR Spectroscopy of Adsorbed CO for the Characterization of Heterogeneous Catalysts Containing Isolated Atoms. *J. Phys. Chem. C* **2021**, *125* (40), 21810−21823.

(46) Calle-Vallejo, F.; Tymoczko, J.; Colic, V.; Vu, Q. H.; Pohl, M. D.; Morgenstern, K.; Loffreda, D.; Sautet, P.; Schuhmann, W.; Bandarenka, A. S. Finding Optimal Surface Sites on Heterogeneous Catalysts by Counting Nearest Neighbors. *Science* **2015**, *350* (6257), 185−189.

(47) Wang, X.; Rosspeintner, A.; Ziarati, A.; Zhao, J.; Bürgi, T. Insight into the Transient Inactivation Effect on Au/TiO_2 Catalyst by in-Situ DRIFT and UV−Vis Spectroscopy. *Nat. Commun.* **2022**, *13* (1), No. 5458, DOI: 10.1038/s41467-022-33187-y.

(48) Wei, S.; Fu, X.-P.; Wang, W.-W.; Jin, Z.; Song, Q.-S.; Jia, C.-J. Au/TiO_2 Catalysts for CO Oxidation: Effect of Gold State to Reactivity. *J. Phys. Chem. C* **2018**, *122* (9), 4928−4936.

(49) Yu, T.; Li, Z.; Lin, L.; Chu, S.; Su, Y.; Song, W.; Wang, A.; Weckhuysen, B. M.; Luo, W. Highly Selective Oxidation of Methane into Methanol over Cu-Promoted Monomeric Fe/ZSM-5. *ACS Catal.* **2021**, *11* (11), 6684−6691.

(50) Hammond, C.; Forde, M. M.; Ab Rahim, M. H.; Thetford, A.; He, Q.; Jenkins, R. L.; Dimitratos, N.; Lopez-Sanchez, J. A.; Dummer, N. F.; Murphy, D. M.; Carley, A. F.; Taylor, S. H.; Willock, D. J.;

Stangland, E. E.; Kang, J.; Hagen, H.; Kiely, C. J.; Hutchings, G. J. Direct Catalytic Conversion of Methane to Methanol in an Aqueous Medium by Using Copper-Promoted Fe-ZSM-5. *Angew. Chem., Int. Ed.* **2012**, *51* (21), 5129−5133.

(51) Tang, Y.; Li, Y.; Feng Tao, F. Activation and Catalytic Transformation of Methane under Mild Conditions. *Chem. Soc. Rev.* **2022**, *51* (1), 376−423.

(52) Protsak, I. S.; Morozov, Y. M.; Dong, W.; Le, Z.; Zhang, D.; Henderson, I. M. A 29Si, 1H, and 13C Solid-State NMR Study on the Surface Species of Various Depolymerized Organosiloxanes at Silica Surface. *Nanoscale Res. Lett.* **2019**, *14* (1), 160.

(53) Gadzała-Kopciuch, R.; Kluska, M.; Wełniak, M.; Buszewski, B. Silicon Dioxide Surfaces with Aryl Interaction Sites for Chromatographic Applications. *Mater. Chem. Phys.* **2005**, *89* (2−3), 228−237.

(54) Mekki, A.; Holland, D.; McConville, C. F.; Salim, M. An XPS Study of Iron Sodium Silicate Glass Surfaces. *J. Non Cryst. Solids* **1996**, *208* (3), 267−276.

(55) Dong, B.; Xu, Y.; Lin, S.; Dai, X. Characterizing and Exploring the Formation Mechanism of Salt Deposition by Reusing Advanced-Softened, Silica-Rich, Oilfield-Produced Water (ASOW) in Superheated Steam Pipeline. *Sci. Rep.* **2015**, *5* (1), No. 17274, DOI: 10.1038/srep17274.

(56) Koller, H.; Engelhardt, G.; Kentgens, A. P. M.; Sauer, J. 23Na NMR Spectroscopy of Solids: Interpretation of Quadrupole Interaction Parameters and Chemical Shifts. *J. Phys. Chem. A* **1994**, *98* (6), 1544−1551.

(57) Li, Y.; Zhang, W.; Zhang, L.; Yang, Q.; Wei, Z.; Feng, Z.; Li, C. Direct Synthesis of Al−SBA-15 Mesoporous Materials via Hydrolysis-Controlled Approach. *J. Phys. Chem. B* **2004**, *108* (28), 9739−9744.

(58) Udayakumar, V.; Pandurangan, A. Synthesis of Hf/SBA-15 Lewis Acid Catalyst for Converting Glycerol to Value-Added Chemicals. *J. Porous Mater.* **2017**, *24* (4), 979−990.

(59) Gabla, J. J.; Lathiya, D. R.; Revawala, A. A.; Maheria, K. C. Propyl−SO3H Functionalized SBA-15: Microwave-Mediated Green Synthesis of Biologically Active Multi-Substituted Imidazole Scaffolds. *Res. Chem. Intermed.* **2019**, *45* (4), 1863−1881.

(60) Raynes, S.; Shah, M. A.; Taylor, R. A. Direct Conversion of Methane to Methanol with Zeolites: Towards Understanding the Role of Extra-Framework d-Block Metal and Zeolite Framework Type. *Dalton Trans.* **2019**, *48* (28), 10364−10384.

(61) Krisnandi, Y. K.; Nurani, D. A.; Alfian, D. V.; Sofyani, U.; Faisal, M.; Saragi, I. R.; Pamungkas, A. Z.; Pratama, A. P. The New Challenge of Partial Oxidation of Methane over Fe_2O_3/NaY and Fe_3O_4/NaY Heterogeneous Catalysts. *Heliyon* **2021**, *7* (11), No. e08305.

(62) Ha, H.; Yoon, S.; An, K.; Kim, H. Y. Catalytic CO Oxidation over Au Nanoparticles Supported on CeO_2 Nanocrystals: Effect of the Au−CeO_2 Interface. *ACS Catal.* **2018**, *8* (12), 11491−11501.